SQUEEZE FLOW DURING ASSEMBLY OF NOVEL JOINTS IN COMPOSITE AIRCRAFT COMPONENTS

By

Dipl.-Ing. Patryk Burka

This thesis is submitted in fulfillment of

the requirements for the degree of Doctor of Philosophy,

Department of Mechanical & Aerospace Engineering

Monash University

December 2009

Summary

An adhesive bonding process for composite spar-to-skin structures which can be found in various aircraft components is proposed. In this process, referred to as the Insertion Squeeze Flow (ISF) bonding process, a spar is inserted into a substructure which is integrated into the composite skin. The cross-sectional shape of the substructure is similar to the Greek letter π (Pi), the roof of the π being attached to the skin, and this substructure is referred to as a Pi-slot. Before the insertion process is started, adhesive is placed into the Pi-slot bottom and due to the insertion of the spar distributes into the gaps, or flow channels, between the spar and the Pi-slot.

The adhesives that can be used for the conduction of the ISF processes were analysed in order to develop an adhesive material model that can be used to represent the adhesive in computational analysis. The adhesives Hysol EA 9395 and Hysol EA 9396 were selected to be used for the ISF bonding process. A mixing ratio by weight of 70 – 30 EA 9395 to EA 9396 was determined to have the lowest acceptable viscosity. The upper viscosity limit was determined as the viscosity of EA 9395, which is the more viscous of the two adhesives. Rheological tests showed that all studied adhesives are non-Newtonian, shear thinning fluids. Furthermore, their time dependence appeared to be small and their elasticity negligible. Constitutive material models (a Power law model and a five parameter rational model) were derived based on shear viscosity versus shear strain rate results.

In order to develop a two-dimensional (2D) numerical model for ISF using computational fluid dynamics (CFD) software, a simplified ISF process was studied first. A Newtonian fluid was specified as the fluid to be displaced by the insertion process and numerical predictions were compared to the solutions of a derived analytical model for the same problem setup, showing good agreement. To simulate the actual ISF bonding process, the material models developed for the adhesives were implemented into this numerical model. The agreement between experimental data and numerical predictions was good.

ISF bonding processes conducted at constant insertion speed were studied numerically applying the developed numerical 2D model. Insertion forces and pressures acting along the Pi-slot walls were predicted and discussed for various insertion speeds, adhesive viscosities, flow channel widths and insertion plate head designs. The main findings were a

linear relationship between the insertion force and the insertion speed as well as a linear relationship between the maximum pressure along the Pi-slot walls and the insertion speed. The pressure was found to distribute approximately linearly along the Pi-slot wall, with a maximum reached at the root of the Pi-slot wall. The ratio between the insertion force and the maximum pressure was found to be independent of the insertion speed and the adhesive viscosity. The established understanding of forces and pressures during ISF supports the development of an ISF bonding process in terms of component design and in terms of bonding facility design.

The effect of lateral misalignment was studied numerically in order to ensure complete adhesive distribution during ISF. A dimensionless parameter ξ was defined referring the wide to the narrow flow channel width and its effect on the adhesive distribution evaluated. A second dimensionless parameter ψ was introduced which defines the ratio between the flow front in the narrow and the flow front in the wide flow channel. One main finding of this evaluation was that these two dimensionless parameters were found to be linearly related with each other. Furthermore, it was found that this relationship was not affected by the insertion speed, adhesive viscosity, initially applied adhesive volume and scarcely affected by the insertion plate width variation. It was, however, affected by the shape of the insertion plate head, with the rectangular head shape found to be the one most difficult to fill. Procedures were proposed to ensure entire filling of the flow channels, consequently leading to a desired Pi-joint quality, for this rectangular head shape.

Finally, the developed 2D numerical model was extended in regard to four aspects: the consideration of the insertion control (at constant insertion speed or constant insertion force), the consideration of a slight variation of the ISF process (ISF with adhesive pre-application), the involvement of a fluid-structure-interaction (FSI) and finally the consideration of ISF modelled three-dimensionally (3D). An ISF process conducted at constant insertion force control was implemented into the numerical model and predictions showed that relationships derived from constant insertion speed simulations were also valid for constant force insertions. The effect of a FSI on the adhesive showed a negative effect on the adhesive distribution compared to rigid Pi-slot walls, and two suggestions were proposed to eliminate this effect in practice. Finally, three-dimensional (3D) simulations were conducted to study the effect of a longitudinal misalignment. In the considered range the adhesive flow was scarcely affected by this misalignment.

The detailed understanding of the adhesive flow during ISF is supportive for the design of an adhesive bonding process that can be used to join spar-to-skin structures as found in

aircraft components. The outcomes of the presented research work can be used as a guide to ensure the joint quality of these spar-to-skin structures.

Declaration of Originality

I, Patryk Burka, declare that this thesis contains no material which has been accepted for the award of any other degree or diploma in any university or other institution.

To the best of my knowledge, this thesis contains no material previously published or written by another person, except where due reference is made in the text of the thesis.

Patryk Burka, December 2009

Acknowledgements

Contents

List of Tables

List of Figures

Abbreviations and Acronyms

AFRL/ML	Air Force Research Laboratory and Manufacturing Directory
BC	boundary condition
CAI	Composite Affordability Initiative
CCD	charged couple device (camera)
CFD	computational fluid dynamics
CFL	Courant-Lewy
CFRP	carbon-fibre-reinforced plastics
CPU	computer processing unit
EWI	Edison Welding Institute
FEA	finite element analysis
FEM	finite element modelling
FRP	fibre-reinforced polymers
FSI	fluid structure interaction
ISF	insertion squeeze flow
LCD	liquid crystal display
MBM	modified Bautisto-Manero (model)
MOJO	Modular Joints for Composite Aircraft Structures
MTI	mouldable thermoplastic interface
NCF	non crimp fabric
NDT	non-destructive testing
RAM	random access memory
VARTM	vacuum assisted resin transfer moulding

Nomenclature

A	shear viscosity extrapolated to zero shear rate
a	half insertion plate width
a	thermal diffusivity
b	half Pi-slot width
c	flow front
c_D	drag coefficient
c_N	flow front (narrow channel)
c_W	flow front (wide channel)l
D	drag force
D^P	rate of plastic shape change
E	Youngs (in-plane) modulus
e	error
F	bending force
F	insertion force
F	tensile loading
F_c	constant insertion force
F_f	acting shear forces
F_p	pressure force
$F_{\tau W}$	wall shear force
h	distance between tooth and crown

h^*	remaining possible insertion plate displacement
H	height of a layer within the gap between cylinder and vessel
H	height of insertion plate
H^*	fill height
H_0	initial adhesive height
$H_{0,stop}$	entire possible insertion plate displacement
H_1	Pi-slot height
H_1^*	non-dimensionalised Pi-slot height
I	Moment of inertia
K	consistency factor
k	Boltzman constant
L	insertion plate length
L	overlap length
L_{spacer}	distance between spacers
l	distance between cylinder and vessel bottom
l	distance between insertion plate and Pi-slot bottom
M	bending moment
N	narrow (flow channel)
N	normalized deviatoric portion of the driving stress state
n	Power law index
p	pressure

R_i	inner radius of vessel,
R_o	outer radius of cylinder
T^*	stress state
t	Pi-slot wall thickness
t	time
U	insertion speed (in analytic model)
$v_c\,(r)$	velocity distribution in flow between cylinder and vessel walls
v_i	insertion velocity
v_{ins}	insertion speed
w	Pi-joint length
W	wide (flow channel)
W	insertion plate width
α	volume fraction
Δ	circular bended insertion plate distance before spacers
δ	circular bended insertion plate distance after spacers
δ	distance between cylinder and vessel walls
δ	flow channel width
$\dot{\gamma}$	shear rate
η	shear viscosity
θ	temperature
κ_1	Newtonian shear viscosity

κ_2	*non-Newtonian shear viscosity*
ξ	*flow channel width ratio*
ρ	*density*
σ_{PM}	*lowest principal stress*
σ_{TM}	*transverse stress*
τ	*shear stress*
τ_0	*Yield stress*
ϕ	*any physical quantity, e.g. p, u, v, w*
ψ	*flow front ratio*
ω	*net angle of rotation between initial and activated configuration of thermal diffusivity*

1 Introduction

Much research has focussed on adhesive bonding of composite components for various applications in the past two decades. This stems from the substitution of conventionally used metals with composite materials in many applications due to their superior specific mechanical properties, so that costs can be lowered and weight saved. Due to these benefits the use of composites for aircraft components is of major interest and has led to an increased use.

Various bonding techniques to join the composite components have been used. Conventional bonding of metal components was achieved through mechanical fastening such as riveting, screwing or bolting, and past research has enumerated the disadvantages of these techniques if they are applied for composite materials. For the joining of composite components adhesive bonding, though, offers great potential since it is considered as a more fibre-friendly bonding method, lacking stress concentration around holes as required for mechanical fastening, and is also considered to reduce weight. However, there has not been enough research on the quality adhesive bonding to substitute mechanical bonding entirely. Hence, adhesive bonding is not applied as the only bonding method, but supported through mechanical fastening techniques, hence eliminating benefits gained from adhesive bonding. More research into adhesive bonding is thus needed to ensure it guarantees equal joint qualities as those which are achievable with mechanical fastening, so that the advantages through adhesive bonding can be realised.

A typical composite joint is a spar-to-skin application, which can be found in aircraft doors, wings and flap track beams. Some research has been conducted to adhesively bond spars to skins, applying different design approaches. All of these designs have been considered as beneficial in cost and weight savings. One specific design, which uses a π-shaped substructure that is attached to the skin, is additionally considered as being capable of reducing undesired peel stresses. This substructure is referred to as Pi-slot. Its roof can be co-cured or stitched to the skin, creating one component. The spar can then be inserted into the Pi-slot and adhesively bonded to it, creating an adhesively bonded Pi-joint. However, most studies of Pi-joint applications did not include any description of the adhesive bonding techniques applied. Where adhesive bonding techniques were described, they appeared to be quite complex. Furthermore, a number of the techniques could only be

used with low viscous adhesives, while many adhesives are high viscous. Thus, a detailed investigation of an alternative adhesive distribution technique is required.

This alternative adhesive distribution technique is referred to as an insertion squeeze flow (ISF) bonding process. There are advantages of the ISF bonding process compared to other adhesive distribution techniques described in the literature, of which the main are that there is no restriction to the type of adhesive used and the simplicity of the setup of the ISF process. In the proposed research study, an insertion squeeze flow (ISF) bonding process is analysed. The adhesive is placed in the bottom of the Pi-slot and the spar (insertion plate) is inserted into the Pi-slot, penetrating into the adhesive and displacing the adhesive into the gaps, or flow channels, that are formed between the insertion plate and the Pi-slot. Fully cured, an adhesive bond is formed between the insertion plate and the Pi-slot. Research studies have investigated similar squeeze flow types, however, the investigated geometries differed from the considered design and the displaced fluids varied from the investigated adhesives.

The broad aim of the project is to study the adhesive flow during the ISF bonding process and to use this understanding to enable the development of an ISF bonding process for composite components. The study of adhesive flow is conducted analytically, experimentally, and particularly numerically.

A specific aim of the project is to predict insertion forces acting during ISF and pressures on the Pi-slot walls from the numerical analysis. An adhesive model developed to represent the adhesive viscosity has to be implemented into the numerical model in order to conduct the simulation of ISF. Knowledge of forces and pressures would be supportive in designing an ISF bonding process. The predictions should be obtained for ISF bonding processes conducted at constant speed and at constant force insertions.

Another specific aim of the project is to predict adhesive flow for misaligned insertions in order to specifie tolerances and guidelines to ensure Pi-joint quality. Pi-joint quality requires that the adhesive distributes evenly between the insertion plate (spar) and the Pi-slot (skin plus substructure). Dimensionless parameters defining the adhesive distribution have to be determined and their effect on the bonding quality evaluated.

Another specific aim is the consideration of how the Pi-slot wall stiffness affects the adhesive distribution compared to the case if the Pi-slot walls are rigid. This includes the incorporation of a fluid-structure-interaction (FSI) type of problem; the adhesive flow implies a pressure on the Pi-slot walls, which may lead to a distortion of the Pi-slot walls, which may in turn affect the adhesive flow.

In this thesis, a comprehensive literature review relavant to the study is conducted in Chapter 2. It includes the general consideration of conventional bonding and adhesive bonding methods for composite structures, especially focussing on advantages and disadvantages of those. Alternative bonding methods are introduced and reviewed, followed by the consideration of Pi-joint application, especially the adhesive distribution during the bonding process. Chapter 2 is concluded with the review of penetration and squeeze flows, and with the presentation of proposed viscosity material models.

The numerical and experimental methodology is described in Chapter 3. The bulk of Chapter 3 deals with the description of the computational method used for the development of the numerical model. It also includes spatial and temporal resolution studies and the two-dimensional (2D) set-up and definition of the problem.

In Chapter 4 the selected adhesives are described in detail and appropriate mixing ratios determined. Results from various rheological tests are presented and the Chapter is concluded with the proposition of two adhesive material models.

Chapter 5 reports a numerical study of ISF conducted at constant speed. Insertion forces and Pi-slot wall pressures for ISF applying the adhesive material model are related to the insertion speed and adhesive viscosities.

Chapter 6 reports on the effect of lateral misalignment on the adhesive distribution during ISF obtained from numerical simulations. It outlines the effect of input variables as insertion speed, adhesive viscosity, initially applied adhesive volume, total flow channel width and insertion plate head design on the adhesive distribution in laterally misaligned insertions.

In Chapter 7, the extension of the 2D numerical model for ISF is outlined. The extensions are the simulation of an ISF bonding process conducted at constant insertion force, the simulation of an ISF bonding process with pre-applied adhesive on the insertion plate side walls, the simulation of a fluid-structure-interaction problem for ISF and finally the three-dimensional (3D) consideration of ISF conducted at constant insertion speed.

Chapter 8 concludes the thesis and suggestions for future work are given.

2   Literature Review

In Chapter 2, a broad discussion of some of the aspects that are potentially relevant to insertion squeeze flow problems applied for adhesive bonding are examined. In Section (2.1) different joining techniques for fibre-reinforced materials are introduced and compared. Section 2.2 focuses on one particular bonding method, the adhesive bonding of fibre-reinforced structures, and comparisons are made between two joining techniques, which are the secondary bonding and the co-curing. Joint design analysis for adhesively bonded joints is also presented within this section. Following, Section 2.3 details the utilisation of Pi-shaped substructures in order to adhesively bond composite structures. Then, in Section 2.4, penetration flows of Newtonian fluids are discussed first, followed by discussion on squeeze flows of Newtonian and non-Newtonian fluids between two approaching boundaries. Finally, material models developed for the characterisation of rheological behaviour of non-Newtonian fluids are presented in Section 2.5.

2.1   Techniques for Joining of Fibre-Reinforced Structures

A good introduction into the topic of joining fibre-reinforced plastics is provided by Matthews in "Joining Fibre-Reinforced Plastics" (Matthews, 1987a). Within this work, joint designs for adhesive bonding and mechanical fastening are compared. Analytical and finite element analysis methods for stress strain analysis of parts joined in both techniques are presented and advantages and disadvantages of each technique are specified.

First, Matthews gives a brief introduction into joining techniques in general (Matthews, 1987b). It is stated that theoretically a structure is desired to lack any joints as those are considered as a source of weakness and excess weight. Practically, though, limitations on component size due to manufacturing processes, inspection requirements and accessibility, repair, transportation and finally assembly mean that loaded joints are inevitable in large structures.

Two techniques are generally applicable for joining fibre-reinforced plastics: mechanical fastening and adhesive bonding. The advantages and disadvantages are summarized in Table 1 according to Matthews (1987b):

Table 1: Advantages and disadvantages of mechanical fastening and adhesive bonding as presented in Matthews (1987b).

	+	-
Mechanically fastened joints	– Disassembly possible – No surface preparation required	– Stress concentration at holes – Large weight due to design requirements and fasteners – 'Fibre-unfriendly' method
Adhesively bonded joints	– 'Fibre-friendly' method and stress minimization – Weight and cost-savings	– Disassembly impossible – Environmentally effectible – Complex inspection methods – Requires quality assurance during manufacturing

On the one hand, mechanical fastening of joints allows disassembly and does not require surface preparation prior to joining. On the other hand, disadvantageous are stress concentrations around the holes that are provided for fasteners. Due to design requirements as a minimum thickness of the bonding partners and due to the fasteners' weight, weight in excess of the one expected for an adhesively bonded joint may be experienced. Adhesive bonding, however, can be considered as a 'fibre-friendly' joining technique as fibres are not damaged through the process of hole drilling. Disassembly of adhesively bonded joints is not possible. Complex inspection methods may be prevented through quality assurance during manufacturing of the bonding partners. Furthermore, joint strength may decrease due to environmental effects.

Considering mechanical fastening more in detail first, Collings (1987) provides a good overview about common mechanical joining techniques. Mechanically fastened joints can be subdivided due to the fastener that is implied. Screws, rivets and bolts have been applied with varying success (Collings, 1987).

Self-tapping screws are considered as a simple and inexpensive connection but accessibility of the reverse side of a joint is impossible. As thread stripping is likely, self-trapping screws are not recommended where frequent demounting is required (Collings, 1987).

The use of rivets is suitable for laminate thicknesses of up to 3 mm (Collings, 1987). Different types and forms are available, varying in being hollow or solid and for a range of head and bolt types and sizes. The riveting process might cause damage to the laminate as discussed by Matthews (Matthews, 1976), where an optimum level of constraint caused by clamping is derived and suggested. In general, non-countersunk rivets are preferred to countersunk ones (Matthews, 1980). Furthermore, the use of solid rivets compared to hollow rivets results in stronger joints.

Finally, bolting is considered as the technique of choice in applications where disassembly due to inspections and maintenance is required. Collings investigated a wide range of variables as lay-up, fibre orientation and bolt diameter and stated bolted joints to be the most efficient form of mechanical fastener (Collings, 1987).

An investigation of effects on mechanically fastened joint strengths always has to consider failure modes (Collings, 1987, Matthews, 1987b). Collings (1987) enumerates five different failure modes: tension, shear, bearing, cleavage and pull-out. The joint strength of mechanically fastened composite joints can be affected by the fibre and matrix material, lay-up, stacking sequence, fibre-orientation or hole and fastener diameter (Collings, 1987, Matthews, 1987b).

Comparing the two bonding methods, there is a vital difference in the size of the adherends whether the bonding method is mechanical fastening or adhesive bonding. A mechanical fastener usually demands adherends of several millimetre thickness compared to fractions of a millimetre for adherends that are bonded applying an adhesive (Matthews, 1987b). In case of adhesive bonding, the bonding mechanism is achieved through adhesion between the adherends and the adhesive. Joint strength is affected by surface ply orientation, stacking sequence, joint geometry, loading, matrix and adhesive material. In many cases the matrix might be much weaker than the structural adhesive so that failure

may occur through delamination or interplane fracture (Matthews, 1987b). Other failure modes are listed and explained in sub-Section 2.2.2.

2.2 Adhesive Bonding of Fibre-Reinforced Structures

In this section, different adhesive bonding techniques for fibre-reinforced structures are considered, which are the adhesive bonding (secondary bonding) and a technique referred to as co-curing (primary bonding). The techniques are explained and compared with each other. Also, work is presented that deals with stress analysis in secondary adhesively bonded fibre-reinforced structures.

2.2.1 Secondary bonding and co-curing

Two methods to join composite structures are adhesive bonding and co-curing. Adhesive bonding, on the one hand, is referred to as secondary bonding which means that the bonding partners (adherends) are manufactured first and then bonded in a second process step. During co-curing, on the other hand, the partners to be bonded are manufactured and joined in-situ. The joint is formed during the composite curing process of each component. This technique is referred to as primary bonding as no additional process step is required. Advantages and disadvantages of primary and secondary bonding are pointed out below.

Shin and Lee (2003) analysed the fatigue behaviour of double lap joints that were co-cured for different bonding parameters such as surface roughness of the steel adherend and stacking sequence of the composite adherend. They considered co-curing to be advantageous compared to secondary bonding as the manufacturing process is simpler. Curing and bonding is conducted at the same time and excessive matrix material from the composite adherend functions as the adhesive (Shin, 2003).

In 2000, Shin, Lee and Lee studied the lap shear strength of a co-cured single lap joint experimentally. Investigated parameters were bond length, surface roughness of the steel adherend and stacking sequence of the composite adherend. The lap shear strength was found to significantly be affected by the bond length and the stacking sequence of the composite laminate. Surface treatment of the adherends, however, appeared to only minorly affect the lap shear strength. In this paper, it was pointed out that co-curing is considered as the most advantageous bonding method. This was based on two comparisons: firstly, a comparison between mechanical fastening and adhesive bonding supported the advantages proposed in the previous section, which are that there is no need

for holes which lead to delamination, fibre cut and stress concentration around the holes, and that adhesive bonding generates a larger stress bearing area, a uniform stress distribution, superior resistance to fatigue or cyclic loads and an attractive strength to weight ratio (Shin et al., 2000). Secondly, comparing primary and secondary bonding, Shin et al. concluded that, due to the aspect that surface treatment only has a minor effect on the lap shear strength of the composite adherends, and hence is not required for co-curing, but for adhesive bonding, the most convenient joining method is co-curing.

However, several other authors considered secondary bonding to be advantageous to primary bonding.

Work by Potter et al. in 2001 investigated adhesive crack propagation in bonded joints (Potter, 2001b). Their scope was the establishing of a measure to control the progress of cracks in adhesives in bonded joints. They selected paste adhesive instead of film adhesive for two reasons: first, an adhesive bonding process can be applied – in contrast to adhesive film bonding – without pressure. This allows bonding of complex geometry joints and also is preferable when tight tolerances cannot be guaranteed. Second, paste adhesives can accommodate incorporation of geometrical details such as reverse chamfers and adhesive fillets. As shown by Adams (Adams, 1986), the level of induced through thickness stresses can be reduced significantly when applying fillets and tapers at the edges of the joint.

Matthews (1987), Liechti (1987), Adams (1987), and Potter et al. (2001) stated that the tensile and shear stress distribution along a joint is not uniform. Moreover, it reaches maximum values at the edges of the joint. Therefore, a design modification can improve the joint strength significantly and is achievable in a simple way when using secondary adhesive bonding.

A summary of advantages and disadvantages of both bonding techniques is given in Table 2.

Table 2: A summary of advantages and disadvantages enumerated for adhesive bonding and co-curing of joints.

	+	-
Adhesively bonded joints	- Pressure-free process allows complex joint designs - Incorporation of geometrical details	- Additional process step - Surface preparation required - Complex inspection methods
Co-cured joints	- Simpler: curing and bonding conducted simultaneously - No surface preparation required	- Pressure required during assembly - No geometrical design freedom to encounter against non-uniform stress distribution in joints

It has been shown that both techniques bare advantages and disadvantages, and depending on the structures to be bonded, the one might be more beneficial than the other. In the presented study, secondary bonding was selected in particular due to the possibility of joining complex structures without pressure (MoJo, 2006).

2.2.2 Effects of joint designs and load cases

In order to use adhesives for the bonding of composite materials the understanding of joint design and loading type effects on the joint strength is substantial. Additionally, failure modes have to be taken into consideration (Adams, 1986).

Joint designs and failure modes are introduced briefly below. Then, work on the stress-strain characterization of joints is presented, including analytical and finite element methods. Finally, the work by Adams et al. (1986) is discussed.

Adhesively bonded joints are used in different configurations. Some of the most common configurations are presented in Figure 2-1:
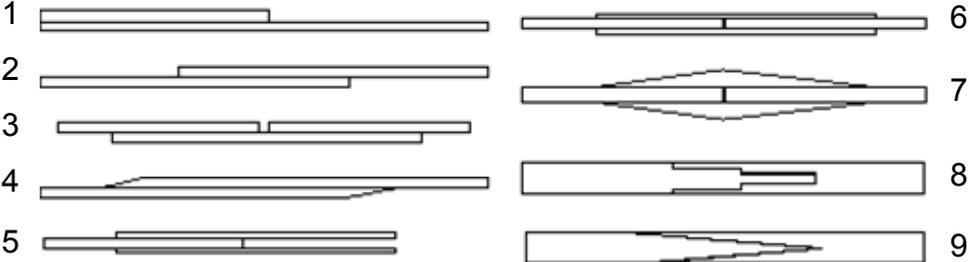
Figure 2-1: Different configurations of commonly used joint types (Hart-Smith, 1987).

From 1 to 8, the joint types can be labelled as follows: bonded doubler (1), unsupported single-lap joint (2), single-strap joint (3), tapered single-lap joint (4), double-lap joint (5), double-strap joint (6), tapered strap joint (7), stepped-lap joint (8) and scarf joint (9).

Their relative usage can be placed in perspective by their bonded joint strength and complexity of the joint, for example a complicated scarfed or stepped-lap joint is able to transfer higher loads than rather simple single-lap or double-strap joints (Hart-Smith, 1987).

The joint that is considered in the presented work is a Pi-joint, which is presented schematically in Figure 2-2, illustrated with three alternative insertion plate head shape designs.
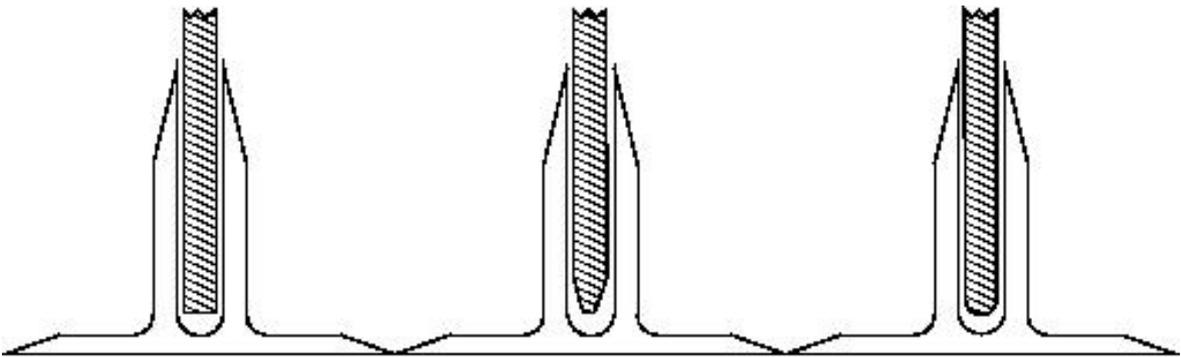
Figure 2-2: The Pi-joint design is illustrated with different insertion head shapes.

None of the common used joint types agrees fully with the Pi-joint. Clearly, all single joints differ significantly from the Pi-joint design. However, there are similarities between the Pi-joint and the double joints as double-lap and double-strap joints, but also between the Pi-joint and the stepped or scarf joint, because all of these designs are comprised of an enveloping and a centre component. Hence, stress-strain analysis of these designs is

considered beneficial for the stress-strain characterisation of Pi-joints. Investigations of the joint design will take into account the bottom shape of the centre adherend of the Pi-joint, as demonstrated in Figure 2-2.

A brief description of failure modes for adhesively bonded joints is given next. Strongest joints fail outside the joint area and show equal to the strength as the adherends. The next highest strengths occur when the joint fails due to the shear strength of the adhesive. Finally, the weakest failure mode is considered to be the one when the joint fails by failure of the adhesive under peel loads (Hart-Smith, 1987). Therefore, peel stresses in the adhesive should be avoided as far as possible. Hart-Smith (1987) suggests tapering to be a good method to avoid peel stresses in the adhesive.

The stress-strain characteristic can be determined analytically and numerically through finite element analysis (FEA) (Keller, 2005). FEA has the advantage of including specific geometries and fillets, or anisotropy and non-linearity in material behaviour when predicting joint strengths. It was shown that these features affect the joint strength significantly (Adams, 1986).

In the literature both ways – analytical and FEA – were investigated frequently. Some examples showing the development of analytical descriptions of stress-strain behaviour are Volkersen's shear lag analysis (Volkersen, 1938, Volkersen, 1965), which only takes shear stresses into consideration and assumes the adherends to be absolutely rigid. This study was extended by Goland and Reissner (1944) who took into account the resulting bending moment in single lap joints. These bending moments cause stresses acting in the through thickness direction and are referred to as peel stresses. Peel stress is the least desirable stress in joints (MoJo, 2006, Russel, 2006). Volkersen (1965) considered bending effects as he introduced a through thickness peel stress variable. Renton and Allaman included bending, shear and normal stresses in their models (Renton, 1977), and Tsai et al. and Tsai and Morton (Tsai, 1994, Tsai, 1998) showed that Oplinger's method, who added the effect of large deflection in the bonding area of single lap joints (Oplinger, 1994), is only valid for thin and flexible adhesives.

FEA was investigated by Adams et al. (Adams, 1986), Adams (Adams, 1987), and Richardson et al. (1993). Several other studies concentrated on the failure modes and crack propagation in the adhesive (Hart-Smith, 1987, Hart-Smith, 2002, Potter, 2001b). The scope of the presented study is not a stress-strain analysis, though, and therefore the aforementioned papers are not reviewed in detail. However, the design of the joint is a parameter that is modified in the presented investigation and as shown above affects the

joint strength. Therefore, one particulat study, Adams et al. (1986), is considered in more detail.

Adams et al. (1986) evaluated strengths of cabon-fibre-reinforced plastics (CFRP)/steel double-lap joints loaded in tension. According to Adams et al. (1986), adhesive bonding is a most attractive method for joining carbon fibre reinforced plastics (CFRP) for many reasons. When compared to optional bonding techniques as riveting and bolting, the main advantages adhesive bonding offers are improved fatigue resistance, the possibility to disregard a minimum sheet thickness required for bolting and riveting and greater design flexibility (Adams, 1986). To fully utilise these advantages, a proper understanding of various design parameters which affect the strength of adhesively bonded joints is necessary. Among others, their main aims were "i) to analyse the stress distributions in the joints, [...], iv) to use these studies to optimise the design of the joint in order to attain a significantly increased failure strength", p. 30, ll. 11-14. These aspects are important for the conducted research for a number of reasons: firstly, when considering the effects of insertion plate head shape on the adhesive distribution within the Pi-joint, the choice of the head shape design should be made regarding the effect of design on the joint strength. Secondly, the resulting distance between the bonding partners in the bottom area of the Pi-joint is considered. And thirdly, the adhesive fillet design at the top of the Pi-slot should be created according to the outcomes presented in Adams (1986).

It is expected and found that a double-lap joint does not fail by shear but by tensile loading. In Figure 2-3 the shear and transverse tensile stress distribution along the overlap length L in an adhesive layer are considered (Adams, 1986).

Region of plastic deformation | Region of elastic deformation | Region of plastic deformation

Yield stress of adhesive

τ

Shear stress distribution in adhesive

0   L

+

0

-

σ_t

Transverse tensile (normal) stress distribution in the adhesive

L
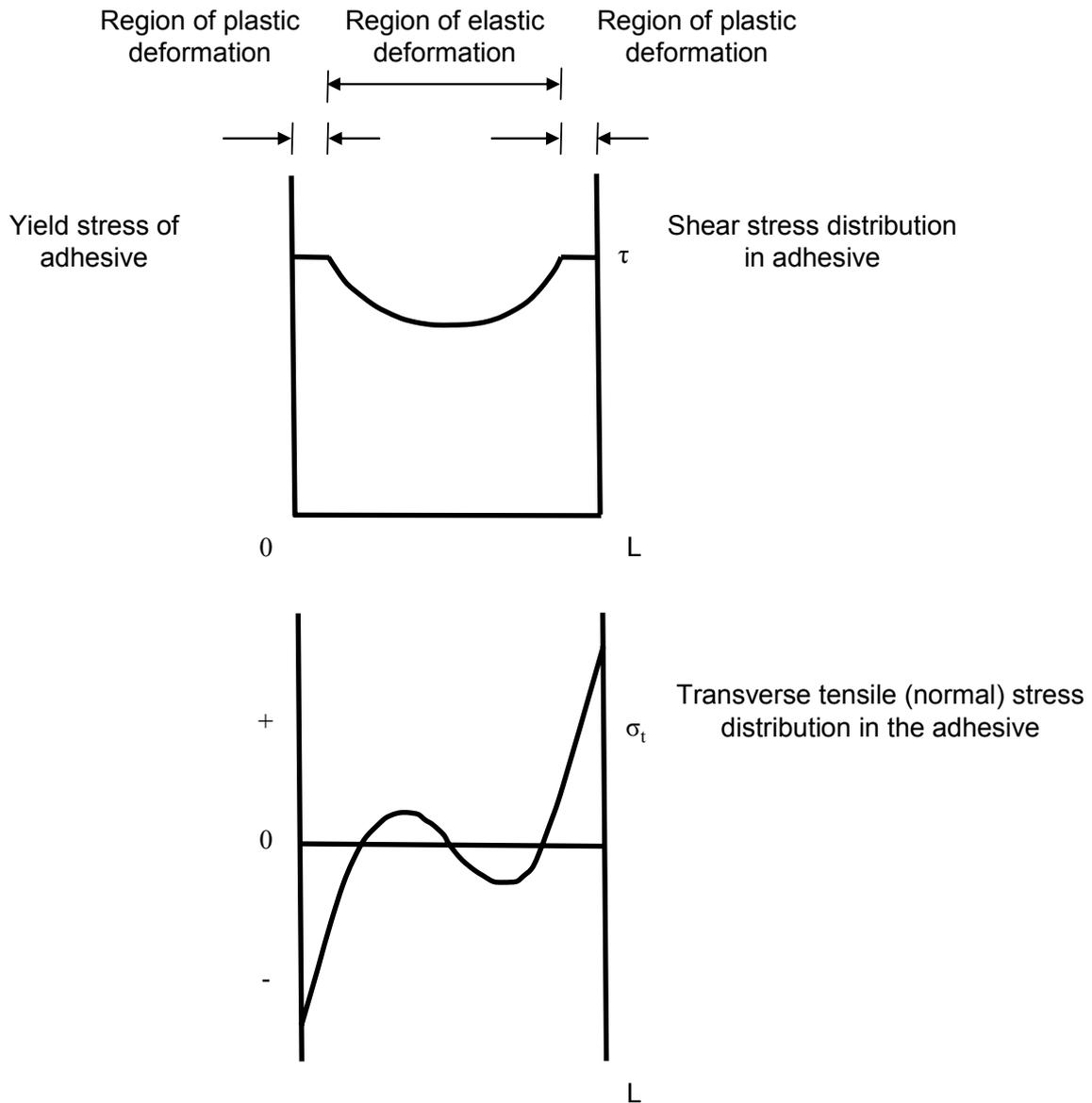
Figure 2-3: Typical shear and transverse tensile stress distribution in a double-lap joint, as presented by Adams (Adams, 1986).

The shear stress distribution shows a constant yield stress of adhesive in the region of plastic deformation at the edges of the overlap length. An elastic deformation region is found in between. The transverse tensile stress distribution shows maximum values at the edges of the overlap length, which, if possible, should be avoided.

Several joint designs were investigated by Adams et al. (1986) to avoid these maxima. The designs were modified by locally changing the geometry in the regions where the maximum loads occur. Special attention was given to the shape of the fillet and the tapering of the adherend edges. Figure 2-4 shows the designs that were investigated, with design 1 being the top one and design 5 being the one on the bottom.
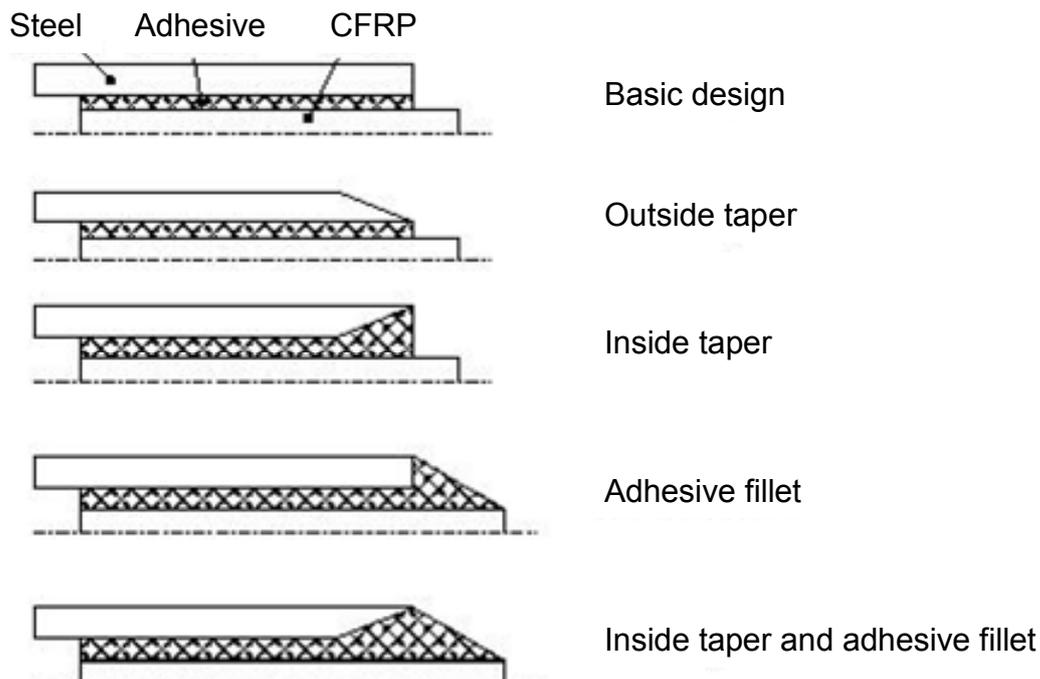
Figure 2-4: Steel-CFRP joints with varying taper-adhesive fillet combinations as investigated by Adams (Adams, 1986).

A finite element analysis (FEA) of the effect of the tensile stresses normal to the loading direction was conducted in both the CFRP inner adherend and in the adhesive layer. Details about methodology of the FEA can be found in Adams et al. (1986). The maximum transverse stresses σ_{tm} in the CFRP occurred in the region adjacent to the edges of the outer steel adherends, as expected. Essentially, the use of a taper only as in the designs 2 and 3 shows a minor effect on the maximum transvers stresses σ_{tm} (Adams, 1986). However, comparing the transverse stress distribution between designs 1 (basic design) and design 5 (inside taper and adhesive fillet) showed that the stress concentration could be reduced from a maximum of $\sigma_{tm} = 35$ MPa for design 1 to a maximum of $\sigma_{tm} = 6$ MPa for design 5, which is a reduction of 83 % (Adams, 1986).

An analysis of the principal stress distribution σ_{pm} in the adhesive layer for different designs underlines the effect that the use of an adhesive fillet combined with an inner taper in the steel adherends also provided the best results, meaning lowest principle stress maxima σ_{pm}. The principal stress maximum can be reduced from $\sigma_{pm} = 101$ Mpa for design 1 to $\sigma_{pm} = 28.9$ Mpa for design 5.

The comparison between experiment and theory shows that in all experimental cases the mode of failure was not due to a shear failure of the adhesive but was due to interlaminar

fracture of the inner CFRP. More specifically, the interlaminar fracture occurred at the region of the overlap length where the steel outer adherends terminated. This failure is obviously caused by the transverse tensile stresses in the joint. It was found that two possible failure mechanisms could account for the interlaminar fracture; either transverse tensile stresses at the edge of the joint close to the interface in the CFRP or concentrations of principal stresses in the adhesive resulting in yielding and straining to failure under predominantly tensile forces. The latter might lead to interlaminar failure as well as cracks would run through the adhesive to the interface of the CFRP. Considering those two failure mechanisms is important when considering the theoretical predictions as the predictions would be different depending on the assumed failure mechanism.

Essentially important for the presented research work is the effect the inside taper and the adhesive fillet have on the failure load. Failure load significantly increased when an inside taper was applied and combined with an adhesive fillet (design 5). This was observed for both the experimental results and the theoretical predictions. These results will be taken into consideration when the effects of designs of the head shape on the adhesive flow are studied.

2.2.3 Spar-to-skin structures

An adhesive bonding application for a spar to skin composite structure is presented in the following. A summary of the work is conducted and comparisons are drawn to the Pi-joint design that will be investigated in the presented study.

In 2001, Potter et al. (Potter, 2001a) investigated adhesive bonding in secondarily bonded I-beam composite structures. The work was carried out as part of the IMI programme 'Innovative Approaches to Composite Structures' and was contributed to by Bristol University, BAE Systems, Airbus, Ltd Filton (BAE), and Cranfield University. Aim of the programme was the demonstration of 'feasibility of utilising bonded construction in heavily loaded composite structures' (Potter, 2001a). Potter enumerates various advantages that justify their investigation on adhesive bonding, being reduced parts count compared to mechanical fastening and minimising necessity of drilling or machining of components (Potter, 2001a). The I-beam test piece was intended to represent a wing skin and spar in the wing box of a commercial jetliner. Details of ultimate shear flows and shear stresses that had to be carried by the test piece can be found in Potter et al. (2001a). After design, manufacture and testing in three-point and four-point bending a post-test evaluation

was conducted to obtain an understanding of the bondline quality and to identify the cause of failure.

The I-beam design is shown as a cross-section in Figure 2-5.
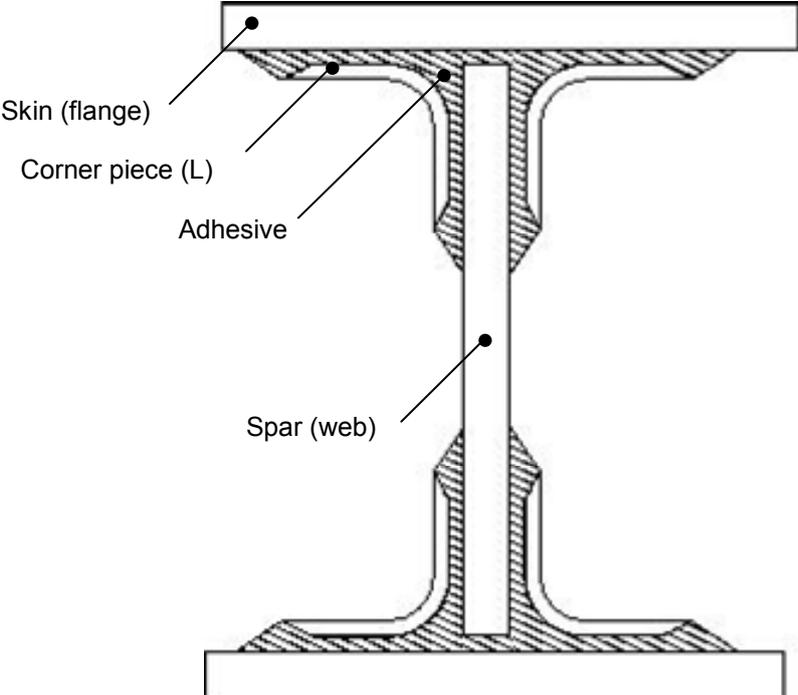
Figure 2-5: I-beam design that was analysed in Potter et al. (2001a).

The design represents two T-joints where the middle I-beam is chosen as the spar within a wing box and the top and bottom parts represent the skin. The modules are considered to be bonded secondarily meaning that they are manufactured first and than adhesively bonded. The separate corner pieces are to strengthen the skin-to-spar-joint and to allow tolerances in the spar height and the skin thickness. Dimensions of the test piece are summarized in Table 3 and were determined by means of scaling.

Table 3: The dimensions of the I-beam components that were tested (Potter, 2001a).

Component	Length [mm]
Spar depth	150
Skin width	150
Skin thickness	10
Spar thickness	8
Overall length	2000

For further details about choice of lay-up design it is referred to Potter et al. (2001a). A more detailed description about the application of the finite element analysis (FEA) method used for determination of the joint design can be found there as well. The methodology provided investigates design freedoms as overlap length and geometry of the ends of the joints, development of the three dimensional analysis using a linear elastic model, and three-dimensional analysis including non-linearity and non-linear adhesive properties.

The manufacturing of the I-beam joint is described in the following. All components used were manufactured using prepreg lay up and autoclave technology. On all surfaces peel ply was used to minimise surface contamination. Furthermore, all bonding surfaces were manually grid blasted. Although a cabinet grid blasting model generally would provide a more even activated bonding surface, the manual option was chosen to simulate the manufacturing according to the feasibility of utilising it for large scale components.

A tooling system had to be developed for the adhesive bonding process. The system should generate the desired adhesive bondline thicknesses without use of spacers. The developed tooling system used is illustrated in Figure 2-6.
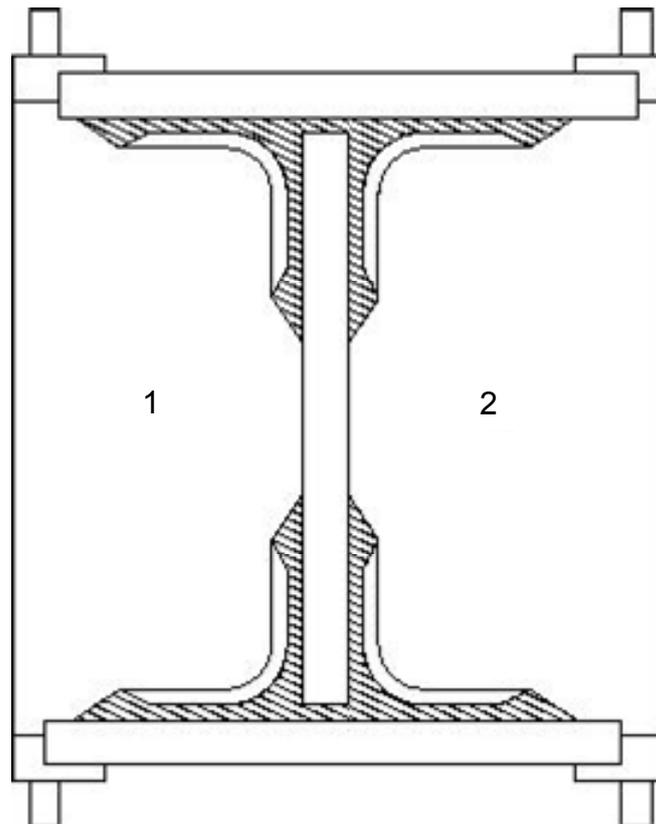
Figure 2-6: Tooling for the assembly of an I-beam using a secondary bonding technique (Potter, 2001a).

After coating part 1 with mould release and setting it on a bench horizontally, adhesive is applied to the first pair of corner pieces. The adhesive is applied on the side facing the spar and the corner pieces are set into place on the tooling side part 1. Then, adhesive is applied on one side of the spar and the spar is lowered on the corner pieces afterwards. Once in place, adhesive is distributed on the other side of the spar which is facing up. The second pair of corner pieces is prepared with further adhesive and placed with its other side on part 2 of the tooling system. Part 2 including corner pieces is then brought into correct register with part 1, squeezing out excessive adhesive during this process. Next, skins are prepared with adhesive and set on the corner pieces. Once in place, skin clamps are tightened up until the skins sit in the correct position of the set up. Finally, the set up is placed in an oven and the adhesive is cured according to the manufacturer's cure schedule.

This assembly procedure provides possibilities of air entrapment and appears quite complicated. This is confirmed by comments about the assembly found in the article: 'The assembly tooling was rather clumsy in use and would not be suitable for much larger structures, but did allow a series of beams to be manufactured to consistent dimensions', ll. 29-32, page 394, Potter et al. (2001a). Incompletely formed fillets and voids in the

adhesive fillets were exhibited in the first test specimen. In latter specimens (2, 3 and 4), improved quality was achieved and ultrasonic non destructive testing (NDT) showed no major defects.

For details about the testing procedure it is referred to Potter et al. (2001a) again. In terms of testing results, the three-point bending test specimens failed at 77% of the predicted load with a scatter of less than 1% of mean strength. The failure load was well above the design ultimate required (123%). Sample 4 was tested in four-point bending and failed at approximately 105% of prediction which was according to 165% of design ultimate load.

Post-test evaluation included video tape evidence, acoustic emission evidence and strain gauge evidence. Furthermore, an inspection of the failed surfaces followed attempting to determine the bondline quality and final failure source.

The test specimens were essentially in three pieces, the tensile surface and the left and right half of the rest of the I-beam. Each halve consisted of the spar, the compression surface and the corner pieces. For an understanding of the causes of failure, the midpoint of the detached tensile skin is the main feature of interest. The rest of the detached tensile skin is separated via delamination in the skin. At the midpoint, though, the separation is within the corner pieces and through the adhesive. This was considered as the initial point of failure. Cracks propagated from the corner pieces through the adhesive and into the tensile skin, resulting in delamination within the tensile skin and leading to separation between the tensile skin and the rest of the beam.

Marks left from the edge of the spar on the adhesive layer indicate the weak bonding at this point. According to Potter et al. (2001a), the bond between the spar and the adhesive must be regarded as of reduced strength. Furthermore, there are areas on the corner pieces showing little or no adhesion at all. Especially some beams show large voids within the adhesive bond line which cover several cm^2 in some cases.

In the discussion, it is mentioned that the preparation of large areas for bonding by hand is very difficult. Despite the limitations of the test assemblies the performance of the beam specimens was very good, exceeding all requirements comfortably.

Comparing Adam's work with the presented research, similarities exist as both studies deal with applications of adhesive bonding for spar-to-skin structures. The difficulties experienced with the method proposed in Potter et al. (2001a) are considered to lay in the assembly of the I-beam and in the preparation of large areas for bonding. The cause of failure was seen to be in the rather weak adhesion between the spar and the adhesive and

some areas of the corner pieces showed large void areas. The present study might contribute to the improvement of spar to skin bonding quality. A different adhesive bonding technique is investigated being insertion squeeze flow (ISF) bonding, where the bonding partners are designed in a different way. Less air entrapment during the bonding process is expected as air is expected to be pushed out of the bonding area in front of the adhesive flow front. The ISF technique is also believed to provide a simpler assembly as less modules are involved. The Pi-joint legs fulfil a similar function as the corner pieces in the I-joint. Both constrain the middle structure and are bonded to it. The roof of the Pi-joint is attached to the skin through stitching and co-curing so that the Pi-joint is already integrated. A T-shaped structure is then achieved when the I-shaped counterpart is inserted into the Pi-joint.

2.3 Adhesive Bonding using Pi-shaped Sub-Structures

Pi-joints – the name originating from the similarity to the Greek letter Π – have been used in various projects and applications involving adhesive bonding before. Some of these applications are summarized below, presenting what was investigated and which results were obtained. Furthermore, it reviews those applications and provides comparisons to the presented research work.

A relatively early example where a Pi-joint design was applied for the bonding of composite structures for aircraft components can be found in Wong (1992). Wong (1992) presents the development of sandwich constructions for the all-composite aircraft "Starship" by the Beech Aircraft Company, Wichita, Kansas. Examples for sandwich construction components are the main wing, forward wing, pressure vertical stabilizer and the control surfaces (Wong, 1992).

It is said that the main wing is a typical low part count bonded structure. The sandwich skins are manufactured first as a one piece cure each, the lower skin having a stiffener assembled into it. Adhesive and scrim cloth is applied into the upper skin which is than lowered into the lower skin, creating a bond with the stiffener. Wong (1992) states that the "key to be successful of this assembly technique is Beech patented 3 dimensional woven fibre joint[s]," ll. 7-8, page 2. Bonding is realized by utilising a cure paste adhesive. Beside the low part count approach advantages are seen in the elimination of peel stresses.

Further low part count structures are the forward wing and the pressure cabin. The forward wing is a structure including two spars and its assembly is completed in a single cure cycle. The spars are held in position through silicon rubber bags inside each wing box

cell while the upper and lower skins are held in a matched female tool. Bonding is realized through co-curing. The pressure cabin consists of a left and right pre-cured half that are bonded together through the utilisation of hot temperature paste adhesive.

In September 2005 the revision of a Navy ManTech program was published that summarized some results from a research program titled "Aircraft Primary Structure Adhesive Bonding Development" (Navy, 2005). Participants of the program were the Edison Welding Institute (EWI), Lockheed Martin Aeronautical Systems, Boeing Integrated Defense Systems and NAVAIR. In the problem description and objectives the potential of adhesive bonding for primary structures is pointed out first: significant cost and weight savings. However, the difficulties in the controllability of manufacturing tolerances lead to a lack of confidence in fulfilling Navy Aircraft service requirements, resulting in an avoiding of adhesive bonding usage. Bonded-bolted designs are used instead. The objective of the Navy ManTech program was the investigation of effects of defects and of manufacturing process variability with the purpose of improving producibilty and reliability of adhesive bonded joints.

Studied process variables were "influences of nominal differences in materials, Pi-joint design variations, assembly and bonding process variations such as adhesive thickness, web offset, poor offset condition, improper cure and joint porosity," ll. 22-26, (Navy, 2005). The results were obtained from testing over 800 specimens and these data were transferred to the Navy/Air Force and Composite Affordability Initiative (CAI), another program investigating the application of adhesive bonding for composite primary aircraft structures that is discussed below.

The revision considers the Navy ManTech program of being a technical success. It is stated that the applicability of adhesive bonded primary structures is seen for fixed-wing aircraft programs. Lockheed Martin used results from the program for the design of the Joint Strike Force (JSF) inlet duct. Benefits resulting from this application are stated to be $200,000 cost and 80 lbs weight savings. Further applications of improved adhesive bonding are for existing co-bonded structures and in repair. Summing up, additional benefits are a 95% reduction of mechanical fasteners for the example of the JSF duct and an improved aerodynamic and signature performance, leading to a more robust and efficient aircraft.

The aforementioned Composite Affordability Initiative (CAI) program is presented next. Russel (2006) summarizes the contents and achievements of the CAI. Motivation for the program was due to the fact that despite the potential of composites for weight

reduction in aircraft "the aircraft industry was reluctant to implement them in new aircraft", ll. 8-9, Russel (2006). Perceived risks and barriers for the implementation of advanced composites in aircraft had to be addressed. Participants of this eleven-year effort were the Air Force Research Laboratory Materials and Manufacturing Directorate (AFRL/ML) and Air Vehicles Directorate, the Office of Naval Research-ManTech, Bell Helicopter Textron, The Boeing Company, Lockheed Martin Corporation, and Northrop Grumman Corporation. It is said that to afford the integration of advanced composites in aircraft the assembly costs had to be cut. The most suitable way to do so was considered in minimizing the number of thousands of parts and hundreds of thousands of fasteners, as this would make drilling holes and installing fasteners unnecessary. Thus, a major source of labour and rework in aircraft structures would be avoided. Part integration and structural assembly through bonding were chosen to track the problem. The objective of the CAI is formulated as "to 'establish the confidence to fly large integrated and bonded structures'", ll. 31-32, page 1, Russel (2006).

The primary technology for the manufacturing of integrated composite structures was vacuum assisted resin transfer moulding (VARTM). In this technology, vacuum is applied to suck the liquid resin into a cavity where the composite preform has been placed before. The main advantages towards state-of-art manufacturing processes are the abandonment of an autoclave leading to reduced capital equipment costs. The second main advantage is seen in the VARTM resins which cure at lower temperatures. This enables the use of more inexpensive tooling reducing system development costs. Several parts were demonstrated and showed fibre-volumes and per ply thickness comparable to autoclave cured parts. VARTM was considered to be a production process ready for aerospace industry (Russel, 2006).

Of greater importance for the conducted research work is the consideration of the bonding process involved in the CAI. Pi-joint bonded primary structure design was chosen as the bonding technique for large integrated structures. The reluctant use of adhesive bonding for primary structures is said to be based on concerns about the judge ability of bond quality. For example, they stated that the distinguishing between a joint where the adhesive is properly distributed and a joint where the bonding partners are in touch with each other without adhesive between them (kissing joint) is difficult to achieve. However, Russel points out the benefits for a proper designed and processed adhesive joint to be what was stated by several other publications, the reduced part and fastener count and reduced assembly times.

The bonded joint design of choice was the Pi-joint (π-joint). The roof of the Pi (π) can be co-cured or co-bonded to the skin. Acting as a stiffener the Pi-joint provides benefits in terms of structural redundancy and is said to be stronger than a double-lap joint. Furthermore reduced assembly times are achieved through the providing of a determinate assembly feature. It is stated that in typical skin and spar bonding processes adhesive out times are experienced. The distribution of the adhesive in the clevis of the Pi-joint is expected to take significantly less time which means out times are avoided. Furthermore adhesive areas exposed to air are smaller for the Pi-joint. The paper gives no information about the way the adhesive is distributed between the adherends within the Pi-joint.

Coupons to full scale testings proved the Pi-joints' robust and predictable performance. One key finding was that the adhesively bonded Pi-joints strength was three to five times higher than the strength of the part of the Pi-joint that was co-cured to the skin. Consequently, the Pi-joint is not considered to be the weak link in the primary structure. Pi-joints with defects as thick bondlines, canted blades, blades skewed to one side of the clevis, voids and peel plies that were not removed prior to bonding still performed well.

Tested applications were the X-45A wing carry through and the X-45C wing to design limit load, design ultimate load and finally to failure. According to Russel (2006) "these structural and ballistic test show that bonded structures can meet structural requirements for military aircraft", ll. 38-41, page 3, Russel (2006). Assembly times could be reduced from 50 – 80% depending on the structure, and cost savings ranged from 20 – 50%.

Within the project, the development of key supporting tools and technologies was also considered. For example computational tools allowing more accurate analysis taking into account peel as well as shear stresses, damage progression evaluation tools, non-destructive testing for production and maintenance and certification approaches were amongst those. For more details it is referred to Russel (2006).

Summing up, Russel considers the CAI to be a "huge technical success", ll. 73-74, page 4, Russel (2006). He states that "technology applications are increasing and are anticipated to continue to expand", ll. 78-79, page 4, Russel (2006). No information could be found investigating the adhesive distribution in the Pi-joint. It is not clear if the adhesive bonding process was conducted using the insertion squeeze flow method that is investigated within the presented research work. Even if the insertion squeeze flow method was applied in the CAI no publishing could be found. Thus, investigations on insertion squeeze flow bonding of composite structures appear to be meaningful and of major

importance, especially considering the huge potential it offers for composite structure applications in aircrafts according to Russel (2006).

A very similar publication dealing with the Composite Affordability Initiative was Russel (2007). Basically, the same approach and results are presented (Russel, 2007).

An article by Ritter published in July 2005 (Ritter, 2005) summarizes the outcomes of the previously discussed works, which were the Navy ManTech program (Navy, 2005) and the Composite Affordability Initiative (Russel, 2006). In general, it states that adhesive bonding was investigated for applications in primary aircraft structures. It repeats the main benefits gained from adhesive bonding compared to the use of mechanical fastening. No additional information is published compared to the prior discussed works.

The Patent Application Publication "Minimum Bond Thickness Assembly Feature Assurance" presents a feature to assure minimum bond thickness for a Pi-joint (Kilwin, 2006a). It is said that Pi-joint assemblies are becoming more prevalent for the assembly of two structures especially if one or both structures are made of composites. Using this assembly may provide a way to reduce weight of the structure and may provide an increased structural strength.

The Pi-joint assembly is shown in Figure 2-7.
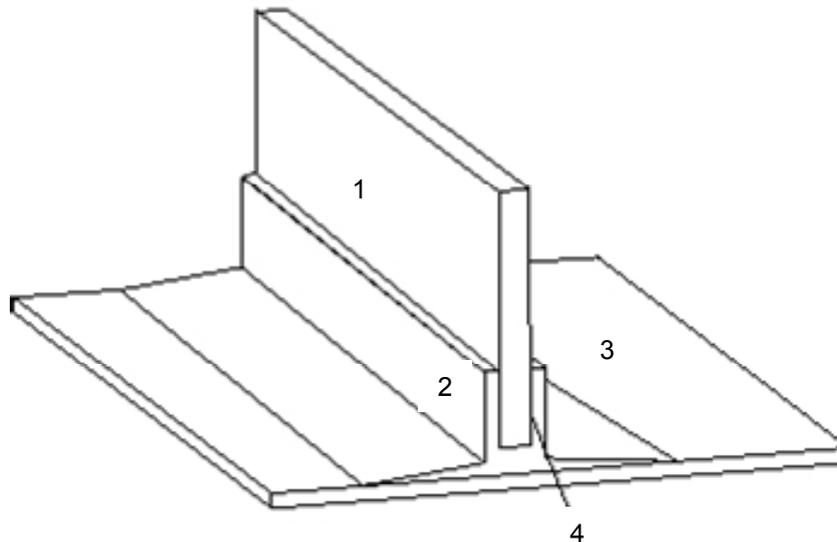
Figure 2-7: A Pi-joint assembly for structural connections as presented in Kilwin (2006a); the Pi-joint contains the spar (1), the Pi-sub-structure (2), the skin (3) and the adhesive (4).

It consists of a spar (1), the Pi-member (2) and the skin (3). To connect the spar with the Pi-member an adhesive (4) is filled in the gap between the spar and the Pi-member. A

disadvantage is seen, however, in the complicated alignment between the Pi-member and the spar prior to filling the gaps with adhesive.

According to Kilwin (2006a), there is a known process to align the parts by the use of holes that are drilled into the parts. This is done when the parts are assembled, then the parts are disassembled to remove any drill lubricant, chips and other foreign matter introduced into the part during the drilling process. Afterwards the parts are assembled again using fasteners to hold them in place to each other. Shims or wires can be used to generate a minimum bondline thickness. These shims or wires are removed after the adhesive starts to set and the so created voids are filled with additional adhesive. In ll. 62-67, page 1, Kilwin (2006a), Kilwin et al. state that "[t]he additional steps of locating, drillilng, cleaning, reassembly, fastening, shimming, unfastening, unshimming, and filling voids […] are termed 'waste' which may be disadvantageous because time and money are lost due to the additional albeit necessary steps for the present method of assembly." To avoid this "waste", Kilwin states that an improved assembly method is required, a reduction of the tooling during the assembly, and an elimination of the usage of shims and wires.

Lean manufacturing concepts are introduced to identify a way to eliminate "waste". It is built on two fundamental principles being the elimination of waste and the accelerating of the process. It is stated that this "attempt is to eliminate all activities that do not add to the value of the assembly or the process", ll. 87-88, page 1, Kilwin (2006a). After a process is fully understood it is possible to improve and optimize it in order to increase its efficiency, for example through simplifications of the design or standardization of the assembly processes.

One concept that is briefly announced for an improved locating and aligning of the Pi-assembly members is the use of a snap joint technology. This technology provides a robust way to position and align several structures with each other. No details are given about this technology.

It follows the description of the invention. The "minimum bond thickness assurance feature for a Pi-joint assembly" allows the spar and the Pi-member to be self located. A thickness control between the bonding partners is provided through "standoffs" that are machined in the part that is inserted into the Pi-member. Optionally, self locating features may be used together with the standoffs providing "horizontal control, vertical control, alignment control, depth control, or edge control," ll. 1-2, page 2, Kilwin (2006a). Figure

2-8 presents a minimum bond thickness assurance feature and a self locating feature, respectively.
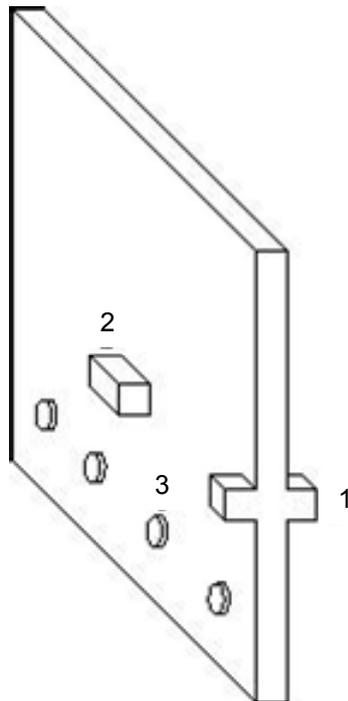
Figure 2-8: Standoffs (3) to assure a minimum bond thickness in a Pi-joint, and self locating features (1, 2) ensure the spar position in the joint (Kilwin, 2006a).

A patent from 2006 presents an adhesive injection process for Pi-joint assemblies for composite structures (Kilwin, 2006b). In this process a vacuum is created to distribute the adhesive in the gaps. The steps involved in the presented patent start with the drilling of at least two holes into the Pi-leg. Those holes act as ports for a vacuum that is applied to distribute the adhesive between the bonding partners. Filler has to be inserted into the gap between the female (Pi-member) and the male (spar/web) part and a sealant is applied above the filler. After the set up is finished, a vacuum is created at one port and the adhesive is injected into the other port as it is drawn into the gap towards the first port. In background descriptions of Kilwin (2006b), alternative methods are described for the adhesive distribution within the male and female part and their disadvantages are explained. One alternative is the "plunge method" where the Pi-member is filled with the adhesive. The spar is than plunged into the pool of adhesive. Kilwin (2006b) mentions disadvantages of the plunge method in the control of spill over so that excessive adhesive needs to be removed and the joint cleaned. The relative positioning between the parts is seen as a second disadvantage.

An alternative state-of-art method is the tube withdrawal method. A tube is placed in the bottom of the female part and the male part is positioned above the tube. All openings except for the opening where the tube will be withdrawn are closed via tapes. The adhesive is inserted into the gaps through the tube while this is removed within a certain time frame from the gap. Problems are seen in the appropriate speed of the withdrawal of the tube which might either lead to voids and air pockets if the withdrawal is to fast or to spilling of the adhesive if the withdrawal is to slow. Removal of the tape before setting of the adhesive starts is mentioned as another difficulty.

The last alternative filling method is an injection method that uses one drilled hole as a port to inject the adhesive into the gaps. To avoid spill out of the adhesive all openings are closed with tape. As the pressure applied to push the adhesive into the gaps has to be quite large depending on the viscosity and the gap dimensions, the tape is difficult to be kept in place. This would lead to spill out resulting in need for cleaning. It is also stated that ports are needed about every 12 in depending on the adhesive properties and the gap.

The adhesive injection process for Pi-joint assemblies is described as providing increased productivity for Pi-joint assemblies.

The method of choice for the presented investigation is similar to the one described in Kilwin (2006b) as plunge method. Although disadvantages are considered in the spilling out of the adhesive resulting in a necessary cleaning, this can as well be considered as an advantage as a proper fillet, which could be created through an appropriate removal of the outspilled adhesive, can provide additional strength to the bonded joint (Adams, 1987, Hart-Smith, 1987, Potter, 2001a, Potter, 2001b). The second disadvantage mentioned, which was the relative positioning of the spar and the Pi-structure, is subject of analysis in the presented research.

The adhesive injection process as presented in Kilwin (2006b) for Pi-joint assembly is considered to have some disadvantages, one being the restrictions of the adhesive that can be applied because its viscosity must be low so that it can be distributed through the applied vacuum. This restriction is not expected in the investigated insertion squeeze flow bonding process. According to the lean technology the drilling of holes into the Pi-legs can be considered as waste of time and waste of money as the holes do not contribute in any way to the Pi-joint. Lastly, it appears that the assembly steps involved in the ISF are less complicated and less preparation is required compared to the adhesive injection process. Main process steps in the ISF bonding process involve the filling of the Pi-member bottom

with adhesive, the insertion of the male part into the Pi-member, and the removal of excessive adhesive in a way to create a bond strength increasing fillet.

2.4 Penetration and Squeeze Flows

As the insertion squeeze flow process involves adhesive flow in order to distribute between the adherends, work is presented that deals with flows caused by moving boundaries. These flows include penetration flows where a solid penetrates into a fluid while displacing it, and squeeze flows, where a fluid is contained between two components that approach each other. Newtonian penetration flows are presented first. Afterwards, squeeze flows for Newtonian and non-Newtonian fluids are considered.

2.4.1 Penetration flows

To start with, Malkin (1994) provides some examples for rheological viscous flows. In sub-section 5.5.4 "Penetration of a cylinder into a viscous medium" one of the examples introduced is the penetration of a cylinder into a vessel with a bottom. Figure 2-9 shows the problem set up schematically.
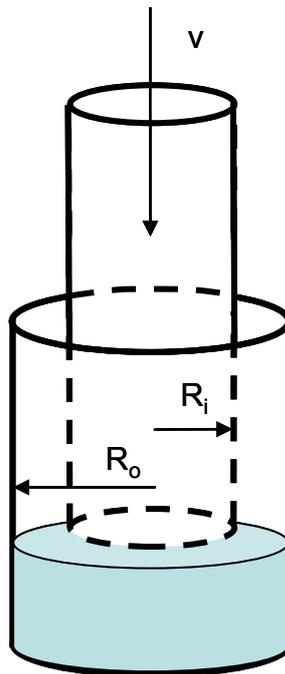
Figure 2-9: Schematic demonstration of a cylinder with radius R_i penetrating into a Newtonian fluid contained in a vessel with radius r_o (Malkin, 1994).

This flow is considered as drag flow resulting from a moving boundary. Malkin states that in general the shape of the cylinder and the vessel can be arbitrary. The shapes are

determined by the cylinder radius $R_i(z)$ and the vessel radius $R_0(z)$ where the z-axis is the axis of the cylinder and vessel.

One main parameter of interest is determined to be the resistance force that has to be applied in order to push the cylinder into the viscous fluid. The resistance force consists of two components: the force due to viscous friction along the sides of the cylinder and the force due to the pressure that acts at the bottom of it. In case $R_i(z)$ is not constant, and the cylinder is shaped in a way that it consists of a flat and a tapered region, the pressure force consists of two parts: the force acting on the tapered areas, which is termed $F_{p,1}$, and the force acting on the flat bottom, termed $F_{p,2}$.

If the gap between the cylinder and the vessel is small, the flow can be treated as one-dimensional (1D). When a constant velocity is applied on the cylinder, at an initial state it starts to touch the liquid and penetrate into it, forcing some liquid to be displaced into the gap. H is specified as the variable height of a displaced fluid layer within the gap and l is variable distance between the cylinder bottom and the bottom of the vessel, both being a function of time.

According to Malkin (1994) information on resistance force can be found by knowing the pressure and velocity distribution. An analytical solution for a Newtonian Fluid is presented. A Newtonian fluid is characterized through a proportional shear stress - shear rate behaviour. For a non-Newtonian fluid, however, the shear stress varies with shear rate nonlinearly. More detail about Newtonian and non-Newtonian fluids is given in Section 2.5. The velocity distribution in the flow between cylinders is known through (Malkin 1994):

$$v_z(r) = -v \frac{\ln r / R_0}{\ln R_i / R_0} + \frac{1}{4\eta} \frac{\partial p}{\partial z} \left(r^2 - \frac{R_i^2 \ln r / R_0 - R_0^2 \ln r / R_i}{\ln R_i / R_0} \right) \qquad (2\text{-}1)$$

The pressure gradient has to be found and substituted into equation (2-1). The shear stresses at the solid surface can be found from equation (2-2):

$$\sigma = \eta \left| \frac{\partial v_z}{\partial r} \right| \qquad (2\text{-}2)$$

The solutions for the acting shear force F_f and the two parts of the acting pressure forces $F_{p,1}$ and $F_{p,2}$ can be found on pages 158-159 in Malkin (1994). Those solutions can be simplified when assuming a small distance δ between the cylinder and vessel walls. For a

cylinder with constant radius $R_i(z) = R$ penetrating into a cylindrical vessel, the following equation for the resistance force is derived (Malkin, 1994):

$$F = \pi \eta v \left(\frac{3}{2} \frac{R^4}{l} + \frac{6R^3 H}{\delta^3} \right) \qquad (2\text{-}3)$$

Within the brackets, the first term represents the viscous forces and the second term represents the pressure forces. It is a reasonable assumption that viscous forces are small compared to pressure forces (Malkin, 1994). In comparison to Malkin's work, the main differences to the here presented research are that the fluid that is displaced is non-Newtonian and that the geometry used is, considering a cross-section, a rectangular plate and a rectangular container.

A similar problem was investigated by Cook (1982). For the process of the seating of a dental crown, different filling materials were investigated and shear rates and acting forces were calculated. As the chosen materials are non-Newtonian but can be considered Newtonian for small shear rates, Newtonian governing equations were used for the modelling of the flow problem. The seating of a crown is shown schematically in Figure 2-10,
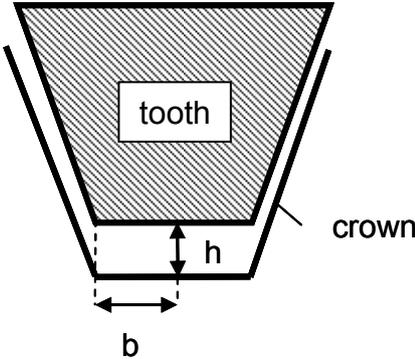
Figure 2-10: Idealized model used for the derivation of acting forces for the seating of a crown in a cross-sectional view, studied in Cook (1982)

where h is the transient distance between the tooth and the crown, and b defines the smallest radius of the crown which is found at its bottom.

Cook separates the problem into three models referring to different flow processes. These models are shown in Figure 2-11.
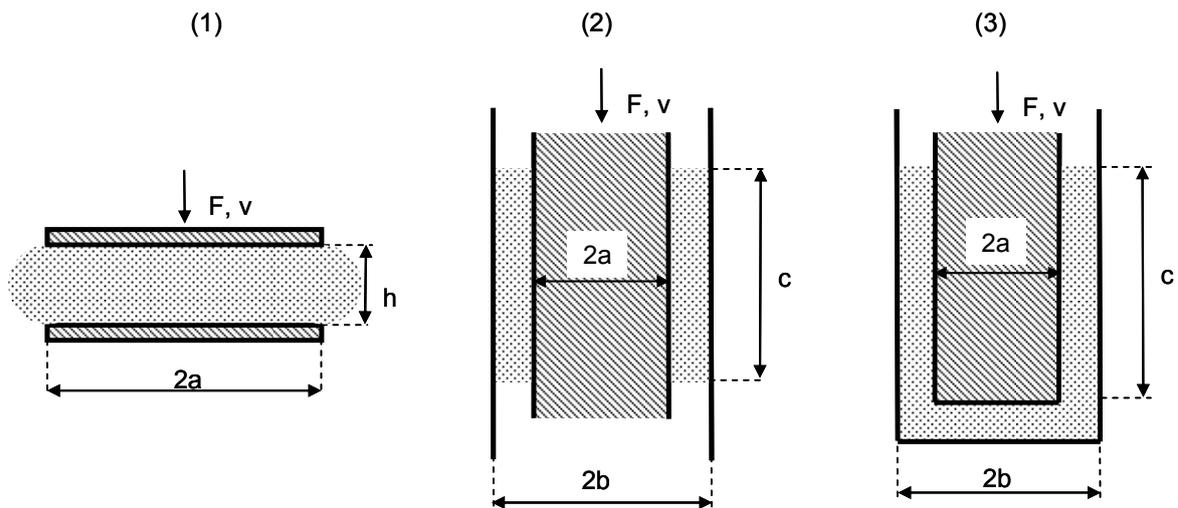
Figure 2-11: Three models used to describe the problem of the seating of a crown by Cook (1982): Parallel plate model (1), Pochettino geometry model (2, cylindrical) and penetrometer geometry model (3, cylindrical).

The parallel plate model (1) represents the flow of the fluid out of the occlusal area which is referred to as squeeze flow. The Pochettino geometry model (2) describes fluid flow between two cylindrical walls. Finally, the penetrometer geometry model (3) is a combination of (1) and (2), representing most authentically what happens in terms of fluid motion, shear rates and acting forces. Subdividing the flow problem as stated above allowed an interpretation of the relative magnitude of the acting forces. Cook (1982) derived equations from Oka (Oka, 1960) and Smith et al. (Smith et al., 1948) to calculate the acting forces due to the fluid motion for each model as shown in Figure 2-11 and compared these. The force equations and forces for the different models for two different distances *h* are presented in Table 4.

Table 4: Force ratios derived for three models that describe the seating of a crown for two different distances between the crown and the tooth (Cook, 1982).

Model	Force equation	h=1 mm	h=0.01 mm
Parallel plate geometry	$F_1 = \dfrac{3\pi\,\eta\,a^4\,V}{2h^3}$	5.0×10^{-4}	4.0×10^{-8}
Pochettino geometry	$F_2 = \dfrac{4\pi\,\eta\,a\,c\,V}{[(b+a)\ln\left(\dfrac{b}{a}\right)]}$	9.0×10^{-4}	8.0×10^{-3}
Penetrometer geometry	$F_3 = \dfrac{2\pi\,\eta\,c\,V}{[\ln\left(\dfrac{b}{a}\right)-\dfrac{(b^2-a^2)}{(b^2+a^2)}]}$	1	1

Cook (1982) concludes from these results that the major forces acting during the seating of a crown are due to the flow from the occlusal area into the gap between the walls.

Finally, Smith et al. (1948) investigated a rod moving axially into a fluid in a closed tube. Cook's and Oka's equations describing the penetration flow are based on Smith's et al. (1948) derivations. Acting forces during the rising of the fluid between the walls of the rod and the closed tube were derived. Starting from the general integral form of the velocity distribution in Poiseuille flow, the velocity was determined to be defined as

$$V = \frac{-pr^2}{4\eta L} + \frac{A}{2\pi\eta L}\ln r + B \,. \qquad (2\text{-}4)$$

Within equation (2-4) V is the axial velocity of the displaced liquid that is flowing up between the walls, p is the pressure acting within the liquid below the rod, r is the radius at which the velocity is determined and finally L is the length between the bottom of the rod and the maximum height of the displaced liquid (also refered to as flow front). A and B are integration constants which result from the double integration of the balanced force equation between the viscous and pressure forces, and can be determined from boundary conditions.

The pressure term can be derived applying the continuity equation as the amount of displaced liquid below the rod has to match the rising liquid (2-5):

$$v_i \, \pi \, r_i^2 = \int_{r_i}^{r_a} v \, 2\pi r \, dr \qquad\qquad (2\text{-}5)$$

Solving the integral and rearranging, the pressure term is derived as:

$$p = \frac{4\eta L v_i}{(r_a^2 + r_i^2)\ln({r_a}/{r_i}) - (r_a^2 - r_i^2)} \qquad\qquad (2\text{-}6)$$

It is assumed that the resistance force is made up of two components, similar to the approach applied by Malkin (1994), which are the shear forces on the side walls of the cylinder and the pressure forces on the bottom of the cylinder. This can be expressed as

$$F = 2\pi \, r_i L \eta \left(\frac{\partial V}{\partial r}\right)_{r=r_i} + \pi \, r_i^2 p \,. \qquad\qquad (2\text{-}7)$$

Substitution of the three unknown variables (*A*, *B* and *p*) into equation (2-7) gives the following equation for the resisting force:

$$F = \frac{2\pi\eta L V_i \left(r_a^2 - r_i^2\right)}{\left[\left(r_a^2 - r_i^2\right)\ln\left(\frac{r_a}{r_i}\right) - \left(r_a^2 - r_i^2\right)\right]\ln\left(\frac{r_a}{r_i}\right)} + \frac{2\pi\eta L V_i}{\ln\left(\frac{r_a}{r_i}\right)} \qquad\qquad (2\text{-}8)$$

From this equation, it can be seen that the force necessary for a rising of the fluid is a linear function of the insertion velocity V_i of the rod, the viscosity η of the fluid and the flow front L (Smith et al., 1948). Furthermore, the force is the sum of two terms which represent the viscous and the pressure forces.

2.4.2 Squeeze flows

Many studies have investigated squeeze flows of various fluid types that are enclosed between two parallel approaching discs or plates. Studied variables were material properties, boundary conditions, dimensions and process parameters.

Adams et al. (Adams et al., 1997) presented a finite element solution for an elasto-viscoplastic material that is squeezed between two approaching plates. No-slip and lubricated wall boundary conditions were considered, with a Coulombic boundary condition for the latter. Fluids exhibiting apparent yield behaviour as pastes or concentrated suspensions were focussed on. For those fluids the constitutive material behaviour is commonly described by one-dimensional forms of the Bingham or Herschel-

Bulkey relationships (Herschel, 1926). However, for more complex flows as the investigated squeeze flows inconsistencies in the flow field are experienced. Therefore, Adams et al. (1997a) suggested the usage of a von Mises yield criterion combined with a linear elastic response and a post-yield viscoplastic constitutive relationship. Experiments were used to validate the finite element solution and good agreement was found for compression forces, radial displacement fields and wall normal and shear stress distributions.

Laun et al. (Laun, 1999) investigated squeeze flows of viscous fluids between parallel approaching plates for a Newtonian and a power-law fluid. Their objective was to establish a relationship between the squeeze force and the squeezing speed for partial slip boundary conditions. The slip velocity is increasing linearly with increasing radius of the parallel plates reaching a rim slip velocity at the edges of the plates. A procedure is proposed to determine the rim slip velocity from squeeze flow experiments when a constant rim shear stress is imposed. This procedure is based on derivations describing the relation between squeezing speed and force. The derivation is conducted in two steps; the derivation for the Newtonian material and small gaps is presented first, then the derivation for the power law fluid is presented. According to Laun et al. (1999) partial slip occurs due to the presence of a thin lubrication layer near the wall.

Newtonian fluids and Non-Newtonian soft solids were investigated experimentally in (Meeten, 2004) while being squeezed between two parallel glass plates, with the motion realised through the application of a constant force. For plate roughnesses varying between 0.3 and 31 μm the separation $h(t)$ and the squeeze rate $V(t)$ were measured. Non-Newtonian soft solids showed boundary-slip being decreased or removed if plate roughness was increased towards the upper range. Even with optically polished plates no perfect slip could be achieved. According to Meeten (2004), a perfect slip boundary condition can be described as an equibiaxial extensional strain on the material. This allows measurement of the extensional rheology of a material. For a no-slip case, however, the material squeezed suffers from an extensional and a shear strain. For $R \gg h$ and sufficient boundary friction, the extensional contribution to the squeeze force is negligible (Meeten, 2002, Meeten, 2004).

Jackson et al. (2006) investigate squeeze flow between two approaching plates in order to analyse a process called "mouldable thermoplastic interface" (MTI) which was developed at the CRC-ACS Ltd., Fishermen's Bend, Australia. MTI is described as a manufacturing process with the purpose of locally altering dimensions of composite

components (Jackson, 2006). It involves the co-curing of a thermoplastic layer on the laminate and can be used for profiling, tolerancing or locating other components. During the MTI process the thermoplastic material is squeezed between the approaching plates so that some material flows out of the approaching area. To determine the final thickness of the thermoplastic layer between the approaching plates, a flow model is derived from the lubrication theory by Scott (1931). It is essential to know the viscosity to predict the final thickness. However, consecutive viscosity measurements in a temperature range from 180-200°C did not provide a repeatable result and the viscosity varied between 20,000 and 100,000 Pa.s. Those test showed a shear thinning fluid characteristic with increasing shear rate, which was found to be approximatable by a power-law relation. Ultimately, the viscosity was determined from squeeze flow tests when a pressure was applied and the displacement of the plates was measured for isothermal conditions. This test allowed a determination of the viscosity values which then were used to calculate the final thickness with respect to various MTI process parameters.

Finally, an example using computational fluid dynamics (CFD) for the analysis of squeeze flows was discussed by Mannan et al. (Mannan, 1995). An analytical and a CFD model was developed to analyse the bonding of liquid crystal display (LCD) chips on glass substrates. Particular interest was given to the establishing of dependences between applied pressure, temperature, adhesive viscosity, and process time. When the pressure is applied, the adhesive flows out of the bonding area while excessive adhesive is squeezed out, similar to processes described above. The process is conducted isothermally near the melting temperature of the thermoplastic adhesive. Several rheological properties had to be determined in order to predict the process time. Viscosity and temperature versus shear rate measurements were conducted as well as relaxation time tests to predict viscoelasticity. A power law relation was found to best represent the adhesives shear thinning fluid characteristics. The relaxation time was determined and was significantly smaller than the expected process time. In this case – according to Leider (1974) – viscoelasticity can be assumed to be negligible (Leider, 1974). To predict the motion of the plates as a function of time analytically, the Scott equation was applied (Scott, 1931). The analytical predictions varied from those predicted by the commercial finite element CFD code FIDAP. Main reason for this discrepancy were found to be due to the different shapes of the plates, as in the analytical case rounded plates were assumed and in the numerical case the predictions were for square chips.

2.5 Non-Newtonian Material Models

In the following section publications are presented that developed constitutive models for the description of Non-Newtonian materials.

An introduction into the topic of flow of polymers is given in Chapter 5 of Menges et al. (Menges, 2002). This Chapter deals with the flow of melted polymers which are considered to be high-viscous fluids. The flow characteristics of high-viscous fluids are governed by their stress-strain behaviour. Two types of deformations are distinguished (Menges, 2002): shear deformation and strain deformation. Another important property of melted polymers is viscoelasticity. A viscoelastic material is characterized through its delayed stress release. Its behaviour is described as a mixture between an elastic solid and a viscous fluid.

During polymer manufacturing processes a polymer melt typically experiences shear deformations (Menges, 2002). This results from the melt's sticking to the walls of the manufacturing machines. The melt usually is high viscous and flows slowly, which results in low Reynolds numbers (*Re*) and laminar flow. These flows can be described by Newton's two plate model. Herein, one of the two plates moves while the other is not. The material between the plates experiences shear stress and becomes deformed. The shear rate is derived from this model, and it is defined as the transient change of the shear angle (Carreau, 1997, Menges, 2002).

If the viscous flow is independent of time, elastic effects do not have to be taken into consideration. A stationary flow can be achieved when the volume flow and the flow geometry are constant. The resistance against flowing results from the inner structure of the material. This flow resistance is defined through the division between shear stress τ and shear rate $\dot{\gamma}$ and is defined as the shear viscosity η. Some fluids have a viscosity that is shear rate dependent. In this case, the fluid is described as a non-Newtonian fluid. To characterize fluids as Newtonian or non-Newtonian, their shear-stress-shear-rate dependence or viscosity-shear-rate relation has to be determined. If the shear stress increases with shear rate with a gradient smaller than one– as experienced by most polymer melts according to Menges et al. (2002) – the fluid is considered as shear-thinning. In this case, the viscosity decreases with increasing shear rate. If the shear stress increases with shear rate with a gradient higher than one, the fluid is shear thickening. If the shear stress increases proportional to the shear rate, the fluid is Newtonian. Finally, if the fluid shows a

yield stress τ_0 before flowing and the shear stress increases proportional to the shear rate the fluid can be described as a Bingham fluid.

Some empirical models describing shear-thinning fluids are also introduced in Menges et al. (2002). These are the power law model according to Ostwald/de Waele and the Carreau model. Considering viscosity versus shear rate on a double logarithmic scale shows two linear regions. These can be expressed through the power law:

$$\eta = K * \dot{\gamma}^{n-1} \qquad (2\text{-}9)$$

K is called the consistency factor or one-viscosity which is the viscosity of the material at a shear rate of $\dot{\gamma} = 1\,s^{-1}$. For a Newtonian fluid the viscous exponent n is 1. For most shear-thinning materials it is said that it varies between 0.7 and 0.2. The disadvantage of this model is the description of the viscosity for very low shear rates as in this case the viscosity gets infinitely large. For some fluids, the viscosity is constant in this region so that the material acts as a Newtonian fluid. According to Menges et al. (2002) this is not the case for rubbers and thermosetting materials so that the power law model is suitable for this type of materials.

The Carreau model is a three parameter model and describes the shear rate dependant viscosity as follows:

$$\eta(\dot{\gamma}) = \frac{A}{\left(1 + B\dot{\gamma}\right)^C} \qquad (2\text{-}10)$$

A is the extrapolated viscosity at a shear rate of 0, B is the reciprocal transition shear rate and C is the slope of the viscosity versus shear rate curve for the shear thinning region. This model can be applied for materials that show Newtonian behaviour for small shear rates and shear-thinning behaviour for larger shear rates.

Menges et al. (2002) state that polymers – independant whether in a solid or a melted state – are considered to be viscoelastic if they experience a deformation that changes with time; in this case the stresses within the material are released with a delay. This differs from an entirely viscous material behaviour as for viscous materials stresses are proportional to the shear rate (Ferry, 1961, Menges, 2002).

Several mechanical models exist that describe viscoelastic material properties. Many models use spring or damper elements and different combination of both. For example, an energy-elastic behaviour is described by a single spring and an entire viscous behaviour is

described as a single damper. A combination of both is the Maxwell model where spring and damper are set in line with each other. The deformation behaviour of the Maxwell model is characterized as hard-elastic and flow resistance decreases with time. Table 5 shows some spring-damper models(Menges, 2002).

Table 5: Spring-damper models for the description of various polymer deformation characteristics as described in Menges et al. (2002).

Deformation characteristic	Model	Symbol	Equation
Hard-elastic	Energy-elastic, Hook behaviour		$\sigma = E_1 \cdot \varepsilon$
Plastic	Viscous behaviour		$\sigma = \eta_1 \cdot \dot{\varepsilon}$
Hard-elastic and less flow resistance with time	Maxwell-Model		$\sigma = \dfrac{\varepsilon}{\dfrac{1}{E_1} + \dfrac{1}{\eta_1}}$
Delayed high plasticity	Voigt-Model		$\sigma = \eta_2 \cdot \dot{\varepsilon} + E_2 \cdot \varepsilon$
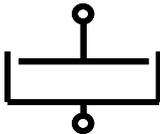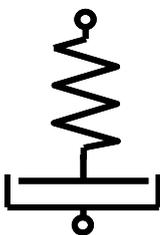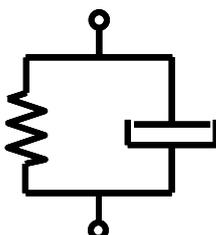
In Boyce et al. (1988) a constitutive law describing the inelastic deformation behaviour of glassy polymers near the glass transition temperature is developed. The deformation behaviour is characterized by the yield depending on pressure, strain rate and temperature as well as softening and hardening after yield. Significance for this work is considered in warm manufacturing processes as extrusion, drawing, blow moulding and calendering in order to avoid expensive trial and error procedures (Boyce, 1988).

A typical schematic description of yield and post-yield behaviour for a glassy polymer at a temperature below the glass transition temperature is shown in Figure 2-12:
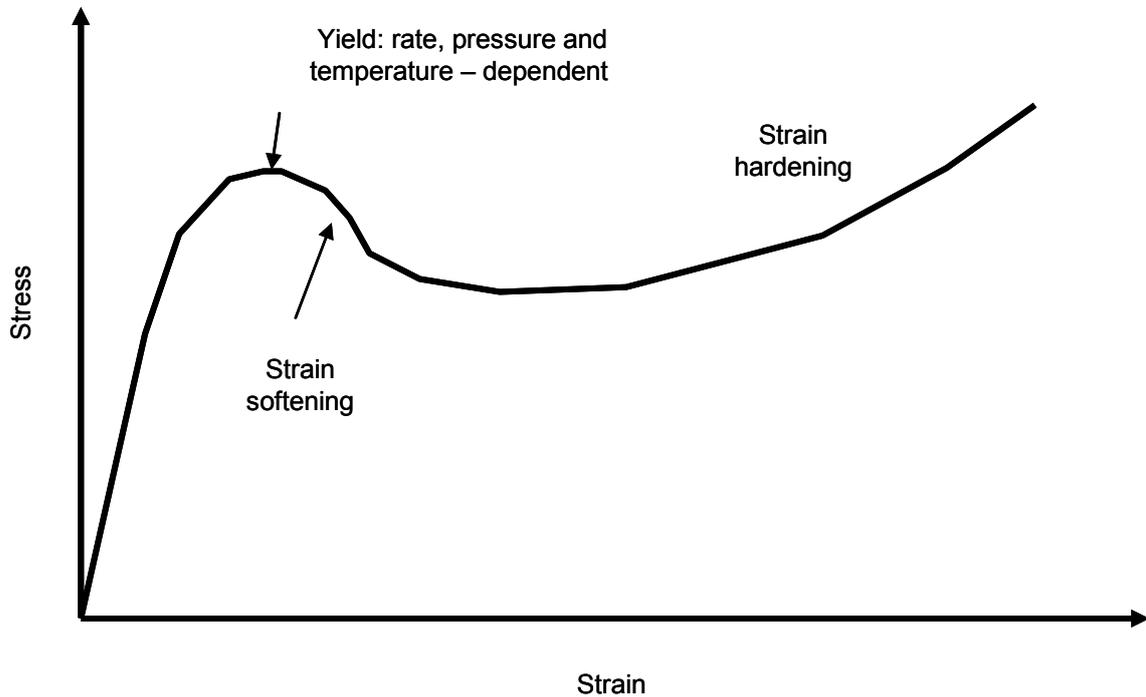
Figure 2-12: Typical stress-strain characteristic of a glassy polymer below the glass transition temperature.

The development of the constitutive model is based on the assumption that the sources of resistance to moving are twofold (Argon, 1973, Haward, 1968): first, prior to initial yield, the material must be stressed to overcome its molecular resistance to segment rotation. Second, once the material flows, molecular alignments occur altering the materials configurational entropy. Boyce et al. (1988) start from the formulation of the kinematics of finite strain and determine the rate of plastic shape change D^P to be:

$$D^P = \dot{\gamma}^P N \qquad\qquad (2\text{-}11)$$

In equation (2-11) $\dot{\gamma}^P$ is the plastic shear strain rate and N is the normalized deviatoric portion of the driving stress state, T^*. The driving stress state is the difference between the true stress and the temperature dependent entropic hardening, and describes the true stress dependence on true strain.

The plastic shear strain rate $\dot{\gamma}^P$, which can be determined applying equation (2-12), was derived taking into consideration the strain rate and temperature dependencies below the transition temperature, the entropic molecular resistance which was derived

by Parks (Parks, 1984), strain softening effects as shown in Figure 2-12, and the pressure dependence of intermolecular resistances:

$$\dot{\gamma}^P = \dot{\gamma}_0 \exp\left[-\frac{A\tilde{s}}{\theta}\left(1-\left(\frac{\tau}{\tilde{s}}\right)^{5/6}\right)\right] \qquad (2\text{-}12)$$

The parameter $\tilde{s}$ depends on the pressure and on the athermal shear resistance s; A is a function of the net angle of rotation ω of the molecular segment between the initial configuration and the activated configuration of the thermal diffusivity a and the Boltzmann's constant k; θ is the temperature and τ is the shear stress. For a detailed derivation of equation (2-12) and its parameters it is referred to Boyce et al. (1988).

A constitutive equation for an epoxy resin is proposed in Wang et al. (2005). The model is proposed on the basis of two assumptions: first, a Bingham model takes into account the yield stress of a material but not its shear thinning characteristics (Spencer, 2001). Second, a shear thinning material can be modelled by a power law (Dupaix, 2007, Menges, 2002) but, however, the power law model does not include presence of elastic properties and yield stress (Sabar, 2002).

Wang et al. (2005) base their investigation on shear stress and viscosity versus shear rate measurements of an uncured epoxy. According to their viscosity measurements in a shear rate region between 0 s^{-1} and 0.08 s^{-1}, it was stated that "a little yield stress exists", l. 10, page 178. Wang et al. (2005) considered the yield stress to be caused by experimental error or that it actually existed.

The established constitutive model is as follows (Wang, 2005):

$$\tau = \tau_0 + \kappa_1\dot{\gamma} + \kappa_2\dot{\gamma}^n \qquad (2\text{-}13)$$

Within equation (2-13) τ_0 is the yield stress, κ_1 is stated to be the shear viscosity that is caused by the Newtonian characteristic of the material and κ_2 is denoted to the non-Newtonian effect on the shear viscosity. Finally, n is the power law index.

The measurement of viscosities for very low shear rates, for example being in the orders smaller than O(-2), is difficult to conduct (Menges, 2002). Thus, it remains unclear from the presented paper by Wang et al. (2005) if an uncured epoxy resin indeed possesses a yield stress. Furthermore, yield stress was said to be rather low ($\tau_0 = 0.2 \text{ Pa}$) and it was determined from an extrapolation of measured shear stress versus shear strain data.

Seevaratnam et al. (Seevaratnam, 2007) studied the effect of a shear thinning fluid on its dynamic wetting of a moving boundary. Motivation for their study is stated to be due to the

fact that although some fluids are considered Newtonian, in regions of high shear rates they actually behave shear thinning. High shear regions appear close to moving boundaries as velocity gradients are large (Seevaratnam, 2005).

In this study, aqueous solutions of Xantham gum were chosen as test fluids for the measurements of dynamic contact angles. The fluids show shear thinning behaviour after exceeding a critical shear rate. The Xantham gum solutions' elasticity is considered to be negligible. Apparatus and experimental set up consist of a Pyrex tube ($r \sim 70$ mm) which penetrates at different speeds ($6 \, \mu m/s < U < 500 \, \mu m/s$) into the test fluid. During penetration the advancing interface shape is captured with a long distance microscope and a CCD camera (15 frames per second).

From rheological measurements using a cone and plate geometry a constitutive model to describe the viscosity of Xanthum solutions with respect to shear rate was derived, specifying the viscosity for two shear rate ranges:

$$\eta = \eta_0 \quad for \; \dot{\gamma}_c \leq \dot{\gamma} \qquad\qquad (2\text{-}14a)$$

$$\eta = \eta_0 \left(\frac{\dot{\gamma}}{\dot{\gamma}_c} \right)^{n-1} \quad for \; \dot{\gamma}_c \geq \dot{\gamma} \qquad\qquad (2-14b)$$

For shear rates smaller than a critical shear rate $\dot{\gamma}_c$ the viscosity equals a specified zero viscosity η_0; η_0 can be found through the extrapolation of viscosity versus shear rate data. For shear rates larger η_0 the viscosity is expressed through equation (14b).

A benchmark was conducted to analyse the wetting behaviour of Xantham gum and a model was selected that was developed to describe wetting of a Newtonian fluid (Cox, 1986, Dussan, 1991, Hocking, 1982).

Sherwood (2008) investigated transient flow of a viscoelastic thixotropic fluid in a vane rheometer (Sherwood, 2008). The investigated fluid is a solution and modelled using the modified Bautista-Manero (MBM) model described by Boek (Boek, 2005). The MBM model predicts the shear stress to be proportional to shear rate in very low shear rate regions for steady shear flows.

The solution is contained between two cylinders of which the inner one rotates. After the inner rotor of the vane rheometer starts to rotate, the shear stress increases to a maximum before decaying to a steady shear stress plateau. The aim of Sherwood (2008)

was to investigate how likely viscoelasticity is to alter stresses that occur during the early stages of rotation.

As mentioned above the investigated fluid is a solution. Therefore the derivation of the constitutive model is based on the assumption that the shear stress consists of two components being the solvent shear stress and the particle shear stress. This is also applicable for the viscosity.

Sherwood (2008) shows that – as widely known in literature – the stress maximum cannot be considered to be a static yield stress if the stress maximum changes for different vane rotation speeds. If the final steady stress is independent of shear rate the fluid can be considered to have a yield stress over the investigated shear rates. However, the MBM modelled fluid does not have a yield stress, because if the rate of rotation decreases sufficiently so does the final steady shear stress.

Summing up, the reviewed publications for this section defined several material models that describe the rheological characteristics of selected fluids. These pieces of information may be applicable for the development of a material model for the adhesives that are used for the conduction of an ISF bonding process. Depending on the results of a number of rheological tests, some of the presented models may be suitable to support the development of a constitutive material model for the viscosity of the selected adhesives.

2.6 Summary

Within the review of the literature, advantages and disadvantages of conventional mechanical fastening methods and adhesive bonding techniques were enumerated and adhesive bonding was found to be the better bonding method for fibre-reinforced materials. Adhesive bonding was considered to be suitable for a wider range of structures compared to alternative bonding techniques as co-curing where scarcely any complex structures were reported to be joinable. Concerning load case considerations, it was found that the use of a taper and adhesive fillet combination can significantly increase the failure load. Alternative adhesive distribution processes for Pi-joints were found to be complex and in some cases restricted to the type of adhesive that can be applied. Penetration and squeeze flows were reviewed; no studies could be found investigating the geometry and fluid under consideration in the presented study. Finally, material models describing the rheological properties of selected fluids were presented and suitable models may be applied for the development of a constitutive material model for the adhesives.

3 Numerical and Experimental Method

3.1 Numerical Method

The numerical work conducted in the current investigation was performed using the commercial computational fluid dynamics (CFD) software Fluent 6. Fluent utilizes a finite-volume approach to numerically solve the Navier-Stokes equations. Its multiphysics capabilities enables the user to simulate a wide range of various physical phenomena, such as solidification of materials, chemical reactions, heat transfer and radiation, turbulence, acoustics, porous flows and free-surface flows. The slight penalty for this diversity is that Fluent is not optimized for one particular problem and as a consequence requires increased computational resources (i.e. cpu-time and memory) to yield solutions.

The state of the system under consideration can be described by the equations governing conservation of momentum and mass. A brief description of the technique to solve these equations is provided. Further details of the technique and a good discussion on the finite volume method in general is given in Versteeg & Malalasekera (Versteeg & Malalasekera, 1995).

The continuity equation or conservation of mass equation which is solved is shown in equation (3-1):

$$\frac{\partial \rho}{\partial t} = \nabla \cdot (\rho\, \boldsymbol{u}) \tag{3-1}$$

Within equation (3-1) ρ is the fluid density and $\boldsymbol{u}$ is the fluid velocity vector. Taking the fluid density as constant, the mass conservation equation (3-2) reduces to the constraint:

$$\nabla \cdot \boldsymbol{u} = 0 \tag{3-2}$$

For an incompressible Newtonian fluid, i.e. assuming the viscous stresses to be proportional to the rate of change of deformation, the Navier-Stokes equations given in equation (3-3) can be derived from the conservation of momentum equations:

$$\rho \frac{\partial \boldsymbol{u}}{\partial t} + \rho\, (\boldsymbol{u}\, \nabla)\, \boldsymbol{u} = -\nabla P + \eta\, \nabla^2 \boldsymbol{u} + \rho \boldsymbol{g} \tag{3-3}$$

Within equation (3-3) P is the pressure, η is the dynamic viscosity and $\boldsymbol{g}$ is the body force vector (typically gravity).

The scalar continuity equation (equation (3-2)) and the vector Navier-Stokes equation (equation (3-3)) are non-trivial to solve. This is due to two features: they are non-linear; and there is no explicit equation for the pressure. The latter shortcoming is overcome through the SIMPLE algorithm by Pantankar and Spalding (Pantankar & Spalding, 1972). The SIMPLE algorithm can be thought of as a *guess-and-correct* iterative procedure, starting from an initial guess for the pressure field P^*. Using P^* in the discretised momentum equations one obtains an initial approximation for the velocity field u^*. As the velocity has to satisfy continuity as well, a correction of the velocity is required. By using the continuity equation, corrections for the velocity and pressure can be determined such that the final velocity field will satisfy continuity by the end of the iterative process. Variations to this approach have been used successfully to solve a wide range of flow problems. The iteration terminates when a specified level of convergence is reached. This is judged by the accuracy to which the discretised equations are satisfied.

For numerical simulations involving skewed rectangular elements, a modified version of the SIMPLE algorithm, called SIMPLEC (also described in Versteeg and Malalasekera (1995)), was applied. It yields better convergency for some of the cases examined in this thesis.

As Versteeg and Malalasekera (1995) show, within a finite volume framework, the governing equations must be converted into algebraic expressions first before they can be solved numerically. This conversion is achieved through the integration of the governing equations over each control volume or *finite volume* of a mesh. The integrations result in *discretized* equations, which are equations describing the discrete conservation of momentum within each control volume. A general transport equation for any quantity ϕ, which can be u, v, w or any other scalar quantity such as the volume fraction, is given by Versteeg and Malalasekera (1995) as:

$$\frac{\partial(\rho\,\phi)}{\partial t} + \nabla\cdot(\rho\,\phi\,\boldsymbol{u}) = \nabla\cdot(\Gamma_d\nabla\phi) + S_\phi \qquad (3\text{-}4)$$

Here, Γ_d is the diffusion coefficient, which is u in case of the momentum equation, and the body forces and pressure gradients are contained in the source term S_ϕ if required.

Integrating the general transport equation over each control volume CV, one obtains

$$\int_{CV}\frac{\partial(\rho\phi)}{\partial t}\,dV + \int_{CV}\nabla\cdot(\rho\,\phi\,\boldsymbol{u})dV = \int_{CV}\nabla\cdot(\Gamma_d\nabla\phi)\,dV + \int_{CV}S_\phi\,dV\,. \qquad (3\text{-}5)$$

Applying the divergence theorem, the second term (convective term) and third term (diffusive term) can be re-written as integrals over the surface A of the control volume:

$$\frac{\partial}{\partial t} \int_{CV} (\rho\,\phi)\,dV + \int_A \boldsymbol{n} \cdot (\rho\,\phi\,\boldsymbol{u})\,dA = \int_A \boldsymbol{n} \cdot (\Gamma_d \nabla \phi)\,dA + \int_{CV} S_\phi\,dV\,. \qquad (3\text{-}6)$$

In words equation (3-6) states that (Versteeg & Malalasekera, 1995):

Rate of increase of ϕ	+	Rate of decrease of ϕ from convection across boundaries	=	Rate of increase of ϕ from diffusion across boundaries	+	Rate of creation of ϕ
(Rate of change)		*(Convection)*		*(Diffusion)*		*(Source)*

For a two-dimensional control volume as shown in Figure 3-1, the rate of change of any quantity ϕ has to balance the convective and diffusive fluxes across the north, south, east and west boundaries as well as the rate of its creation within the control volume.
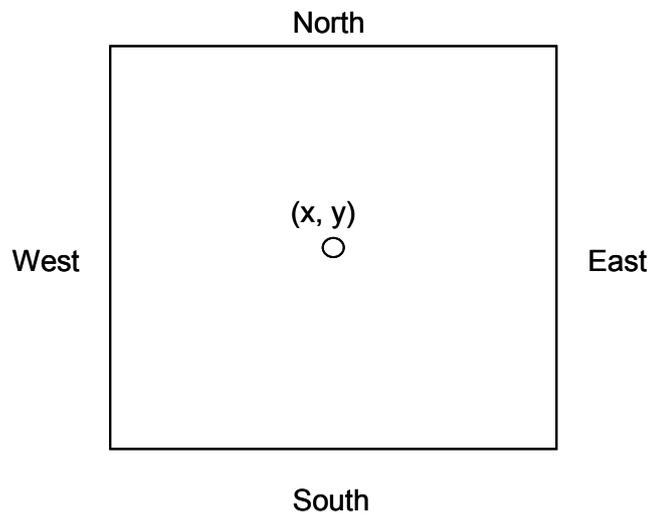
Figure 3-1: Two-dimensional illustration of a control volume.

From this balance an algebraic expression relating values of ϕ for the cell and its neighbours is derived. As in Fluent the quantities ϕ are stored at the cell centre – consider Figure 3-1 – but for the convection terms face values are required, these quantities have to

be interpolated. This interpolation is accomplished through so-called *upwind schemes*, which means that the face quantity values are obtained through interpolation between the considered control volume and its neighbouring control volume in an upstream direction of the flow. Several upwind schemes are available, e.g. first and second order upwind, or the QUICK (Quadratic Upwind Interpolation for Convective Kinetics) scheme. A description of the discretisation scheme, which is used, will be presented in the Section 3.2.

Finally, it should be noted that for the current investigation a segregated solver is used. This approach iterates the component momentum equations sequentially, uncoupled from one another. The converged solution is obtained after many iterations if the method converges. Tolerances are specified to terminate the iterative process. These are referred to as convergence criteria. These are the maximum differences allowed in satisfying the discrete equations, generally measured as an average value, such as an rms error.

3.2 Discretisation Schemes

3.2.1 Spatial discretisation

The spatial discretisation of the momentum equation is generally achieved through the application of the first- or the second-order upwind scheme.

The first-order upwind scheme is, as the name implies, only first-order accurate; however, convergence of the iterative approach is generally better than for higher-order schemes. The cell quantity value ϕ is held constant throughout the entire cell. As a result the face quantity ϕ_f is obtained by simply setting it to be equal to the cell quantity value ϕ of the *upstream* cell.

For the second-order upwind scheme, the cell face quantities ϕ_f are computed using a multidimensional linear reconstruction approach (Barth & Jespersen, 1989). Second-order accuracy is achieved through a Taylor series expansion of the cell-centred solution about the cell centroid. A detailed discussion can also be found in Versteeg and Malalasekera (1995), and in Fletcher (Fletcher, 1991). Basically, the face value of any quantity is calculated as

$$\phi_f = \phi + \nabla \phi_f \cdot \Delta \boldsymbol{s} \,, \qquad\qquad (3\text{-}7)$$

where ϕ_f and $\nabla \phi_f$ are the cell-centred value and its gradient in the upstream cell, and $\Delta \mathbf{s}$ is the displacement vector between the cell-face centroid and the cell centroid of the

upstream cell. Applying the divergence theorem, the required gradient $\nabla\phi_f$ in each cell can be calculated as

$$\nabla\phi_f = \frac{1}{V}\sum\widetilde{\phi}_f \mathbf{A} , \qquad\qquad (3\text{-}8)$$

where $\widetilde{\phi}_f$ is computed as the average of the two cells adjacent to the face.

3.2.2 Temporal discretisation

For the simulation of transient problems the governing equations have to be discretised in both space and time. The spatial discretisation remains the same for both steady and transient simulations. The temporal discretisation effectively involves integrating all terms in the governing equations over a time step Δt.

The approach is demonstrated by considering the generic ordinary differential equation for the time evolution of a variable ϕ (equation (3-9)):

$$\frac{\partial\phi}{\partial t} = F(\phi) \qquad\qquad (3\text{-}9)$$

Within equation (3-9) $F(\phi)$ incorporates terms which have already been discretised in space. A first-order accurate temporal discretisation, introducing a truncation error of $O(\Delta t)$, is given by

$$\frac{\phi^{n+1} - \phi^n}{\Delta t} = F(\phi) , \qquad\qquad (3\text{-}10)$$

where the method can be implicit or explicit depending on when the $F(\phi)$ is evaluated.

For the current implementation of Fluent, the first-order implicit temporal discretisation had to be chosen as it was the only option if the volume-of-fluid method and the transient segregated solver were used. Therefore only the first-order implicit temporal discretisation method is described.

The implicit temporal discretisation solves for $F(\phi)$ at a future time level:

$$\frac{\phi^{n+1} - \phi^n}{\Delta t} = F(\phi^{n+1}) , \qquad\qquad (3\text{-}11)$$

which is solved by initializing ϕ^i to ϕ^n and iterating the equation to

$$\phi^i = \phi^n + \Delta t \cdot F(\phi^i) \,. \qquad\qquad (3\text{-}12)$$

Using the segregated solver – as done in the present study – the overall time discretisation error is comprised of two parts: the order of the temporal discretisation scheme, i.e. first or second-order implicit, and the accuracy in which the scheme is advanced from one time level to the next. The latter is referred to as the *time-advancement* scheme. Temporal discretisation introduces a truncation error whose order depends on the order of the temporal discretisation scheme: $O(\Delta t)$ for first-order implicit and $O(\Delta t^2)$ for second-order implicit. The advancement to the next time level introduces a splitting error, which is controlled by an iterative time-advancement scheme in the present study. In this scheme, for a given time step Δt all equations are solved iteratively until convergence criteria are met. Thus, several outer iterations are performed before advancing to the next time level. These iterations consist of the following steps:

- Solve the momentum equations,
- Solve the pressure correction,
- Correct the pressure velocity flux,
- Solve for scalars,
- Check for convergence;
    - If convergence is not met: repeat the iteration;
    - If convergence is met: advance to the next time level.

3.3 Multiphase Flow, Non-Newtonian Fluids and Moving Boundaries

3.3.1 Multiphase flow applying the Volume-of-Fluid method

To model a fluid-fluid interface the volume-of-fluid (VOF) method is used. This is incorporated in Fluent. The VOF method is described in Hirt and Nichols (Hirt & Nichols, 1981). The main assumption made for the VOF method is that the fluids do not interpenetrate. The physical properties that are assigned to a cell are based upon the volume fraction of each phase within the cell. In solving the volume fraction equation the interface is tracked while ensuring the amount of fluid in a cell is conserved.

The transport equation for the volume fraction is given by:

$$\frac{\partial \alpha_1}{\partial t} + u \cdot \nabla \alpha_1 = 0 \, , \qquad\qquad (3\text{-}13)$$

with α_1 being the volume fraction of phase 1. Volume fractions of all phases sum up to a value of 1. The physical properties for each cell are calculated by:

$$\phi = (1 - \alpha_2) \phi_1 + \alpha_2 \phi_2 \, , \qquad\qquad (3\text{-}14)$$

where ϕ can be the phase density or the phase viscosity.

A single momentum equation is solved throughout the entire domain resulting in a velocity field that is shared among the different phases. The drawback of the VOF method is that for cases in which large velocity differences exist between the two phases the interface becomes less certain. This can be overcome by using higher resolution in the areas where significant velocity differences are expected.

Some details follow about the tracking of the interface. If a cell is occupied by two phases an interpolation near the interface has to be conducted in order to maintain a required balance between convective and diffusive fluxes into a cell. For the interpolation near the interface, the geometric reconstruction scheme is used. The geometric reconstruction scheme is a piecewise linear approach providing the most accurate interface shape and is generalized for unstructured meshes from the work of Youngs (Youngs, 1982). The scheme assumes that the interface between two fluids has a linear slope within each cell. It starts from calculating the position of the linear interface relative to the centre of each partly occupied cell based on local volume fraction information. The second step is to calculate the amount of fluid convected through each cell face using the interface position and the velocity field information. Finally the volume fraction in every cell is calculated using the flux balance from the previous step.

This section concludes with information about setting up transient VOF simulations (Fluent, 2005d). The time step Δt used for the volume fraction calculations differs from the time step used for the rest of the transport equations. The time step for VOF is refined automatically based on the maximum Courant Number allowed near the interface. The Courant Number is a dimensionless parameter that compares the time step in a calculation (Δt) to the characteristic time of transit of a fluid element across a control volume ($\Delta x_{CV} / v_{Fluid}$):

$$Co = \frac{\Delta t}{\Delta x_{CV} / v_{fluid}} \, , \qquad\qquad (3\text{-}15)$$

The characteristic time of transit is the time taken to traverse the cell given the fluid velocity within. Based upon this characteristic time of transit and the maximum allowed Courant Number near the interface, a time step is computed for use in VOF calculations. For a default (given) Courant Number of 0.25, which is the Courant Number used in the current analysis, the time step is restricted to be 25% of the minimum transit time for any cell near the interface.

3.3.2 Non-Newtonian fluid viscosity

For incompressible (constant density) Newtonian fluids, the shear stress is proportional to the rate-of-deformation tensor D_{ij}:

$$\tau_{ij} = \eta D_{ij}, \qquad (3\text{-}16)$$

where the shear viscosity η is constant and the rate-of-deformation tensor D_{ij} is defined as:

$$D_{ij} = \left(\frac{\partial u_j}{\partial x_i} + \frac{\partial u_i}{\partial x_j} \right). \qquad (3\text{-}17)$$

For some non-Newtonian fluids the shear-stress can similarly be written as

$$\tau_{ij} = \eta\left(D_{ij}\right) D_{ij}. \qquad (3\text{-}18)$$

The shear viscosity η in general is a function of all three invariants of the rate-of-deformation tensor. In the viscosity models available in Fluent (Fluent, 2005d), though, the viscosity is defined as a function of the shear rate $\dot{\gamma}$ which is related to the second invariant of the rate-of-deformation tensor as follows:

$$\dot{\gamma} = \sqrt{\frac{1}{2} D_{ij} D_{ij}} . \qquad (3\text{-}19)$$

The non-Newtonian viscosity models that are available in Fluent are the Power law model, the Carreau model for pseudo-plastics, the Cross model and the Herschel-Bulkey model for Bingham type of plastics. Further there is an option to implement an alternative model via a user-defined function (UDF). This option was chosen in many of the conducted simulations, and the model developed to relate the shear viscosity to the shear rate will be described in sub-Section 4.4.5. The Power law model is the other model that was applied and therefore is described here briefly.

The non-Newtonian power law model relates the shear viscosity and the shear rate in a power law form:

$$\eta = k\dot{\gamma}^{n-1} e^{\frac{T_0}{T}} .$$

Within equation (3-20) k is the consistency coefficient and n is the Power law index, which is less than 1 for shear-thinning fluids. T_0 is the reference temperature, so that the last term in equation (3-20) becomes one for isothermal considerations.

An upper and lower viscosity limit has to be specified for smallest and greatest shear rates, respectively. A typical viscosity versus shear rate relation for a shear thinning fluid is illustrated in Figure 3-2:
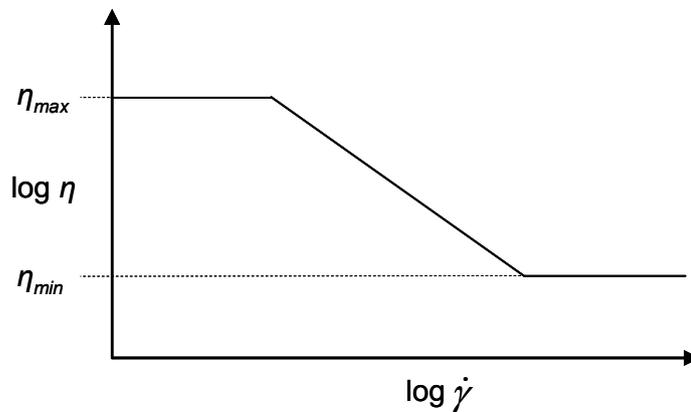
Figure 3-2: Log viscosity versus log shear rate plot for a shear thinning fluid.

3.3.3 Dynamic mesh model

The dynamic mesh model incorporated into Fluent enables simulations where the domain changes with time due to motion of domain boundaries. Details are given in the Fluent User Guide in the section on flow modelling in moving and deforming zones (Fluent, 2005d). The motion of the boundaries can be either a prescribed motion, i.e. a specified velocity profile is attached to a boundary, or an unprescribed motion, i.e. a subsequent motion which is determined based upon the results of the current time step (such as due to the force on the boundary). The available mesh updating schemes that can be used to alter the domain will be discussed shortly. First the governing equations applicable to the dynamic mesh model are introduced.

The conservation equation for a general scalar quantity ϕ on an arbitrary control volume V with a moving boundary can be expressed as

$$\frac{\partial}{\partial t}\int_V \rho\phi dV + \int_V \rho\phi(\boldsymbol{u}-\boldsymbol{u_g})d\boldsymbol{A} = \int_{dV} \Gamma\Delta\phi d\boldsymbol{A} + \int_V S_\phi dV \ . \qquad (3\text{-}21)$$

The nomenclature is specified according to the definitions used for equation (3-4) on page 44. Note, $\boldsymbol{u_g}$ specifies the grid velocity of the moving mesh. The first term – the time derivative with respect to the control volume – is defined as

$$\frac{\partial}{\partial t}\int_V \rho\phi \ dV = \frac{(\rho\phi V)^{n+1} - (\rho\phi V)^n}{\Delta t} \ . \qquad (3\text{-}22)$$

The superscripts indicate the time levels with n indicating the current time level. For the following time level, i.e. the $(n+1)^{\text{th}}$ time level, the volume V^{n+1} is

$$V^{n+1} = V^n + \frac{dV}{dt}\Delta t \ . \qquad (3\text{-}23)$$

The volume time derivative of the control volume is the dot product between the grid velocity of the moving mesh $\boldsymbol{u_g}$ and the face area vector of face j, as is defined in equation (3-24):

$$\frac{\partial V}{\partial t} = \int_{\partial V}\boldsymbol{u_g} \ d\boldsymbol{A} = \sum_j^{n_f}\boldsymbol{u_{gj}}\boldsymbol{A_j} \ . \qquad (3\text{-}24)$$

Finally the dot product in equation (3-24) is evaluated through the following relation:

$$u_{gj}A_j = \frac{\delta V_j}{\Delta t} \ . \qquad (3\text{-}25)$$

δV_j represents the volume that has been swept out over the control volume face during the time step Δt.

As mentioned above there are different schemes available in Fluent to conduct the remeshing of the domain that changes with time. These methods can be subdivided into three groups: smoothing methods, dynamic layering methods and local remeshing methods.

The spring-based smoothing method can be idealized as a network of interconnected springs between the edges of any two mesh nodes. This method is applied when the domain consists of triangular elements. The displacement of a specific boundary results in a force proportional to the displacement along all springs so that applying Hooke's Law this force can be written as

$$F_i = \sum_{j}^{n_i} k_{ij}\left(\Delta x_j - \Delta x_i\right).$$ (3-26)

where Δx_i and Δx_j represent the displacement of one cell i and its neighbour j, n_i is the number of nodes connected to node i, and k_{ij} is the spring constant between nodes i and j. As the net force must be zero at equilibrium an iterative equation results from this condition (Fluent, 2005d):

$$\Delta x_i^{m+1} = \frac{\sum_{j}^{n_i} k_{ij} \Delta x_j^{m}}{\sum_{j}^{n_i} k_{ij}}.$$ (3-27)

Equation (3-27) can be solved applying a Jacobi sweep and knowing the displacement at the boundaries after boundary node positions have been updated, so that the positions can be updated according to

$$x_i^{n+1} = x_i^{n} + \Delta x_i^{m,\,converged}.$$ (3-28)

Here, n and $n+1$ denote positions at the current and the next time step.

For meshes containing rectangular or hexahedral elements the dynamic layering method can be applied. Layers of cells are removed or added adjacent to the moving boundary. An ideal layer height h_{ideal} is specified and using a layer split factor α_s for the addition of cells, a cell height is allowed to increase according to the condition

$$h_{min} > \left(1 + \alpha_s\right) h_{ideal}.$$ (3-29)

For the deletion of a cell layer, a collapse factor α_c is used and the condition for the collapsing of a layer is given by:

$$h_{min} < \alpha_c\ h_{ideal}.$$ (3-30)

Finally, for zones with triangular meshes involving large displacements compared to local cell sizes a local remeshing scheme is applied. It can also be used in combination with the spring-based smoothing method. Cells are marked based on cell skewness and minimum and maximum length scales, which can be defined. Thus remeshing takes place if e.g. cell skewness is greater than a specified maximum skewness or a length scale is smaller than a minimum specified length scale.

3.4 Validation

Multiphase flow problems can be solved in Fluent with the *Volume-of-Fluid* (VOF) method. Hirt and Nichols (Hirt & Nichols, 1981) simulated a spinning bowl containing two fluids initially at rest to validate the VOF method. Reichl (Reichl, 2002) used this problem to validate the implementation of Fluent and investigate its ability to obtain accurate results. Details and outcomes are presented in sub-Section 3.4.1. In sub-Section 3.4.2, a comparison is drawn between analytic results and numerical predictions for a flow very similar to the one expected during insertion squeeze flow (ISF), analysed two-dimensionally. Next, a mesh resolution study and a mesh type independence investigation (triangular versus rectangular elements) are performed and the results presented. This section concludes with the determination of appropriate convergence criteria required for solving the momentum and continuity equations to sufficient accuracy.

3.4.1 Spinning bowl problem

To test the ability of the *volume-of-fluid* (VOF) method to model multiphase flows, and the Fluent implementation, Reichl (2002) chose the problem of a spinning bowl containing two fluids initially at rest. This problem has been used as a validation problem before, e.g. by Hirt & Nichols (1981). One advantage lies in the opportunity to compare numerical results with analytical results for the same flow process as done by Reichl (2002). The analytical solution is given by Hughes & Brighton (Hughes & Brighton, 1991). It indicates that the free surface position of the heavier fluid at the bottom is described by a paraboloid of revolution with the following form:

$$z = z_0 + \omega^2 \frac{r^2}{2g} \qquad (3\text{-}31)$$

This parabolic free surface shape results from a rotational motion of the container. Through this motion the fluid starts to move through the action of viscous shear. Eventually a steady state solution results with the prescribed parabolic free-surface shape. It is assumed that only pressure differences are responsible for balancing the centripetal acceleration experienced by the fluid. This assumption is based on the assumption that acceleration is constant with time.

The analysis performed by Reichl focussed on the density and viscosity ratios of the two fluids involved. The results for the position of the free surface when a steady-state is reached were compared with the analytic results calculated using equation (3-31). In

general, the comparison showed good agreement with the variation of the L2 error norm ranging in an order of magnitude between 10^{-3} and 10^{-4}. The L2 error is given by the square root of the sum of squares of the differences between the numerical and analytical results, divided by the number of grid points.

Concerning the effect of density ratio it was found that good agreement was obtained for ratios of 100 and 811; however, for the higher ratio it was found harder to obtain convergence. When the density ratio was decreased to 10 the agreement was poorer with over- and under-prediction in different regions. The explanation given was that for the analytical solution a vacuum is assumed above the free surface and therefore no resistance to the movement of the heavier fluid is expected. In terms of the viscosity ratio there was only little impact noticed on the solution for viscosity ratios between 60 and 500.

The conclusion from these tests was that the VOF method produced reasonably accurate predictions for this and presumably similar two phase flow problems.

3.4.2 Penetration flow in an open rectangular container

As a further test, a simplified ISF process is setup and modelled in Fluent. This is conducted two-dimensionally, with a justification of this simplification provided in the problem set-up description (Section 3.5.1). The VOF and dynamic remeshing features are included in this simulation. Outcomes are compared with an idealised analytical solution that is derived for the identical flow problem.

The problem setup is illustrated in Figure 3-3:
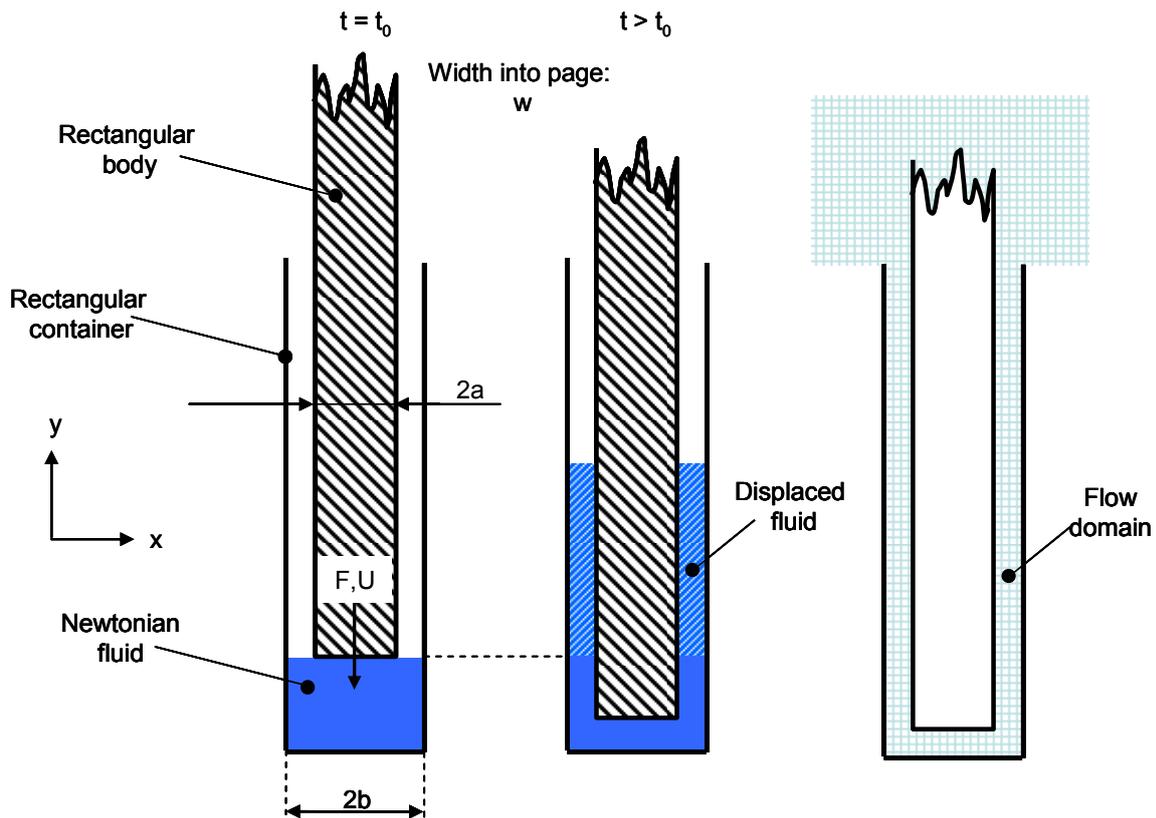
Figure 3-3: Penetration flow in a rectangular container analysed as a validation case for the adhesive flow in ISF.

The rectangular body is forced to move down with a prescribed constant velocity into a Newtonian fluid contained in the bottom of an open rectangular container. The fluid becomes displaced into the channels that are formed between the body and the container walls. The widths of the body and the container are $2a = 5.0$ mm and $2b = 6.0$ mm, respectively. The prescribed velocity v is one of two varied input parameters; the other is the Newtonian fluid viscosity. In the numerical model, the rest of the flow domain, which is illustrated as a sketch on the right hand side of Figure 3-3, is filled with a second phase (lighter gas).

Based on work by Smith, Ferry & Schremp (Smith et al., 1948), we derive an analytical solution for the flow problem under consideration. This derivation enables us to calculate the drag forces that act on the body during the insertion process. In the following the drag force will be referred to as the insertion forces. A detailed derivation of the analytical solution will be presented in Section 5.1. The insertion force is made up of the pressure force that resists the downward motion at the bottom of the body plus the viscous forces that act on the side walls of the body.

$$F = -2\,\eta\,w\,U^2\,t\,\frac{a}{a+b}\left[3\frac{(a+b)^2}{(a-b)^3}+\frac{1}{a-b}\right] \qquad (3\text{-}32)$$

The symbols used in equation (3-31) have the following meanings:

F: Insertion force;

η: Shear viscosity of Newtonian fluid at container bottom;

w: Length;

U: Insertion velocity;

t: Flow time;

a: Half width of insertion plate;

b: Half width of Pi-slot.

The insertion force was calculated applying this equation. One comparison between the calculated and computationally predicted insertion force for a particular case is presented in Figure 3-4:
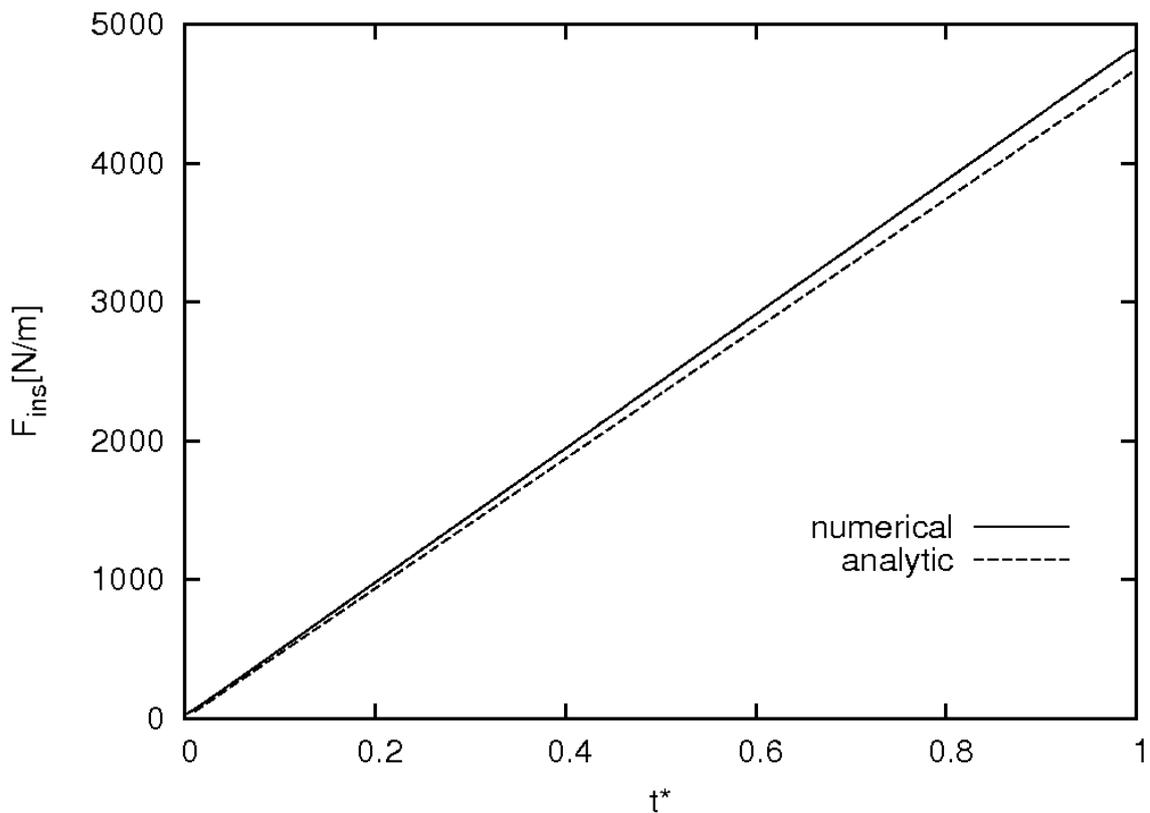
Figure 3-4: Comparison between calculated and numerically predicted insertion force with respect to flow time for an insertion speed of 5 mm/min and a constant viscosity of 1000 Pas.

The insertion force increases linearly with increasing flow time for both cases. Considering Figure 3-3 again we understand that the amount of displaced fluid increases as well as the body displacement with increasing flow time. Therefore an increase in insertion force would be expected due increasing resistance towards flow resulting in an increasing pressure underneath the insertion plate; further, increasing shear stresses that result from an increasing surface area along the body walls being covered with the displaced fluid, also add to the insertion force.

One fluid parameter (the shear viscosity) and one process parameter (the insertion velocity) were varied and the effect on the insertion force and on the accuracy was studied. Results are presented in Table 6:

Table 6: Comparison of calculated and numerically predicted insertion forces for different density and viscosity ratios at various insertion speeds.

ρ_1/ρ_2	η_1/η_2	U [mm/min]	$1-F_{num}/F_{analyt}$
1000/10	1000/1	2	$5.55 \ 10^{-2}$
1000/10	500/1	5	$3.60 \ 10^{-2}$
1000/10	1000/1	5	$3.96 \ 10^{-2}$
1000/10	2000/1	5	$3.78 \ 10^{-2}$
1000/10	1000/1	10	$4.66 \ 10^{-2}$

Subscripts 1 and 2 in Table 6 denote the fluid and gas, respectively. The fluid density is adjusted according to the density of the adhesives that will be used for ISF. The choice of the density ratio is based on the findings of Reichl (2002) i.e., that a density ratio of 100 is sufficient to produce very similar predictions to those closer to the density ratio of about 1000, without requiring excessive computer-time and under-relaxation (see sub-Section 3.4.1). The shear viscosity of the heavier fluid was varied between 500 and 2000 $kgm^{-1}s^{-1}$, the shear viscosity of the lighter phase remaining at 1 $kgm^{-1}s^{-1}$. The insertion velocity was varied from 2 to 10 mm/min.

According to Table 6 the differences between the analytical and numerical insertion force are relatively small and vary between 3.6 % and 5.6 %. Note that these values represent average differences. These relatively small discrepancies are not surprising

considering slightly different assumptions made for the two solutions. On the one hand, the analytic predictions are based on a single phase, without the presence of air above the fluid. For this case it is also assumed that movement of fluid into the gaps occurs as a plug flow. On the other hand, the numerical solution takes the density of the lighter phase into consideration, which is artificially inflated by an order of magnitude relative to air, and hence is expected to slightly over-predict the insertion force relative to the analytic case which does not have a second phase, or the physical situation where air is actually displaced.

3.4.3 Domain size, resolution and mesh type independence

3.4.3.1 Domain size

A typical flow domain that is used to perform various tests on domain sizes, mesh resolutions and mesh type interdependencies is shown in Figure 3-5:
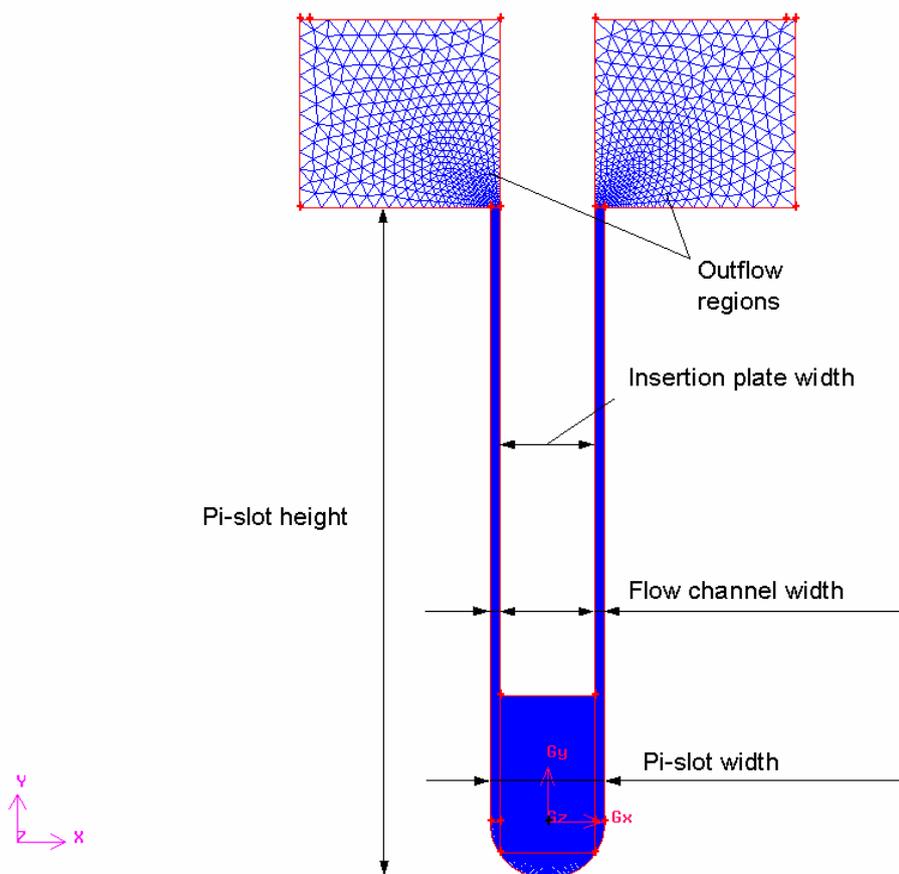
Figure 3-5: Typical mesh set-up and domain size used for the simulation of adhesive flow in ISF bonding processes.

Additional details about the problem setup are given in Section 3.5. The key dimensions in Figure 3-5 are:

Insertion plate width = 5.0 mm,

pi-slot width = 6.0 mm,

pi-slot height = 35.5 mm,

flow channel width each side = 0.5 mm and

outflow region = 10 x 10 mm^2 or 20 x 20 mm^2.

The outflow region is the part of the domain above the Pi-slot. Its purpose is to accommodate the adhesive that is displaced out of the flow channels. A second purpose is to allow the specification of a pressure outlet boundary condition at a position that is furthest away from the part of the flow domain which is of most interest. The position of the pressure outlet boundary is selected this way as to prevent an effect on the flow within the channels.

To investigate the effect of the size of the outflow region and thus the position of the pressure outlet boundary on the solution, two different grids were tested varying only in the size of the outflow region. Another consideration is to avoid the excessive size of the outflow regions to reduce the computational time requirement. As the flow in the outflow region is not really considered in the investigation, a relatively coarse triangular mesh was developed for this part of the domain.

The results obtained for the two grids are presented in Table 7. The key parameter that is compared is the drag coefficient on the insertion plate. The drag coefficient is selected as it is a useful global measure of the accuracy, efficiency and robustness of the solution. It is of interest for the development of an ISF process, as well as for pressure predictions along the Pi-slot walls. The drag coefficient along the insertion plate is a measure for the drag force along the plate, which consists of the pressure forces on the bottom of the plate and wall shear forces at the side walls of the plate.

Table 7: Drag coefficient variation for varying sizes of the outflow region.

Outflow region [mm^2]	Drag coefficient c_D
10 x 10	705.98
20 x 20	709.85

The presented results are obtained with specification of the following input parameters:

- a prescribed moving boundary condition of 10 mm/min,
- a power-law viscosity material model for the adhesive ($K = 337.97$ kgm^{-1} and $n = 0.3795$) and a density of 1270 kgm^{-1}s^{-1},
- an air density and air viscosity of 0.1 kgm^{-1} and 0.001 kgm^{-1}s^{-1},
- convergence criteria of 10^{-4} for the mass and momentum equations,
- a time step of 0.1 s and
- a mesh domain with 34249 elements.

It is noticed that the variation in drag coefficient was only 0.545 %. Therefore in further investigations a 10 x 10 mm^2 size for the outflow regions is used if not otherwise specified since it yields solutions at lower computational costs, without seriously compromising accuracy.

3.4.3.2 Resolution

Seven different grids were used to examine the effect of varying the grid resolution on the force predictions. The grids comprise of mostly rectangular elements except in minor regions within the radius of the Pi-slot and the outflow regions. The domain sizes and geometrical specifications are held constant for this study. Thus, the insertion velocity was selected as 10 mm/min and the shear viscosity of the fluid representing the adhesive was specified as a power-law fluid with the viscosity given by equation (3-33):

$$\eta = K \cdot \dot{\gamma}^{n-1}, \qquad\qquad (3\text{-}33)$$

with $K = 337.97$ [kgm^{-1}] and $n = 0.3795$, as described above.

If not otherwise specified these input variables remain constant for all cases in sub-Section 3.4.3.

The grid resolutions are increased from 14053 cells to 136724 cells for the finest mesh. The grid resolution variation is based on the variation of the vertical number of cells within the flow channels. The resolution within the flow channels appears to be the most critical as highest velocity and pressure gradients are expected there. Furthermore, a main outcome of the study is the distribution of the adhesive within the flow channels, so a sufficiently well resolved flow field has to be guaranteed in this region. Note that the flow channel is divided into eight vertical cell layers in the case of a total cell number of 14053 elements and into 20 vertical cell layers in the case of 136724 elements.

Figure 3-6 indicates the level of convergence for each studied grid. The drag coefficient of the insertion plate is plotted against the number of cells:
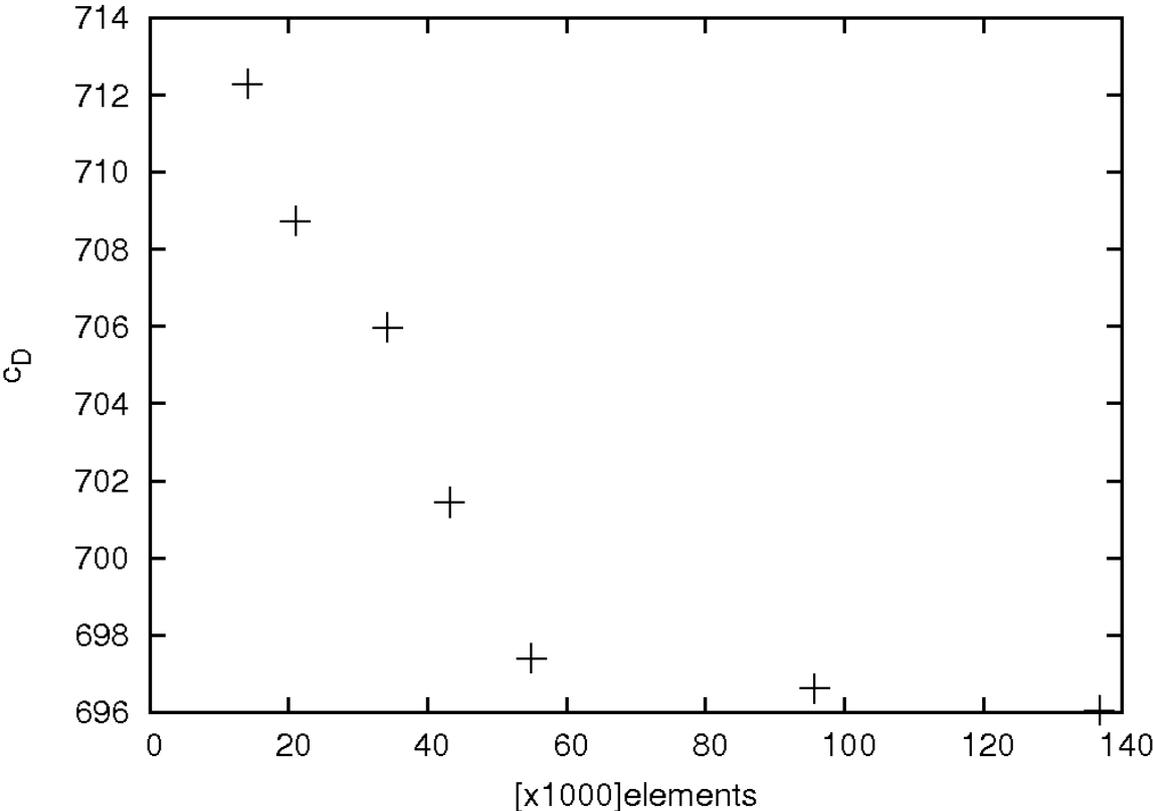
Figure 3-6: Drag coefficient of insertion plate against element number indicating the effect of grid resolution on the predictions.

Table 8 summarizes the variation of the drag coefficient from the value of the finest grid.

Table 8: The effect of the grid resolution on the drag coefficient.

Number of elements	Drag coefficient at body	Percentage difference from highest resolution
14053	712	2.3
21001	709	1.8
34249	706	1.4
43142	701	0.8
54949	697	0.08
95674	697	0.08
136724	696	0

As presented the drag coefficient variations are within 1 % of the finest grid value for the four finest grids studied. The number of mesh points increases approximately 10 fold between the coarsest and finest grids, equating to an increase in (linear) mesh resolution of about 3 fold. Thus, it can be assumed that the highest resolution is sufficiently well resolved to not warrant further testings of even finer grids. The result obtained for the case with 43142 grid cells is sufficiently well resolved to suggest this mesh is appropriate for the remainder of the study. A finer resolution will result in only minor changes to the solution accuracy while increasing the required computational time substantially.

Further validation studies were conducted to investigate the effects of different process parameters on solution convergence and accuracy. It was found that convergence is more difficult to achieve for those simulations in which the insertion speed and the adhesive viscosity are highest. Hence, the most extreme test case is for the highest insertion plate speed of 120 mm/min and the adhesive with the highest viscosity (EA 9395). Note the material model used to represent the adhesive viscosity with respect to shear rate is the five parameter rational model. The development of this model will be discussed in sub-Section 4.4.5 in detail.

In Figure 3-7, the drag coefficient on the insertion plate is plotted against the number of elements:
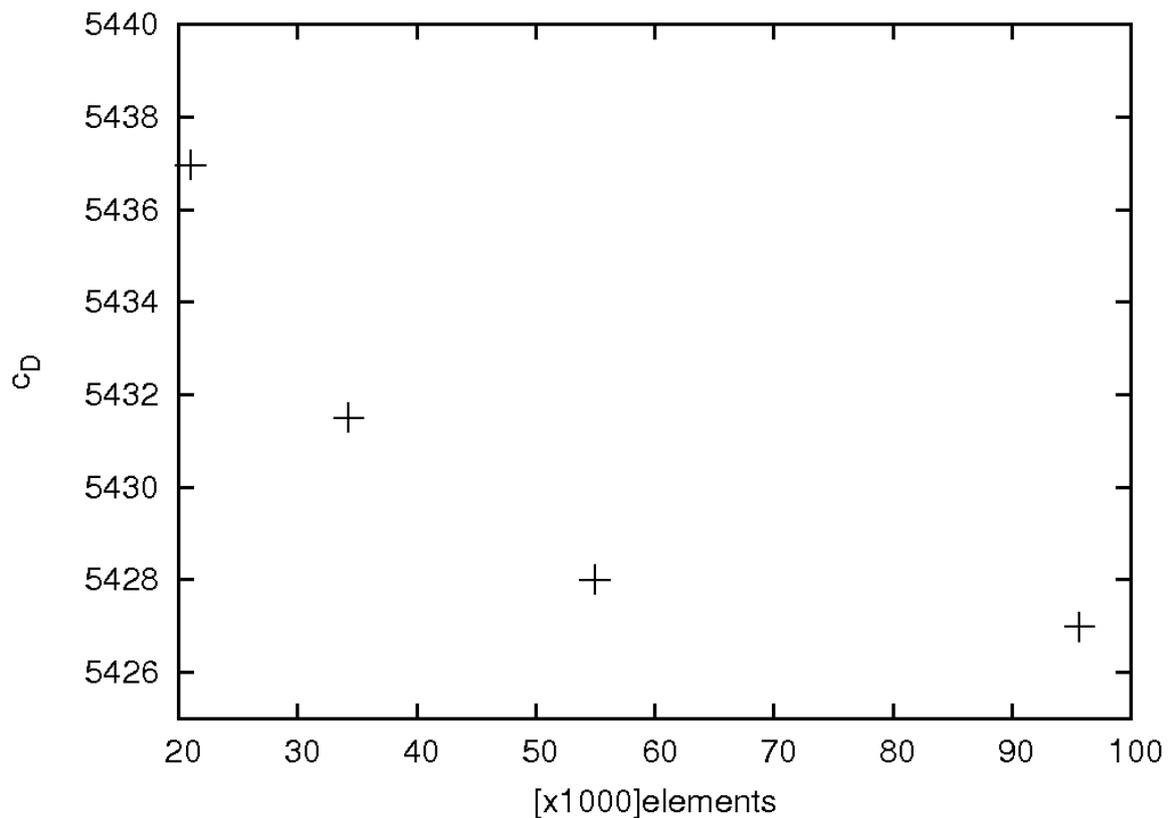
Figure 3-7: Spatial resolution study for maximum applicable insertion speed and adhesive viscosity.

Again, little difference is experienced in the drag coefficient when the element number is increased further than 43142 elements ($\ll$1 %). This mesh is selected for further analysis.

3.4.3.3 Mesh type independence

In this Section the effect of different cell types, rectangular and triangular, on the solution is evaluated. The necessity for this evaluation results from comparisons between simulations that are setup with different element types. For example, in the study on the insertion plate bottom shape (Sections 5.4 and 6.3.3), tapered and square shapes are simulated using rectangular elements, while the simulations involving a rounded insertion plate shape, however, require meshing with triangular cells due to dynamic remeshing restrictions. As the insertion plate shape effect on various output data will be studied, there arises the necessity of estimating differences that are not due to the insertion plate bottom shape, but due to the mesh type.

For the same problem set up in terms of design, dimensions, process and material parameters, a comparison is conducted between the solution obtained from a simulation that contained mainly rectangular cells and solutions for four different simulations from meshes built up of triangular cells only. The numbers of cells for the triangular grids are 24083, 49061, 110150 and 153418. The triangular-cell based meshes were constructed in a similar way to the construction of the rectangular-cell based meshes, i.e. the entire number of cells was adjusted according to the number of vertical cell layers in the flow channels. Results are compared to those from the simulation for the rectangular-cell based mesh (43142 elements). In Table 9 the drag coefficients at the insertion plate are presented for the different solutions as well as the percent difference between the results of the triangular and rectangular meshes.

Table 9: Mesh type independence analysis results.

Mesh type	Number of elements	Drag coefficient	Percent difference from rectangular grid
triangular	24083	749	6.4
triangular	49061	729	3.7
triangular	110150	714	1.8
triangular	153418	714	1.8
mainly rectangular	43142	701	0

The drag coefficientsfor the triangular grids indicate that the predictions become accurate to within a few percent for a mesh size of 100000 cells. Further increases in resolution appear unwarranted given the associated increase in the computational requirements.

Note that the difference between the triangular and the rectangular drag predictions on the finest meshes used is 1.8 %. The reason for this difference is probably due to a combination of factors including: errors induced due to the different remeshing schemes for the different mesh types, under-convergence during the iterations involved in each timestep, and small solution errors even on the finest meshes.

It is decided to use the mesh of 110150 elements for simulations where triangular meshes are required. The chosen meshes, both rectangular and triangular, are consistent with prediction accuracy of a few percent.

3.4.4 Convergence

As the numerical technique applied solves for the flow variables iteratively, it is necessary to specify a limit at which the iterative process terminates. The difference between all numerical solutions and the solutions of the discretised equations is referred to as a residual. The average of these residuals over all cells is specified as the global residual, which is used as the limit to terminate further iteration. The minimal global residuals for convergence tests are set to 10^{-3}, 10^{-4} and 10^{-5}. This means that for each timestep iteration continues until the mass and momentum equations are satisfied to better than these fractional accuracies. As before, the variable selected for comparison is the drag coefficient of the insertion body. Results for the simulations are presented in Table 10:

Table 10: Effect of convergence criteria on the drag coefficient at the body.

Convergence criteria	Drag coefficient at body	Percentage difference from highest resolution
10^{-3}	704.4	0.44
10^{-4}	701.5	0.02
10^{-5}	701.3	0

Relative to a convergence criterion of 10^{-4} an increase to 10^{-5} improved the solution accuracy only marginally – about 0.02 %. However, the higher accuracy required results in a significant increase in computer time. Thus, a convergence criterion of 10^{-4} is found to resolve the simulation sufficiently well in a reasonable computation time and is chosen for further simulations if not otherwise stated. Note that Fluent allows the convergence criteria for each equation to be selected independently; however, for the simulations reported in this thesis, the same criterion was used for all equations.

3.4.5 Time step tests

In this sub-Section the effect of varying the time step is examined. For two different time steps ($\Delta t_1 = 0.1$ s, $\Delta t_2 = 0.01$ s) the drag coefficient of the insertion plate was again compared. Additionally, a local output variable is also compared – the maximum pressure acting at the Pi-slot wall boundary. Table 11 summarizes the results:

Table 11: Time step size effect on the solution.

Output variable	Δt_1	Δt_2	% difference
Drag coefficient [-]	701.5	709.0	1.07
Maximum pressure [Pa]	79469	80138	0.83

The differences in the drag coefficient at the insertion plate and the maximum pressure at the Pi-slot wall are noted as 1.07 % and 0.83 %, respectively, on reducing timestep size by an order of magnitude. As these variations are small, but at considerable expense in terms of computer time, it was decided to use the larger timestep for the majority of simulations. Note however, that for some simulations with different moving boundary conditions it was necessary to decrease the timestep size in order to obtain convergence.

3.5 Problem Setup and Post Processing

This Section is divided into two parts: a description of the problem setup; and how the results are post-processed. The problem setup description begins with a definition of nomenclature and explanations about key dimensions. After this the specification of boundary conditions is given by information about the mesh. The sub-Section concludes with a description of the material properties used in the numerical code.

In the post-processing sub-Section, focus is first given to the calculation of transient insertion forces. Then it is explained how the pressure is examined along the Pi-slot walls during ISF. Finally, the tracking of the interface, which represents the adhesive distribution within the flow channels, is presented.

3.5.1 Problem setup

Shown on the left-hand side of Figure 3-8 is a typical example of a joint considered during the current research. This is composed of an insertion plate and a Pi-slot for the simulation of the adhesive flow. As the joint made by the ISF process is relatively long (typically to be more than 1000 mm in length), and the adhesive will be pre-applied into the Pi-slot relatively uniformly along the length, it was assumed that for most cases the adhesive flow could be simplified as a two-dimensional (2D) flow on a cross section of the joint. Key dimensions defining the geometry to be simulated included: height of the Pi-slot, H_1, initial height of the adhesive, H_0, and widths of the insertion plate and Pi-slot, $2a$ and $2b$, respectively. The length of the joint (dimension into the paper) is defined by w.

On the right-hand side the corresponding flow domain is illustrated. The initial adhesive would be contained below the insertion plate before this boundary starts its downward motion with a prescribed velocity. The rest of the domain is filled with air. The domains above the flow channels are referred to as outflow regions. Their purpose is to provide space to accommodate displaced adhesive and specify pressure outlets to avoid compression.

In the flow model setup, each solid wall was specified as a wall entity, which was rigid and impermeable with a no-slip boundary condition applied. The flow domain was then defined between these walls and is illustrated on the right-hand side of Figure 3-8. Furthermore the insertion plate walls are specified as moving walls. A prescribed translational motion is attached to these boundaries.
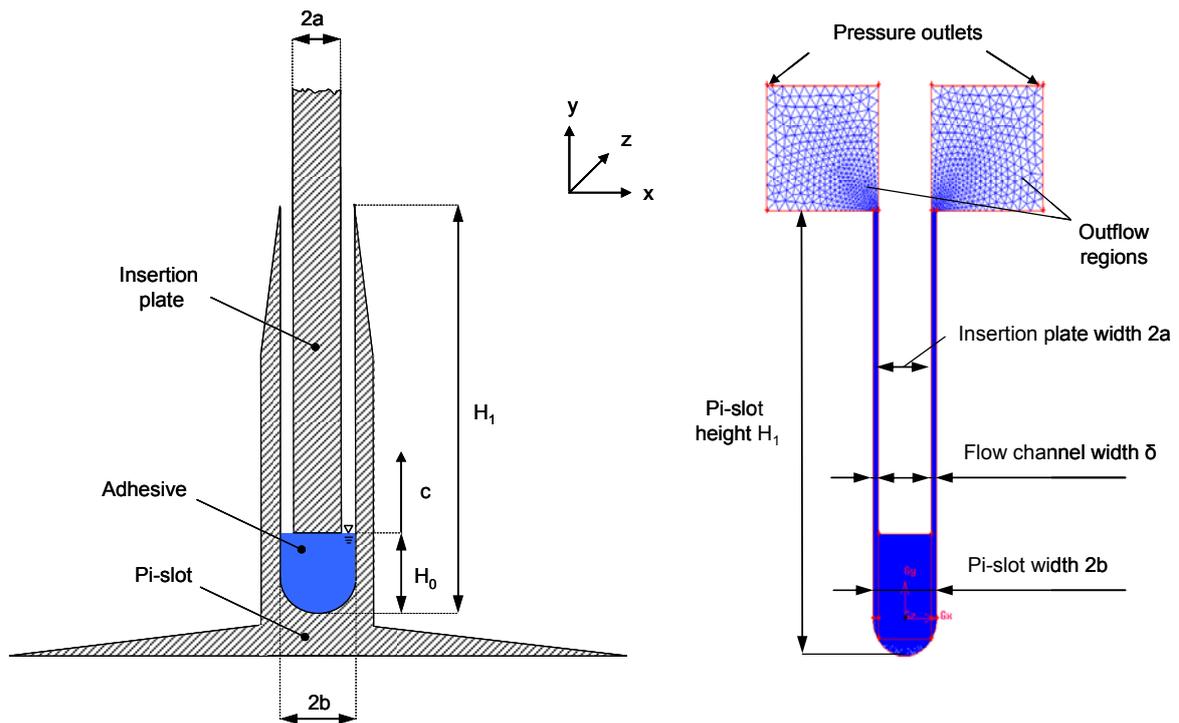
Figure 3-8: Key dimensions for 2D flow simulations (schematic and corresponding mesh).

In practice, the insertion plate can be inserted into the slot with either constant force or constant speed. Most simulations considered a constant speed insertion. In these simulations, the insertion plate is forced to move down at a constant speed and, in turn, the adhesive is displaced into the side-gaps formed between the insertion plate and the Pi-slot. Assuming a perfect alignment between the insertion plate and Pi-slot, the gap width on each side of the insertion plate was *b-a* for the geometry considered. These gaps will be referred to as flow channels in the following discussions. They become bond-lines if fully filled by the adhesive and cured.

To enable the moving boundary, interfaces between the mesh domain that is below the insertion plate and the mesh domain representing the flow channels have to be applied. These interfaces are emphasized in Figure 3-9.
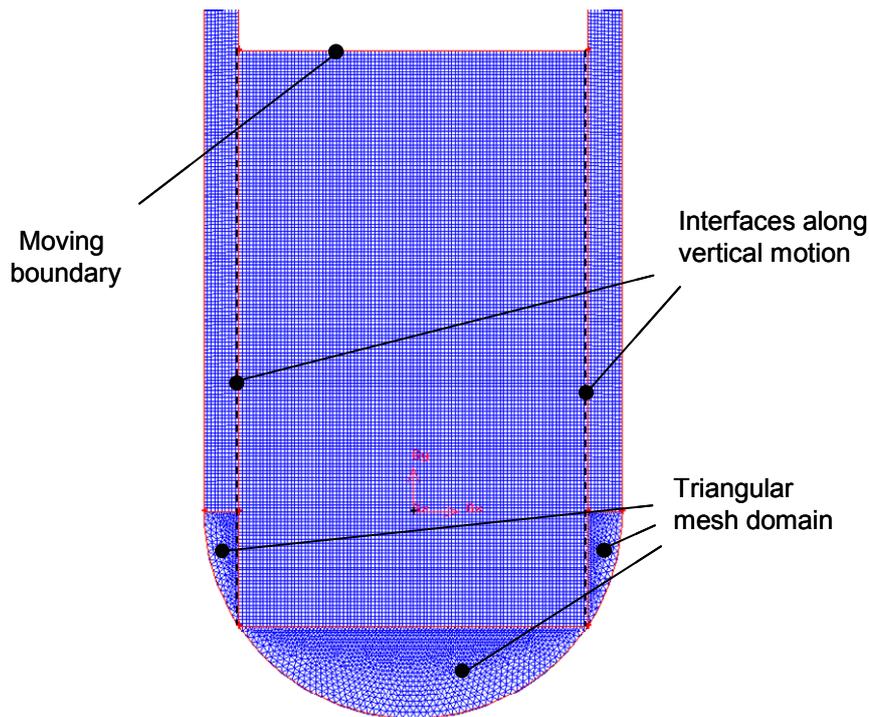
Figure 3-9: Mesh domain details indicating the moving boundaries and the necessary interfaces between sliding elements.

The purpose of the interface is to allow a sliding between adjacent cells of different mesh domains. In addition, in Figure 3-9 the moving boundary is indicated. A triangular mesh is used in part of the domain due to the difficulty in meshing with only quadrilateral elements.

Except for the indicated regions and the coarse mesh domains in the outflow regions, the rest of the domain was meshed with rectangular cells. A very similar mesh was developed for other geometries, such as when the insertion plate bottom shape is tapered (see Figure 3-10). The insertion plate bottom shape is referred to as insertion head shape in the following discussion. A third design uses a rounded insertion head shape. All head shape designs are illustrated in Figure 3-10. In the case of the rounded head shape only triangular cells are used for meshing as already was indicated in the mesh type validation study, sub-Section 3.4.3.3. As a consequence, a different remeshing scheme had to be applied, which is explained in sub-Section 3.3.3.
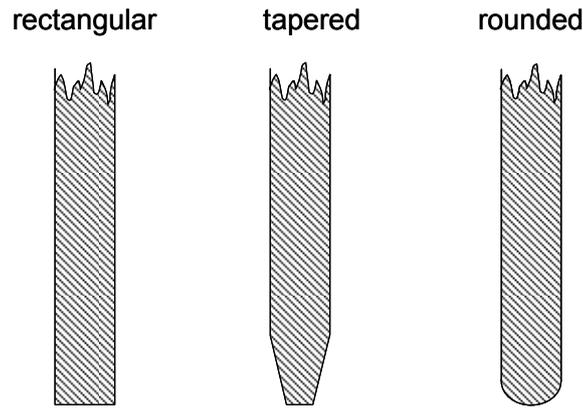
Figure 3-10: Different insertion plate bottom shapes (also referred to as insertion head shapes).

The fluids within the domain were modelled as two phases: air and adhesive. Material properties that are chosen for the two phases are investigated and results are presented in Section 3.4. Thus, the density of air is selected for most simulations as $\rho_{air} = 1$ kgm^{-3} and air viscosity is specified as $\eta_{air} = 0.001$kgm^{-1}s^{-1}. In cases where convergence difficulties were experienced these parameters had to be adjusted. The adjustment involved an increase of air density with the limitation that the condition $\rho_{air}/\rho_{adhesive} \leq 0.01$ is met. This is in line with the free surface spinning-bowl test, discussed above, which indicated that the predictions for the heavies phase are not sensitive to the viscosity ratio if it was at least 100. In addition, air viscosity always remains ≤ 1 kgm^{-1}s^{-1}. Again, previous tests indicate that the predictions for the heavier phase are not sensitive to the viscosity ratio.

Adhesive density is specified as $\rho_{adhesive} = 10^3$ kgm^{-3} as given in the data sheet. Adhesive viscosity varies according to the mixture of adhesives components. This is modelled with the code using the power law model and the five parameter rational model. The development of these models and the determination of coefficients characterizing each model will be discussed in Chapter 4.4.5.

3.5.2 Post processing

One variable of considerable interest is the insertion force, which is equivalent to the drag force of the insertion plate resulting from its downward motion. The insertion force direction is the same the motion of the insertion plate. As mentioned earlier, the insertion force is made up of two components, the pressure force at the bottom of the plate and the viscous forces on the side walls. The insertion force can be determined from the transient

drag coefficient along the insertion plate in the *y*-direction. The drag coefficient is defined as

$$c_D = \frac{2F}{\rho U^2 A},$$
(3-34)

with ρ being the reference density, U being the reference velocity, A being the reference area and F being the drag force. The drag coefficient can be directly obtained from the simulation so that the insertion force can be calculated.

The reference values can be specified and are used for post-processing only. By default, the reference values are specified as a value of one for velocity and area and the density is specified as air density, so that the drag coefficient and the insertion force are related as

$$F = 0.6125[kgms^{-2}]c_D.$$
(3-35)

A second output variable of interest for the ISF process is the pressure distribution in the flow domain. Pressure builds up below the insertion plate during its downward motion. A pressure-contour plot within the flow domain as obtained from the software is illustrated in Figure 3-11:
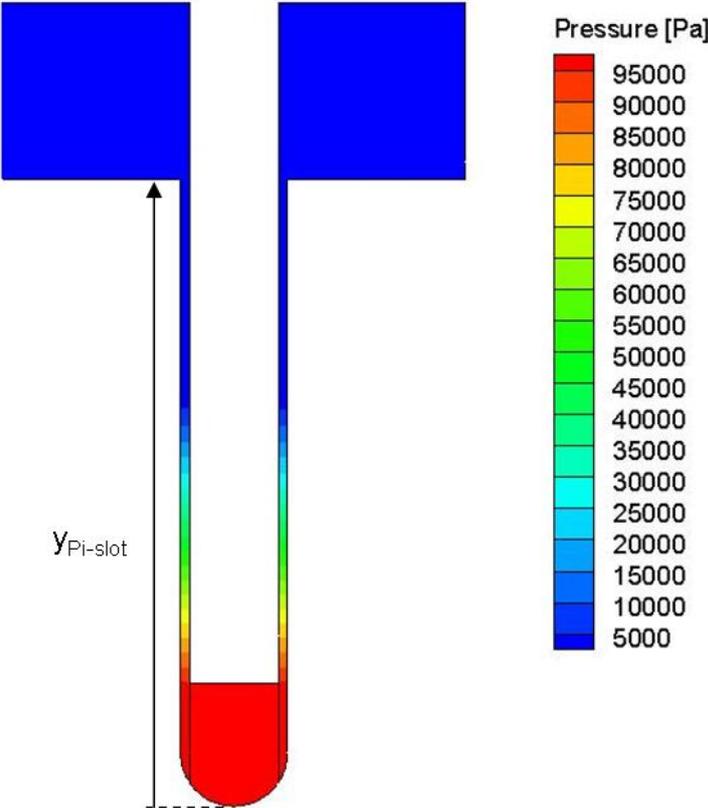
Figure 3-11: Typical pressure-contour plot during ISF.

The pressure distribution in the flow domain can be used to predict the quantitative pressure that loads the composite Pi-slot walls (Figure 3-12). This information is vital as it is necessary for the design of composite Pi-joints. These might distort during ISF or even get damaged. To obtain these pieces of information from experiments would be very complicated. The gauge pressure is plotte along the Pi-slot wall, which is indicated in Figure 3-11:
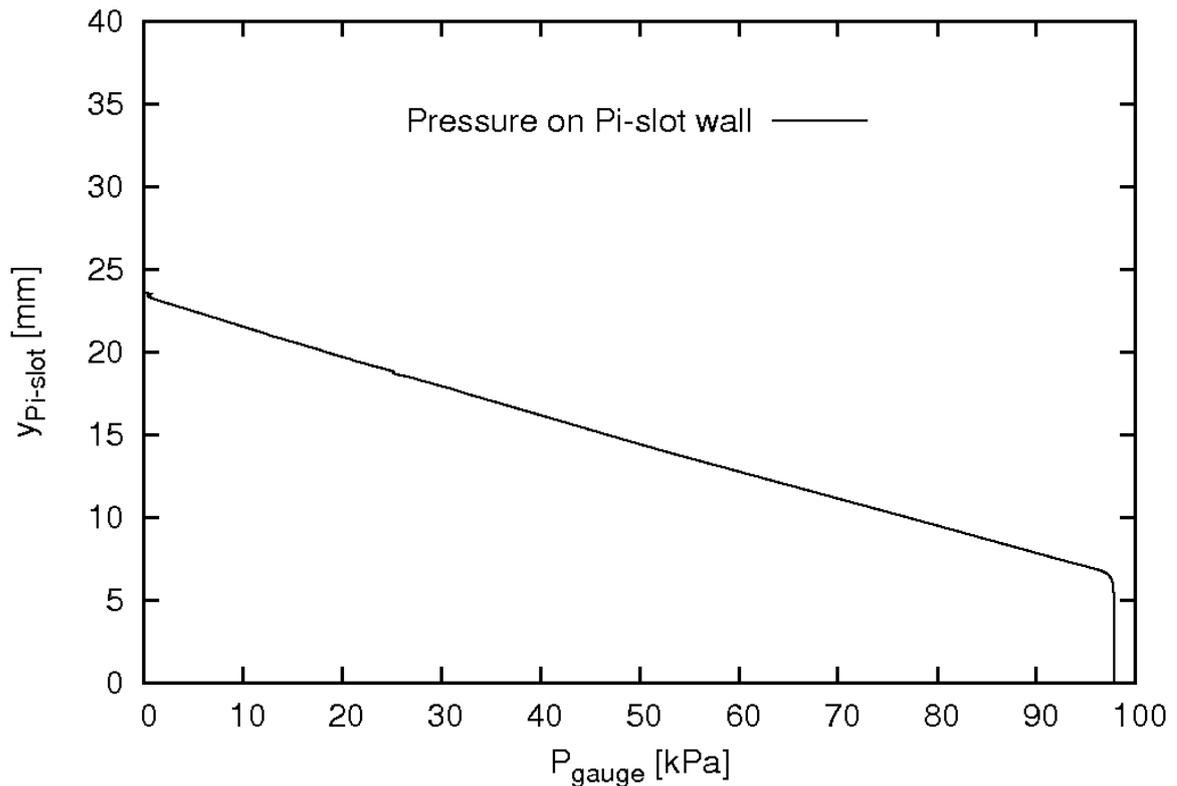
Figure 3-12: Pressure distribution at the slot wall for the above presented pressure-contour plot.

In the real case, the Pi-slot walls distort in response to the pressure resulting in an increase in flow channel width; these events are the subject of analysis in the fluid-structure interaction (FSI) (Section 7.2).

To obtain information about the distribution of both phases within the flow domain, the VOF method is implemented. VOF prescribes flow characteristics for each cell according to the volume fraction of each phase within each cell. In the phase transition region – that close to the fluid-fluid interface – the volume fraction of both phases changes rapidly from 0 to 1. As this change in general occurs over a range of finite thickness, the location of the fluid-fluid interface becomes smeared. The thickness of this interface region is largely

determined by the spatial resolution in this region. Figure 3-13 indicates the interface for a sufficiently resolved spatial simulation:
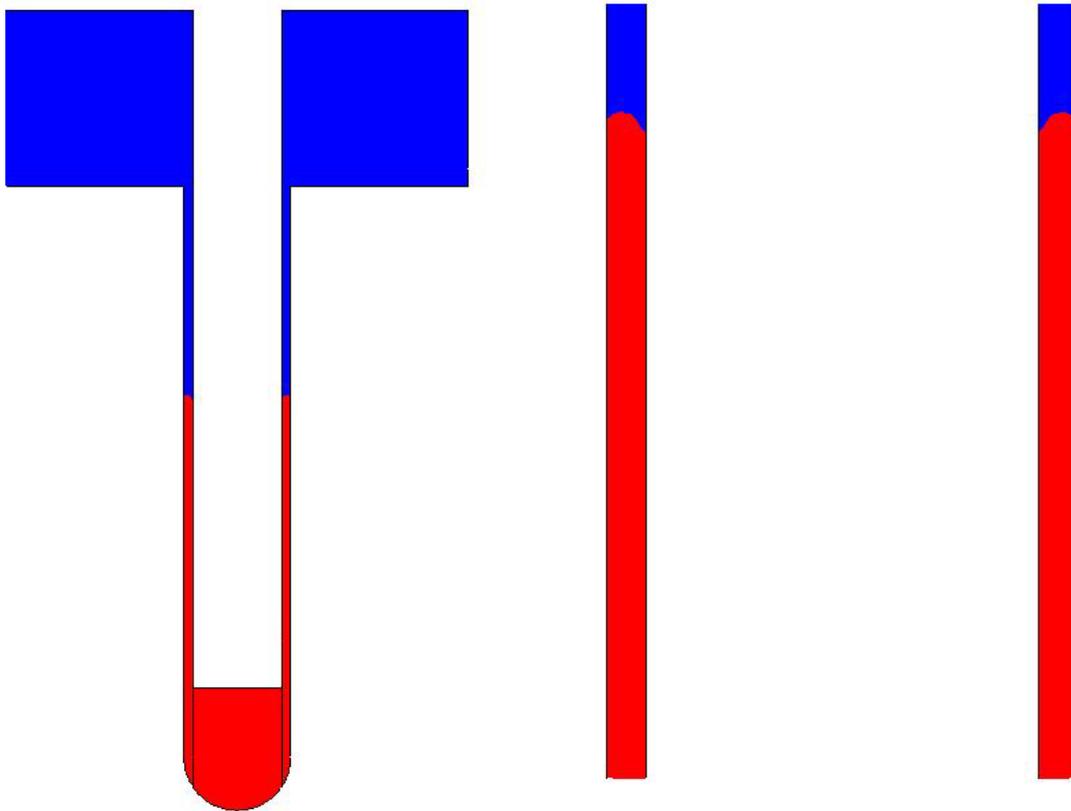
Figure 3-13: Phases distribution within the flow domain and a detailed interface of the flowfronts (adhesive coloure red, air in blue).

Red and blue colours represent adhesive and air, respectively. In Figure 3-13 the insertion plate has already moved into the adhesive and displaced it into the flow channels. The remainder of the flow channels and the outflow chambers are filled with air. The position and shape of the adhesive flow fronts are clearly indicated. For the simulations conducted the resolution of the interface is believed to be sufficient. This view is based on examining predictions of the interface shape and position from meshes with other resolutions. The right-hand side of Figure 3-13 illustrates a magnified view emphasizing the shape of the adhesive flow fronts.

3.5.3 Dimensionless parameters

The adhesive flow during ISF can be characterised through two dimensionless parameters: the Reynolds number and the Weber number.

The Reynolds number is a measure of the ratio of the inertia force on a fluid element to the viscous force on an element (Munson, 2006). It is defined as

$$Re = \frac{\rho \, V \, l}{\eta} \, . \tag{3-36}$$

In the present study, the Reynolds number is $\ll 1$, indicating viscous forces to be much greater than inertial forces. These types of flows are referred to as Stokes flows.

The second dimensionless number, the Weber number, is important for flows with an interface between two fluids. It relates the inertia force to the surface tension force of a fluid element. The Weber number is defined as

$$We = \frac{\rho \, V^2 \, l}{\sigma} \, , \tag{3-37}$$

and is less than 1 for the considered ISF. Hence surface tension forces are dominant compared to inertial forces and are taken into consideration.

Relating the Weber number to the Reynolds number through We/Re, and hence comparing the visous forces to the surface tension forces, we determine a value of an order of 10^1 for insertion speeds of O (10^{-3}) indicating viscous forces being dominant compared to surface tension forces. However, reducing the insertion speed has a higher impact on the Weber number (quadratic dependence compared to linear dependence for Re), so that consequently surface tension forces become more important for insertions at low speeds.

3.6 Experimental Method

Over the period of the conducted research work, two sets of experimental tests on the insertion squeeze flows were conducted with the purpose of measuring insertion forces during insertion. These tests mainly differed in the sample sizes (short and long) and the insertion speeds (low and high); additional information about the tests is given in the sub-sections below.

3.6.1 Experimental equipment

Both sets of tests were conducted with the aid of an Instron universal test rig. The test rig is a dual column system suitable for tension and compression applications. The capacity of the machine is 10 kN, which is sufficient for insertion forces that are expected during ISF. The tests are conducted at constant speed while recording the acting forces with respect to time or displacement.

To eliminate effects of machine load train compliance, which might cause inaccuracies when attempting to measure the insertion plate position using crosshead displacement, the

displacement is measured using a linear variable differential transformer (LVDT) that is mounted to the test sample. Machine load train compliance may be experienced through bending of machine parts which would falsify measured displacement, which therefore is expected to be more accurately measurable with the use of LVDTs. This inductive displacement transducer measures the position of the insertion plate and transfers the data to a computater. For a second set of tests – that is for the longer test samples – a second and third LVDT were mounted on each side of the Pi-slot sample to measure the distortion of the Pi-slot walls. The test rig, including the crosshead [1], is shown together with a sample [2] and the mounted LVDTs [3] in Figure 3-14 .
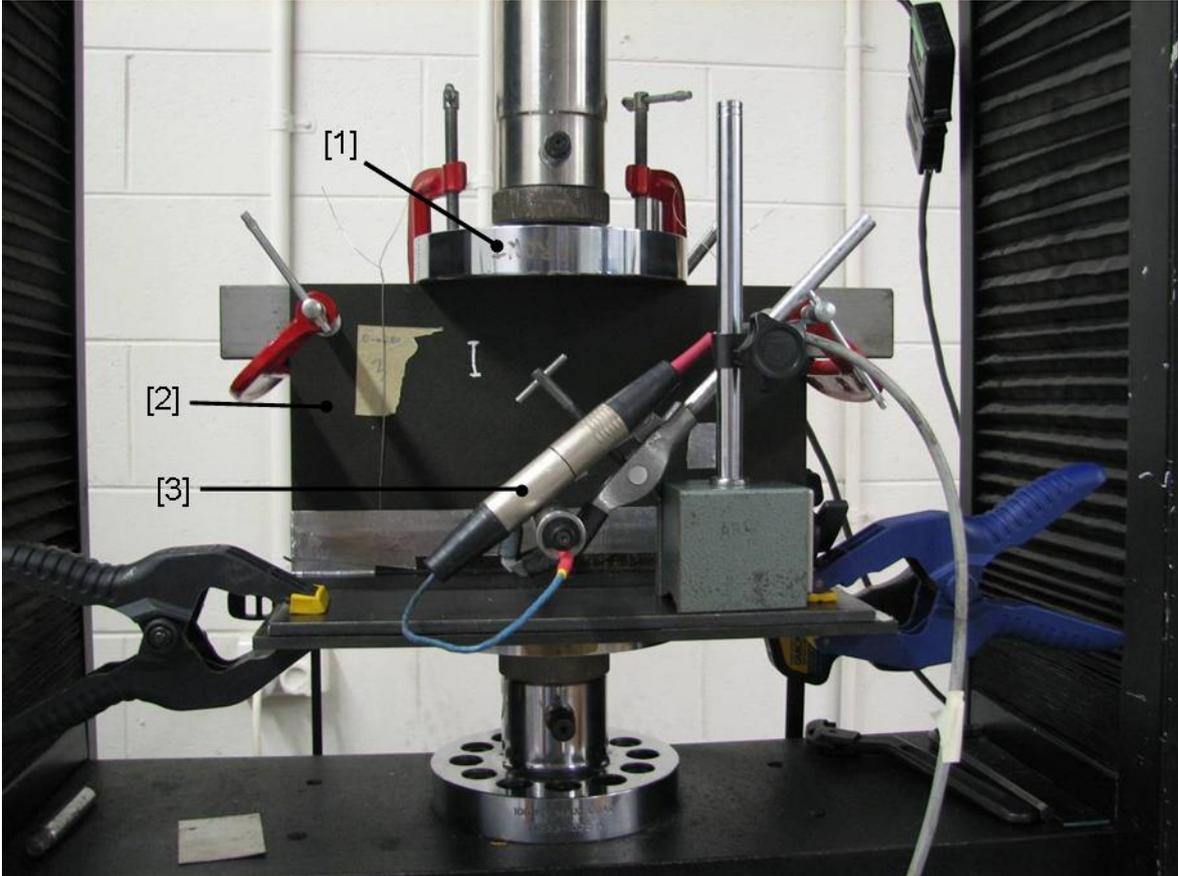
Figure 3-14: Experimental test setup to measure the insertion force versus displacement during an ISF bonding process.

As the adhesives to be used are two component paste materials, the components have to be mixed before inserting the adhesives into the Pi-slot and starting the ISF process. Therefore, during the first set of experiments a dual asymmetric centrifugal mixing device (trademark SpeedMixer^{TM}) is used to uniformly mix the components together (SpeedMixer^{TM}, 2009). The rotational speed in revolutions per minute (rpm) and the mixing time are adjustable and are chosen in a way to mix both components

sufficiently while avoiding prolonged or intense mixing, thus avoiding viscous heating and potential premature curing. For the second set of tests the components had to be mixed by hand as a mixing device was not available.

3.6.2 Dimensions of specimens, process parameters and materials

As stated above the main difference between the two sets of conducted tests is the dimension of the specimens. For the first conducted experiments, the nominal length $L_{\text{insertion plate}}$ of the square insertion plate specimen was 99.2 mm. The width $2a$ of the specimen varied due to the manufacturing process between 5.02 and 5.21 mm. The insertion plate head shape for all conducted experiments was rectangular.

The Pi-slot width $2b$ was 6.2±0.02 mm, the Pi-slot height H_1 was 35.5 mm and the Pi-slot length $L_{\text{Pi-slot}}$ was 100 mm. The resulting flow channel width for a perfectly aligned joint therefore is b-a. The Pi-slot is closed at its ends to avoid sideways adhesive outflow.

The insertion speeds for the first set of experiments were 2, 5 and 10 mm/min. The speed was kept constant during insertion. The amount of adhesive inserted initially is about 25 volume-percent in excess of the necessary amount to fill the flow channels. Furthermore, the viscosity is adjusted through mixing two different adhesives with each other. These adhesives are the paste Henkel Hysol EA 9395 and the less viscous Henkel Hysol EA 9396. The mixing ratios by weight were selected to be 70-30, 85-15 and 100-0, EA 9395 to EA 9396. Two or three repetitions were conducted for each tested parameter combination. A test matrix below summarizes the input parameters.

Table 12: Test matrix for ISF experiments conducted at low insertion speed.

Test number	2	5	10	70-30	85-15	100-0
-	mm/min	mm/min	mm/min	Weight-percent EA 9395 – EA 9396	Weight-percent EA 9395 – EA 9396	Weight-percent EA 9395 – EA 9396
1-3	x					x
4, 5		x				x
6-8			x			x
9, 10		x			x	
11, 12		x		x		

The composites specimens were manufactured using the vacuum assisted infusion process (VAP). The composites comprise high tensile strength (HTS) biaxial and unidirectional carbon fibre clutch and RTM 6 resin according to AIMS 05-04-100, IPS 05-04-100-01, with the lay-up as described within the MoJo deliverable specification D2.1.1 (MoJo, 2007). A detailed characterization of the two applied adhesives can be found in Section 4.2.

The second set of ISF experiments was conducted at a higher constant insertion speed (60 mm/min). This is in accordance with the required ISF process time. The insertion plate and Pi-slot dimensions are as follows.

Table 13: Specimen dimensions for the second row of ISF experiments.

Dimensions [mm]	Insertion plate	Pi-slot
2a	4.85 – 5.14	-
2b	-	6.06 – 6.27
H_1	200	35.5
L	279	280

Furthermore, the insertion head shape was varied, unlike for the first set of experiments. The insertion head was not rectangular in all tests: also tested were the tapered head shown in Figure 3-10, with tapers extending 5 mm vertically and 2 mm on each side horizontally, and the rounded head, shown in the same figure, with 2.5 mm radii. The adhesive amount applied initially is again 25 volume-percent in excess of the total amount necessary to fill the flow channels. Also, the Pi-slot ends are closed in a similar fashion to the first set of experiments.

3.7 Summary

This chapter presents a brief overview of the numerical methodology used for the numerical experiments conducted as part of this research program. Validation studies are performed both to test the implementation of various physical models within Fluent and perhaps more importantly to establish that the input of the model into Fluent is set up correctly within the software. The resolution, iterative convergence and domain size studies establish that predictions, at least for insertion forces and pressure, have a characteristic accuracy of a few percent or better. The chapter also provides information on setting up the problem, assumptions made and implementation of boundary conditions. Finally, the parameter matrices for the two sets of experiments are provided and briefly discussed in terms of the relevance to the numerical program and the proposed ISF applications specified as part of the Mojo program.

4 Development of the Constitutive Adhesives Material Model

In Chapter 4 the development of a constitutive material model representing the rheological properties of the adhesives used for ISF is presented. The material model will be implemented in the computational fluid dynamics software. The materials to be modelled are adhesives by Loctite Aerospace, Loctite Corporation, Bay Point, California, brand names Hysol EA 9395 and Hysol EA 9396.

Within this chapter, the selection of suitable adhesive mixing ratios is presented first. Then, in Section 4.2, an overview of material data provided by the manufacturer is given, then the equipment used for the measurements is described and finally the rheological tests to be conducted are introduced and explained. In Section 4.3 calibration and validation tests are presented and discussed. In Section 4.4 all rheological results and the development of the constitutive adhesive models used in the modelling are presented. The chapter is summarised in Section 4.5.

4.1 Selection of Adhesives

As mentioned previously, two different adhesives were chosen with the purpose of adjusting the shear viscosity. An important requirement for the choice of the mixing ratio is that the mixture should not flow under the action to gravitation. Therefore, a test was developed to determine the lowest mixing ratio to meet this condition. Highest viscosities were simply determined by using only EA 9395.

A plate was placed at an angle of 60° from the horizontal and six different ratios were mixed and applied on specified positions on the plate. Time between mixing and application was chosen to be 120 s for each ratio. After a further 300 s the flow behaviour was evaluated. The test set up and the final stage of all mixing ratios is shown in Figure 4-1.
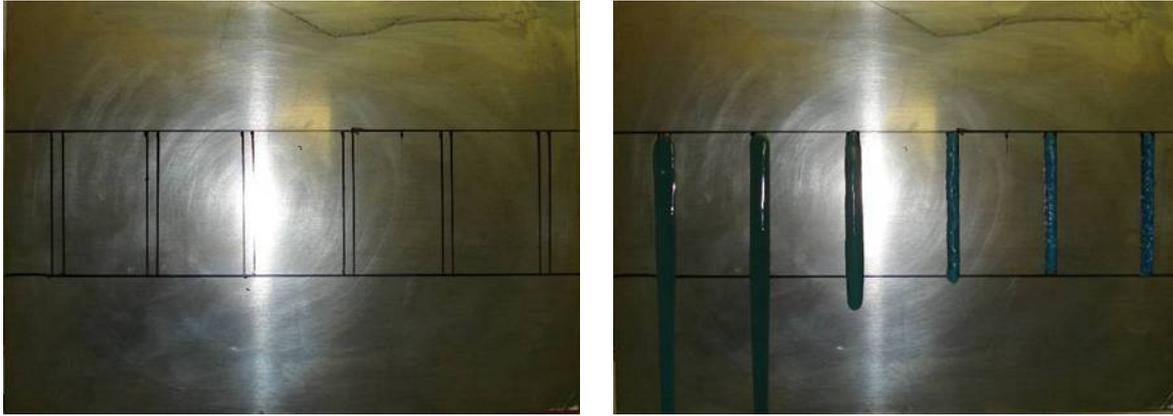
Figure 4-1: Test set-up and results for suitable weight percentage ratios of EA 9395 to EA 9396.

The mixing ratios for the samples shown are presented in Table 14, numbered by sample, with sample 1 being the leftmost one and sample 6 being the one on the far right:

Table 14: Investigated adhesive mixing ratios for determination of lowest ratio.

Amount of adhesive by weight-%	Sample 1	Sample 2	Sample 3	Sample 4	Sample 5	Sample 6
EA 9395	50	60	70	80	90	100
EA 9396	50	40	30	20	10	0

From the right photograph in Figure 4-1 no flow is evident for samples 4 – 6, which are 80% EA 9395, 90% EA 9395 and EA 9395. Samples 3, 2 and 1 show clear signs of flow. However, the flow for sample 3 was quite small and so that a ratio of 70:30 weight percent EA 9395 to EA 9396 was selected as the lowest acceptable adhesive viscosity mixture. Ratios of 85 – 15 and 100 – 0 EA 9395 to EA 9396 mixing ratios by weight were also investigated.

4.2 Methodology of Rheological Tests

Both the adhesives used are epoxy resins. EA 9395 contains a non-metallic filler and therefore can be considered a suspension. EA 9396 is less viscous than EA 9395 and was

added to adjust the viscosity. From experience little effect on the adhesive bonding properties would be expected.

According to the material manufacturer EA 9395 is characterized as an ambient temperature curing two-component adhesive with excellent strength properties (Loctite, 2007). Viscosities for EA 9395 were determined on a Brookfield, HBT rheometer and ranged between 100 and 300 Pas at 25°C. Furthermore, the adhesive is characterized as thixotropic. The two parts were mixed with each other in a 100:17 weight percent ratio of part A to part B. The pot life is given as 95 – 100 min for a mixture of 450 g at 25°C.

EA 9396 is a low viscous two-component ambient temperature curing adhesive. Its viscosity compared to EA 9395 is lower and the value provided by the manufacturer is 3.5 Pas measured on a Brookfield HBT rheometer at 2.1 rad/s at 25°C. The recommended mixing ratio is 100:30 (part A: part B) by weight percent. Pot life is specified as 75 to 90 min at 25°C for a mass of 450 g.

The rheological measurements were conducted on a rotational type rheometer with the brand name "Rheometrics Fluid Spectrometer II (RFS II)" by Rheometrics Inc., New Jersey, USA. Several references have previously used this type rheometer and recommended it for the measurements such as those conducted. Malkin (1994), Sheney (1999) and Menges (2002) recommend a rotational rheometer as being suitable for conducting rheological tests in which the shear viscosity is to be plotted versus time or shear rate. Also, testing standards ASTM D 2196 – 05 (ASTM, 2005) and ASTM D 4440 – 01 (ASTM, 2001), which provide the recommended procedures and equipment for rheological tests, suggest the use of a rotational or Brookfield type rheometer. As further evidence in support of using such a rheometer it is noted that the manufacturer provided data obtained on a Brookfield rotational rheometer.

The RFS II consists of the Control Computer, the System Control, the test station and the test control and analysis station (Rheometrics, 1991). An oscillatory, steady or step shearing mode is applied to the test sample and the precise response (e.g. torque) is measured. Correlating the applied strain and resulting response the rheological properties were determined. Principally, the RFS II contains three subsystems which are the actuator, transducer and environmental control. All of these are directed and monitored by the control computer which controls and directs instructions to each subsystem and receives all information from the subsystems. The central processing unit (CPU) and the random access memory (RAM) contain test sequences and store data, respectively. When preparing the sample and device, linear and rotational servo control systems of the force rebalanced

transducer (FRT) ensure that no normal force or torque is applied to the sample during loading of the apparatus.

The set-up of the rotational discs can either contain two parallel flat plates or a cone and plate. The advantage of the cone and plate is that the shear rate is constant across the whole cone surface (Sheney, 1999). The cone and plate geometry was used for all testings. The upper plate is shaped conically and mounted to the transducer. The flat circular bottom plate is mounted to the actuator and rotates at a controlled angular velocity. A sketch of the apparatus is shown in Figure 4-2:
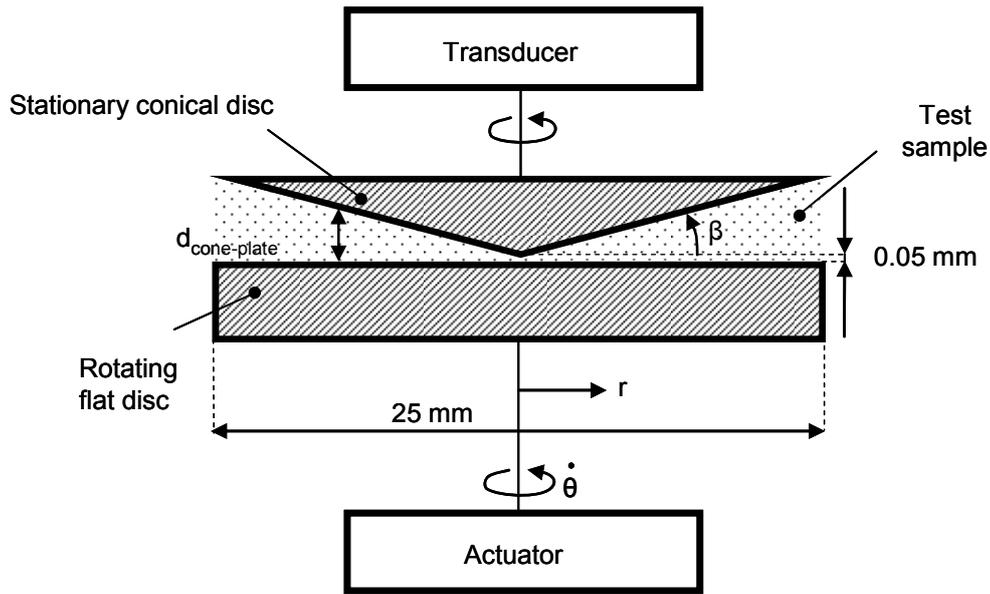
Figure 4-2: Cone and plate viscometer illustration of the equipment used for the rheological tests.

As illustrated in Figure 4-2 the diameter of both discs is 25 mm and the minimum gap between the conical and flat disc is 0.05 mm. The cone angle β of the upper plate is 0.1 rad (5.7296°) and is determined according to the previously stated condition that a constant shear rate should be reached on the cone surface (Sheney, 1999). The shear rate is calculated as follows:

$$\dot{\gamma} = K_\gamma \dot{\theta}, \quad K_\gamma = \frac{1}{\beta} \qquad (4\text{-}1)$$

Within equation (4-1), β is the cone angle (rad), K_γ is the strain constant (rad^{-1}) and $\dot{\theta}$ is the actuator angular velocity (rad/s). The dynamic strain is calculated using:

$$\gamma = K_\gamma * \theta \qquad (4\text{-}2)$$

To transform the measured torque T into shear stress the following relationship is applied (Sheney, 1999):

$$T = 2\pi\tau_{21}\int_0^R r^2 dr = \frac{2}{3}\pi R^3 \tau_{21} \qquad\qquad (4\text{-}3)$$

Thus, shear stress is calculated from the measured torque as:

$$\tau = \frac{3T}{2\pi R^3} \qquad\qquad (4\text{-}4)$$

When making the measurements, it is important that the material sample covers the whole fixture surface without overflow. Otherwise the prior presented equations will not obtain correct results.

The following tests were conducted:

  – Shear viscosity versus time measurements for several constant shear rates, also referred to as apparent viscosity measurements in ASTM D 2196 – 05,

  – shear viscosity versus step-wise increasing shear rate measurements according to ASTM D 2196 – 05, to derive the shear thinning characteristics of the adhesives, also referred to as quasi-dynamic viscosity,
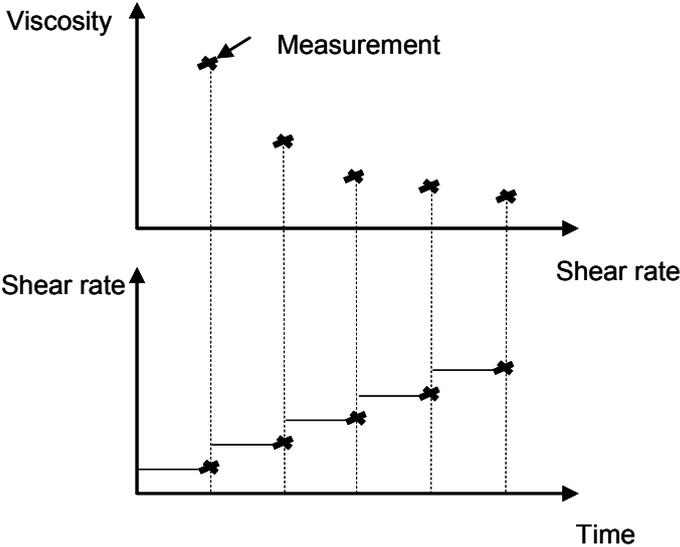
Figure 4-3: Method of measurements for viscosity versus stepwise increasing shear rate tests.

  – thixotropic loop test measurements of the shear viscosity with increasing and then decreasing shear rates as described in ASTM D 2196 – 05 and Malkin (1994), to derive the adhesives' time-dependence,
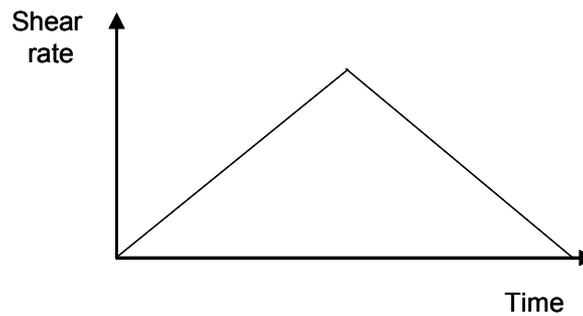
Figure 4-4: Applied shear rate with respect to time graph for the thixotropic measurements.

– and finally viscoelastic measurements, according to ASTM D 4440 – 01, to describe whether elastic effects have to be taken into account.

The shear viscosity versus time measurements were conducted to determine the time for the adhesive viscosity to reach a constant value. The shear viscosity of shear thinning non-Newtonian fluids can change at the start of measurement as described in the literature (e.g. Menges 2002, Malkin 1994) due to the restructuring processes of macromolecules. As the second test – the shear viscosity versus shear rate – was conducted in a step wise manner, it is important that the shear viscosities are measured when the viscosity has reached a constant value.

For the shear viscosity versus shear rate measurements the range of shear rates occurring during the ISF process needs to be determined before measurements can be conducted. Predictions for this shear rate range were determined from CFD results for a Newtonian fluid with constant viscosity. This would not affect the acting shear rates as the shear rate is independent of viscosity. From these simulations, the highest acting shear rates can be expected for the highest applied insertion speeds (120 mm/min) and the smallest flow channel widths. The shear rate range for this case was determined to be between 0 and 200 s^{-1}. Spatially, the highest shear rates were found to occur close to the boundaries, hence along the Pi-slot and insertion plate walls.

Due to equipment limitations meaningful viscosity measurements can only be conducted for shear rate ranges between 0.1 and about 30 s^{-1}. Below 0.1 s^{-1} the applied test standards cannot be applied and the transducer has insufficient sensitivity. Above 30 s^{-1} a careful consideration of the sample must be conducted during testing in order to check whether the whole cone surface area is covered. This is important because centrifugal forces acting on the sample can cause some material under test to flow out of the testing area, falsifying measurements.

There are shear rates experienced during ISF that are out of the possible shear rate range that can be tested. The developed material models cover that part of the viscosity curve in the missing range by extrapolation of the measured values.

4.3 Calibration and Validation of Equipment

Before all measurements were taken the equipment was calibrated. This included normal force, torque, angular velocity and alignment calibrations.

After the final measurement the equipment was again tested with a calibration liquid. For this purpose shear viscosity was measured with respect to time and the following results were obtained:
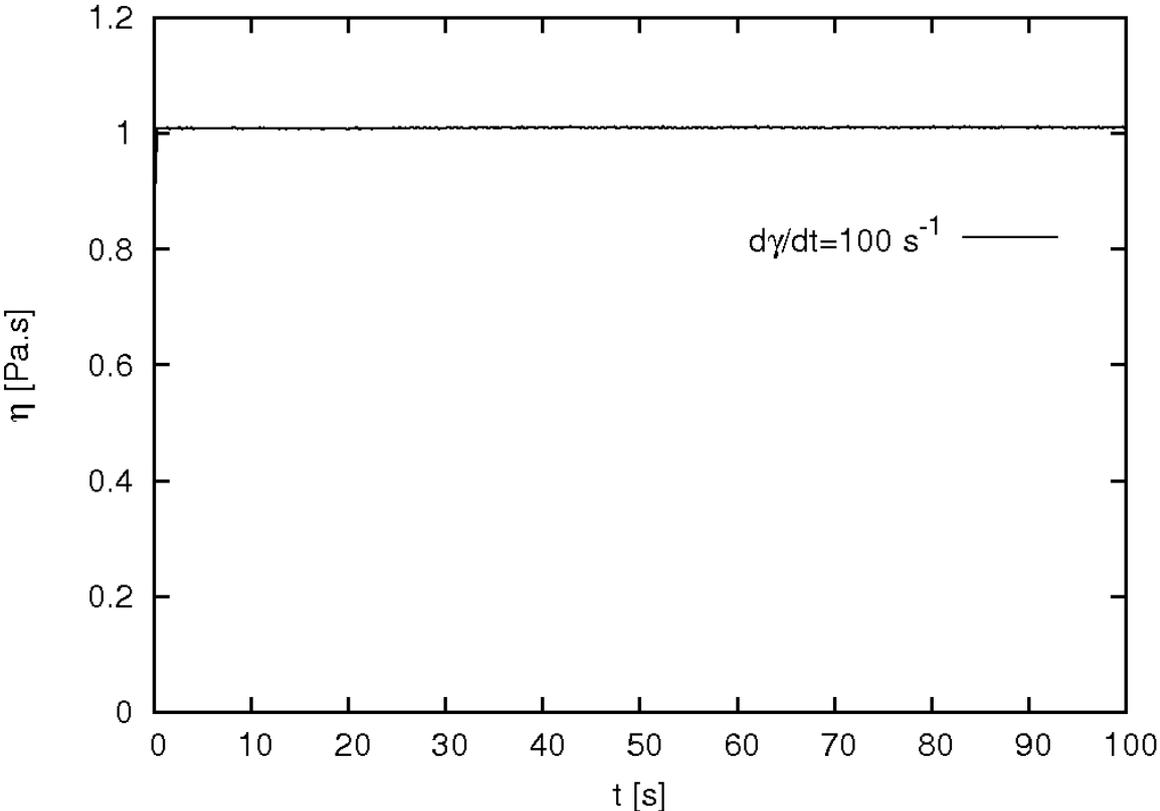
Figure 4-5: Shear viscosity of a calibration liquid with respect to time at a constant shear rate of 1 s⁻¹.

From Figure 4-5 an average shear viscosity of 1.0103 Pa.S at a temperature of 22.8°C could be determined. This shear viscosity value was compared with values provided by Cannon (Table 15):

Table 15: The shear viscosity of a cannon certified viscosity standard liquid silicone at different temperatures as provided by the manufacturer.

T [°C]	η [Pa.S]
20	1.123
23	1.055
25	1.033

At a temperature of 22.8°C the shear viscosity can be calculated to be 1.0595 Pa.S applying an exponential fit between the shear viscosities at 20°C and 23°C (see Figure 4-6).
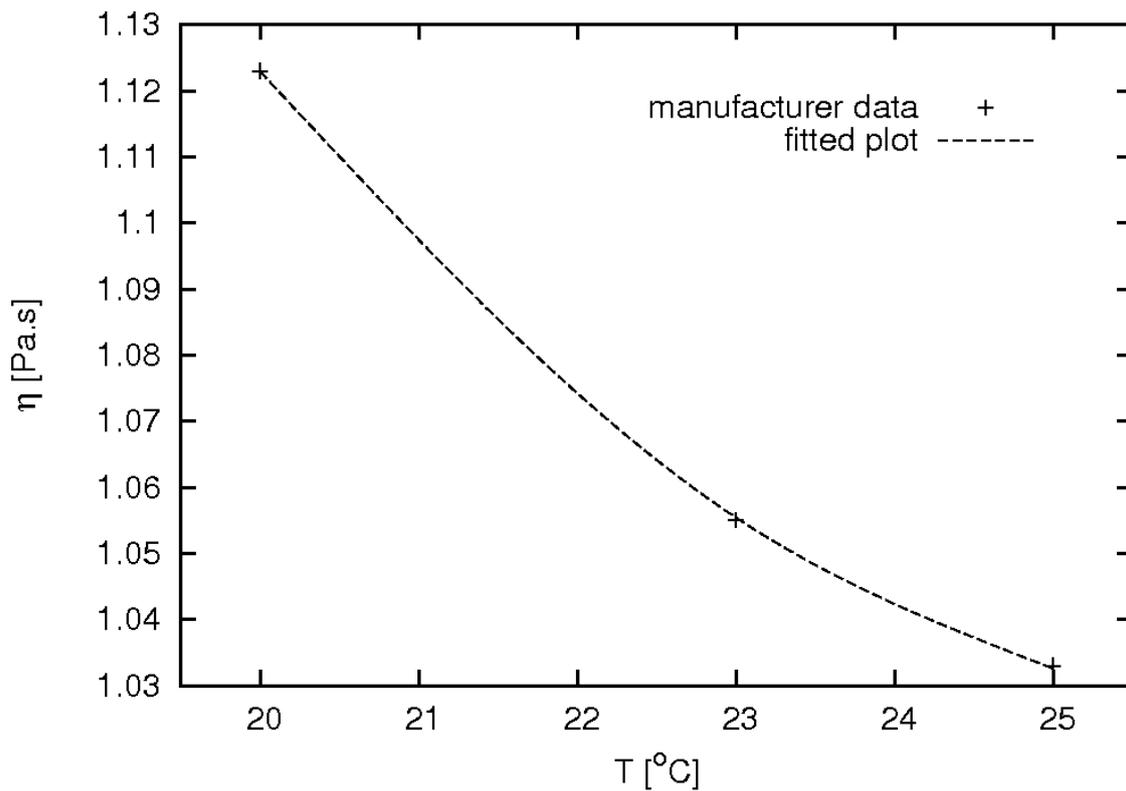
Figure 4-6: Polynomial fit of the calibration liquid viscosity versus temperature.

For a temperature of 22.8°C the deviation between the manufacturer data and the measured data was calculated as:

$$\chi = 1 - \frac{\eta_{linear\ fit}}{\eta_{measured}} = 1 - \frac{1.0595}{1.0103} = 1 - 1.0487 = 0.0487 \qquad (4\text{-}5)$$

According to ASTM D 2196 – 05, section 7, it is reasonable to assume that a viscometer is calibrated if the measured viscosity is within ±5% of the stated value, which is true for the presented case. The calibration liquid viscosity was also measured for 10 1/s and returned an average of 1.0106 Pa.S. As this is slightly higher than the shear viscosity for 100 1/s ($\eta_{100\ 1/s}$ = 1.0103 Pa.S) this measurement is also within the specified tolerance. Thus, after conducting the measurements the equipment still was correctly calibrated according to ASTM D 2196 – 05.

The procedure that was applied during the adhesive testings is described next. For each sample preparation, the components were weighed and mixed first. The necessary mass to fill the volume between the cone and plate was calculated to be 1.07 g. As the mixing ratio of component A to component B of EA 9395 is 100:17 by weight it was convenient to use 1 g of component A and 0.17 g of component B. This ensured entire filling of the testing capacity. Excessive adhesive was squeezed out and removed using a spatula as described in ASTM D 2196 – 05 and ASTM D 4440 – 01. The procedure for mixing and weighing when a mixture of EA 9395 and EA 9396 was used was the same except for the amount of material applied. It was decided to mix and apply a sample of 2 g as otherwise the fractions would get very small and therefore hard to mix and weigh. From an uncertainty analysis of the mass applied the calculated uncertainties were 0.58 % and 0.60 % for a sample size of 2 g, hence four components, and 1 g, hence two components, respectively (Holman, 1994).

At this stage a comment is needed on the sample size proposed in ASTM D 2196 – 05: this standard was used as it describes testing methods for rheological properties of non-Newtonian materials. However, this testing standard applies to material samples of paint, and therefore the sample sizes proposed are 0.5 l, i.e. very large in the current context. The sample sizes specified in ASTM D 4440 – 01 are very small amounts of material, approximately 3 to 5g. The ASTM D 4440 – 01 standard normally applies to materials such as thermoplastic resins. Therefore an application of the test standard described in ASTM D 2196 – 05 using an amount of material sample that is small and inline with the recommendations of ASTM D 4440 – 01 seemed justified and was used in the presented study.

As the material was mixed manually after weighing, it was decided to apply a delay before starting the measurements. The purpose was to suppress any effects introduced into

the sample through the mixing process. The delay remained the same for all conducted measurements. Furthermore, the delay was chosen so as to not be too long to avoid setting of the material; it was set to 120 s. As the results obtained were repeatable according to the applied test standards, it was assumed that this delay is sufficient.

Two transducers were available for the tests. They had different torque sensitivity: transducer 1 was accurate within a range of 0.2 – 200 gfcm and transducer 2 was accurate within a range of 2 – 2000 gfcm. Before starting a new measurement, which could be either pure EA 9395 or a mixture of EA 9395 and EA 9396, one test run was conducted to verify if the torque sensitivity that was chosen was sufficient. All conducted measurements are within one of the two specified ranges with one exception; the measurements of shear viscosity versus shear rate (0.01 – 100 s^{-1}) are out of this range for shear rates below 0.1 s^{-1}. In developing the adhesive material model this range was consequently not taken into account.

Next, validation and repeatability of the conducted measurements are discussed. For validation purposes the comparison between measured viscosity data and manufacturer data has already been shown. Repeatability of measurements is considered here with the process being according to ASTM D 2196 – 05.

For EA 9395 the shear viscosity was determined at a constant shear rate of 1 s^{-1} for two measurements. It was found to be 310 Pa.s at 22.6°C and 327 Pa.s and 22.7°C. The manufacturer specifies the apparent shear viscosity to be between 100 and 300 Pa.s at 2.1 s^{-1} and 25°C. As the adhesive is shear thinning (this is shown later in shear viscosity versus shear rate measurements) the viscosity is expected to decrease for higher shear rates. Hence, the measured viscosities would be expected to decrease for a shear rate of 2.1 s^{-1} compared to 1 s^{-1}. Furthermore, the adhesive viscosity is also expected to decrease with increasing temperature. Therefore, although the measured apparent shear viscosities are higher nominated as the maximum in the range specified by the manufacturer the results are taken with different testing parameters. The higher values here are consistent with the effects expected from lower shear in a shear thinning fluid and it is believed that for the same test parameters the measured data would fall within the range nominated by the manufacturer. To validate this assumption, the apparent shear viscosity was determined from the shear viscosity versus shear rate measurements. Applying the best fitting to obtain the apparent shear viscosity at 2.1 s^{-1}, the viscosity was determined as 176 Pa.s, thus falling in line with the manufacturer's data.

When analysing measured values against criteria for repeatability (as specified in ASTM D 2196 – 05) it is observed that the data lies within the specified tolerance. The tolerance specified in ASTM D 2196 – 05 is 7 % for apparent shear viscosity measurements and 9 % for the shear thinning index. Comparing the apparent shear viscosity data first, Table 16 shows apparent viscosities determined for EA 9395 and 70 – 30 weight percent mixtures of EA 9395 to EA 9396. Deviations for each case are also included:

Table 16: Apparent shear viscosities at different shear rates for two adhesive viscosity ratios, indicating the deviation between two different measurements.

Weight-% EA 9395 – EA 9396	100 – 0			70 – 30		
Shear rates [s^{-1}]	η_1 [Pa.S]	η_2 [Pa.S]	Deviation (η_{max}/η_{min} -1)*100 [%]	η_1 [Pa.S]	η_2 [Pa.S]	Deviation (η_{max}/η_{min} - 1)*100 [%]
0.1	2350	2230	5.38	423	452	6.8
1	311	327	5.14	90	86.3	4.3
10	81.2	79.4	2.27	X	X	X

All presented measurements lie within the tolerances specified in ASTM D 2196 – 05 for apparent shear viscosities.

Considering shear viscosity versus shear rate measurements, ASTM D 2196 – 05 proposes comparative shear thinning indices. The shear thinning index is the ratio of the shear viscosity at a small shear rate and the shear viscosity at a ten times larger shear rate, e.g. shear viscosities at 0.1 and 1 s^{-1}, 1 and 10 s^{-1} etc. Shear thinning indices were determined for the conducted measurements. According to ASTM D 2196 – 05, discrepancies are acceptable within 9%.

For EA 9395, the shear thinning indices were calculated for four shear viscosity versus shear rate measurements. All shear thinning indices for a fraction based on shear rates of

0.1 and 1 s^{-1} are within the specified tolerance, the largest deviation between two measurements being 6.3 % (Table 17):

Table 17: Comparison of shear indices that were determined for EA 9395 for four different data sets.

Shear thinning index	Data set 1	Data set 2	Data set 3	Data set 4
$\eta_{0.1}/\eta_1*100[\%]$	6.6	6.2	6.5	6.3

For the other considered adhesive mixtures – 70 – 30 and 85 – 15 weight percent EA 9395 to EA 9396 – the same method was applied to judge repeatability. Both mixtures were found to be within a deviation of 9%, the lower viscous (70 – 30) mixtures differing by less than maximum 7.8% and the higher viscous (85 – 15) mixture showing differences of less than 4.1%. Hence, repeatability criteria according to ASTM D 2196 – 05 were met for all shear viscosity versus shear rate measurements.

The thixotropic loop test can be conducted according to ASTM D 2196 – 05 and the degree of thixotropy can be determined. The degree of thixotropy is the fraction of the shear viscosity at the lowest increasing shear rate to the shear viscosity at the lowest decreasing shear rate. The higher determined fraction is the higher the amount of thixotropy in the material (ASTM, 2005).

Viscoelastic measurements were conducted according to ASTM D 4440 – 01. The storage and loss modulii were determined with respect to dynamic oscillation within the linear viscoelastic region of the material. The linear viscoelastic region was determined first. The relaxation time sought is defined as $\lambda = (2\pi f)^{-1}$, with the frequency *f* defined as that when loss and storage modulus are equal (Mannan, 1995). Knowing the relaxation time and the process time the Deborah number *De* can be calculated, giving an indication whether elastic effects can be neglected or not.

4.4 Rheological Results

In this Section, shear viscosity versus time measurements are summarized before shear viscosity versus shear rate results are presented; the adhesives' time-dependent rheological characteristics were determined and results of thixotropic loop tests are discussed; measured loss and storage modulus versus strain and frequency are then presented. Results

for both pure EA 9395 and a mixture of 70 – 30 weight-% EA 9395 to EA 9396 are presented. Shear viscosity versus shear rate results are also presented for a mixture of 85 – 15 weight percent of EA 9395 to EA 9396. The Section concludes with a presentation of how the material models for ISF adhesives were determined.

4.4.1 Shear viscosity versus time

<u>EA 9395</u>

To determine the apparent shear viscosities, the shear viscosity was measured at a constant shear rate with respect to time. The shear viscosities were determined for three different shear rates: 0.1, 1 and 10 s^{-1}. Two data sets showing the apparent shear viscosity at a constant shear rate of 0.1 s^{-1} are shown in Figure 4-7. The first measurement (data set 1) was conducted for a period of 1200 s. The second measurement, however, was conducted for a period of 500 s only. This was because no major changes in shear viscosity could be detected for the first data set after about 250 s (Figure 4-7) and so this time period was considered to be sufficiently long for the adhesive's shear viscosity to reach a constant value.
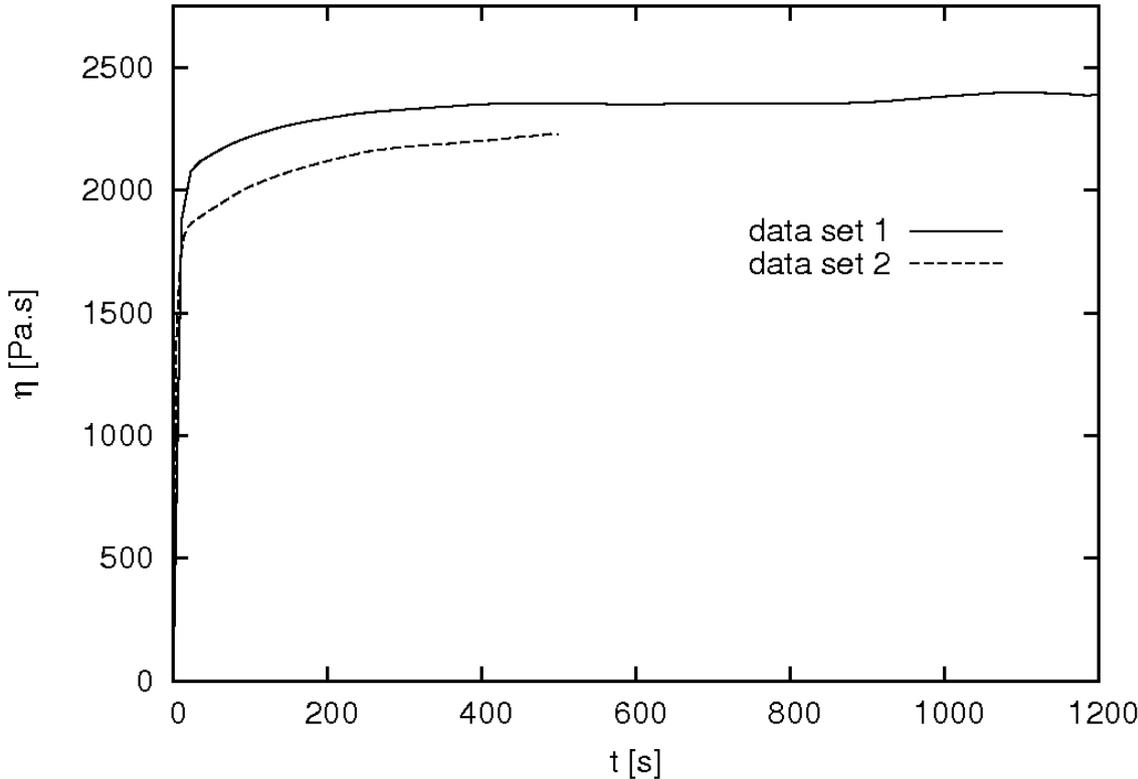
Figure 4-7: Two apparent shear viscosity graphs as a function of time for EA 9395 at a shear rate of 0.1 s^{-1}.

Figure 4-7 demonstrates that the shear viscosity increases with time and shows how it reaches a value of about 2320 Pa.s after 250 s for data set 1. For data set 2, at a time of 250 s the shear viscosity is 2160 Pa.s and continues to increase. This increase is relative small compared to the entire measured data. It is 0.9 % from a measurement time of 250 s till the end of measurement. However, the measurement time of 250 s was considered as too long to be used in the shear viscosity versus shear rate measurements, as will be explained in the final paragraph of this sub-Section. Therefore, a shorther measurement time was sought, and the shear viscosities at a time of 100 s were considered more in detail; after 100 s the shear viscosities were 2220 Pa.s and 2020 Pa.s for data set 1 and 2, respectively, which means that the changes in apparent shear viscosities from a time of 100 s to 250 s (when the change in apparent shear viscosity is small) were 4.3 % for data set 1 and 6.5 % for data set 2 (average of 5.4 %). Consequently, at a shear rate of 0.1 s^{-1} the shear viscosity would actually be about 5.4 % higher than the one measured in shear viscosity versus shear rate tests. Those tests are used to derive a material model for the adhesive. The impact of the 5.4 %-discrepancy on the model derivation depends on the accuracy of the apparent shear viscosity measurements at 100 s at shear rates higher than 0.1 s^{-1}, which is discussed in the following paragraph.

Shear viscosities were also determined at constant shear rates of 1 and 10 s^{-1}. The results are presented in Figure 4-8 for two data sets per shear rate:
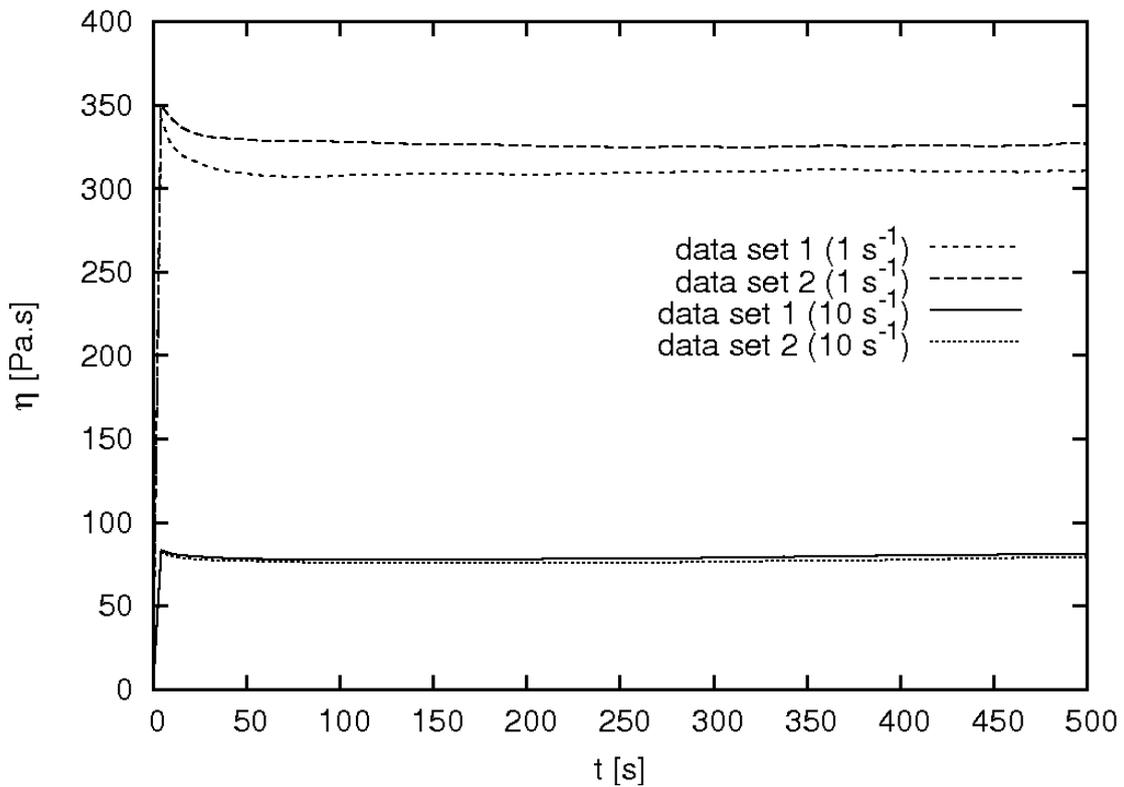
Figure 4-8: Two apparent shear viscosity graphs as a function of time for EA 9395, each at shear rates of 1 s^{-1} and 10 s^{-1}.

It is noticed that there is a slight overshoot in apparent shear viscosity in the first 30 s for a shear rate of 1 s^{-1} and in the first 15 s for a shear rate of 10 s^{-1}. Following this a constant value is reached, which is an average of about 320 Pa.S and about 80 Pa.S for 1 and 10 s^{-1}, respectively. Given these results, the material model development would hardly be affected by the 5.4 % discrepancy experienced at 0.1 s^{-1}.

As described previously in Section 4.2 the purpose of the viscosity versus time measurements was to determine the time after which the shear viscosity reaches a constant value. According to the results this time can be specified as 100 s. Thus, for further tests, the shear rate was held constant for this time in the shear viscosity versus shear rate tests (Chapter 4.4.2). After 100 s it was increased to the next shear rate and the same process applied. Five measurements were taken per decade.

If the time period was taken as 250 s, based on Figure 4-7, the measurements for one decade would have taken 1250 s. Three shear rate decades had to be measured (0.1 to 100 1/s) which means a testing time of 3750 s. This time would have resulted in curing effects becoming evident during measurements, which clearly was undesirable. Therefore, as changes in shear viscosity of about 5% were determined to occur after 100 s (discussion

Figure 4-7), this time period was applied for the shear viscosity versus shear rate measurements. The total measurement time was then 1500 s which is a reasonable compromise in providing accurate results without material setting effects.

EA 9395 and EA 9396 mixture (70 – 30)

The same procedure as described for the 100% EA 9395 was applied for the 70 – 30 weight percentage mixture of EA 9395 to EA 9396. The tested shear rates were 0.1 and 1 s^{-1}. No tests were conducted for 10 s^{-1} because it is assumed that similar trends would be observed to those seen for 100% EA 9395; this is that a constant apparent shear viscosity is reached earlier for higher shear rates. This trend is also observed for the 70 – 30 measurements, as illustrated in Figure 4-9, where the shear viscosity is plotted with respect to time for 0.1 and 1 s^{-1}:
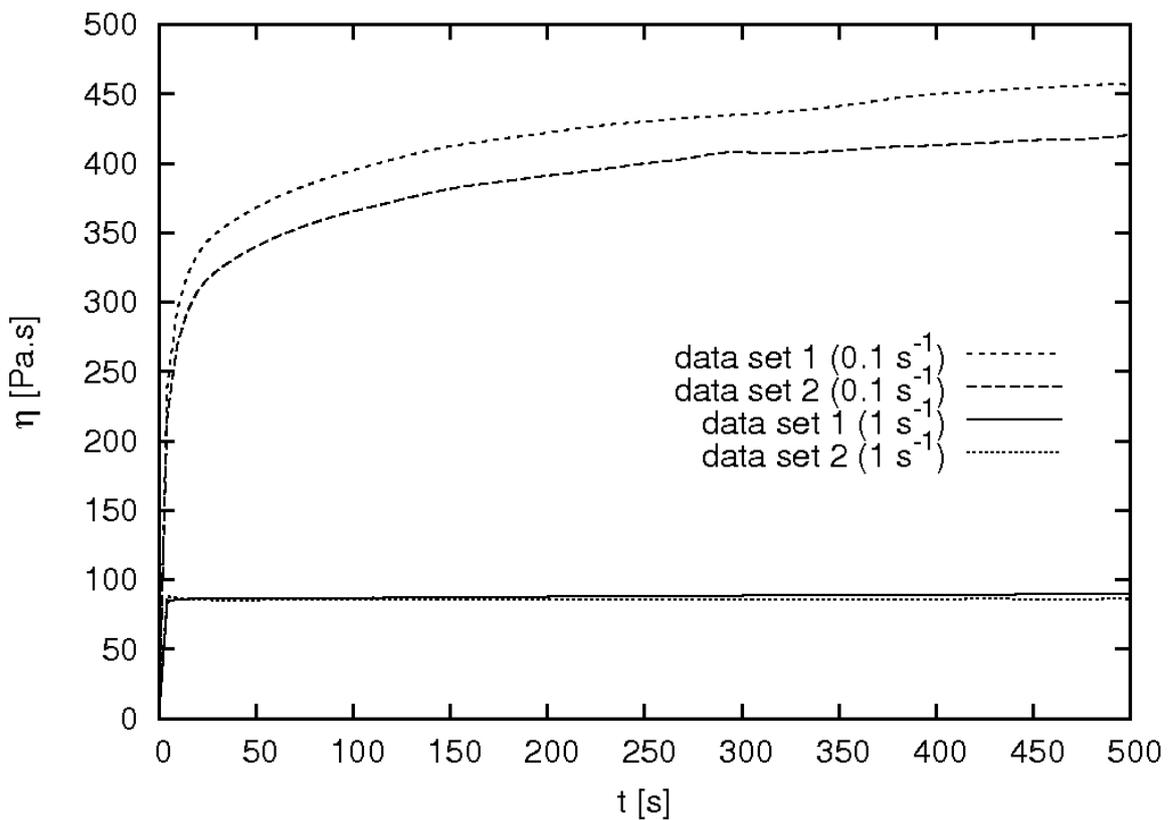
Figure 4-9: Two apparent shear viscosity graphs as a function of time for a 70 – 30 weight percentage mixture between EA 9395 and EA 9396, each at shear rates of 0.1 s^{-1} and 1 s^{-1}.

Figure 4-9 shows that for 0.1 s^{-1} the shear viscosity increases continuously for a time of 500 s. However, major changes occur only at the start of the measurement. From 100 to 500 s the shear viscosity of data set 1 changes 8.9 % and that of data set 2 12 %. As the

changes from 100 s onwards are relative small, a period of 100 s was selected as the constant shear rate time for the shear viscosity versus shear rate measurements.

Apparent viscosity measurements at a constant shear rate of 1 s^{-1} do not show any major changes after the initial peak. Data set 2 remains constant; data set 1 shows a 3.5 % increase with time so it was considered justified neglecting it. As discussed previously for the EA 9395 adhesives only, for shear viscosity versus shear rate measurements a testing period per constant shear rate of 100 s appeared to be a good compromise to ensure meaningful results in a reasonable testing time.

4.4.2 Shear viscosity versus shear rate

<u>EA 9395</u>

Four measurements of the shear viscosity versus stepwise increasing shear rate are presented in Figure 4-10. The shear rates range from 0.01 to 100 s^{-1} but due to difficulties experienced during testing only one measurement (data set 2) was conducted over the full range. The other measurements had to be terminated after 39.8 s^{-1}(data set 3 and 4) and 25.1 s^{-1}(data set 1).
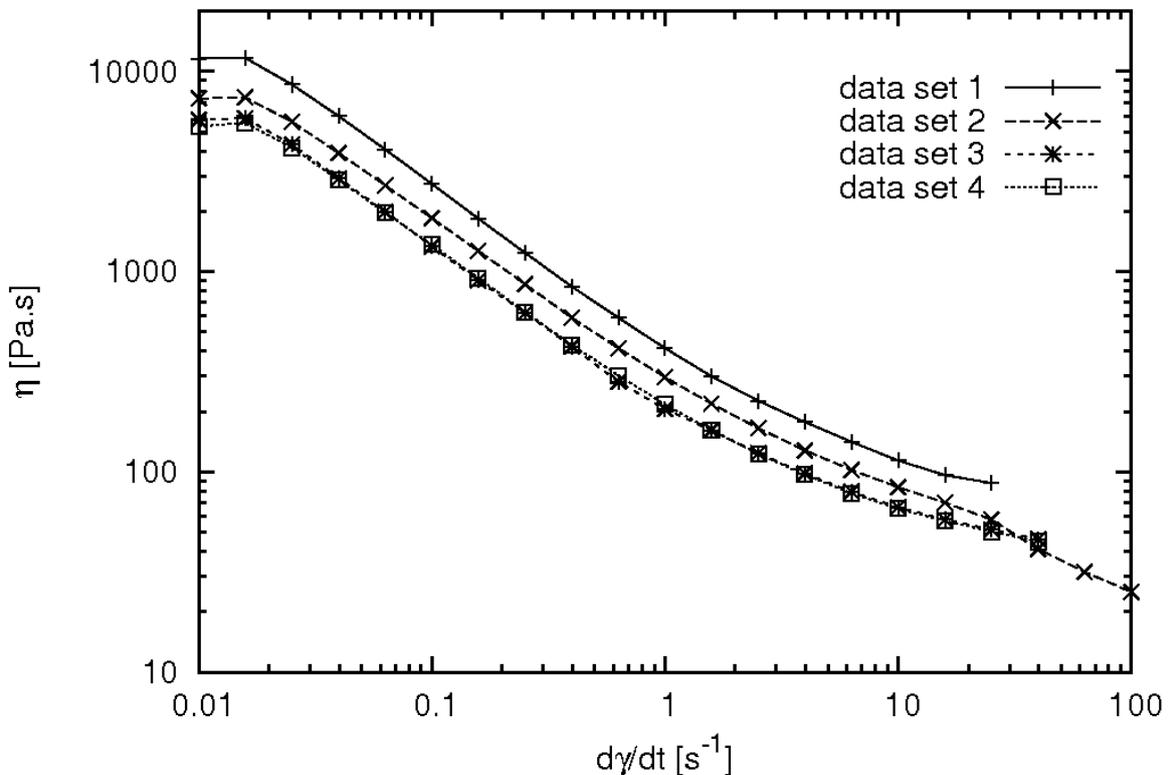
Figure 4-10: Four data sets showing shear viscosity as a function of shear rate measurements for 100% EA 9395.

All graphs are very similar in shape indicating a non-Newtonian, shear thinning material behaviour. An initially minor increase is followed by a continuous decrease of the logarithmic shear viscosity with logarithmic shear rate. In Section 4.3 we mentioned that data below 0.1 s^{-1} is less accurate due to insufficient transducer resolution for the very small shear rates. Hence, the region between 0.01 and 0.1 s^{-1} was not be considered when deriving the adhesive material model.

However, this initial increase was still considered with a view to explaining it. Measurements of shear viscosity versus constant shear rate for shear rates of 0.01 s^{-1}, which are not presented here, showed that after a period of 100 s the apparent shear viscosity still increased quite significantly, most probably as restructuring processes of macromolecules within the sample still occur. Hence, considering the results presented here we believe that for the second constant shear rate of 0.0251 s^{-1} the unfinished restructuring processes of macromolecules lead to an increased shear viscosity.

The differences experienced between the different data sets are most probably due to differences in temperature during testing which varied between 20.4 and 21.7°C. For data set 1 the testing temperature was the lowest compared to the other data sets. The derivation of the material model was based on the average data from these measurements for a shear rate range between 0.1 and 25.1 s^{-1}.

Inconsistencies between data sets where data is available occur for shear rates higher than 25.1 s^{-1} e.g. data set 2 shows a sudden drop in shear viscosity between 25.1 and 39.8 s^{-1}. At this shear rate detachments of the sample and the cone surface were observed.

Equations (4-3) and (4-4) used to calculate torque and shear stress, respectively, are restated to explain the effect detachment has on the determination of the shear viscosity:

$$T = 2\pi\tau_{21}\int_0^R r^2 dr = \frac{2}{3}\pi R^3 \tau_{21} \qquad (4-3)$$

$$\tau = \frac{3T}{2\pi R^3} \qquad (4-4)$$

The integration limit R in equation (4-3) is smaller for the cases where the cone surface was not covered completely with the sample. If R was smaller the shear stress value would become larger (equation (4-4)). If the shear stress was larger the shear viscosity would become larger as the shear viscosity is the ratio of shear stress and shear rate (equation (4-6)):

$$\eta = \frac{\tau}{\dot{\gamma}}$$
(4-6)

Thus, shear viscosity of data set 2 should be larger than presented at a shear rate where detachment occurs, in this case 38.9 s^{-1}.

Finally, we compare the averaged values of these measurements with results that were obtained from apparent shear viscosity measurements.

Table 18: Effect of the test type – either apparent or quasi-dynamic viscosity - on shear viscosity data at three different shear rates.

Shear rate	Apparent shear viscosity	Quasi dynamic shear viscosity
[1/s]	[Pa.s]	[Pa.s]
0.1	2120	1822.5
1	319	283.5
10	80	82.5

Discrepancies between data from both test types are evident and reasons for these discrepancies are not obvious. One possible explanation is that the adhesive is time dependent with the viscosity changing with time. To evaluate this explanation, thixotropic loop tests were conducted and results are presented sub-Section 4.4.3.

Another explanation is the possibility of micro-curing occuring in the adhesive, causing an increase in shear viscosity. Occurrence of micro-curing can be caused by the shearing of the adhesives as this is larger for the shear viscosity versus shear rate measurements than for the apparent viscosity measurements. Considering the viscosity change with increasing shear rate, we notice that the rate of change is greater for the apparent shear viscosity measurements. For example the apparent viscosities are greater for 0.1 and 1 s^{-1}, but smaller for 10 s^{-1}, so the longer the quasi dynamic test lasts the greater its viscosity value as more shear was induced on the sample.

It also is possible that the temperature variation, from 20.4 to 21.7°C, affects the shear viscosities. However, this seems doubtful as no particular trend can be observed. The apparent shear viscosity measurements were taken at higher as well as lower temperatures

compared to the temperatures at which the shear viscosity versus shear rate measurements were conducted.

Finally, a non-slip boundary condition has to be fulfilled in order to generate correct results and this may not have been reached. Non-slip boundary conditions apply if the test sample sticks to the cone-and-plate surface of the testing device during the entire measurements. It is not possible to determine with absolute confidence whether the adhesive is not slipping at the upper conical plate. However, in general this possibility is unlikely if smooth graphs are obtained; the measured shear viscosities appear not to fluctuate in this manner (see for example Figure 4-10).

The decision on whether to derive a material model based on the quasi dynamic measurements or on several measurements of apparent viscosities was made due to the nature of the ISF process; during ISF the adhesive is subject to various shear rates at once, e.g. the shear rates within the flow channels are higher closer to the Pi-slot and insertion plate walls. As these various conditions are imposed on the adhesive simultaneously, it was concluded that the quasi dynamic shear viscosity results would provide a better approximation of viscosities during the ISF process than the apparent shear viscosity results.

<u>EA 9395 and EA 9396 mixture (70 – 30)</u>

For a 70 – 30 weight percentage ratio of EA 9395 to EA 9396 three data sets are presented in Figure 4-11.
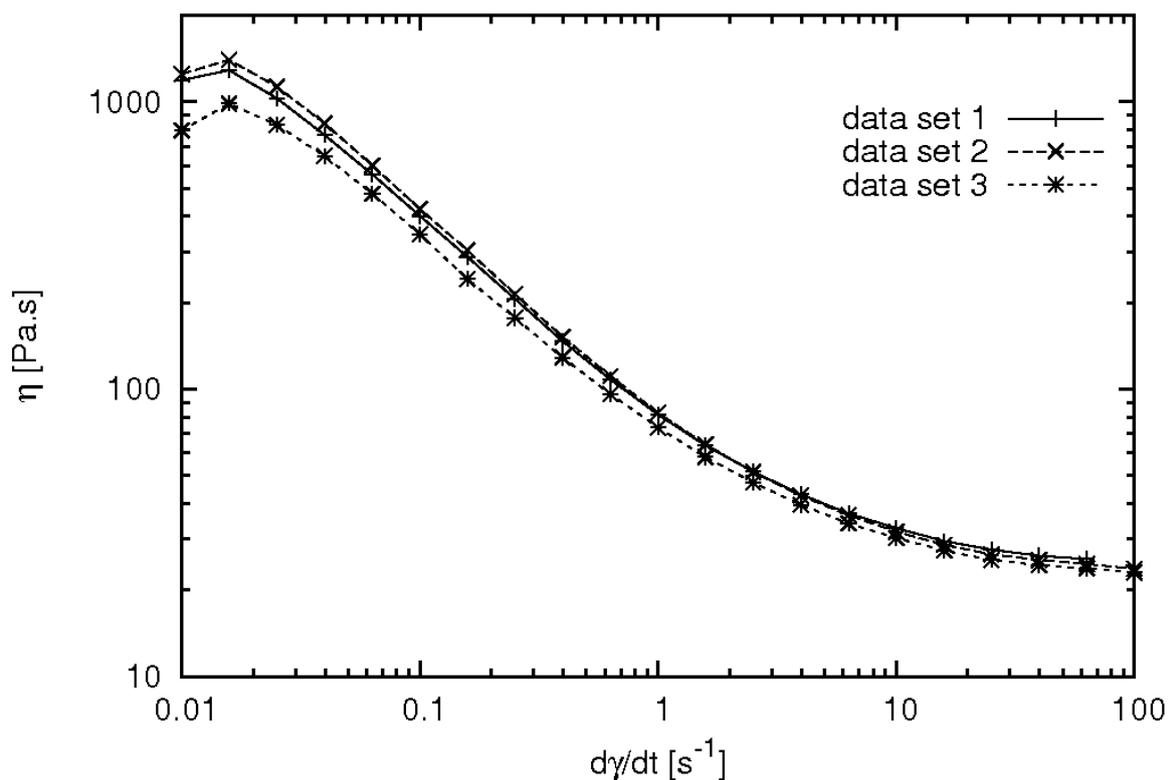
Figure 4-11: Three data sets showing shear viscosity as a function of shear rate measurements for 70 – 30 weigth percentage mixtures of EA 9395 to EA 9396.

A similar graph shape as the one for EA 9395 is observed, indicating a shear thinning material characteristic. In general, shear viscosities are lower compared to EA 9395. This is expected as the lower viscous adhesive EA 9396 is added to the sample.

The shear viscosities at higher shear rates, i.e. above 25.1 s^{-1}, seem to continue its smooth decreasing shape. A judgement about detachment is hard to conduct but it appeared that for these mixtures the cone surface remained covered with adhesive during the entire testing period.

A comparison between apparent shear viscosity measurement data and quasi dynamic shear viscosity data is presented in Table 19.

Table 19: Adhesive shear viscosities determined from apparent and quasi dynamic tests at different shear rates for 70 – 30 weight percentage mixtures of EA 9395 to EA 9396.

Shear rate	Apparent shear viscosity		Quasi dynamic shear viscosity		
[s⁻¹]	[Pa.s]		[Pa.s]		
0.1	423	452	424	401	346
1	90	86	83	83	74

Little differences are noticeable for shear viscosities for different test types. The apparent shear viscosity values are slightly higher with one exception which is data set 1 for 0.1 s⁻¹.

<u>EA 9395 and EA 9396 mixture (85 – 15)</u>

Lastly, shear viscosity versus stepwise increasing shear rates is presented for a mixing ratio of 85 – 15 weight percent EA 9395 to EA 9396. The data are illustrated in Figure 4-12.
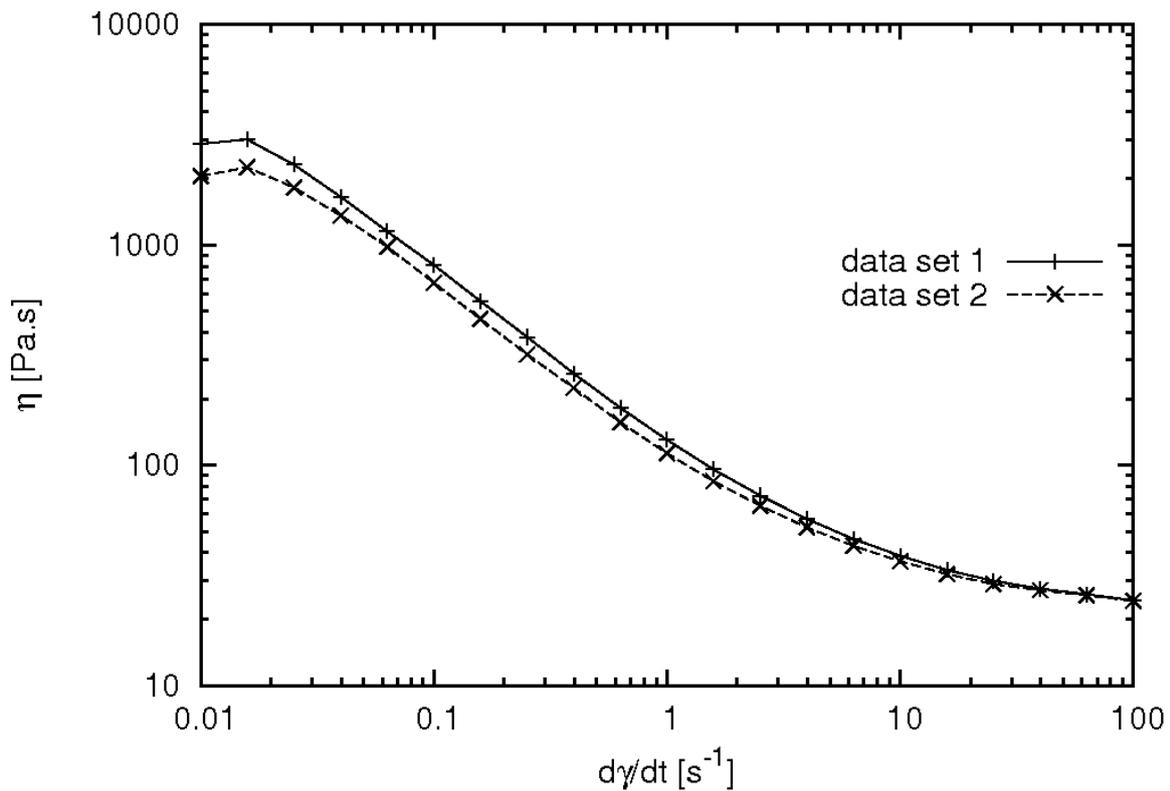
Figure 4-12: Shear viscosity as a function of shear rate measurements from two data sets for a 85 − 15 weigth percentage mixture of EA 9395 to EA 9396.

A shear thinning non-Newtonian behaviour is observed as in the two previously presented measurements within Chapter 4.4.2. A comparison with data for the 70 − 30 mixture is conducted and presented in Table 20. In the table it is noticed that the shear viscosity differences between 85 − 15 and 70 − 30 are larger for smaller shear rates. For 0.1 1/s the shear viscosity of 85 − 15 is almost double that for 70 − 30. For a shear rate of 100 1/s the shear rates are almost identical. This trend – that the shear viscosity differences decrease with increasing shear rate – could be explained as follows: It is shown that EA 9395 is clearly a non-Newtonian shear thinning fluid. The material manufacturer provides a constant shear viscosity of 3.5 Pa.S for EA 9396, indicating that the adhesive shear viscosity is independent of shear rate, and therefore a Newtonian fluid. If it is assumed that EA 9395 is shear thinning and the addition of 15 weight percent EA 9396 decreases the shear viscosity, a combination between shear thinning and decreased shear viscosity might lead to the observed results. For a 70 − 30 weight percent ratio the shear thinning effect is smaller and therefore might lead to similar shear viscosities compared to a 85 − 15 weight percent ratio mixture for higher shear rates.

Table 20: Adhesive shear viscosities determined from apparent and quasi dynamic tests at different shear rates for 85 – 15 and 70 – 30 weight percent mixtures of EA 9395 to EA 9396.

	Quasi dynamic shear viscosity			
Shear rate	85 – 15		70 – 30	
$[s^{-1}]$	[Pa.s]		[Pa.s]	
0.1	809	672	424	346
1	130	113	83	74
10	39	37	32	30
100	24	24	24	23

4.4.3 Time-dependence

During the thixotropic loop tests the shear rate was increased from 0.1 s^{-1} to 30 s^{-1} and to 10 s^{-1} while recording the shear stress and then decreased through the same range. The loop duration was 300 s in total, i.e. the shear rate was increased within the first 150 s and then decreased within the next 150 s. This duration was varied in another measurement where the entire loop was conducted within 20 s only. Two measurements were conducted for each loop and the typical shear stress versus shear rate graphs are presented in Figure 4-13 and Figure 4-14 for EA 9395.
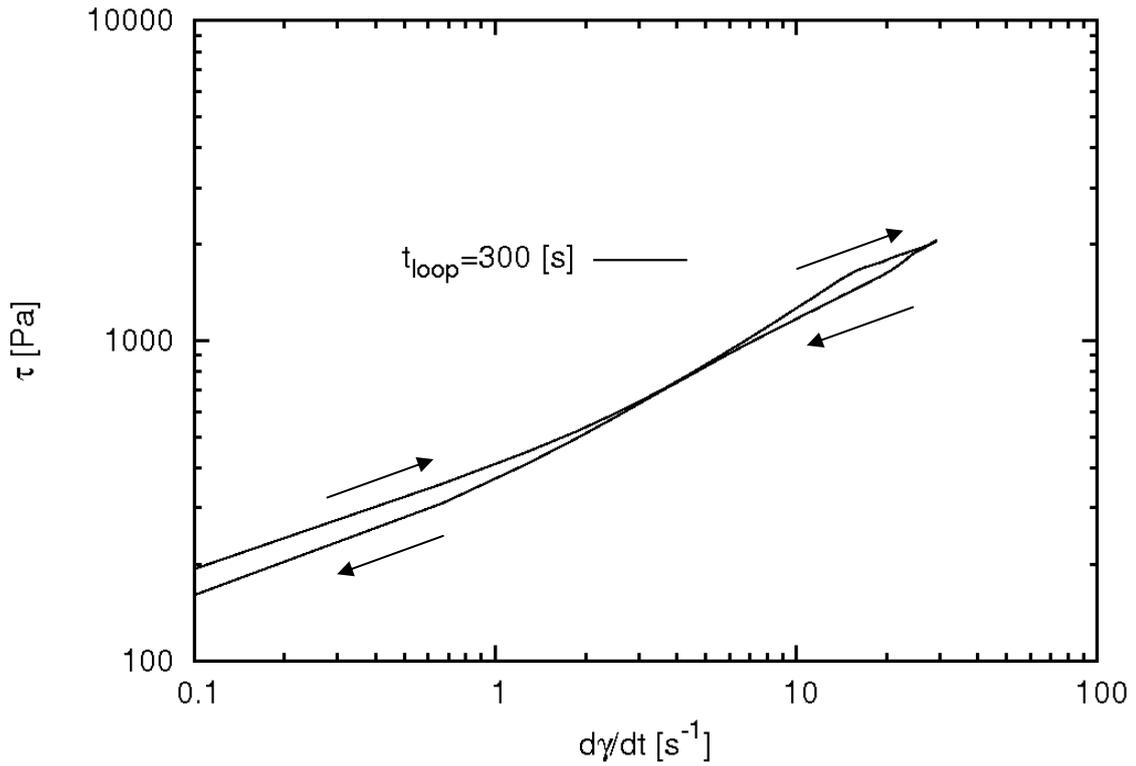
Figure 4-13: Shear stress versus shear rate for a thixotropic loop test for 100% EA 9395 (300 s loop).
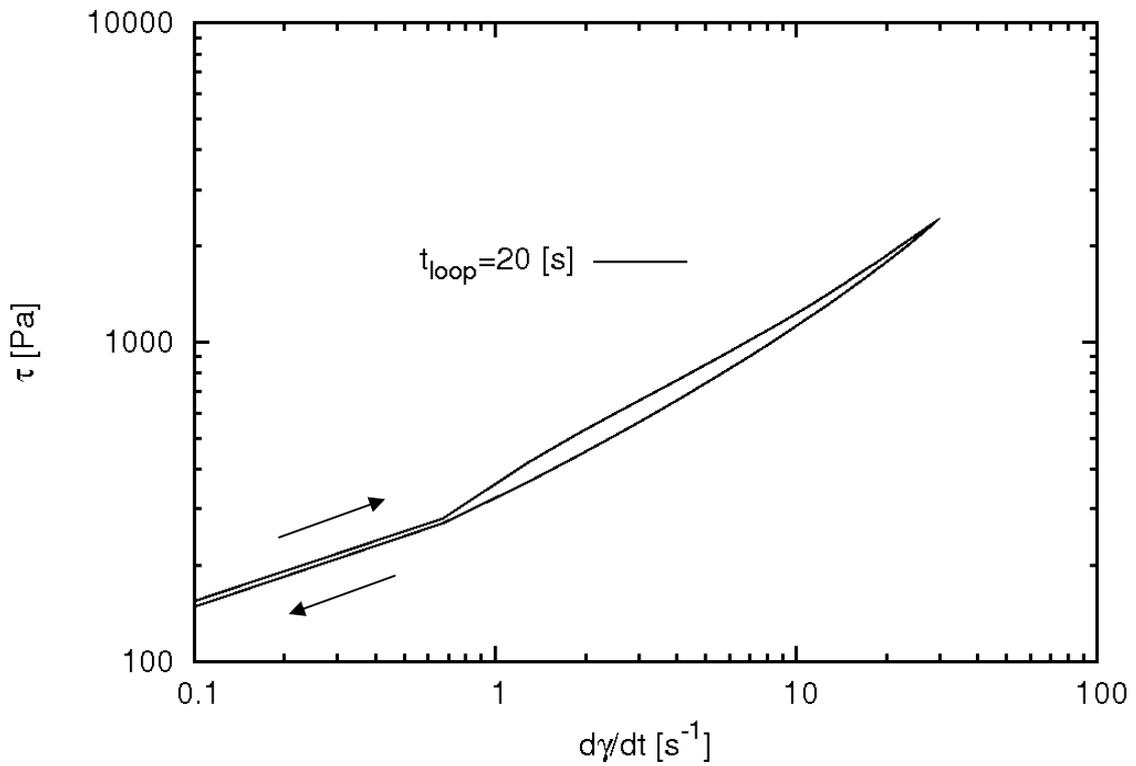
Figure 4-14: Shear stress versus shear rate for a thixotropic loop test for 100% EA 9395 (20 s loop).

It is observed that the shear stress increases with increasing shear rate and then decreases with decreasing shear rate. The degree of thixotropy is defined in ASTM D 2196 – 05 as the ratio between shear viscosity at the lowest shear rate for increasing shear rates and shear viscosity at the lowest shear rate for decreasing shear rates. In the above presented figures the degree of thixotropy is 1.20 and 1.04 for the 300 s loop and the 20 s loop, respectively. According to Uhlherr (2009), these loops show little thixotropy.

The differences in the shear stress for the lowest shear rates for the increasing and the decreasing shear rate range presented for the 300 s loop shown in Figure 4-13 most probably resulted again from difficulties experienced during the measurements at higher shear rates (Uhlherr, 2009). At those shear rates outflow of the test sample due to centrifugal forces can occur. To avoid the possible outflow and hence effect on the results, the thixotropic loop for 300 s measurement time was repeated for a shear rate range from 0.1 to 10 s^{-1}. Results are shown in Figure 4-15.
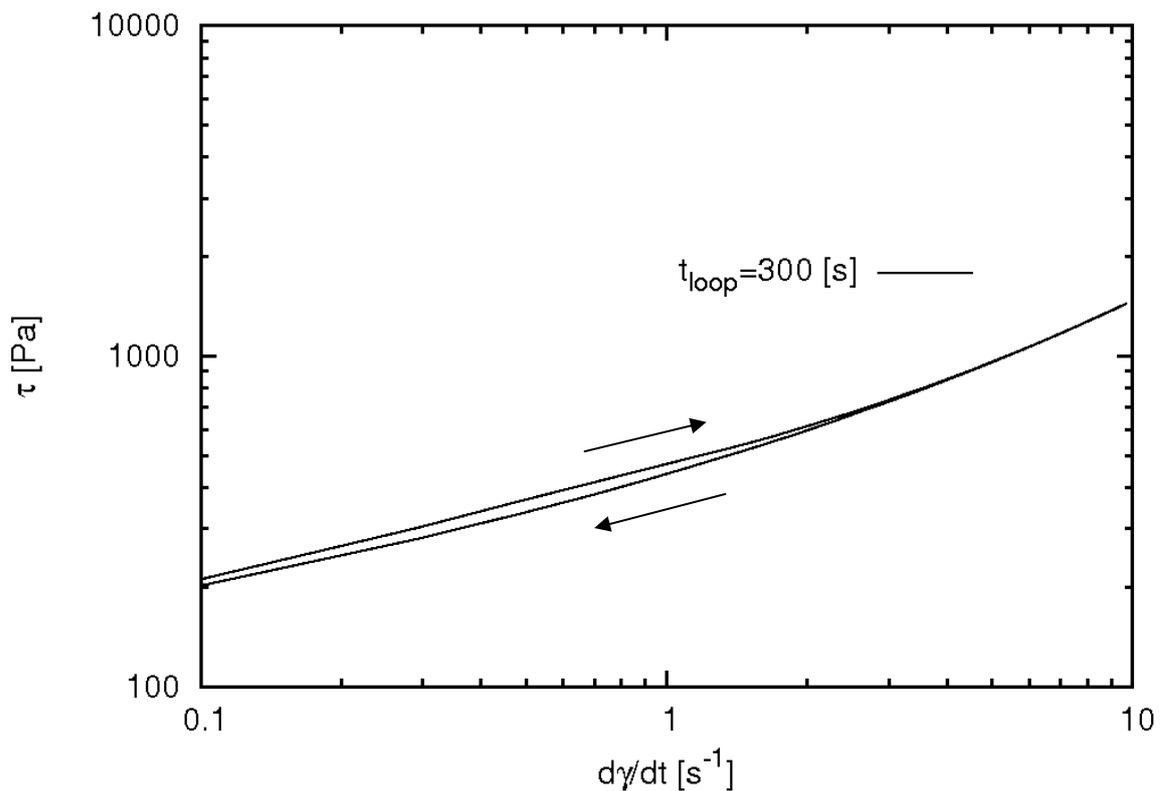
Figure 4-15: Thixotropic 300 s loop for a shear rate range from 0.1 to 10 s^{-1} for 100 % EA 9395.

The graphs obtained for both shear stress branches show little difference for the lowest tested shear rates compared to the results presented in Figure 4-13. The degree of

thixotropy is determined as 1.04. Given the presented results and in addition the discussion with Peter Uhlherr (Uhlherr, 2009), it is believed that the discrepancies experienced result from inaccurate measurements and not from the adhesive's thixotropy. Therefore, the adhesive time dependence was neglected for material model development.

For the measurements of a 70 – 30 weight percent ratio of EA 9395 to EA 9396, the results of the thixotropic loop test are shown below in Figure 4-16. These tests were conducted at a shear rate range from 0.1 s^{-1} to 10 s^{-1} to avoid outflow of the test sample as experienced for EA 9395.
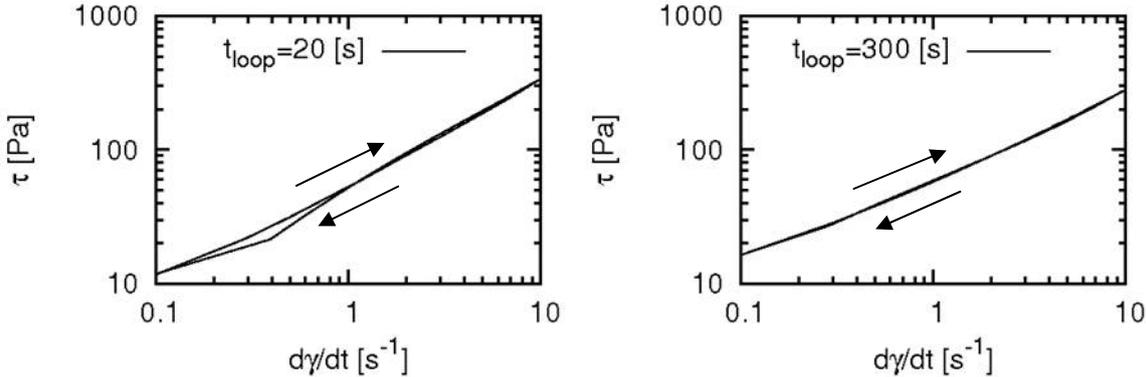
Figure 4-16: Shear stress versus shear rate for a 20 s- and a 300 s-loop up to 10 s^{-1} for an EA 9395 to EA 9396 mixing ratio of 70 – 30 by weight.

In general, the shape of the shear stress versus shear rate curves is similar to the one observed for measurements of EA 9395, that is an increase of shear stress with shear rate and then a decrease of shear stress with decreasing shear rate. It also is observed that the shear viscosity is higher for the increasing shear rates. Scarcely any differences are detected between the two branches of the 300 s-loop. The degree of thixotropy is calculated as 1.01 (20 s-loop) and 1.00. This degree of thixotropy was considered as small (Uhlherr, 2009). Hence, it is believed that the degree of thixotropy determined in these tests would not affect the analysis of the ISF and therefore has not been taken into account when establishing the material model for the 70 – 30 mixture.

4.4.4 Viscoelastic properties

Determination of the linear viscoelastic region

In order to conduct measurements of the storage modulus G' and the loss modulus G'' versus dynamic oscillation, the linear viscoelastic region had to be first determined. The storage modulus represents the materials' elasticity and the loss modulus represents the materials' viscous losses (Rheometrics, 1991). As described in Chapter 4.2 the linear

viscoelastic region can be evaluated through measurements of the storage and loss moduli with respect to strain for a constant frequency. Results presented in Figure 4-17 and Figure 4-18 illustrate shear and loss moduli measurements for increasing strains at a constant frequency of 100 rad/s for EA 9395 and the 70 − 30 weight percent ratio mixtures of EA 9395 to EA 9396.
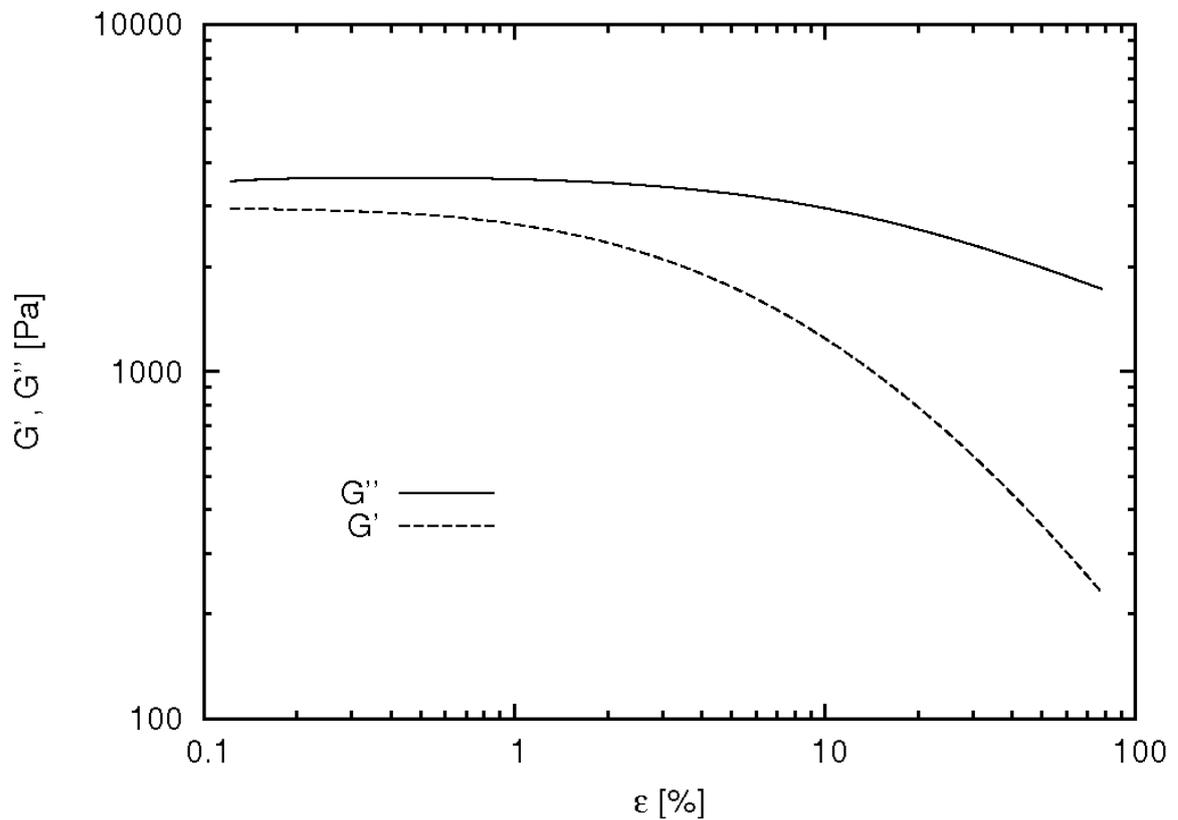
Figure 4-17: Storage and loss modulus versus strain at a frequency of 100 rad/s (100 − 0).
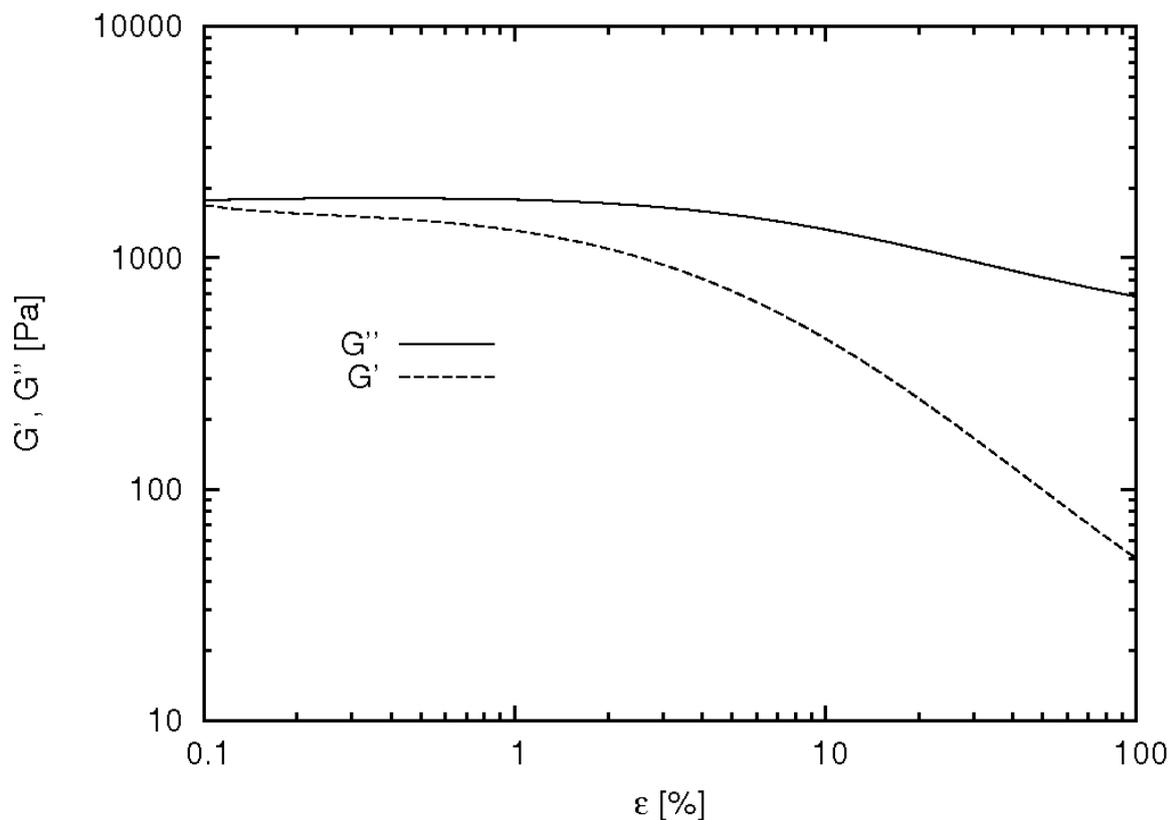
Figure 4-18: Storage and loss modulus versus strain at a frequency of 100 rad/s (70 – 30).

In both cases storage and loss moduli remain constant up to a strain of about 1 %. After a strain of about 1 % the storage modulus starts to decrease. The loss modulus starts to decrease at strains above 5 %. Two measurements were conducted and the recorded values agree well, with 0.2 % difference of the strain detected when the storage moduli begin to decrease. On the basis of the data presented here, it was decided to conduct storage and loss moduli measurements for two different constant strains, 0.5 % and 1 %.

Estimation of relaxation time through storage and loss moduli measurements with dynamic oscillatory tests

Figure 4-19 and Figure 4-20 present storage and loss moduli measurements with respect to frequency for a constant strain of 0.5 % and 1 %, respectively, for EA 9395 only:
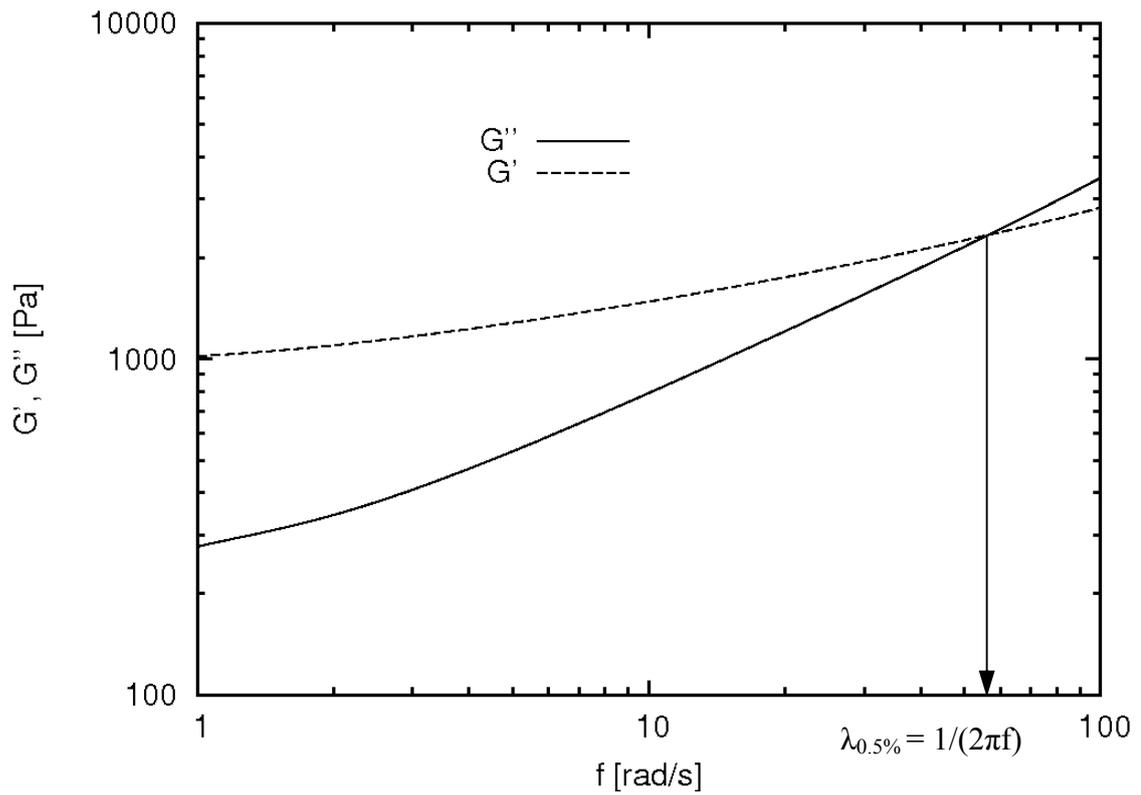
Figure 4-19: Storage and loss modulus versus frequency for a constant strain of 0.5 % for 100 % EA 9395.
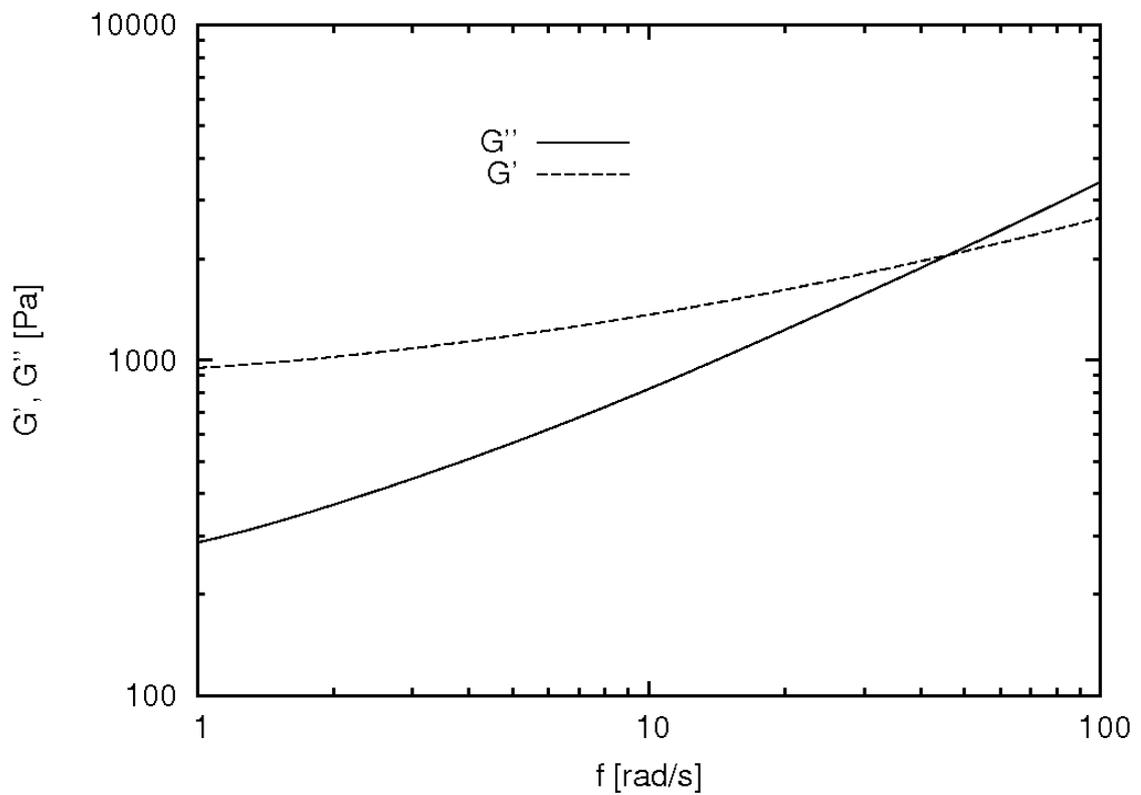
Figure 4-20: Storage and loss modulus versus frequency for a constant strain of 1 % for 100 % EA 9395.

Both moduli increase with increasing frequency, and the loss modulus in both cases shows a steeper slope. The frequency at which the two graphs intersect is 55 rad/s for 0.5 % and 45 rad/s for 1 % strain. The reciprocal multiplied by 2π determines the relaxation time which results in $\lambda_{0.5\%} = 2.865 \ 10^{-3}$ s and $\lambda_{1\%} = 3.501 \ 10^{-3}$ s.

For a 70 – 30 weight percent mixing ratio the measurements were only conducted at a strain of 1 % as a longer relaxation time was known to occur for EA 9395 in this case. Results are shown in Figure 4-21:
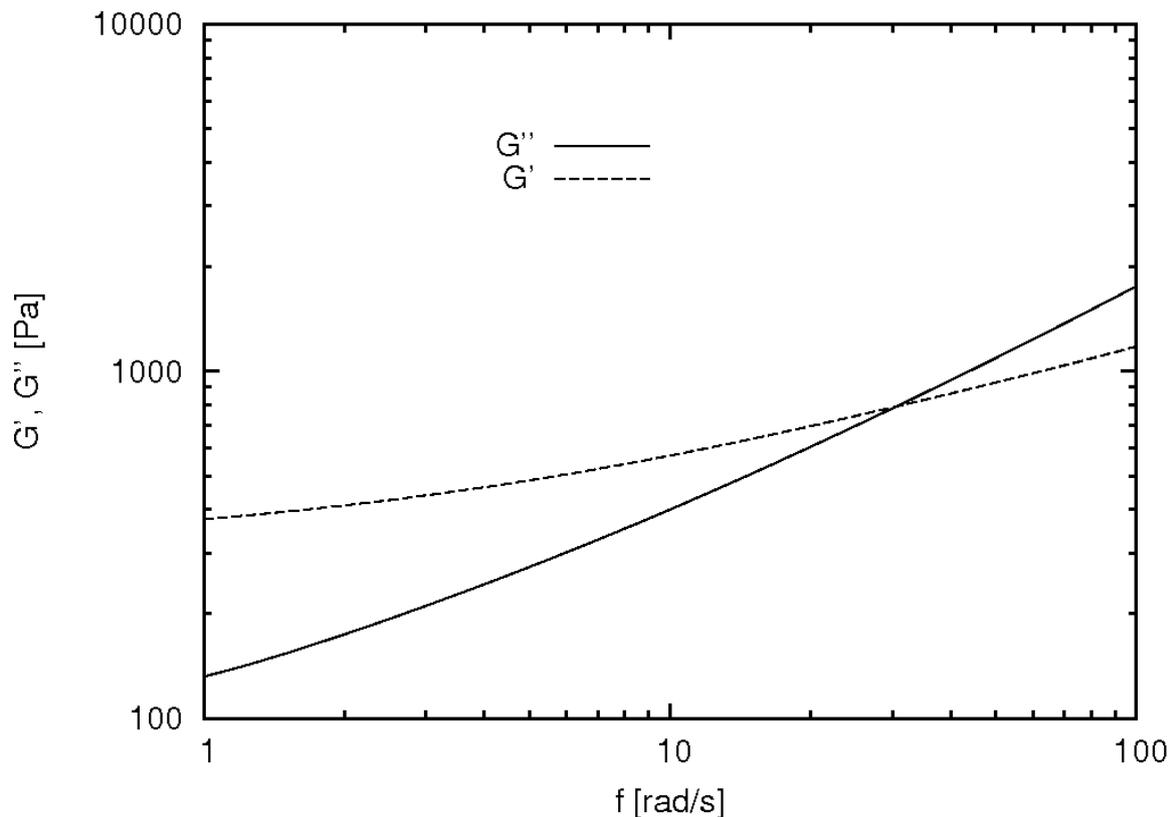
Figure 4-21: Storage and loss modulus versus frequency for a constant strain of 1 % (70-30).

As for EA 9395 the storage and loss moduli increase with frequency at different rates, the loss modulus increases at a higher rate. The graphs intersect at a frequency of 30 rad/s, resulting in a relaxation time of $\lambda_{70\text{-}30, \ 1\%} = 5.305 \ 10^{-3}$ s.

All relaxation times presented here are in the order of 10^{-3} s. Estimated process times for ISF are about 60 s. To calculate the Deborah number *De* the relaxation time is divided by process time (Menges, 2002).

$$De = \frac{\lambda}{t_{process}} \qquad\qquad (4\text{-}7)$$

Taking the longest relaxation time determined, which is for 70 – 30 weight percent EA 9395 to EA 9396 ($\lambda_{70\text{-}30,\ 1\%} = 3.979\ 10^{-3}$ s), the *De* was calculated to 6.63 10^{-5}. As *De* << 1, elastic effects are assumed to be negligible for the adhesives used in ISF.

4.4.5 Constitutive model development

The adhesive material model development for EA 9395 was based on the average of four different shear viscosity versus shear rate measurements that were presented in sub-section 4.4.2. A shear viscosity plot with respect to stepwise increasing shear rate was illustrated in Figure 4-10 on page 96.

According to ASTM D 2196 – 05 the testing should only be applied for shear rates higher than 0.1 s^{-1} and, as mentioned previously, our transducer resolution was insufficient for measuring shear viscosities below 0.1 s^{-1}. Hence, shear viscosities below 0.1 s^{-1} have not been included in the adhesive model development. Furthermore, measurements taken above a shear rate of 25.1 s^{-1} were also not considered due to the sample detachment problems, also previously explained. For the 85 – 15 and 70 – 30 mixtures the average was taken out of two and three measurements for the same shear rate ranges.

In Figure 4-22, material models derived for EA 9395 and mixtures of EA 9395 to EA 9396 are shown based on results presented in sub-section 4.4.2:
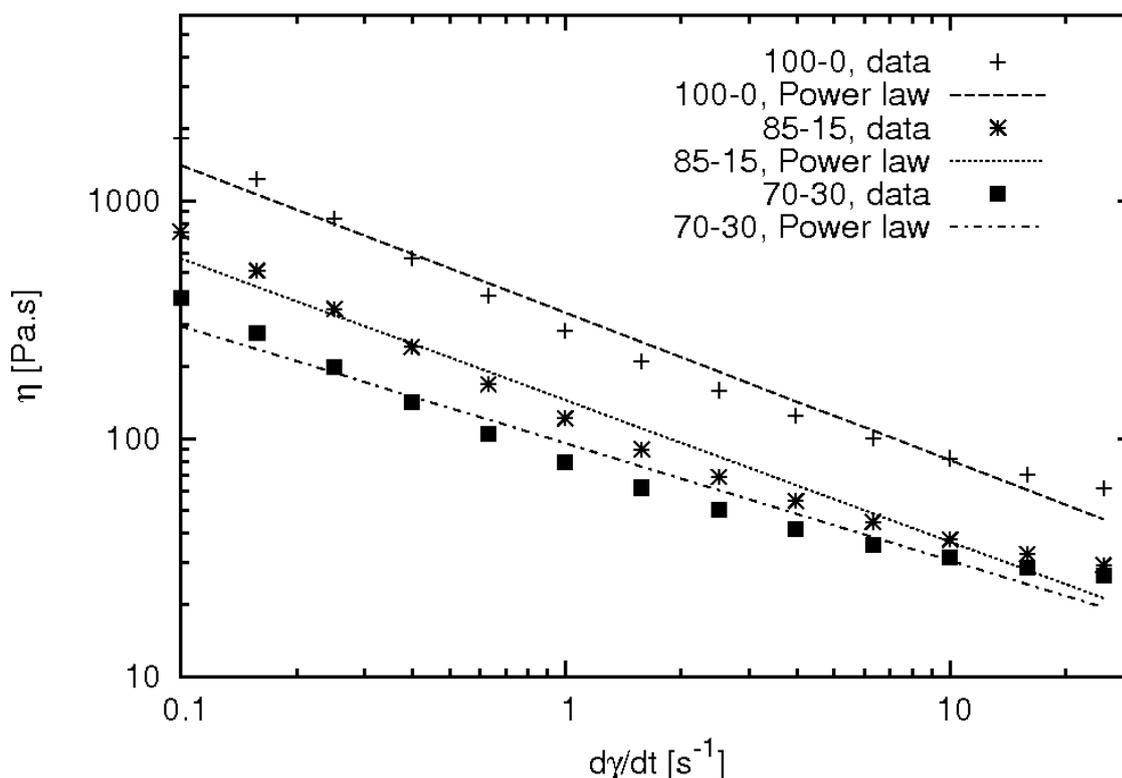
Figure 4-22: Power law viscosity fits for EA 9395 and mixtures of EA 9395 and EA 9396.

In all cases the shear viscosities were fit with a power law relationship to shear rate. The power law models appear to provide only an approximate fit to the measure of shear viscosities. It is clear that they do not account for all variation, given the residual curvature when plotted in log-log form. This necessitates a refined fit, which is outlined and discussed below.

When applying the power law model, the specification of minimum and maximum viscosity limits for very high and very low shear rates was required. If this were not done at these extreme shear rates the viscosity would tend towards infinity for very low shear rates and zero for very high shear rates; this would clearly be contradictory to the adhesive behaviour in those shear rate regions.

Hence, a second fit was proposed. For all adhesives, a five parameter rational fit was applied and is plotted in combination with experimental data in Figure 4-23:
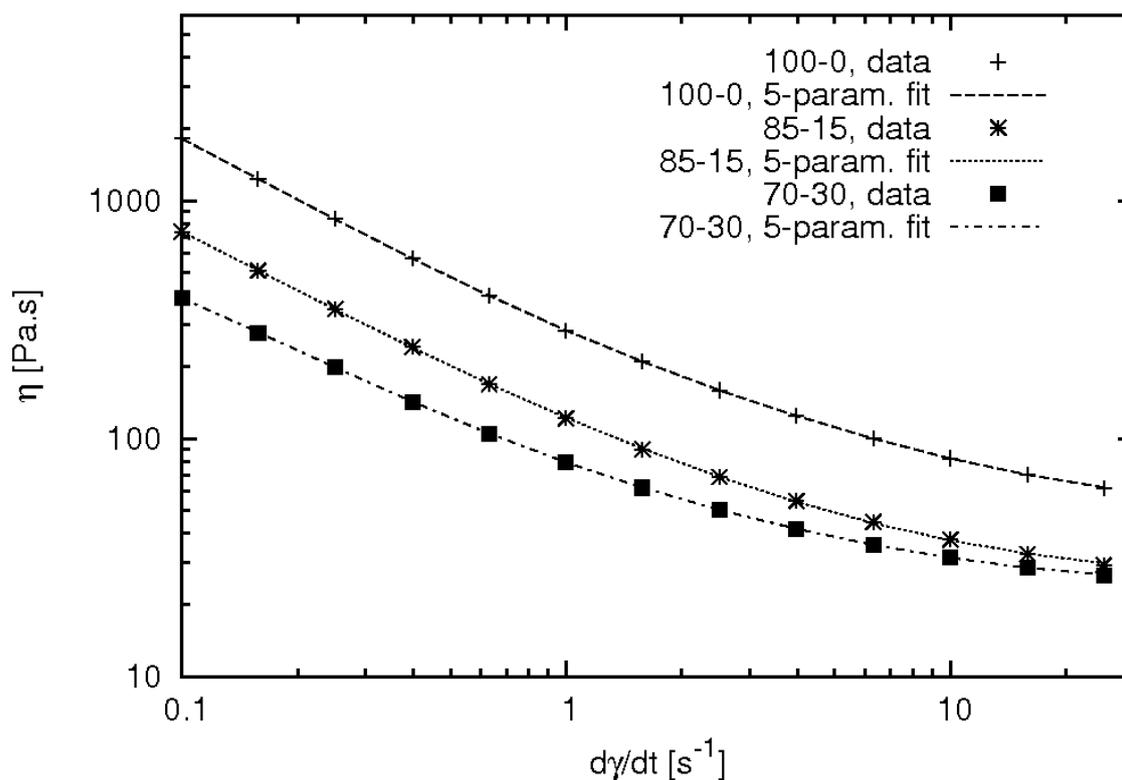
Figure 4-23: Five parameter rational model fit for all adhesives mixtures.

The new fit matches the recorded measurements better than the power law model, especially for higher shear rates, and also agrees well for low shear rates. Furthermore, no viscosity limits have to be applied for very low or high shear rates as would be necessary for the power law models. The equation for the five parameter rational model fitting is:

$$\eta = \frac{a + b\dot{\gamma} + c\dot{\gamma}^2}{1 + d\dot{\gamma} + e\dot{\gamma}^2}. \qquad (4\text{-}8)$$

The parameters for EA 9395, 85 − 15 and 70 − 30 weight percent ratios of EA 9395 to EA 9396 can be found in Table 21:

Table 21: Parameters for the five parameter rational model fit that are used to define the adhesive mixtures viscosities.

Weight percentage EA 9395 – EA 9396	a	b	c	d	e
100-0	16024.99	13515.67	1080.79	83.276	23.120
85-15	5293.645	6541.795	891.0529	66.909	36.160
70-30	1738.666	2216.062	318.678	38.981	13.796

4.5 Summary

Appropriate mixing ratios between the adhesives EA 9395 and EA 9396 according to ISF bonding process requirements were determined as 70 – 30 weight percent of EA 9395 to EA 9396 for the lowest and 100 % EA 9395 for the highest possible adhesive viscosity. The methodology of rheological testings was presented along with calibration of the equipment and description and validation of the tests to be conducted. The adhesives tested showed small time-dependence and small viscoelasticity. Two material models were determined to specifiy the adhesive shear viscosity with respect to shear rate best, the power-law and the five parameter rational model.

5 Insertion Squeeze Flow at Constant Insertion Speed

5.1 Analytical and Numerical Solutions for Insertion Squeeze Flow with Newtonian Fluids

An analytic solution was derived for the flow of a Newtonian fluid during ISF conducted at constant insertion speed. We adopted a method that was applied for a similar flow problem and modified it where necessary. This method was applied by Smith, Ferry and Schremp (Smith et al., 1948) to investigate the force required when a rod penetrates into a Newtonian fluid contained in a cylinder; the fluid, in turn, is forced to rise between the walls of the cylindrical vessel and the rod. While the problem that they analysed is axi-symmetric, we assumed in-plane two-dimensional (2D) flow in our problem. A perfect alignment between the insertion plate and Pi-slot was also assumed such that only half of the domain needed to be considered.

The set up of our problem is illustrated in Figure 5-1. In the figure, h is the displacement of the insertion plate, V is the constant insertion speed, c is the adhesive flow front in the flow channel referenced to the initial adhesive height H_0, and $v(x)$ is the adhesive flow velocity in negative y-direction (insertion direction) and was assumed to be a function of x only.
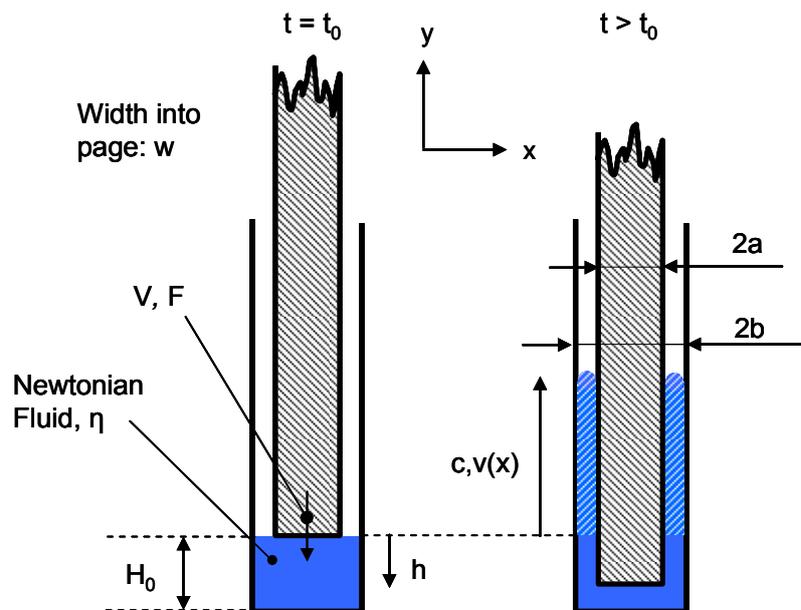
Figure 5-1: Key dimensions for the analysis of insertion squeeze flow with a Newtonian fluid.

The relationship between c and h was derived by applying the principle of mass conservation, from which the flow front c can be determined, as follows:

$$c = (H_0 - h)\frac{a}{b-a} \qquad (5\text{-}1)$$

Balancing pressure and viscous forces on an infinitesimally small Newtonian fluid element in the flow channel led to (Schroeder, 2000)

$$-\frac{\partial p}{\partial y} + \eta \frac{\partial^2 v}{\partial x^2} = 0 \qquad (5\text{-}2)$$

where p is pressure and η is the viscosity. Note that the derivation presented was based on two assumptions to simplify the model: the pressure p and velocity v are functions of y and x, respectively, only.
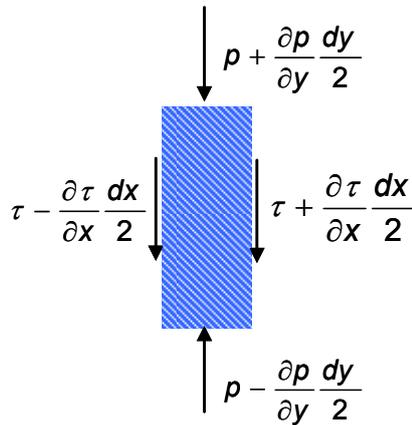
Figure 5-2: Force balance between pressure and shear stress on an infinitesimally small Newtonian fluid element (Schroeder, 2000).

Double integration of the force balance equation (5-2) with regard to x and solving for the integration constants with no-slip boundary conditions at $x = a$ and at $x = b$, the following expression for the velocity distribution with respect to x was obtained:

$$v(x) = \frac{1}{\eta}\frac{\partial p}{\partial y}\frac{x^2}{2} + \left(-\frac{V}{a-b} - \frac{1}{\eta}\frac{\partial p}{\partial y}\frac{a+b}{2}\right)x + V\frac{b}{a-b} + \frac{1}{\eta}\frac{\partial p}{\partial y}\frac{ab}{2} \qquad (5\text{-}3)$$

To determine the pressure gradient the principle of mass conservation was used again. The mass flow rates into and out of the control volume have to be equal. The following expression was obtained:

$$\frac{\partial p}{\partial y} = 6\eta V \frac{b+a}{(a-b)^3} \qquad (5\text{-}4)$$

Assuming a linear pressure increase in the negative y-direction, the pressure gradient with respect to y can be written as

$$\frac{\partial p}{\partial y} = -\frac{P}{c}, \qquad (5\text{-}5)$$

where P is the pressure acting on the insertion plate.

Combining Equations (5-5) and (5-6), the pressure P was obtained as

$$P = -6\eta cV \frac{b+a}{(a-b)^3}. \qquad (5\text{-}6)$$

Finally, the total insertion force was considered to be made up of two components (Smith et al., 1948): a pressure force due to pressure built up at the bottom of the moving insertion plate and a viscous drag force at the contact surface between the insertion plate and the Newtonian fluid. This can be expressed as

$$F = A_1 \tau_{wall} + A_2 P = A_1 \eta \frac{\partial v}{\partial x}\bigg|_{y=a} + A_2 P, \qquad (5\text{-}7)$$

where F is the insertion force, τ_{wall} is the viscous drag shear stress, and A_1 and A_2 are the areas on which the viscous drag shear stress and pressure act, respectively.

Substituting each of the above-derived expressions into Equation (5-7), the insertion force required for a Newtonian fluid was determined per length-unit as

$$\frac{F}{w} = -2\eta cV \left[3\frac{(a+b)(b+a)}{(a-b)^3} + \frac{1}{a-b} \right]. \qquad (5\text{-}8)$$

The above equation indicates that for a Newtonian fluid, the insertion force increases linearly with viscosity, insertion speed and flow front.

Insertion forces calculated applying equation (5-8) were compared with numerical predictions of the insertion forces and results are presented in Figure 5-3 and in Figure 5-4. Dimensions, insertion speed and Newtonian fluid viscosity were identical for both models. In Figure 5-3 the input parameter that was varied is the insertion speed.
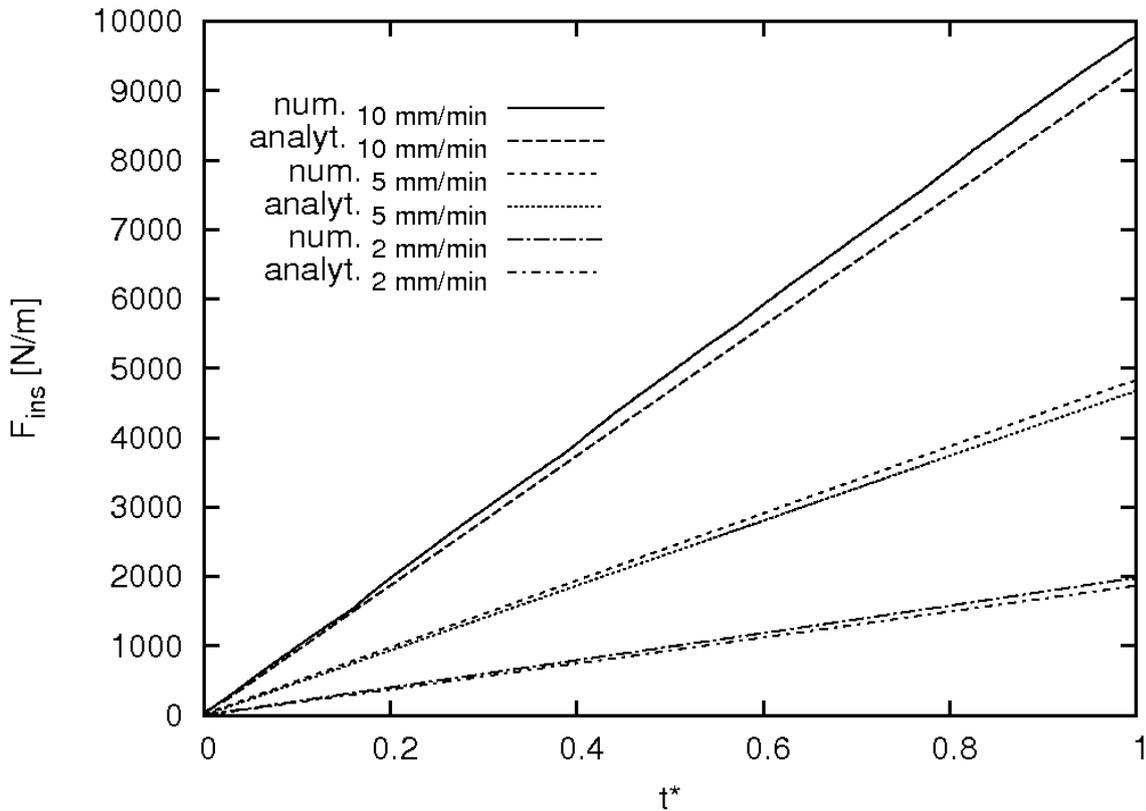
Figure 5-3: Numerically and analytically predicted insertion forces as a function of dimensionless time for different insertion speeds for an ISF process with a Newtonian fluid.

The insertion force increases linearly with respect to time over the time range considered. Further, the insertion force also increases linearly with respect to insertion speed. For example, increasing the insertion force by a factor of two (5 to 10 mm/min) leads to an approximately doubling of the insertion force (at $t^* = 1$, the numerical predictions were 4842 N/m to 9782 N/m).

The numerically predicted and analytically calculated insertion forces exhibited small differences. At 2 mm/min the differences are 5.6 %, at 5 mm/min they are 4.0 % and at 10 mm/min 4.7 %. The numerical model consistently predicts higher insertion forces.

The differences observed between the analytical and numerical insertion force predictions are caused by simplifications in the analytical model. The factors include the neglect of hydrostatic pressure and the air phase, and the simplification to just one-dimensional flow. In addition, as discussed previously, the second phase (air) density for the numerical model is increased by an order of magnitude to improve the stability of the computations. Of these factors, the neglect of hydrostatic pressure and the different

treatment of the second phase should account for a difference of less than a percent between the models. The main difference is presumably caused by the simplification to one-dimensional flow in the analytic model. At the base of the insert the flow must be two-dimensional as the fluid passes from the bottom region into the gaps.

The effect of a variation of the fluid viscosity on the insertion force was also compared:
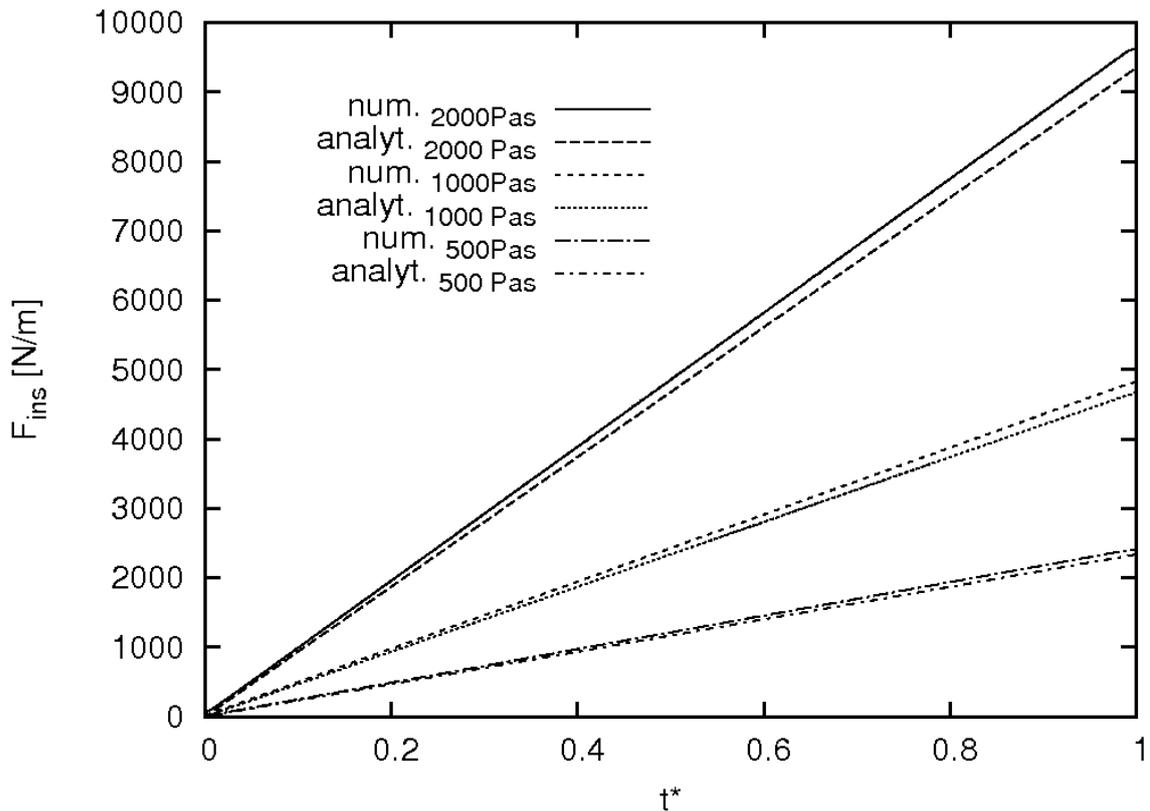
Figure 5-4: Numerically and analytically predicted insertion forces as a function of dimensionless time for different fluid viscosities for an ISF process with a Newtonian fluid.

Similar to the above-presented effect of the insertion speed on the insertion force, it is found that the insertion force varies linearly with the viscosity. The insertion force also increases linearly with time. The numerical model again predicts higher insertion forces than the analytical model. The discrepancies are 3.60 %, 3.96 % and 3.78 % for 2000, 1000 and 500 Pa.s, respectively. The causes of these differences are the same as those discussed above for the effect of insertion speed.

Finally, the flow velocity distribution $v(x)$ within the flow channel was compared using one specific case of $v_{ins} = 5$ mm/min and $\eta_{fluid} = 1000$ Pa.s. The results are illustrated in Figure 5-5.
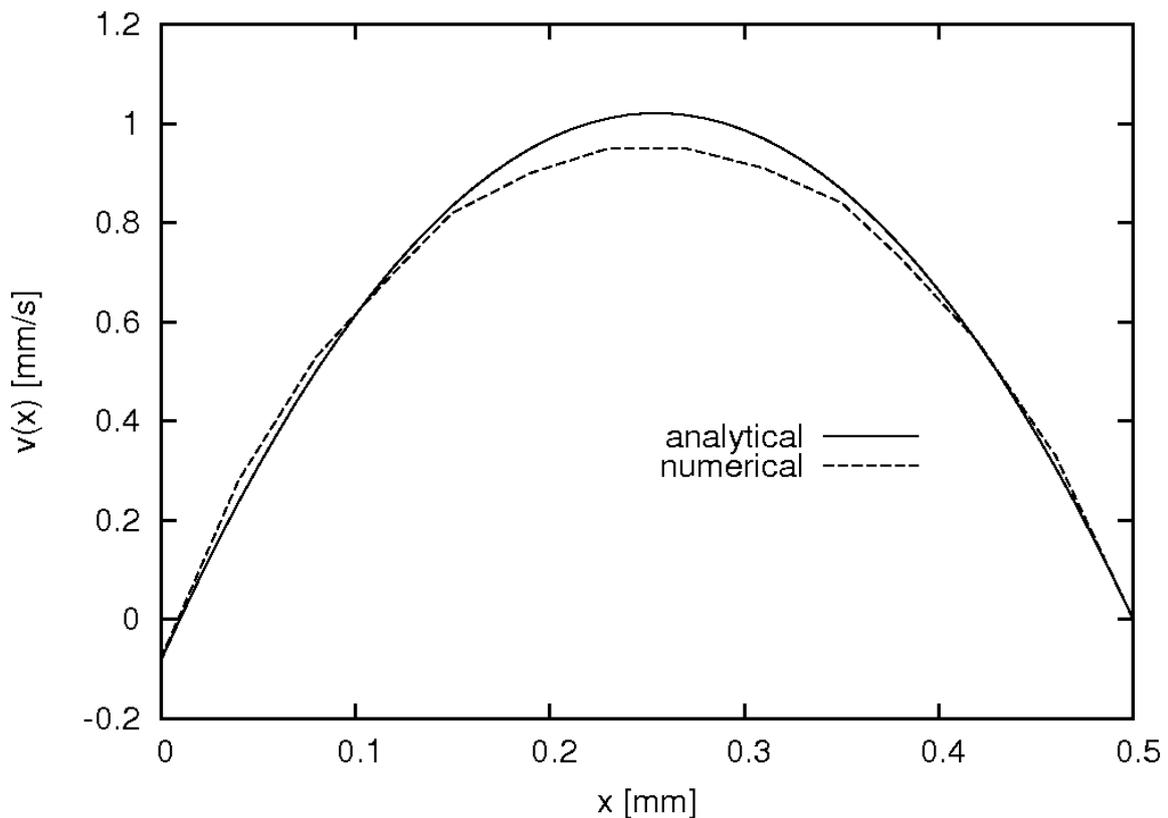
Figure 5-5: Comparison of the velocity distribution with respect to flow channel position predicted from the analytical and numerical models.

An *x*-position of 0 and 0.5 mm represents the right insertion plate side wall and the right Pi-slot wall, respectively. The fluid velocity is negative and equal in magnitude to the insertion speed of the insertion plate at $x = 0$ mm. At the other boundary the fluid velocity is 0. Both observations can be explained through the conditions set at the wall boundaries, where the no-slip condition was applied, resulting in the fluid velocity being equal to the velocity of the boundaries.

The integrated area under the two graphs is identical. This area is the volume flow per unit length and represents the amount of displaced fluid. Given the areas are equal it can be deduced that the continuity condition is fulfilled.

There is a small discrepancy in the shape of the velocity distributions, with the analytical solution showing a slightly higher maximum. This is attributable to the assumptions made when solving the problem analytically. The flow velocity *v* in the flow channel was assumed to vary only with *x*, and the pressure in the flow channel in the insertion direction was assumed to vary only with *y*. As equation (5-3) shows, the flow velocity is considered a function of the pressure distribution in the insertion direction so

the pressure constraints will also affect the fluid velocity. These simplifications were not imposed on the numerical model, hence it is expected that they account for some small discrepancies in the solutions, which are expressed through the observed small differences in the velocity profiles.

In summary, an analytical solution for the considered squeeze flow problem for purely Newtonian fluids in the specified geometry has been presented. A comparison was conducted between analytical and numerical predictions for the insertion force and the maximum difference was found to be 5.6 %. The difference results from differing assumptions for the numerical and the analytical model. In both models the insertion force has been found to linearly depend on the insertion speed and also to linearly depend on the fluid viscosity. Another comparison was drawn between the flow velocity distributions within the flow channels and it has been found that the flow velocities are identical for both models at the wall boundaries and, further, that continuity is maintained in both cases.

5.2 Insertion Squeeze Flow at Low Insertion Speeds

The main objective of this section was to draw a comparison between numerically predicted and experimentally measured insertion forces acting during ISF at low constant insertion speeds. First, the effects of insertion speed and adhesive viscosity on the insertion force were examined by analysing predictions obtained from the CFD simulation. Then, results from insertion force measurements during ISF experiments conducted on a universal Instron testing rig are presented. Finally, a comparison is made between the numerical and experimental insertion forces.

As described in Section 3.5 the ISF process was modelled two-dimensionally (2D) on a cross section of the joint (consider Figure 3-8 on page 69). A constant speed condition was applied on the wall boundaries that represent the insertion plate walls. Due to this motion the adhesive was displaced into the flow channels that form between the insertion plate side wall and the Pi-slot wall boundaries. The input parameters that were varied were the insertion speed and the adhesive viscosity. The insertion speeds investigated were 2.5, 5 and 10 mm/min.

The adhesive viscosity was adjusted according to suitable weight percent ratios of the higher viscous EA 9395 and the lower viscous EA 9396. The selected ratios were $70 - 30$, $85 - 15$ and $100 - 0$ weight percent EA 9395 to EA 9396 which were derived in Section 4.1. The material model to represent the adhesive viscosity was the power law model although the five parameter rational model provided a much closer approximation of

the measured viscosities (compare Figure 4-22 and 4–23). The power law model offers an easily implemented and low computational cost viscosity model that results in small errors at the low strain rates that would be found at low insertion speeds. However, it is clear that for a broader range of insertion speeds a better model is needed and this is discussed below.

Shear rate distributions within one flow channel for the highest and the lowest applied insertion speeds are shown in Figure 5-6.
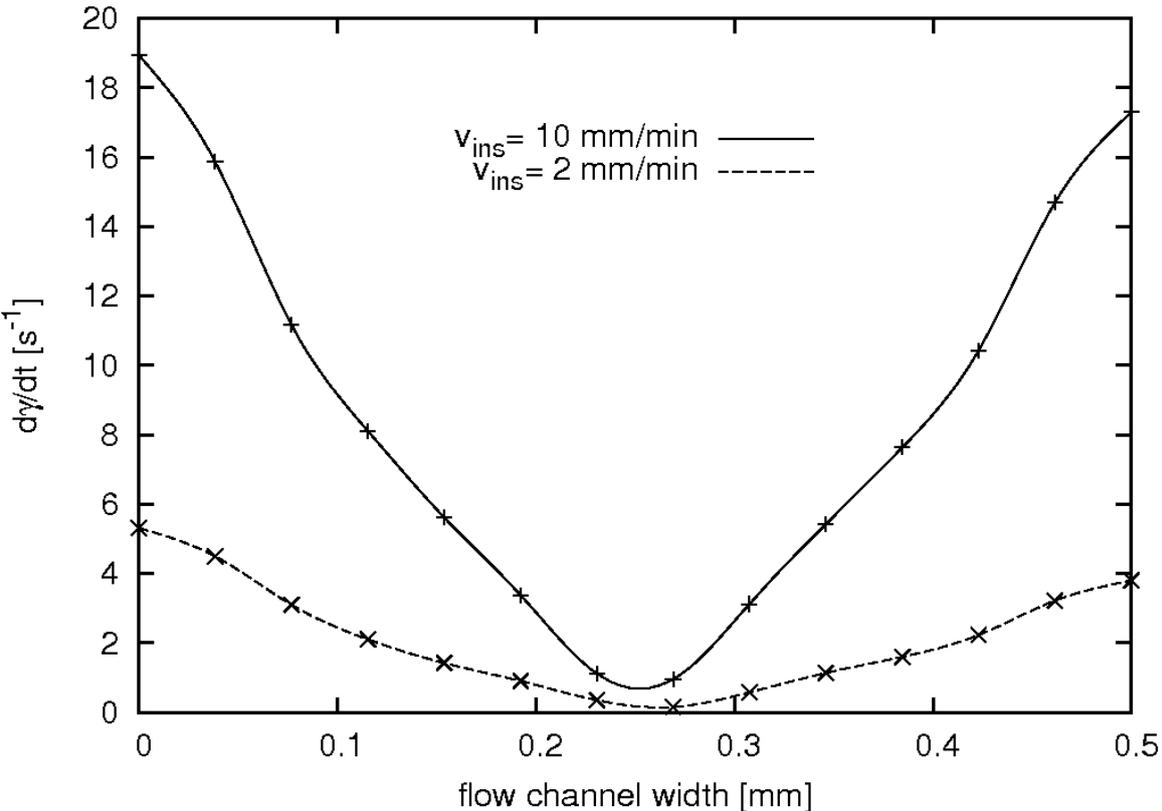
Figure 5-6: Numerically predicted shear rates in the adhesive within the flow channel for insertion speeds of 2 and 10 mm/min.

The x-axis represents the position along a horizontal line within the flow channel that is fully occupied by adhesive. The 0 mm x-position is at the wall boundary of the insertion plate while an x-position of 0.5 mm represents the Pi-slot wall boundary. The shear rate maxima are found at the insertion plate wall boundary and are 19 s^{-1} and 5.2 s^{-1} for the higher and the lower insertion speed, respectively. With increasing distance from this boundary the shear rate decreases and reaches a minimum at an x-position of 0.255 mm. As the shear rate is defined as a function of the second invariant of the rate-of-deformation tensor (see equations (3-17) and (3-19) on page 50) and the y-component of the velocity

vector reaches its maximum at an *x*-position of 0.255 mm (see Figure 5-5), the shear rate at this position is expected to be 0 given the rate of change of the *x*-component of the velocity vector is negligible. This indeed is predicted in the numerical model but not illustrated in Figure 5-6 due to insufficient resolution in the region around 0.25 mm. In fact the shear rate, which is effectively $|\partial v/\partial x|$, will have a discontinuous gradient as it reaches zero. The shear rate increases steadily towards the other wall boundary, which is the Pi-slot wall. As conservation of mass is one principle applied within the CFD, the velocity distribution, and hence the velocity gradient, within the adhesive in the flow channel is constant with respect to its vertical position (*y*-position). Thus, the shear rate is also constant with respect to its vertical position as the width of the flow channel remains constant. Consequently, the viscosity must remain constant in the flow channel with respect to its vertical position, which is demonstrated by the viscosity field illustrated in Figure 5─7. The viscosity field for the entire flow domain is presented for an insertion speed of 10 mm/min and adhesive viscosities of the 70 – 30-mix and 100 percent EA 9395.

a)   *b)*
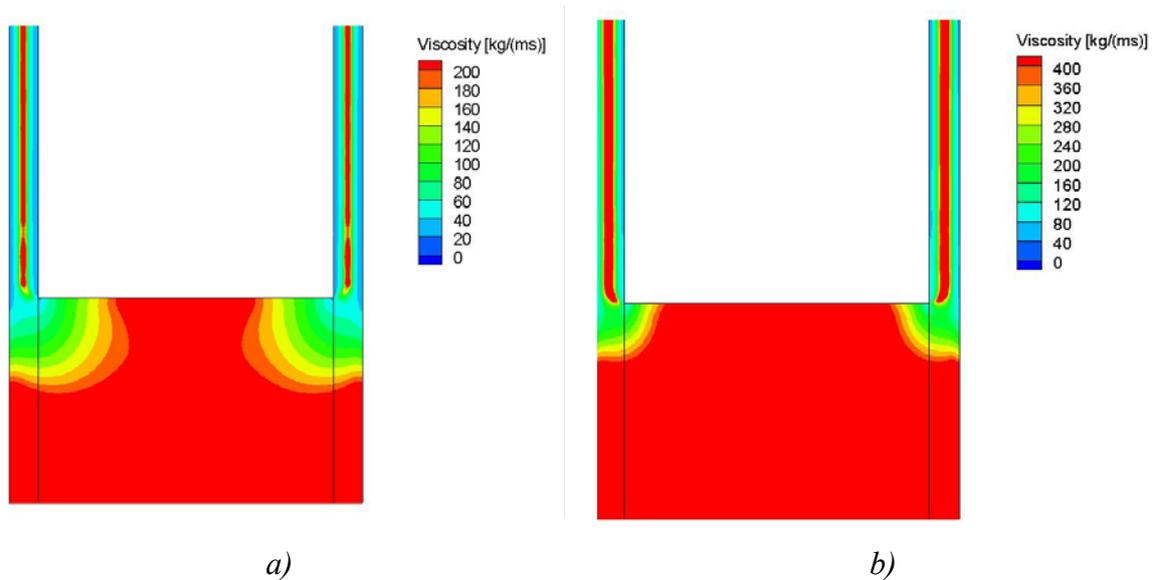
Figure 5-7: Viscosity fields at t* = 0.21 at an insertion speed of 10 mm/min for a) a 70-30 weight percentage ratio of EA 9395 to EA 9396 and b) 100 % EA 9395.

The viscosity fields show that highest viscosities for both adhesives are in the region underneath the insertion plate and in the middle of the flow channel, hence where the lowest shear rates are expected. The viscosity field for 100 % EA 9395 shows overall higher viscosities compared to the 70 – 30 adhesive mixture of EA 9395 to EA 9396, as expected.

In general, the shear rate is a function of the derivative of the velocity vector as stated above, and so shear rate maxima are expected at highest velocity gradients. Velocity gradients depend on two parameters: the velocity magnitude and the flow channel width. As the flow channel width is held constant at 0.5 mm, it can be concluded that the shear rate depends on the moving boundary velocity magnitude only. Thus it is believed that the highest acting shear rates during the ISF occur at the highest insertion speeds. So, the highest shear rate that was predicted from the numerical model is $19 \, \text{s}^{-1}$ (as shown in Figure 5-6) which is lower than the highest shear rate used to derive the adhesive material model which was $25.1 \, \text{s}^{-1}$; within this shear rate region the adhesive viscosity is represented reasonably well by the Power law model, as was shown in Figure 4-22.

As stated above, there was a second reason to select the power law model within this Section. A power law-like material model can be selected for a fluid viscosity in the Fluent software by simply providing values for the non-Newtonian exponent n and the consistency factor K. An implementation of the five parameter rational model, though, requires the development of a script file to be used as a user defined function (UDF) that can then be implemented in Fluent. The power law model promised to provide results for the ISF process in a much shorter time. For those two reasons it appeared meaningful to begin with the Power law model for representing the adhesive viscosity.

Other input parameters that remained constant throughout this Section were both flow channel widths, $\delta = 0.5$ mm. The Pi-slot height H_1 was 35.5 mm. Material properties of air were density $= 1 \, \text{kgm}^{-3}$ and viscosity $= 0.001 \, \text{kgm}^{-1}\text{s}^{-1}$. The initial adhesive amount was 105 volume percent of the amount necessary to fill the flow channels completely at a final bonding position. The initial adhesive height H_0 could be derived from this amount.

The effect of insertion speed on the insertion force with respect to dimensionless time is presented in Figure 5-8 for an adhesive viscosity according to a EA 9395.
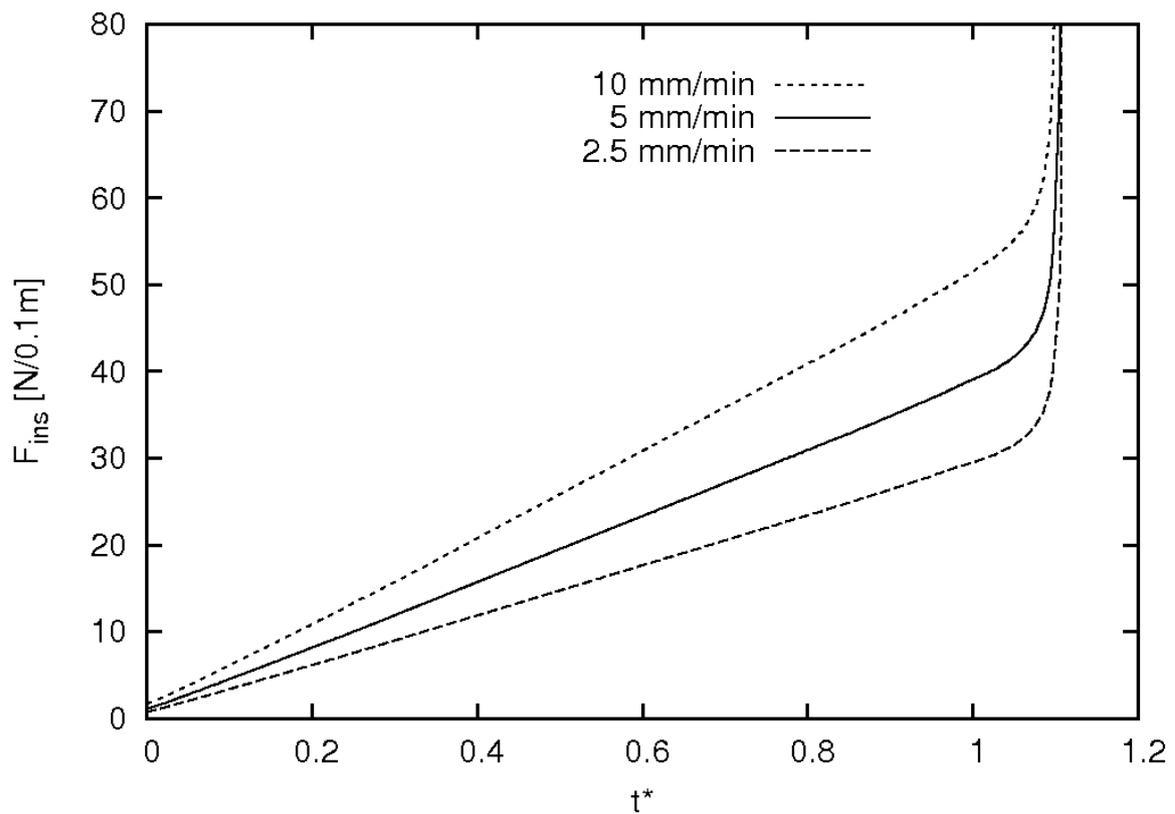
Figure 5-8: Insertion force as a function of dimensionless time at different insertion speeds for EA 9395.

The insertion force presented in Figure 5-8 is composed of two components, the pressure force that acts perpendicular to the insertion plate head and the shear force acting along the side walls of the insertion plate. The insertion force acts in the y-direction due to the resistance of the adhesive to move. The dimensionless time is defined as the ratio between the process time and a time T which is the duration for the adhesive to fill both flow channels entirely in a non-misaligned insertion process. For t^* greater than one, the adhesive flows out of the top of the flow channel.

From Figure 5-8, it can be seen that the insertion force increases linearly with respect to dimensionless time followed by a significant increase that begins to appear at a dimensionless time of about 1.05. This significant increase results from a significant pressure increase underneath the insertion plate which in turn is a result of the insertion plate closely approaching the Pi-slot boundaries. A pressure distribution that is typical of those seen when these boundaries are close to each other is shown for a dimensionless time of 1.11 in Figure 5-9.
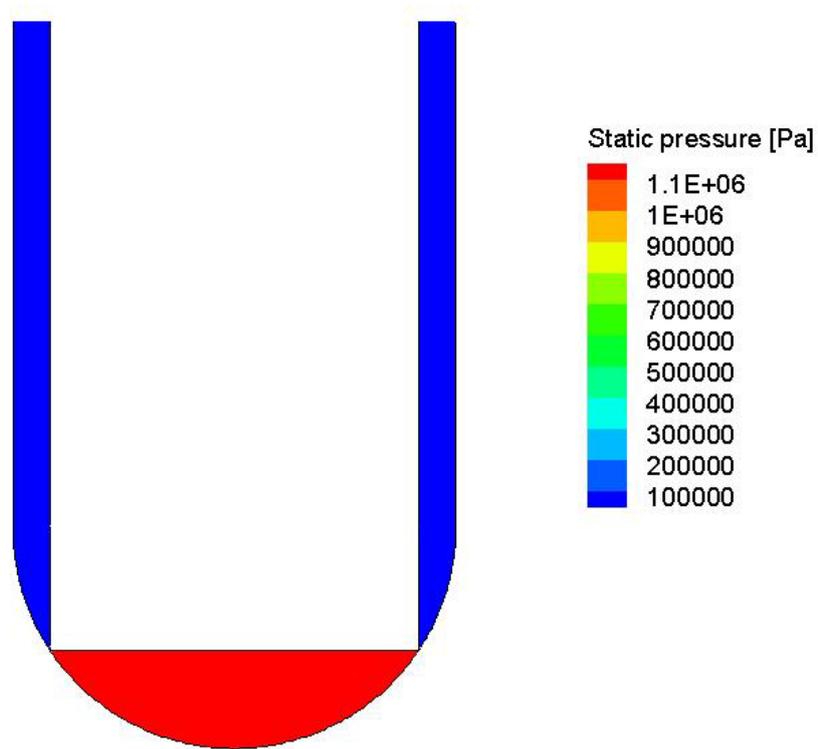
Figure 5-9: Pressure contours at one specified dimensionless time of t* = 1.11 for an insertion speed of 2.5 mm/min and EA 9395.

This pressure-contours plot shows a pressure of about 1.1 MPa underneath the insertion plate and about atmospheric pressure within the flow channels. It also shows that the distance between the insertion plate corners and the Pi-slot bottom has almost vanished. To fulfil the law of continuity, the velocities between the insertion plate and the Pi-slot must become very high as the area between these boundaries becomes increasingly small. Only a small amount of adhesive can flow through the gap in-between the boundaries as this becomes very small until finally, when the boundaries touch, no adhesive can be displaced. This eventually results in the pressure being equal in the entire flow channel area. The adhesive remaining under the insertion plate therefore experiences a higher resistance to flow which is expressed as the increased pressure. This results in the much higher insertion force seen in the latter stages of the insertion, as shown in the figure.

It can be seen that with increasing insertion speed the insertion force also increases. However, this dependence is weaker compared to that observed for Newtonian fluids, as described in Section 5.1. At a dimensionless time of $t* = 1$, the insertion force is 29.4 N/m for an insertion speed of 2.5 mm/min. Doubling the insertion speed results in an insertion force of 38.9 N/m and a further increase by a factor of 2 leads to an insertion force of 51.5 N/m. Thus doubling the insertion speed results in an insertion force increase of

33.3 % and 32.4 % when the insertion speed is increased from 2.5 to 5 mm/min and from 5 to 10 mm/min, respectively. This indicates a quasi-linear relation between the insertion force and the insertion speed. Comparing this relation with the one derived for the Newtonian material in the previous section, for both the numerical and the analytical models studied the insertion force was predicted to increase 100 % with a 100 %-increase of the insertion speed. The difference between the relations derived for the non-Newtonian and the Newtonian fluids can be explained through the shear thinning material characteristic of non-Newtonian adhesives. With increasing shear rate due to increasing insertion speed the viscosity would not decrease but for a Newtonian fluid it would remain constant. This would result in a stronger effect of the insertion speed on the insertion force compared to the one for a non-Newtonian, shear thinning fluid.

The second input parameter varied was the adhesive viscosity. For a constant insertion speed of 5 mm/min, the insertion forces are plotted in Figure 5-10 with respect to dimensionless time for different adhesive viscosities.
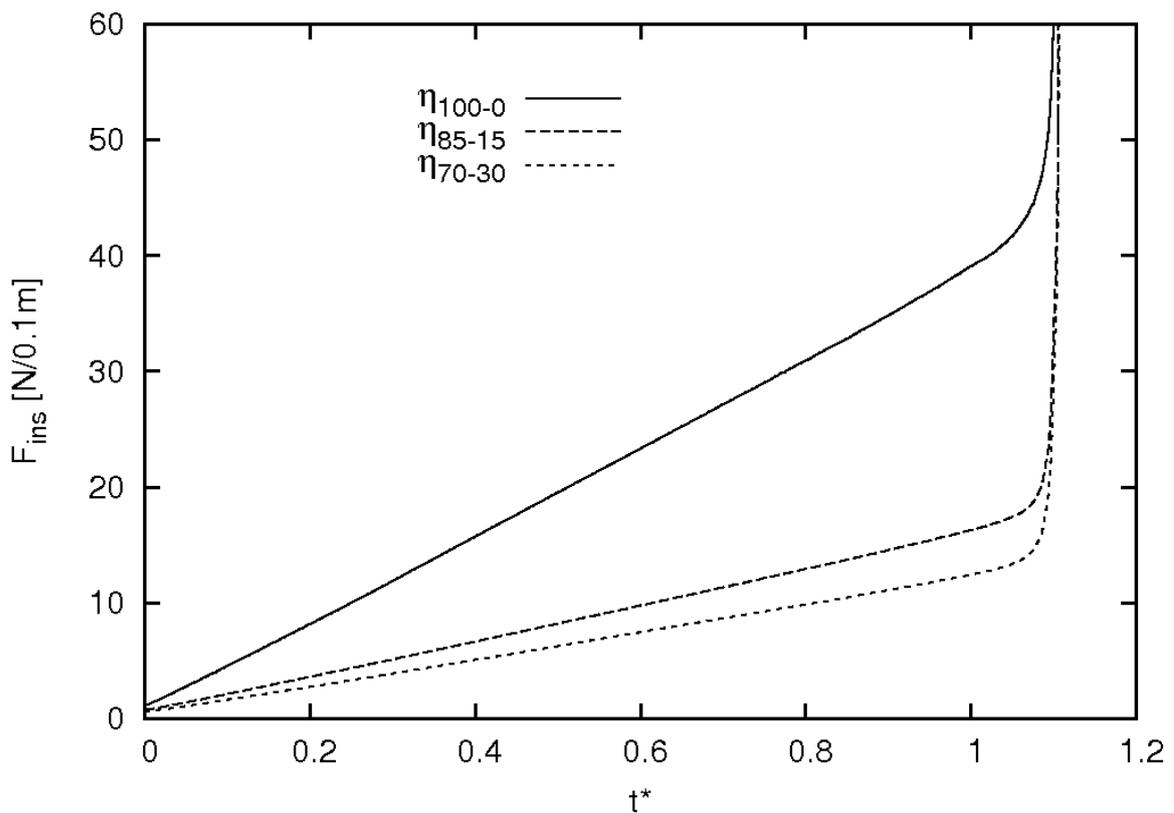
Figure 5-10: Insertion force versus dimensionless time for different adhesive viscosities at an insertion speed of 5 mm/min.

The full line represents the transient insertion force for an insertion speed of 5 mm/min and an adhesive viscosity according of EA 9395. The same data is plotted in Figure 5-8 as the full line. The graphs in Figure 5-10 show that an addition of 15 weight percent of the lower viscous adhesive EA 9396 to the higher viscous EA 9395 decreases the insertion force by more than 50 %. Again the insertion force values were compared with each other at a dimensionless time of $t^* = 1$; when EA 9395 only is applied the insertion force was 38.9 N/m. The insertion force decreases to 16.1 N/m after addition of the first 15 weight percent of EA 9396 (a decrease of 58.6 %). Increasing the amount of EA 9396 within the mixture to 30 weight percent results in an insertion force at $t^* = 1$ of 12.4 N/m which represents a decrease of another 23.0 %.

One objective of this sub-section was to draw a comparison between measured and predicted insertion forces. The experimental approach used was the ISF test described in Section 3.6. The experiments were conducted at low insertion speeds and were referred to as the first set of experiments in Section 3.6. The tests were conducted in a 10 kN universal testing machine using specimens made of carbon epoxy composites and which were 100 mm in length. In terms of the Pi-slot and the flow channel, all specimens were made to the baseline dimensions with the nomenclature defined in Figure 3-8. The nominal dimensions and baseline parameters are as follows:

Table 22: Nominal dimensions and baseline parameters applied for the first set of ISF experiments.

Labelling	Unit	Symbol	Value
Insertion plate width	[mm]	$2a$	5.0
Pi-slot width	[mm]	$2b$	6.0
Flow channel width	[mm]	δ	0.5
Pi-slot height	[mm]	H_1	35.5
Initial adhesive amount	[%]	$V_0/V_{100\%}$	1.25
Insertion speed	[mm/min]	v_{ins}	5
Adhesive viscosity	[kgs^{-1}m^{-1}]	η_{adh}	$100 - 0$[1]

To ensure good alignment between the insertion plate and the Pi-slot, spacer wires were used. The wire diameter was adjusted based on the actual flow channel width, as determined by the insertion plate and Pi-slot dimensions. These can vary from the nominal values due to manufacturing issues. The initial adhesive amount placed into the Pi-slot before starting the insertion process was 125 volume percent of the amount necessary to fill the flow channels completely at the final bonding position.

Figure 5-11 shows two typical insertion force measurements with respect to dimensionless time.

---

[1] The values are derived from the viscosity for EA 9395 only
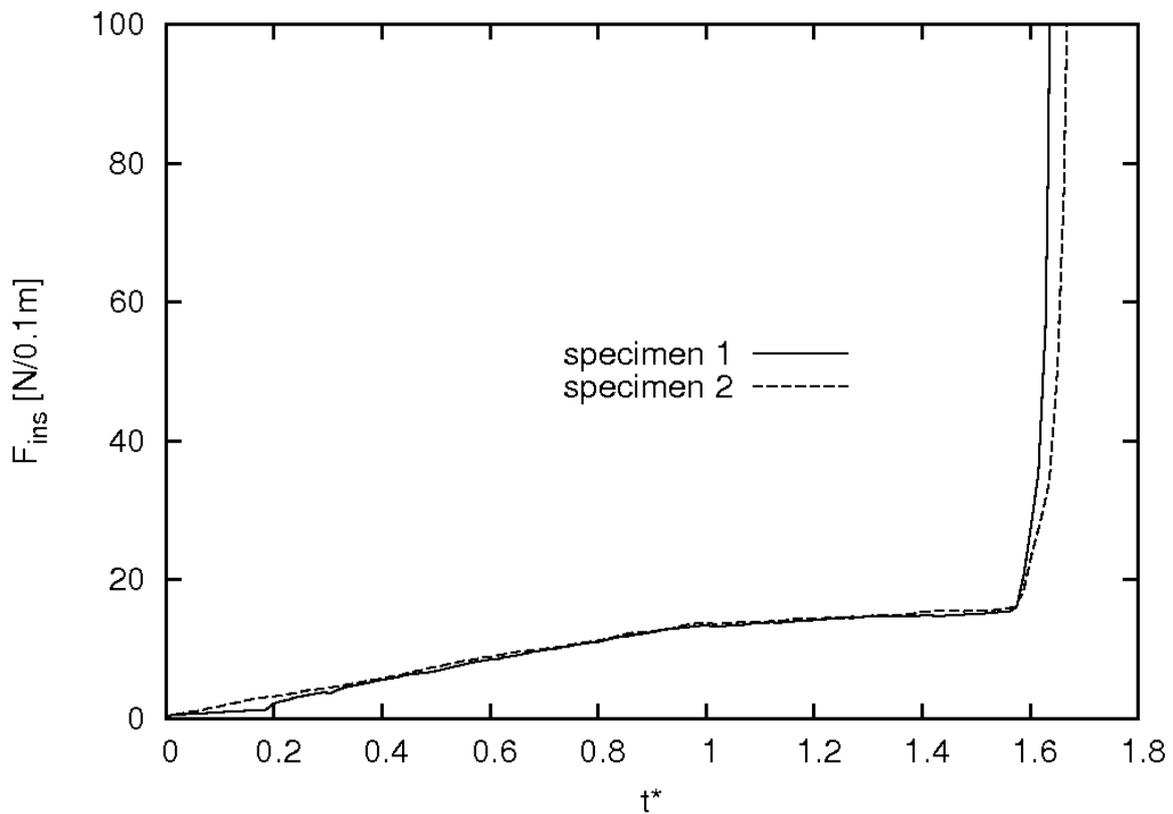
Figure 5-11: Two insertion force versus dimensionless time plots for v_{ins} = 5 mm/min and η_{adh} = 70 – 30 as measured in the ISF experiments.

The dimensionless time was derived as described above for the numerical results. The measurements were taken at an insertion speed of 5 mm/min and 70 – 30 weight percent ratio EA 9395 to EA 9396. At the start of the insertion, a slower increase in the insertion force was recorded, resulting from the compaction of the initially uneven adhesive surface. For the second specimen, however, this compaction is not observed due to a more even adhesive surface. For both specimens a linear increase in insertion force with time is observed until the adhesive starts to flow out of the flow channels at t^* = 1. The insertion force becomes approximately constant after this before increasing significantly when the insertion plate and Pi-slot wall become very close and finally touch. The insertion forces that were used for comparison and which are presented in the following analysis were taken when the adhesive flows out of the flow channels, i.e. at t^* = 1. They are referred to as typical insertion forces in the following discussion.

The typical insertion forces compared in Figure 5-12 are those for the adhesive with 100 weight percent EA 9395.
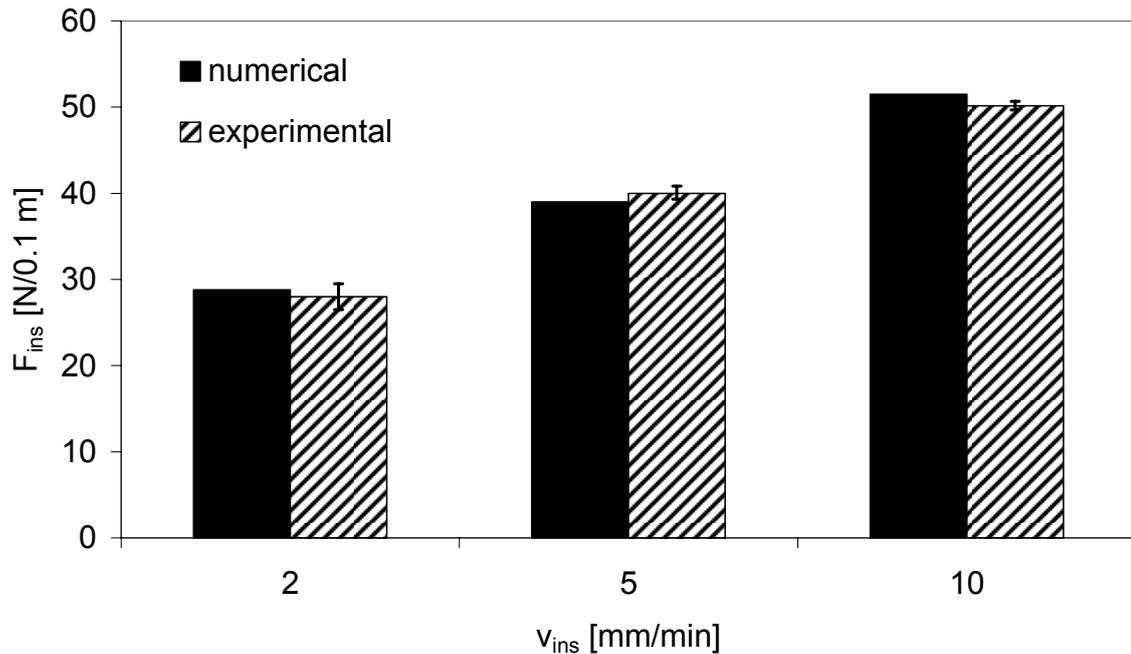
Figure 5-12: Comparison between measured and predicted insertion forces with respect to insertion speed at t* = 1.

From the figure it can be observed that there is good agreement between the predicted and measured typical insertion forces. The measurements shown were the result of averaging over two or three experiments for each insertion speed. The error bars indicate repeatability, which was within ± 2.5 %.

The effect of adhesive viscosity on the measured and predicted typical insertion forces is presented in Figure 5-13 for three different mixing ratios and a constant insertion speed of 5 mm/min. Good agreement exists between the predicted and measured insertion forces for each of the adhesives considered. The typical insertion forces measured experimentally are slightly higher than the predicted ones. This is mainly caused by the differences in specimen dimensions resulting from the manufacturing process. The widths (thicknesses) of the insertion plates were found to vary between 5.08 and 5.20 mm and this is wider (thicker) than the insertion plate width modelled (5.00 mm). This results in slightly narrower flow channel widths for the test specimens, and hence higher insertion forces being recorded during the experiments.
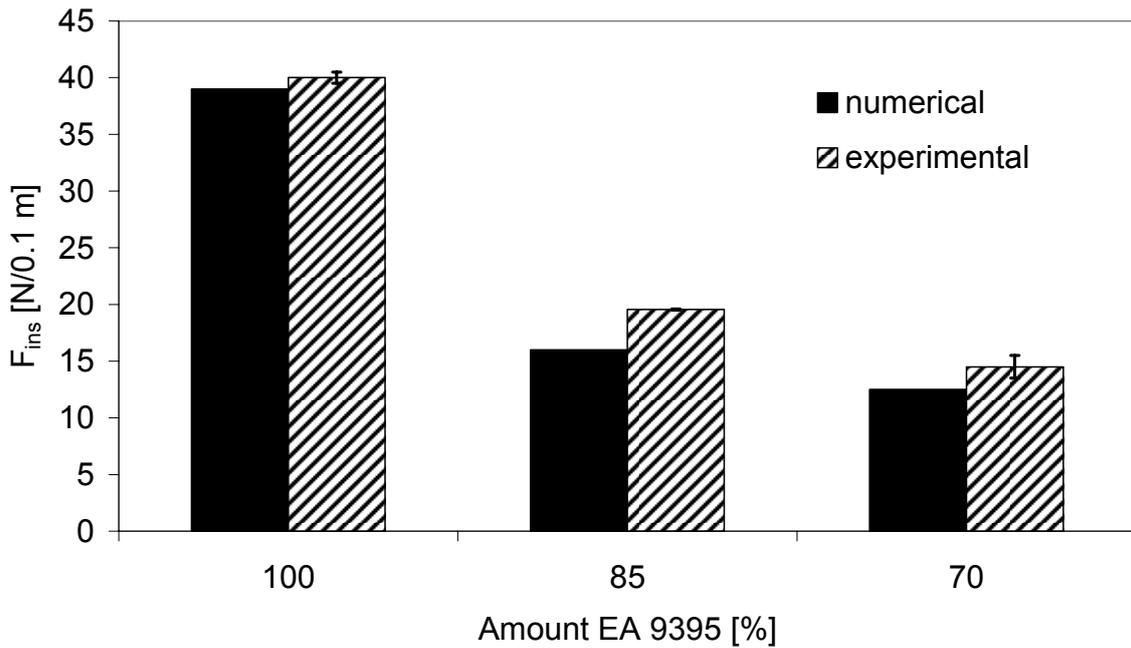
Figure 5-13: Comparison between measured and predicted insertion forces with respect to adhesive viscosity at t* = 1.

To support this reasoning a consideration of the insertion plate width and the process parameters for each experiment conducted are provided in Table 23. Note that the thicker the insertion plate the greater the measured typical insertion force. For example, for the last four specimens, for which the viscosity was varied, the insertion plate widths were larger than those of the previous specimens. Hence, those experiments in which the adhesive viscosity was varied provide larger typical insertion force values than those predicted numerically.

Table 23: Insertion speeds, adhesive viscosities and insertion plate widths for the tested specimens in low insertion speed ISF experiments.

Specimen number	Insertions speed	Viscosity	Insertion plate width
[-]	[mm/min]	[weight-% EA 9395]	[mm]
1	5	100	5.10 – 5.17
2	5	100	5.10 – 5.13
3	5	100	5.09 – 5.15
4	2	100	5.09 – 5.12
5	2	100	5.09 – 5.12
6	2	100	5.08 – 5.16
7	10	100	5.08 – 5.09
8	10	100	5.09 – 5.12
9	5	85	5.14 – 5.20
10	5	85	5.12 – 5.18
11	5	70	5.14 – 5.19
12	5	70	5.13 – 5.18

To summarise, results for the insertion forces acting during ISF at low constant speed were presented. The parameters varied were the insertion speed and the viscosity of the adhesive. Good agreement was obtained between the experimentally measured and the numerically predicted typical insertion forces. Discrepancies between both are caused by differences between the numerical model and the conducted experiments.

5.3 Insertion Squeeze Flow at High Insertion Speeds

The results presented so far were for ISF processes conducted at low insertion speeds, while now results for an ISF process at insertion speeds typical of those expected in practice are presented. The insertion speeds investigated were 60 mm/min and 120 mm/min. This ensures that the process time for ISF remains around one minute or less. The insertion speed effect and the effect of adhesive viscosity on the insertion force were studied with the results presented in sub-Section 5.3.1. In sub-Section 5.3.2, a second output variable, the pressure on the Pi-slot walls during insertion, was evaluated, with the independent variables remaining as the insertion speed and the adhesive viscosity. Relationships between the insertion force and the pressure were established and are presented in sub-Section 5.3.3. The effect of using the two developed adhesive material models on both the insertion force and the Pi-slot wall pressure was analysed and is presented in sub-Section 5.3.4. This section concludes with the effect of the entire insertion speed range on the specific insertion force and Pi-slot wall pressure.

5.3.1 Results and discussion for insertion forces

Nominal dimensions and baseline process parameters remain the same as presented in Table 22 except for the insertion speed and adhesive viscosity. The baseline insertion speed was 60 mm/min and the baseline adhesive shear viscosity was 70 – 30 weight percent EA 9395 to EA 9396. In the figures these are the graph labels "100 – 0" or "70 – 30". To model the shear viscosity of the adhesive, the power law model derived in sub-Section 4.4.5 was used. In these simulations the insertion head shape was rectangular until the set of experiments in which the insertion head shape was varied is discussed (Section 5.4).

The output variable considered was the drag force that acts on the insertion plate. The drag force is referred to as the insertion force as it specifies the force necessary to push the insertion plate into the adhesive, which forces the adhesive to distribute in the flow channels. A typical transient insertion force curve is plotted below in Figure 5-14; the figure also includes illustrations of the flow fronts for specified times.
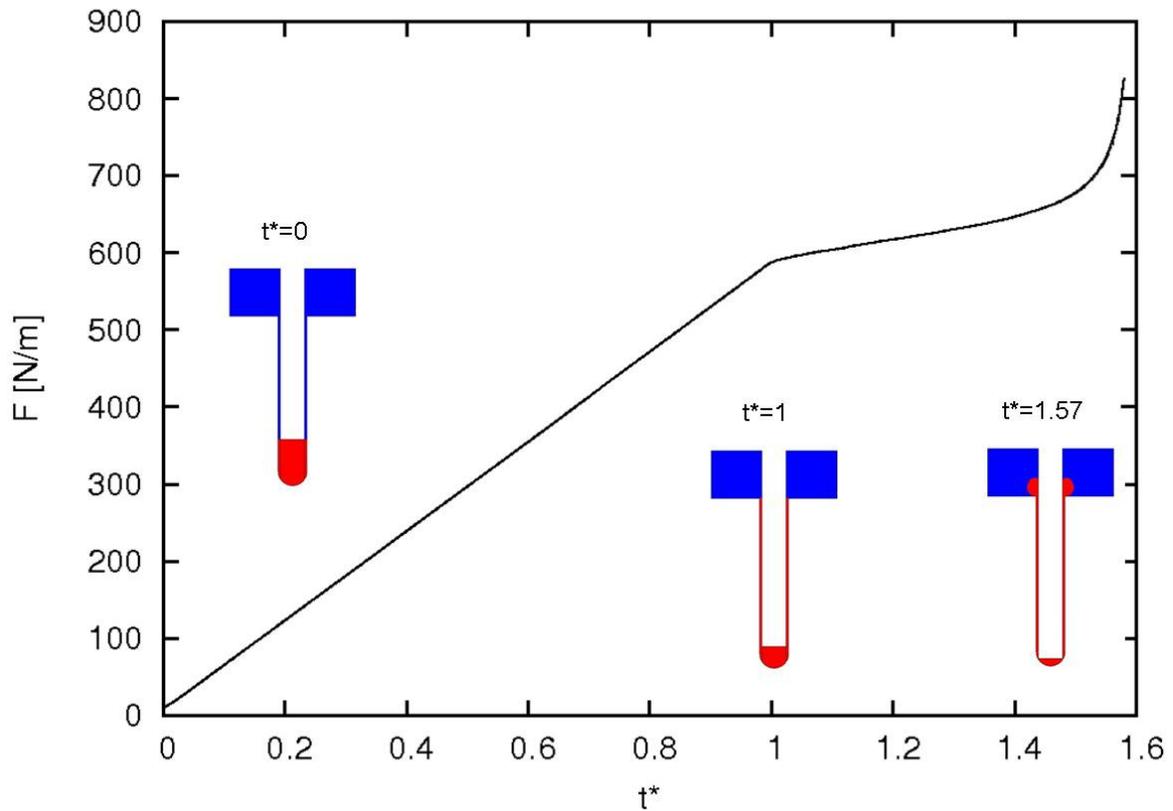
Figure 5-14: Predicted transient insertion force and images of specified flow fronts at three different times for baseline parameters.

The insertion force increases with dimensionless time. Initially, the adhesive which is coloured red in the images in Figure 5-14 is contained below the insertion plate (air is blue). The increase is linear until the flow channels are completely filled with adhesive ($t^* = 1$). As an excess amount of adhesive was placed within the Pi-slot initially, the insertion plate has not reached the bottom of the Pi-slot at that time and thus can continue to move downwards. From $t^* = 1$ onwards, the insertion force increases at a lower rate than the linear increase experienced between $t^* = 0$ and $t^* = 1$. At a dimensionless time of 1.57 the insertion plate touches the Pi-slot walls. Slightly earlier the insertion force increases significantly because the adhesive is being forced to squeeze through the narrowing gap between the approaching wall boundaries of the insertion plate head and the Pi-slot bottom. This increase is enhanced when the wall boundaries actually touch, at this point the simulation diverges. In practice the ISF process would terminate at a pre-defined position before the insertion plate and the Pi-slot touch. Thus, this divergence would not be seen critical.

Effects of insertion speed and shear viscosity on the transient insertion force were evaluated and these results are presented and discussed next. The insertion speed and the shear viscosities were varied from 60 to 120 mm/min and 70 − 30 to 100 − 0 weight-percent ratio of EA 9395 to EA 9396, respectively (Figure 5-15).
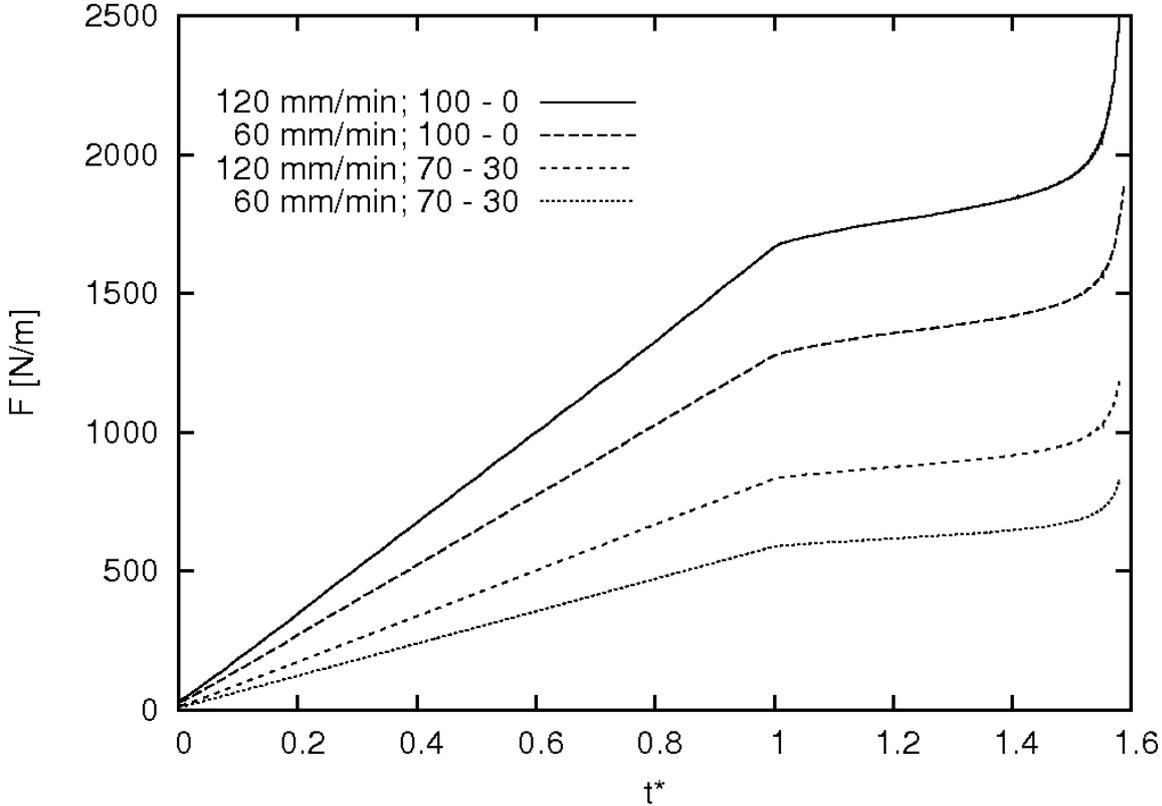
Figure 5-15: Predicted insertion forces versus dimensionless time for different insertion speeds and adhesive viscosities.

For all the plots a similar shape is observed to the one presented for the baseline parameters in Figure 5-14. The insertion force increases linearly before an increase at a lower rate is experienced. After about $t* = 1.4$ a more significant increase starts to appear. The physical explanation of these trends remains the same as those presented above for the baseline case. At $t* = 1$ for a shear viscosity according to $70 − 30$, the insertion force increases from 590 N/m for 60 mm/min to 835 N/m for 120 mm/min (increase of 44.1 %). For the same insertion speed increase but for the more viscous adhesive, the insertion force increases from 1280 N/m to 1670 N/m representing an increase of 30.5 %. This indicates that the insertion speed has a larger effect on the insertion force when using less viscous adhesives.

For a constant insertion speed of 60 mm/min, the insertion forces for 70 – 30 and 100 – 0 weight percent EA 9395 to EA 9396 are 590 N/m and 1280 N/m, an increase of 117 %. Similarly, comparing the insertion forces at a higher insertion speed level of 120 mm/min, there was an increase of 100 % (from 835 to 1670 N/m). This indicates that the insertion force can be significantly reduced by lowering the adhesive viscosity. Furthermore, this reduction has a higher impact for lower insertion speeds. This aspect is supported by the results obtained for lower insertion speeds, as reported in Section 5.2. The insertion force increases from 124 N/m to 389 N/m, an increase of 214 %, when the viscosity is changed from 70 – 30 weight percent EA 9395 to EA 9396 to 100 percent EA 9395 at an insertion speed of 5 mm/min.

Compared to the solutions derived for a Newtonian fluid in Section 5.1, the effect of the insertion speed on the insertion force is weaker for the non-Newtonian, shear thinning adhesives. There are two effects taking place simultaneously for a shear thinning adhesive when the insertion speed is increased: on the one hand, the insertion force is increased due to the increased insertion speed; on the other hand, the viscosity is decreased as the increased insertion speed increases the shear rate, which for a shear thinning material means a decrese in viscosity. The decrease in viscosity leads to a decrease in insertion force. Both effects together result in an increase of insertion force due to insertion speed, but at a lower rate than for Newtonian materials.

5.3.2 Results and discussion for the Pi-slot wall pressure

Another variable of interest in the development of ISF bonding processes is the pressure distribution on the Pi-slot walls. This is important as high pressures could distort or even damage the composite Pi-slots. A distortion of the Pi-slot walls would increase the flow channel width and this would affect the flow of the adhesive in the flow channels.

Figure 5-16 illustrates the pressure distribution along the Pi-slot wall for the baseline case at a process time shortly before the flow channels are filled completely ($t^* = 0.89$):
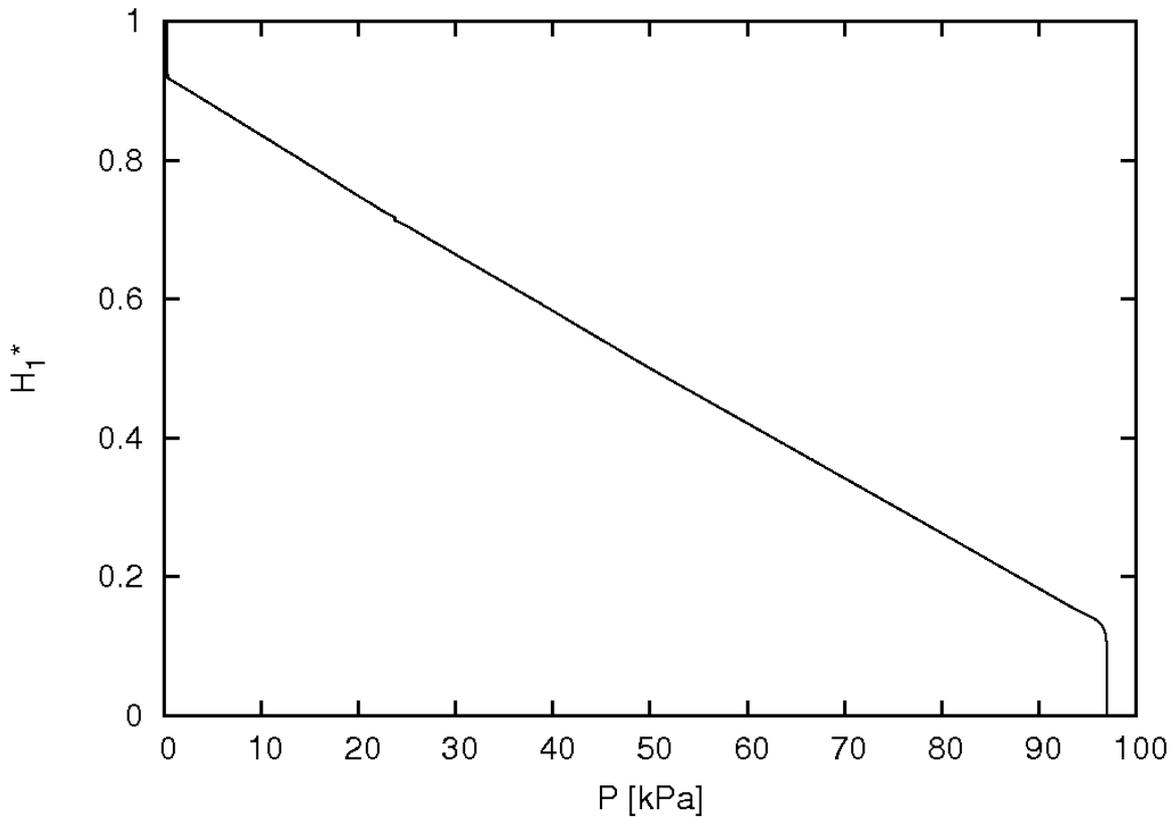
Figure 5-16: Pressure distribution along the Pi-slot wall boundary for baseline parameters at t*=0.89.

The *y*-axis represents the non-dimensionalised height of the Pi-slot wall, H_1*, a value of 0 is at the bottom of the Pi-slot and 1 at the top. The adhesive flow front at t*=0.89 is at a position of about H_1* = 0.91. At that position the absolute pressure is equal to ambient pressure and the gauge pressure is zero. From this position downwards there is a linear increase of pressure. The maximum is reached at H_1*=0.13, the position of the insertion head at that time. From this point down the pressure remains constant to the bottom of the Pi-slot. The maximum pressure is the output variable of interest for analysing the distortion or predicting the damage of the Pi-slots. Therefore the transient maximum pressure is predicted with respect to different input variable effects in the following discussion.

In Figure 5-17, the effect of insertion speed and shear viscosity of the adhesive on the transient maximum pressure is shown. The maximum pressure is plotted with respect to dimensionless time:
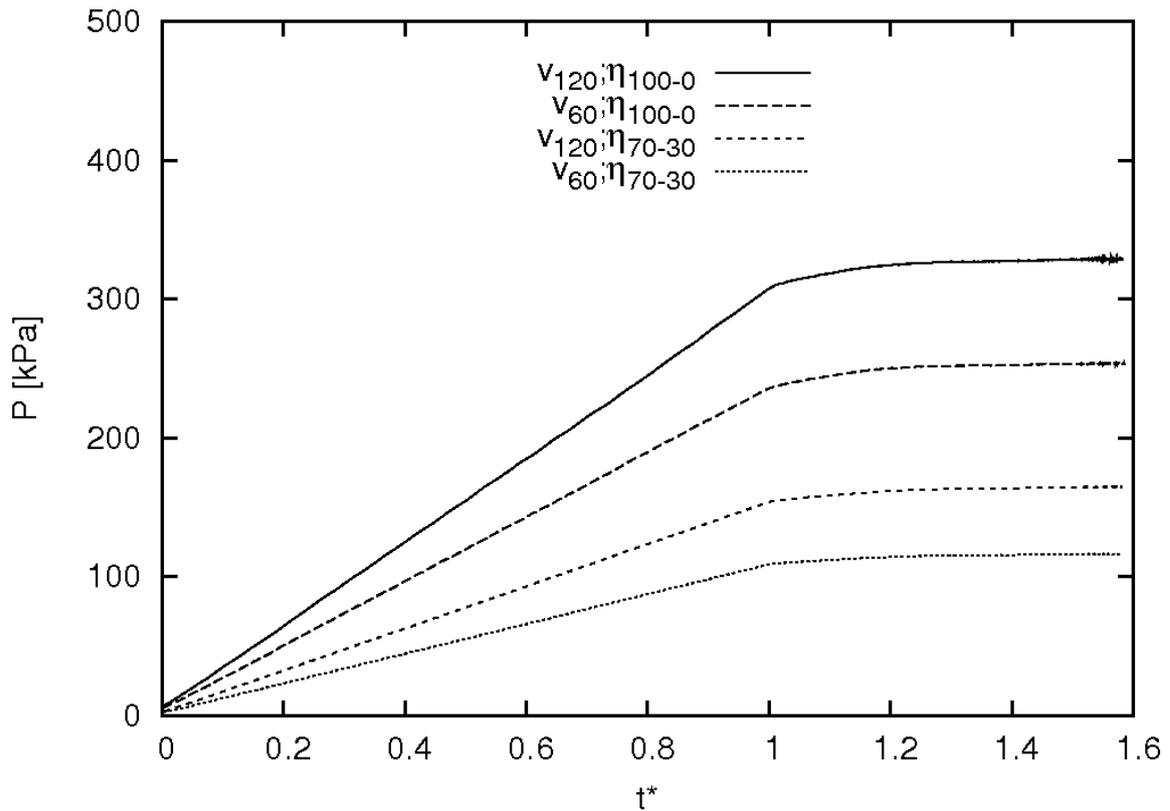
Figure 5-17: Effect of insertion speeds and adhesive shear viscosities on transient maximum Pi-slot wall pressure.

The pressure increases linearly with time until the adhesive reaches the top of the flow channels ($t^* = 1$). From that time onwards, the pressure increases at a low rate before reaching an asymptotic value at a dimensionless time of about 1.3. This shows that the flow channel width is the main parameter causing the pressure at the Pi-slot walls to increase with respect to time. Once the adhesive flows out of the flow channels, which means that the adhesive is not constrained by the flow channel width above the flow channels, the transient pressure remains approximately constant.

The effect of the insertion speed and the adhesive viscosity on the pressure is similar to their effect on the insertion force. The pressure increases with increasing insertion speed and with increasing adhesive viscosity.

The maximum pressures for the studies cases are considered at $t^* = 1$, taken from Figure 5-17. Increasing the insertion speed from 60 to 120 mm/min at a lower adhesive viscosity level (70 – 30) results in a pressure increase from 109 kPa to 154 kPa (increase of 41.3 %). For the higher viscous adhesives, an increase from 236 kPa to 308 kPa, which is an increase of 30.5 %, is noticed. This trend agrees well with what has been observed from

the insertion force data, that the insertion speed effect is greater for lower adhesive viscosities. An increase of insertion speed leads to an increase in pressure, however this effect is expected to be greater for a Newtonian material, as the viscosity would remain constant. For a shear thinning fluid, however, the viscosity would decrease with increasing insertion speed, as the shear rate would also be increased.

A similar trend is observed when comparing an increase of adhesive shear viscosities at different insertion speed levels. Increasing the shear viscosity at the lower insertion speed level (60 mm/min) results in a pressure increase of 117 % (from 109 kPa to 236 kPa). A pressure increase of 100 % (from 154 kPa to 308 kPa) is noticed for the higher insertion speed level. Again, the trend between the insertion speed and viscosity effect on pressure is similar to the one noticed for the insertion force. The higher the insertion speed level the less is the increase in pressure due to increasing adhesive viscosities. Here, the same explanation can be used as in the previous paragraph. At higher insertion speeds the effect of increasing the adhesive viscosity is smaller because the pressures are lower. The pressures are lower as the viscosities are lower due to higher shear rates that result from the higher insertion speed. This effect is more prevalent in materials that have a stronger shear thinning material characteristic, i.e. their viscosity dependence on the shear rate is stronger. This is the case for 100 – 0 EA 9395 and 70 – 30 EA 9395 to EA 9396, with the latter one being the less shear-thinning material.

5.3.3 Insertion force and Pi-slot wall pressure dependence

Due to the similar trends observed for both the insertion force and the Pi-slot wall pressure with respect to time, it was postulated that there could be a correlation between those two parameters. Hence, the maximum pressure on the Pi-slot walls was compared with the insertion force at $t^* = 1$ and $t^* = 1.54$ (Table 24). The dimensionless time of 1.54 was chosen as it is the time when the insertion plate head and the Pi-slot walls are 0.4 mm apart in the vertical direction. For the analysed ISF process setup this distance would represents a suitable position at which to terminate the motion of the insertion plate, due to the use of spacers to align the insertion plate within a required tolerance inside the Pi-slot. (A detailed discussion about the use of spacers is presented in sub-Section 6.4.1).

Table 24: Insertion force/maximum pressure – ratio for dimensionless times of 1 and 1.54 for different insertion speeds and adhesive shear viscosities.

$\eta_{Adhesive}$ [vol-% EA 9395]	v_{ins} [mm/min]					
70	60			120		
t*	F [N/m]	P [kPa]	F/P [10^3m]	F [N/m]	P [kPa]	F/P [10^3m]
1	590	109	5.41	835	154	5.42
1.54	711	116	6.13	1008	164	6.15
$\eta_{Adhesive}$ [vol-% EA 9395]	v_{ins} [mm/min]					
100	60			120		
t*	F [N/m]	P [kPa]	F/P [10^3m]	F [N/m]	P [kPa]	F/P [10^3m]
1	1280	236	5.42	1670	308	5.42
1.54	1541	253	6.09	2017	328	6.15

The ratio between the insertion force and the maximum pressure remains approximately constant with little dependence on the insertion speed and the shear viscosity within the studied ranges. At $t^* = 1$ the ratio is between 5.41 10^3m and 5.42 10^3m. Hence, the maximum pressure can be approximated if the insertion force is known independent of the insertion speed applied or the adhesive used for the ISF process. Further, knowing the maximum pressure gives an excellent approximation of all pressures acting along the Pi-slot walls, as the pressure decreases linearly towards the adhesive flow front position.

The insertion force/maximum pressure – ratio increases to a value between 6.09 10^3m and 6.15 10^3m for $t^* = 1.54$. The reason for the increase is due to the insertion force increasing slightly after the adhesive flows out of the Pi-slot. The pressure on the slot

walls, however, remains approximately constant as shown in Figure 5-17. The reason for the slight force increase seems likely to be caused by the increase in shear forces along the insertion plate walls due to an area increase as the insertion plate continues to move down, which would appear even after the adhesive flows out at the top of the Pi-slot. The pressure, however, is not affected by this increase. Therefore, the ratio between the insertion force and pressure has to increase after the adhesive flows out of the flow channels.

This finding is particularly important for the design of the composite Pi-slot. If the insertion force is known, the maximum pressure acting on the Pi-slot walls can be approximated. For the considered parameter range and assuming a spacer diameter of 0.4 mm, this pressure could be estimated by multiplying the insertion force by a factor of 6.15 10^3m. Having a method to predict the pressure is important because of the difficulty of measuring it experimentally.

To show how the dependence between the insertion force and Pi-slot wall pressure is affected by the process time, the force-pressure-ratio is plotted against dimensionless time in Figure 5-18 for simulations varying in the insertion speed and the adhesive viscosity.
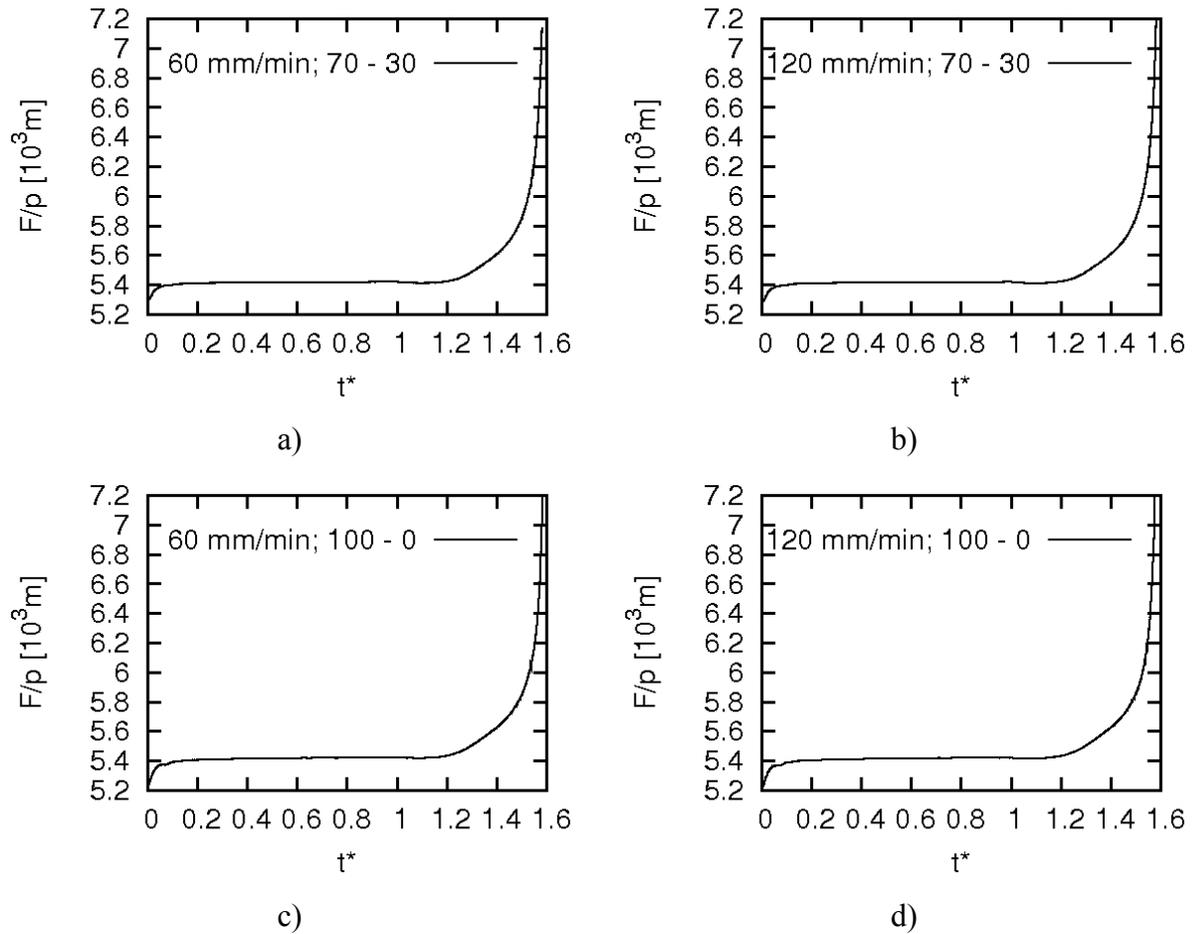
Figure 5-18: Effect of the insertion speed and the adhesive viscosity on the insertion force/maximum Pi-slot wall pressure – ratio with respect to dimensionless time.

The transient ratio initially shows an increase from about $5.3 \cdot 10^3$m to $5.4 \cdot 10^3$m because the shear forces do not contribute to the insertion force as they do after $t^* = 0.05$, when the velocity profile and hence velocity gradients within the flow channels have developed. The pressure, however, is not affected by this process. Until the flow channels are filled entirely, the ratio remains approximately constant. An increase can be observed after $t^* = 1.2$. The shear forces at the insertion plate lead to an increase in insertion force but not in pressure on the Pi-slot walls. The insertion terminates when the insertion plate can no longer move further down, this happens when the insertion plate head and the Pi-slot bottom boundaries become very close to each other, leading to a significant increase in the insertion force. The flow velocities within the narrow gap between the boundaries become very large, resulting in high pressures being required under the plate to overcome the resistance to the flow with a consequent rapid increase in insertion force. However, the pressure within the flow channels and hence the Pi-slot wall pressure hardly increases when this occurs as only a small amount of adhesive can still be squeezed through the

narrowing gaps between the insertion plate head and the Pi-slot bottom. This is the same as was shown for a different case in Figure 5-9.

Figure 5-18 can be used to estimate the maximum pressure at the Pi-slot walls for different process times if the insertion force is known. When designing an ISF process, the total process time would normally be known in advance as the necessary initial adhesive amount is known. Assuming there is a nominated intended stop of the insertion plate's motion, the maximum pressure at the Pi-slot walls at that time could be estimated.

Thus, the maximum pressure at the Pi-slot walls for perfectly aligned cases can be estimated for the entire ISF process. This is valid for the considered insertion speed range (60 – 120 mm/min) and adhesive viscosities (70 – 30 and 100 – 0 weight percent EA 9395 to EA 9396) for given insertion forces. However, based on the arguments presented here it is expected that the form of the relationship between the variables would also be more generally applicable.

5.3.4 Insertion force and Pi-slot wall pressure for different adhesive material models

As shown in Figure 4-23 on page 113 (sub-Section 4.4.5) the shear viscosity versus shear rate data can be more accurately represented by the five parameter rational model, especially at higher shear rates. Thus, the prediction of the insertion force with respect to time was predicted again applying this model. The resulting insertion forces were compared with those predicted using the power law model for an insertion speed of 60 mm/min and an adhesive viscosity of to 70 – 30 weight percent EA 9395 to EA 9396. Other input parameters were the standard set used above. The resulting insertion forces are plotted in Figure 5-19:
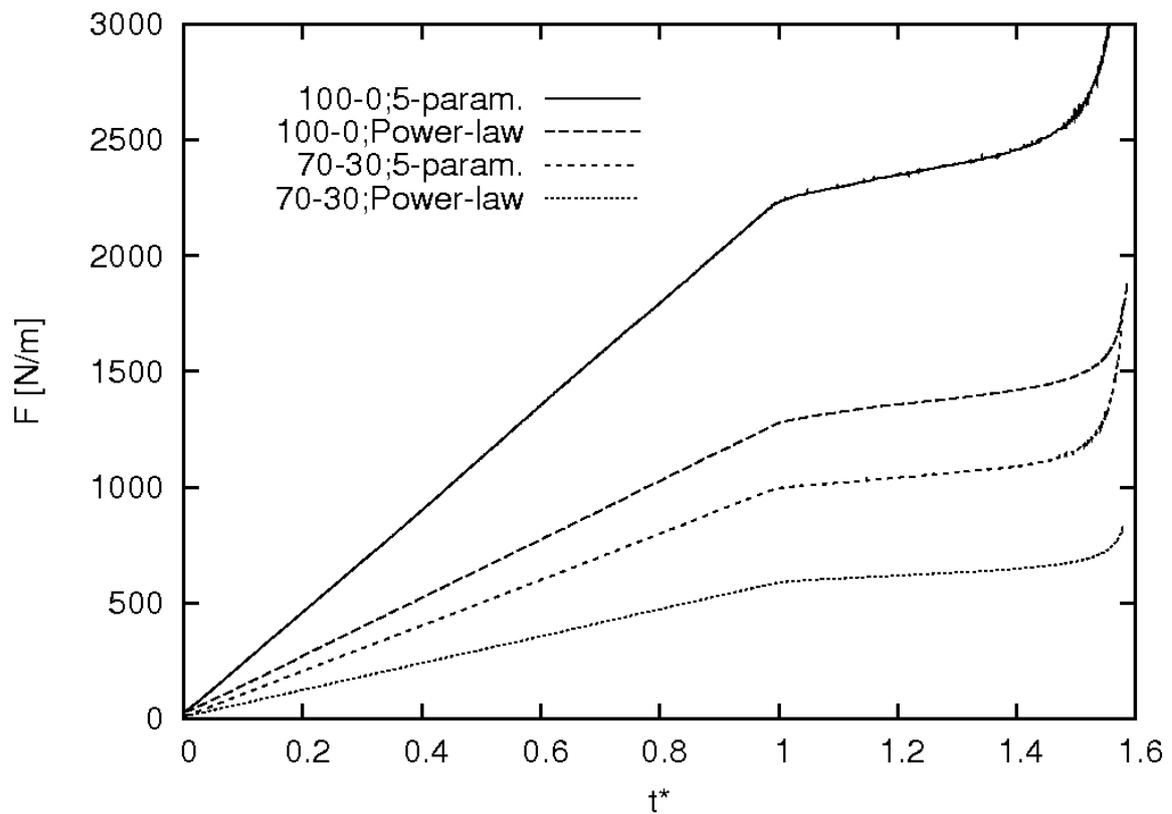
Figure 5-19: Effect of the adhesive material model on the predicted transient insertion force for two adhesive viscosities.

The plotted graphs have a similar shape to those previously seen. A linear insertion force increase is followed by an increase at a lower rate after the flow channels are filled entirely before a significant increase is noted when the insertion plate head approaches the Pi-slot boundary. However, the differences resulting from the different viscosity models are quite substantial, as is expected given that the Power law models provide a rough approximation of the measured viscosities.

The predictions were considered at $t^* = 1$. At the lower shear viscosity level of $70 - 30$, the insertion forces are predicted as 590 N/m and 993 N/m for the power law and the five parameter rational model, respectively. For the higher shear viscosity level $(100 - 0)$ the insertion forces are 1280 N/m and 2232 N/m for the power law and the five parameter rational model, respectively.

The reason for these differences can be explained with the different shear viscosities within the flow domain for the different adhesive models. The viscosity fields for a $70 - 30$ mix and an insertion speed of 120 mm/min at t* = 0.21 are illustrated for the power law and the 5 parameter rational model in Figure 5-20.
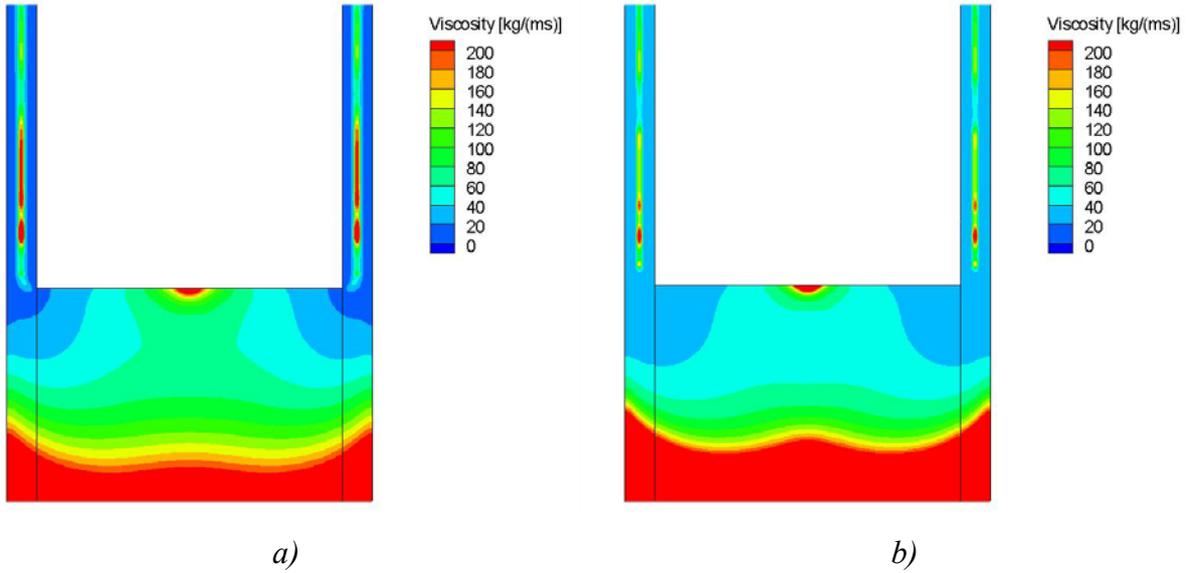
Figure 5-20: Shear viscosity field at an insertion speed of 120 mm/min at t* = 0.21 for a) the power law model and b) the five parameter rational model.

The measured shear viscosity with respect to shear rate as presented in sub-Section 4.4.2 is illustrated again in Figure 5-21.
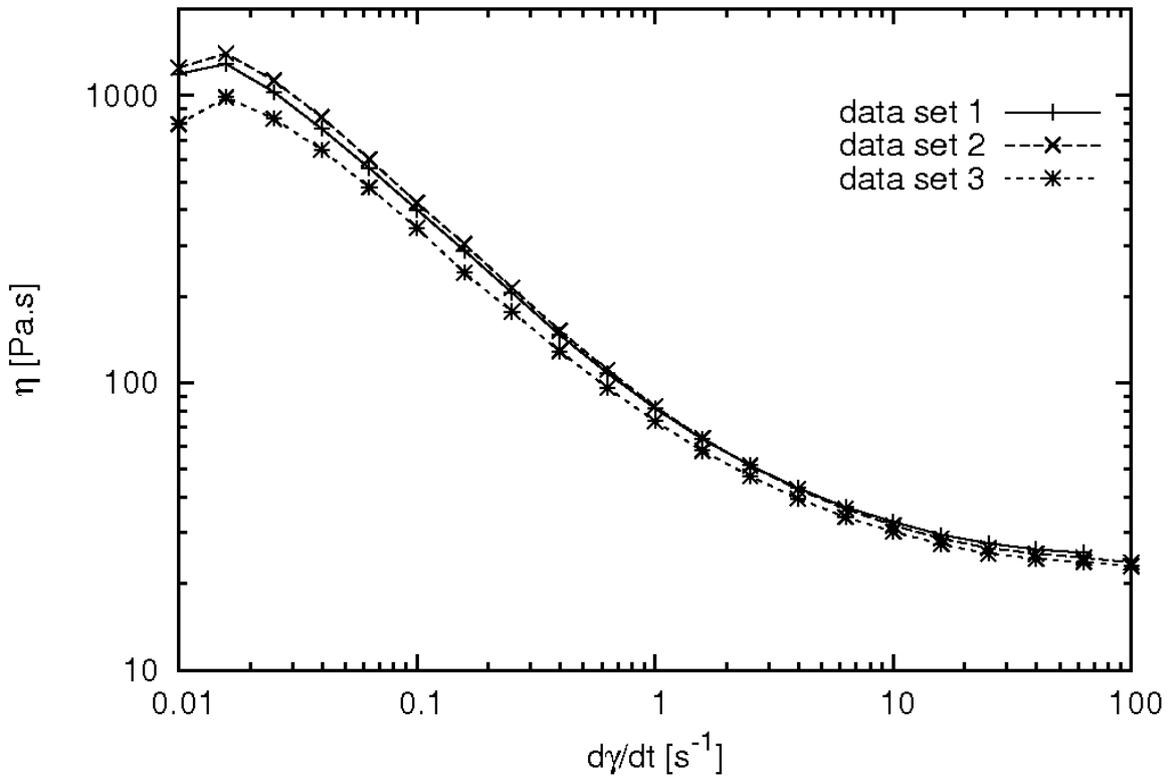
Figure 5-21: Measured adhesive viscosity with respect to shear rate for three samples of a 70 – 30 mix of EA 9395 to EA 9396.

At an insertion speed of 120 mm/min, which is high for the in this study considered insertion speed ranges, the shear rates are high, therefore it is important to consider the lower limits of the viscosity field, as the viscosity decreases with increasing shear rates.

The problems in using the power law model are evident in Figure 5-20, in which there are regions where the adhesive viscosity is between 0 and 20 kg m^{-1}s^{-1} in contrast with the measured adhesive viscosities in Figure 5-21, which shows no values below 20 kgm^{-1}s^{-1}. In contrast, the results of simulations using the five parameter model are consistent with the measured results across the full range of shear rates.

Due to the fact that the predictions at higher insertion speed were inaccurate when the Power law model was used for the adhesive, the maximum pressure was predicted at the Pi-slot walls again using the adhesive viscosities predicted by the five parameter model for $t^* = 1$ in Table 25.

Table 25: Maximum pressure at Pi-slot walls for five parameter rational adhesive viscosity models at t* = 1 for different adhesive viscosities and insertion speeds.

η_{adh} [weight-percent EA 9395 to EA 9396]		v_{ins} [mm/min]		P_{max} [kPa] at $t^* = 1$
70 – 30	100 – 0	60	120	
X		X		184
	X	X		513
X			X	348
	X		X	748

The physical effect of insertion speed and adhesive viscosity on the pressure is as discussed previously, Table 25 provides the quantitative values of using the five parameter rational model. To show that the insertion force – Pi-slot wall – pressure dependence which was derived is not affected by the adhesive material model, the force/maximum Pi-slot wall pressure-ratio is plotted with respect to dimensionless time for the 70 – 30 mix and 100 % EA 9395 in Figure 5-22.
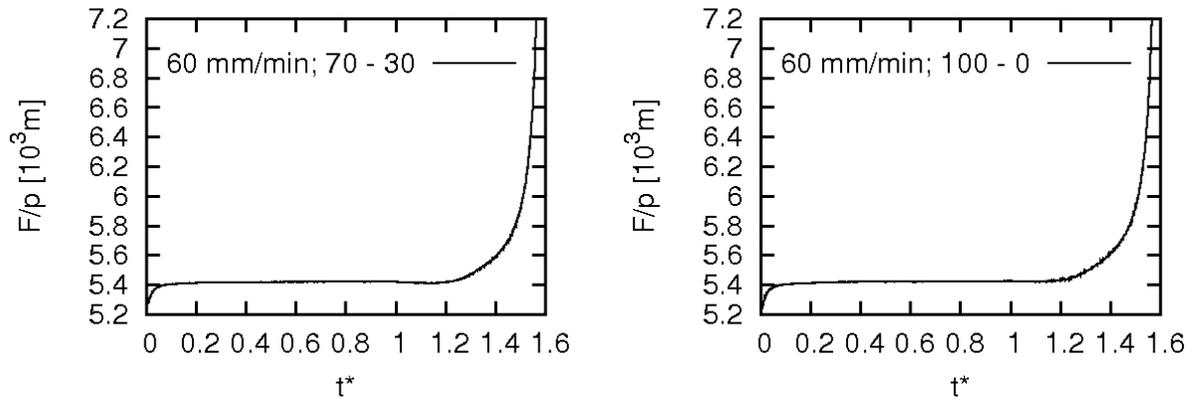
Figure 5-22: Effect of the adhesive viscosity (70-30 left, 100-0 right hand side) on the insertion force/maximum Pi-slot wall pressure – ratio with respect to dimensionless time, predicted applying the five parameter rational model.

The dependence between the insertion force and the maximum Pi-slot wall pressure presented in Figure 5-22 is identical to that presented in Figure 5-18. Hence, the maximum pressure and also the pressure distribution along the entire Pi-slot can be estimated if the insertion force is known, providing important information for the support of Pi-slot design for ISF processes.

As the effect of the adhesive material model on the output variables is quite significant quantatively, and in addition having shown that the five parameter model predicts the adhesive viscosity more accurately for high shear rates, from the following sub-Section 5.3.5 onwards, the predictions shown were obtained using the five parameter rational material model instead of the power law model.

5.3.5 Effect of insertion speed on specific insertion force and Pi-slot wall pressure

Here the effect of the insertion speed on the insertion force and the maximum pressure acting along the Pi-slot walls is examined for the entire insertion speed range considered. The adhesive viscosity (70 – 30 mixture) was represented by the five parameter rational model and the results presented are compared at one specific time ($t^*=1$). The specific insertion force and the maximum pressure along the Pi-slot wall are shown with respect to insertion speed in Figure 5-23:
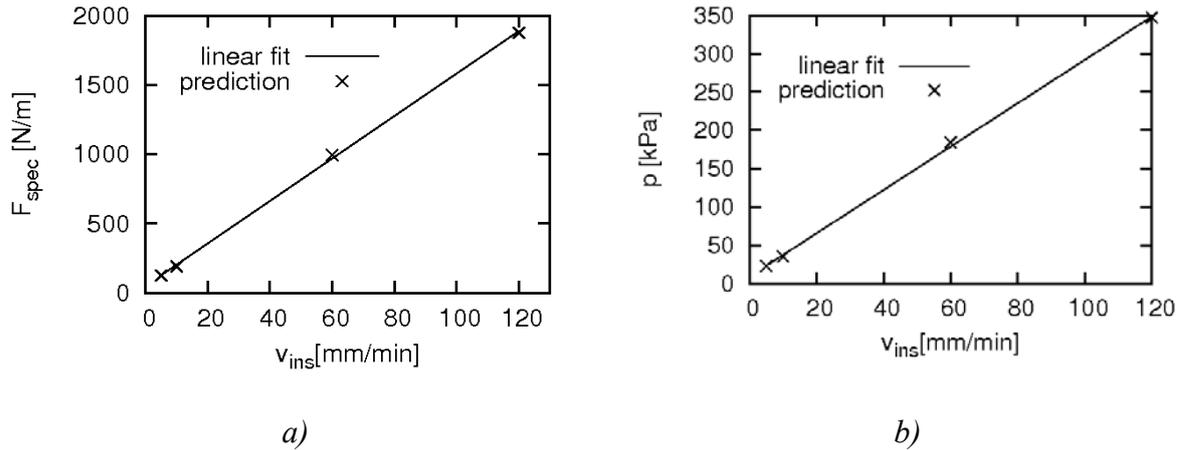
Figure 5-23: Insertion speed effect on a) specific insertion forces and b) maximum pressures on the Pi-slot walls at t* = 1 and a 70 – 30 adhesive mix.

A linear fit applied to the force and maximum pressure agrees well with the numerical predictions. The agreement between the linear fit and the values for the insertion forces is an over four values averaged 8.6 N according to the root square mean deviation (1.6 kPa for the pressure values). Hence, to predict the specific insertion force using a 70 – 30 weight-percent mixture of EA 9395 to EA 9396 a linear relation of the form

$$F_{spec} = 15.324 v_{ins} + 49.2 \text{ with } 5 < v_{ins} < 120 \text{ mm/min} \tag{5-9}$$

can be used and the maximum pressure can be predicted as

$$p_{max} = 2.827 v_{ins} + 9.076 \text{ with } 5 < v_{ins} < 120 \text{ mm/min.} \tag{5-10}$$

The linear relation between the maximum pressure and the insertion speed as shown in equation (5-10) results from the linear relation between the insertion force and the insertion speed as shown in equation (5-9). This is because the maximum pressure depends on the insertion force, which was presented in sub-sections 5.3.3 and 5.3.4. So the relation between the insertion force and the insertion speed is considered in more depth, as findings can also be applied to explain the dependence between the maximum pressure and the insertion speed.

The adhesive flow under consideration is a low *Re* flow (Re < 1). For these types of flow the drag force is expected to be a function of the velocity (Munson, 2006). The drag force on the insertion plate in the considered problem is the insertion force, consisting of viscous and pressure forces. Both are linearly related to the insertion speed, so it would be expected that the insertion force is a linear function of the insertion speed, which is the case, as seen from equation (5-9). The gradient in equation (5-9) results from the adhesive

viscosity and the dimensions of the insertion plate and the Pi-slot. The maximum pressure therefore is also linearly dependant on the insertion speed.

The linear fit is only valid where the insertion force is dependent on viscous and pressure forces arising from the insertion process, hence when the insertion plate is in motion. This was also applied in the force balance of the analytical model (Section 5.1). At initiation of the insertion process, non-linearities are likely to exist and hence equations (5-9) and (5-10) may not be valid. According to equation (5-9), an insertion speed of 0 does not result in an insertion force of 0, as is physically expected. More analysis would be needed to clarify events at very low insertion speeds. As the bonding process time is expected to be within seconds, however, insertion speeds in the range smaller than 60 mm/min are considered to be of minor importance. Given this requirement, a further analysis at very low insertion speeds, typically smaller than 2 mm/min, would be considered as unjustified.

It also is highly likely that at higher insertion speeds than those under consideration other forces become dominant and again non-linearities are expected.

5.4 Insertion Squeeze Flow at High Insertion Speeds with Different Insertion Head Shapes

In sub-Section 3.5.1 it was indicated that the insertion head shape was another parameter to be varied during this research. The term "insertion head shape" specifies the design of the bottom of the insertion plate that is inserted into the Pi-slot. The insertion head shape used up until this point was rectangular (Sections 5.1 to 5.3).

Three alternative insertion head shapes were analysed. Two of them were tapered, varying in the length of the taper and consequently in the taper angles, and one was rounded. These are illustrated in Figure 5-24 together with the studied rectangular shape:
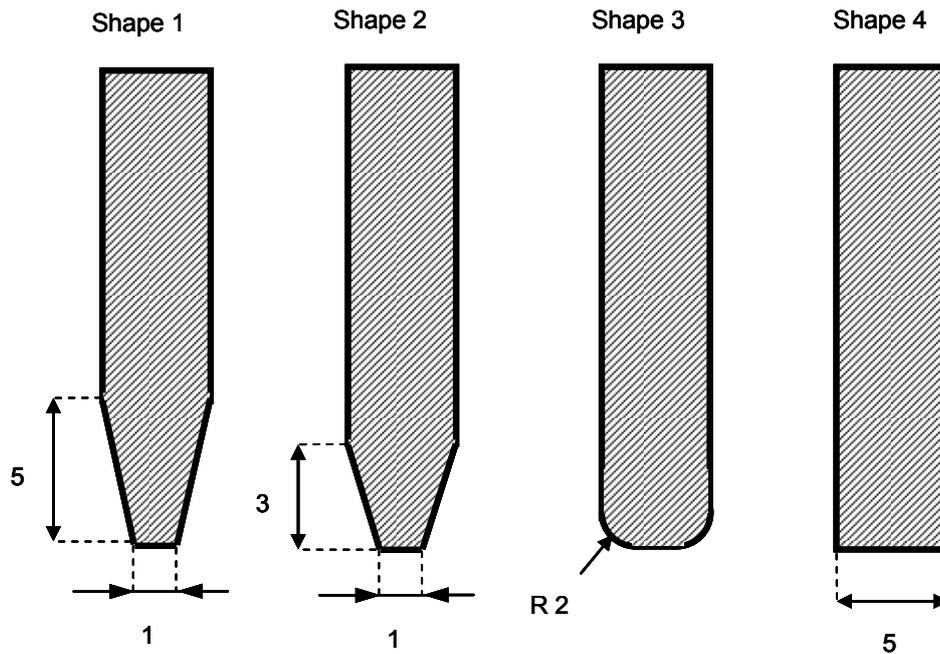
Figure 5-24: Insertion head shape variations.

Given that the mechanical effectiveness of the bonded joints is known to be influenced by the shape of the insertion head shape, the effect of different head shapes on the insertion forces and slot pressures were examined for the higher insertion velocity of 60 mm/min, which is more like the speed that would be used in practical applications.

The dimensions and process parameters were as presented in Table 22. The adhesive viscosity was a $70 - 30$ weight percent EA 9395 to EA 9396, modeled using the five parameter rational model. The adhesive was initially applied at 125 volume-percent, noting that this means the absolute volume varies for the different head shapes, which results in different initial adhesive heights.

In Figure 5-25 the insertion force is plotted with respect to time for the three alternative insertion head shapes and the already presented case when the insertion head shape is rectangular.
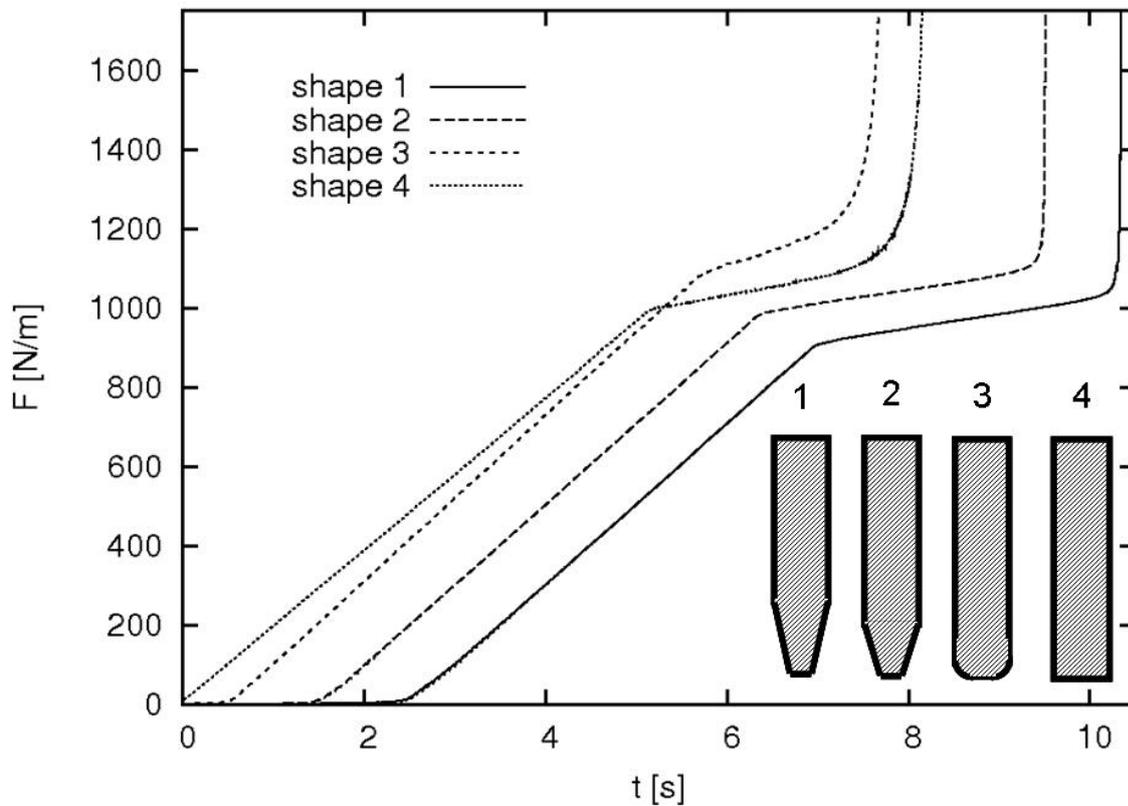
Figure 5-25: Predicted transient insertion force for different insertion head shapes.

The insertion force increases linearly for all cases until the flow channels are filled, and this is followed by an increase at a lower rate. When the insertion plate approaches the Pi-slot a significant increase occurs. This occurs earliest for shape 3, then for shape 4 and finally for shapes 2 and 1. These differences result from the differences in insertion head shapes and in the consequential different absolute initial adhesive amounts. For example in the case of shape 3 less adhesive is necessary because the insertion plate and the Pi-slot can approach each other more closely compared to the other cases where more "free volume" remains in the final bonding position.

From Figure 5-25, it can also be seen that it is only for shape 4 that the insertion force starts increasing immediately. For all other cases a delay is observed. This delay can be explained by illustrating the initial adhesive distribution within the flow channels as shown in Figure 5-26, which also indicates the differences in the initial adhesive amount.
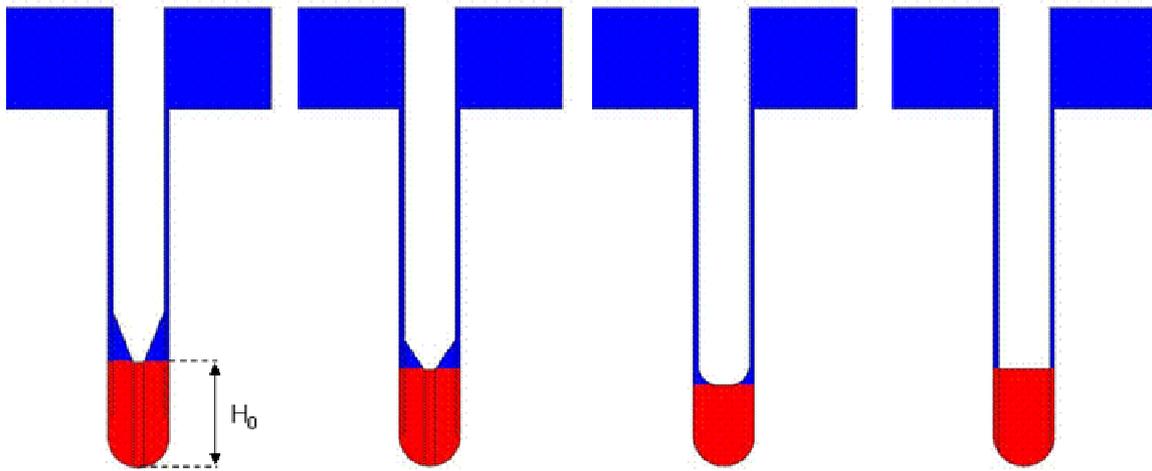
Figure 5-26: Initial adhesive distribution for the four investigated head shapes. Adhesive is represented by the red colour, air is blue.

It can be seen that different parts of the insertion plate are in contact with the adhesive. For the two tapered shapes only the flat bottom touches the adhesive initially. The adhesive does not start to flow into the flow channels until the area between the tapered head and the Pi-slots is filled. When this area is filled with adhesive, the insertion force begins to increase. Thus the delay observed in Figure 5-25 is characterised as the time to fill the area between the tapered walls of the insertion plate and the Pi-slot walls. Similarly, for the rounded case a delay is observed that is smaller than the one for the tapered heads. The delay is caused by the filling of the area between the rounded parts of the insertion plate and the Pi-slot. As this area is smaller than the area for the tapered insertion plates the filling time and thus the delay is shorter. No delay is observed for the rectangular shape as the adhesive flows into the flow channels directly.

The graph shows that the rounded shape (shape 3) results in the highest insertion forces. This is due to the fact that in case of shape 3 the insertion plate can descend further than shape 4 and as a result the insertion plate and the Pi-slot would touch later. The lowest insertion forces occur for the longer tapered head shape (shape 1). The main reason for this is that the pressure that acts within the Pi-slot bottom is smaller compared to the rounded or rectangular shape. The comparable pressure is smaller for the tapered shape as more space is provided between the insertion plate head and the Pi-slot bottom. Thus the pressure force component of the drag force is smaller resulting in the lowest total insertion force observed.

For the maximum pressure at the Pi-slot wall variation with flow time, the different insertion head shapes have similar effects to those observed for the transient insertion forces. This can be seen in Figure 5-27.
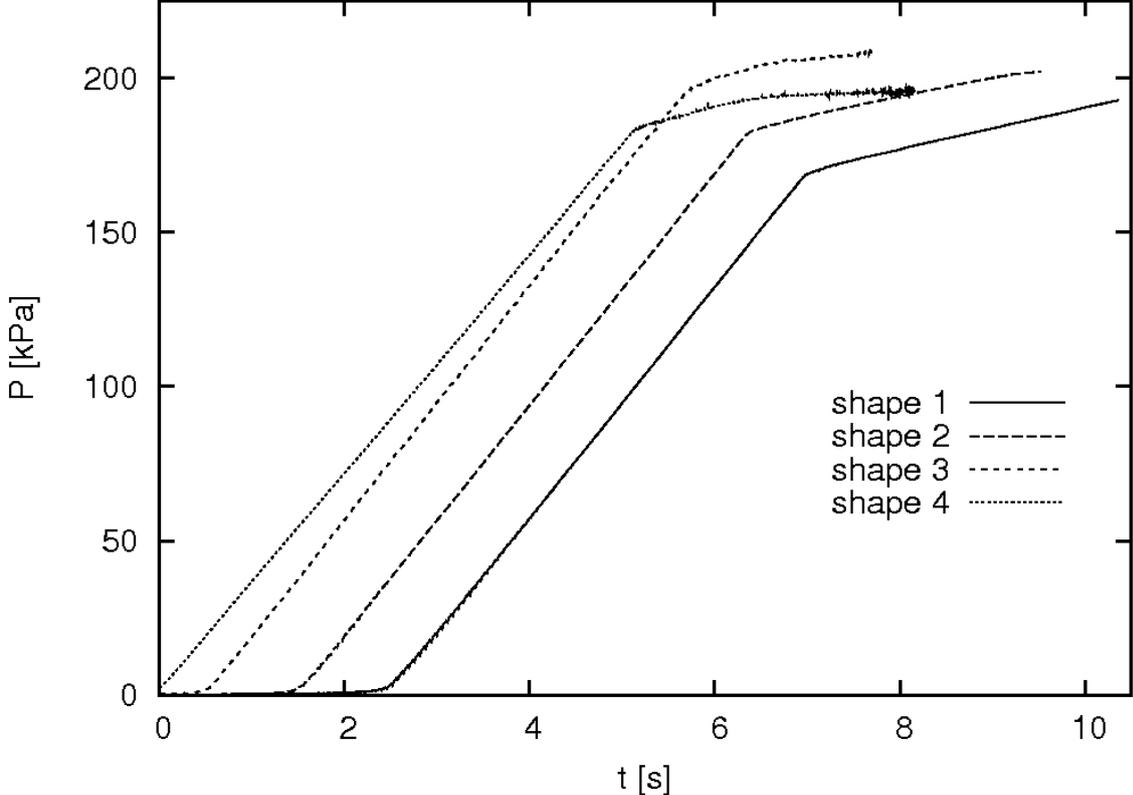
Figure 5-27: Transient maximum pressure along the Pi-slot wall with respect to different insertion head shapes.

Figure 5-27 presents the transient local maximum pressure value along the Pi-slot. The local maximum pressure can be found as presented in Figure 5-16 on page 138 at the edge of the Pi-slot wall. The maximum pressure increases roughly linearly with time. When the adhesive reaches the top of the flow channels the transient pressure increases at a lower rate as the resistance towards flowing of the adhesive through the flow channel widths disappears above the top of the Pi-slots.

The highest pressures acting along the Pi-slot walls are detected for the same case as the highest drag coefficients, this is for shape 3. As the insertion plate can move down further than the rectangular plate and also provides less space compared to the two tapered heads, the pressure within the Pi-slot is considerably larger. As found for the insertion force and for the same reasons, the lowest pressures are detected due to the reasons described for the insertion forces for shape 1.

Finally, the dependence between the insertion force and the Pi-slot wall pressure was evaluated and is presented. Dividing the insertion force by the maximum Pi-slot wall pressure results in the following factor for the investigated head shapes if the adhesive flow front is within the 0.5 mm wide region of the flow channel:

- Shape 1: 5.35 10^3m;
- Shape 2: 5.38 10^3m;
- Shape 3: 5.50 10^3m;
- Shape 4: 5.41 10^3m.

Again, if the insertion force is known the maximum pressure can be approximated, providing a useful approach for the design of Pi-slot components to be used for ISF.

5.5 Experimental Study of ISF at High Insertion Speeds

The experimental approach used was as described in Chapter 3.6. The insertion force at constant insertion speed was measured with respect to time on a 10 kN Instron universal testing rig. Test specimen length in the longitudinal direction (*z*-direction) were 282 mm and 283 mm for the insertion plates and the Pi-slots, respectively, with all other dimensions being according to baseline parameters. The insertion plate head shapes were rounded (*R*=2.5 mm) and tapered (2 mm vertical, 5 mm horizontal), according to Figure 5-24, and two measurements per head type were conducted. To connect the insertion plate to the cross head of the test rig, the insertion plate was clamped to a rigid steel angle. The other end of the steel angle was clamped to the cross head of the testing machine. This can be seen in Figure 5-28, where the experimental test set up is illustrated; the same image is shown in Figure 3-14.
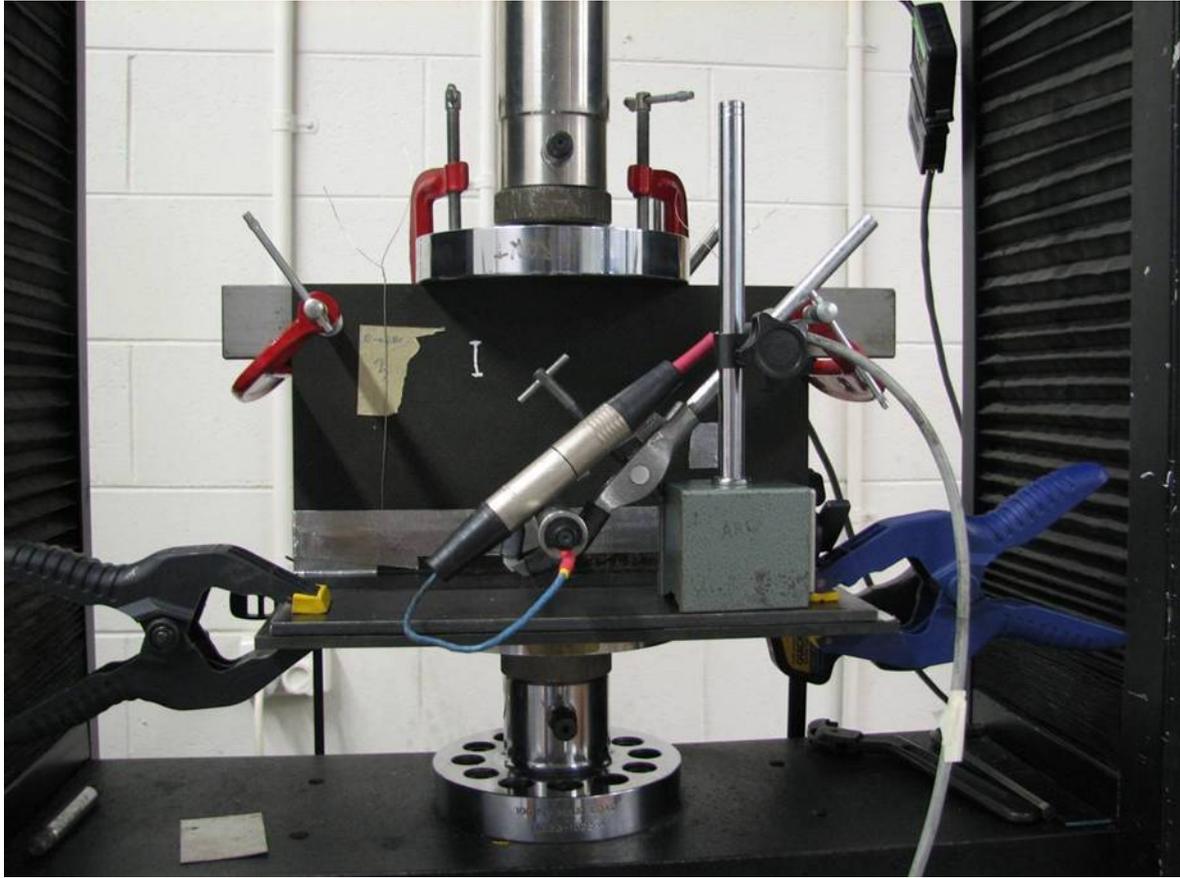
Figure 5-28: Test setup for the second set of experiments to measure the insertion force during an ISF bonding process.

For three of the experiments two wires were used to ensure that good alignment was maintained between the insertion plate and the Pi-slot. For the last experiment, the number of wires was increased to three.

The insertion force was plotted with respect to time for the experiments for the rounded and tapered insertion plate heads in Figure 5-29. The measurements were conducted at an insertion speed of 60 mm/min and an adhesive mixing ratio of 70 – 30 EA 9395 to EA 9396. Also shown in Figure 5-29 are the numerical results for the rounded and the short tapered insertion head for a total flow channel width of 1 mm.
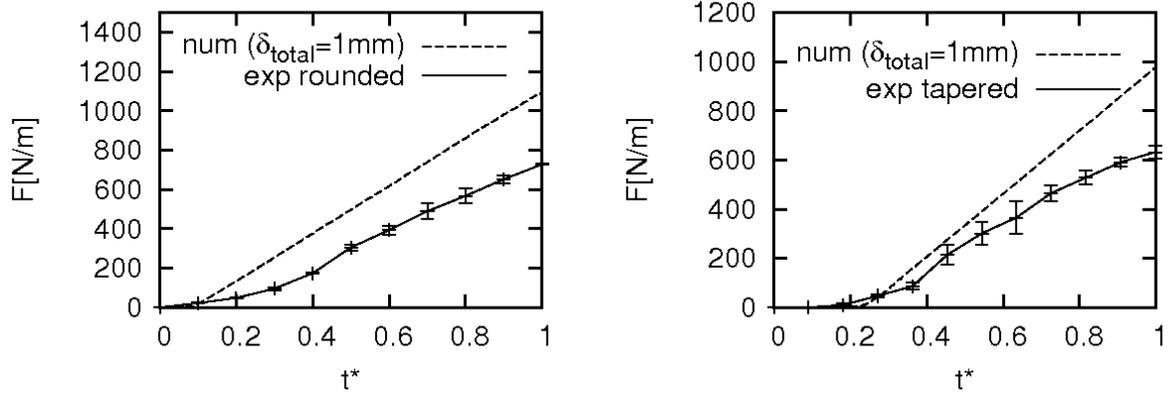
Figure 5-29: Measured insertion forces plotted against dimensionless time for the rounded and the tapered insertion plate heads in comparison to numerical results for the same cases with a total flow channel width of 1 mm.

Before analysing the differences between the numerically predicted and the experimentally measured insertion forces, the general shape of the insertion force is discussed, followed by a discussion of discrepancies detected between two experiments for the same set, as indicated by the error bars. After this analysis, a comparison between the numerical results and the experiments is made.

Two insertion force regions are noticed for both insertion heads: in the very beginning, the measured and predicted insertion forces are only slightly above zero, which is when the insertion plate heads touches the adhesive. The little force detected results from the filling of the area around the insertion plate radius and the tapered ends of the insertion plate, respectively, with adhesive, before the adhesive is displaced into the flow channels (0 − 0.2 s). In the experiments, this increase might also correspond to the compaction of the initially uneven adhesive surface. The second region shows an insertion force increase at a higher rate until the adhesive eventually flows out of the flow channels at $t^* = 1$, which was not achieved for all of the experiments.

From observations of the previous set of experiments as well as of numerical results for insertion forces at constant insertion speed a plateau-like region would be expected to occur before a final significant increase indicates the touch between the insertion plate and the Pi-slot. However, this is not observed here. Analysis of the specimens indicated that the adhesive in some cases did not fill both flow channels entirely. For the experiments in which two spacers were used, the adhesive flowed out in the middle on one side and at the ends on the other side of the insertion plate. This adhesive distribution implies a bending of the insertion plate. A possible explanation is that the clamping of the insertion plate to the

steel angle imposes an angular misalignment. Due to the spacers that are wrapped around the head of the insertion plate, the angular misalignment might lead to a bending around the spacers – a similar bending effect as experienced during a three point bending test. Calculations of the loads necessary to bend the insertion plate show that a loading of less than 10 N/m would be sufficient to bend the insertion plate (sub-section 6.4.2). This possible explanation was supported by two further observations; first, the adhesive distribution is the same for all three experiments conducted with two spacers, being that the insertion plate side where the adhesive flows out at the ends faces the angle. Second, the adhesive is distributed evenly along the joint for the last conducted experiment when three wires were used. The Pi-joint bonded with three spacers is shown in Figure 5-30.
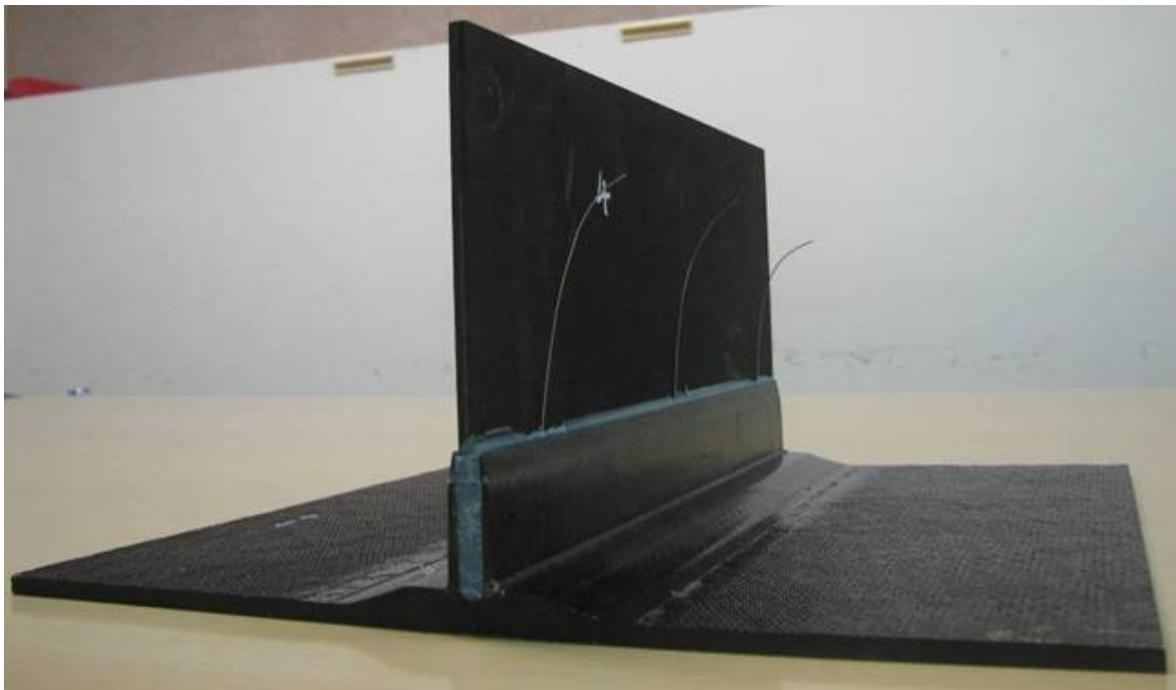
Figure 5-30: A Pi-joint after bonded applying the ISF process at constant speed; three spacers were used to align the insertion plate in the Pi-slot.

Considering Figure 5-29 again, possible explanations are given for the differences between the two conducted experiments, as indicated by the error bars:

- Variation of joint dimensions may lead to differences in flow channel widths,
- weighing of four different components of the adhesive can lead to different adhesive viscosities, calculated as 0.545 % by uncertainty analysis (Holman, 1994)
- due to manual mixing a proper distribution of the components cannot be guaranteed,

−   different amounts of different adhesive components may remain in the mixing devices leading to different adhesive viscosities.

The last two uncertainties cannot be estimated, but they are expected to be within a similar range for each experiment because same procedures were applied for every experiment.

The width of the flow channels is the parameter that mainly would affect the insertion forces. More discussion on the point that the flow channel width is the main cause for discrepancies is provided in the following comparison between the numerical and experimental results.

Comparing the insertion forces at $t^* = 1$, these were found to be an average of 732 N/m for the rounded insertion head from the experiments, but 1044 N/m from numerical predictions. For the tapered insertion head (shape 2) the measured insertion force at $t^* = 1$ was 621 N/m, while the numerically predicted one was 985 N/m. This is a difference of 30 % for the rounded and of 37 % for the tapered head.

The total flow channel width for the rounded insertion plate varied between 1.07 mm and 1.38 mm, whereas the one for the tapered insertion plate head resulted in a variation between 0.92 mm and 1.42 mm. As mentioned above, this was suspected to be the main reason for the differences experienced between the numerical and experimental results. Hence, two more numerical simulations were setup matching the smallest and the largest resulting flow channel widths. The insertion plate widths and the Pi-slot widths were setup according to those used for the most extreme cases appearing in the experiments, so that the insertion plate width for the first simulation was 5.14 mm and the Pi-slot width was 6.06 mm, and for the second simulation these were 4.85 mm and 6.27 mm. The simulations were conducted for the tapered insertion head. The results are shown in Figure 5-31:
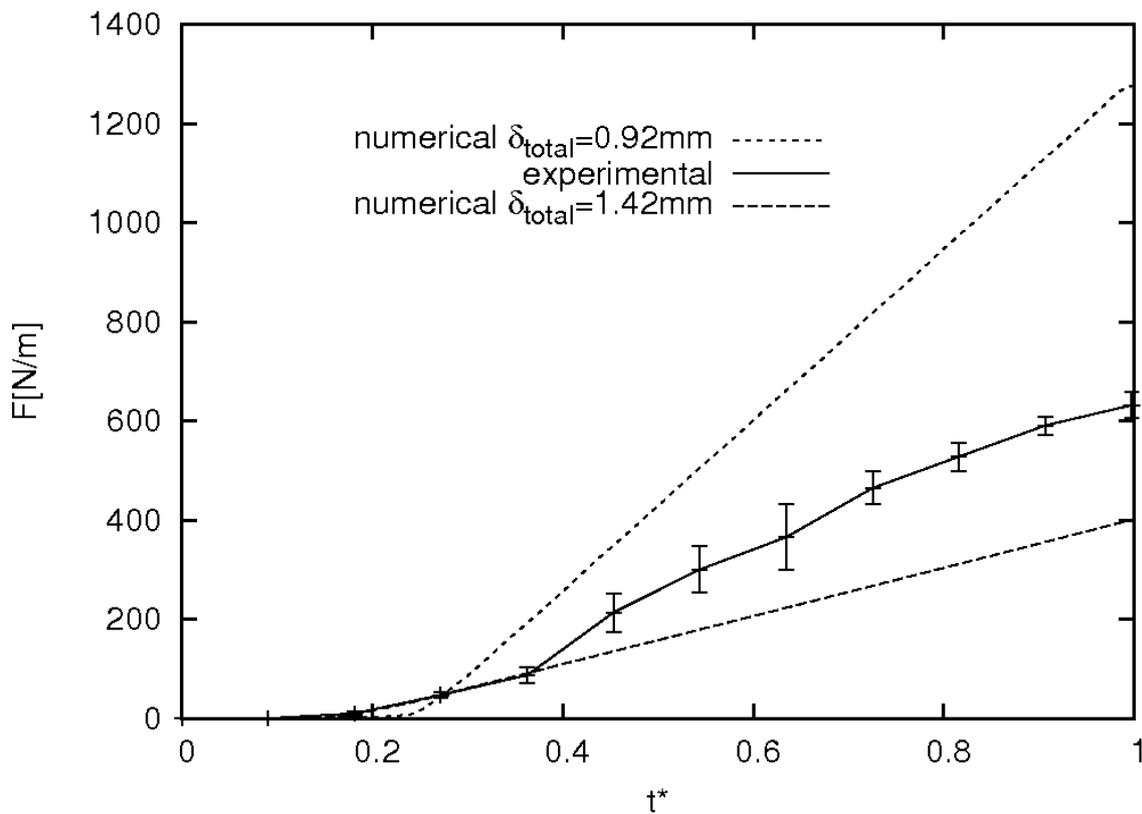
Figure 5-31: Numerically predicted insertion forces for a narrow and a wide total flow channel width compared to experimentally measured insertion forces, plotted with respect to dimensionless time for the tapered insertion head shape.

It was found that the numerical predictions of the insertion force for the widest and for the narrowest flow channel width derived from the experiments envelope the insertion force measurements. This shows that the numerical and the experimental insertion forces do not contradict. Hence, the differences experienced and shown in Figure 5-29 clearly result from the different dimensions used for the experiments and the numerics.

For the rounded design, this strongly suggests that the discrepancies experienced are also caused by the different flow channel widths for the experiments and numerical simulations. The flow channel widths in those experiments were larger than 1 mm, varying between 1.07 mm and 1.38 mm, thus being expected to predict lower insertion forces than those predicted when the flow channel width is 1 mm.

The conclusions obtained from the above presented experiments are as follows:

- The test rig concept should be designed to guarantee a symmetrical loading of the insertion plate so that bending of the bonding partners is circumvented which in general may occur at low loadings;

– the adhesive amount applied initially should be at least 50 weight-percent in excess of the necessary amount if the insertion head shape is rounded; this becomes even more important when the accuracy of the component's dimensions are unknown; the usage of optical measurement devices is suggested, and this would also support the selection of spacer diameters;

– from the conducted experiments it appears that three spacers or more along a 280 mm long joint are necessary to ensure the desired adhesive distribution; however it is believed that the test rig setup had inadequacies that led to the unequal distribution so that the number of spacers most likely can be reduced if the test rig concept enables a symmetrical loading of the insertion plate during clamping;

To sum up, there was a discrepancy of about 30 % detected between the measured and predicted insertion forces, which was shown to be due to different flow channel widths, and numerical predictions from two further simulations did not contradict the insertion forces measured. It was difficult to conduct experiments that agree entirely with the numerical setup so that results can be used to conduct correct comparisons.

5.6 Summary

In this chapter analytical and numerical predictions for insertion forces and velocity distributions within the flow channels were compared for a Newtonian ISF process and showed good agreement. Insertion force predictions also agreed well with experimental results obtained for ISF conducted at low insertion speed. A further output variable that was predicted by the numerical model is the pressure distribution along the Pi-slot walls, which is maximum at the root of the Pi-slot. How this pressure varies with the insertion force was also found and specifed. The insertion force and the maximum Pi-slot wall pressure were found to vary linearly with the insertion speed. Experiments were also conducted at high insertion speeds with the insertion force being measured. Discrepancies between the experimentally measured insertion forces and the numerically predicted insertion forces were found and attributed to differences between the setups, which were different in terms of flow channels width. Insertion force predictions for the widest and smallest flow channel width did not contradict with experimental insertion forces. Suggestions were provided for the conduction of an ISF process in practice.

6 Insertion Squeeze Flow considering Lateral Misalignment

In Chapter 6 the dimensional variations that are possible during ISF, and which consequently affect adhesive flow, are introduced in Section 6.1. Causes of lateral misalignments are presented in Section 6.2. Lateral misalignment effects on the adhesive flow are evaluated numerically in Section 6.3. Procedures are then proposed to estimate a minimum necessary initial adhesive amount to ensure complete flow channel filling, with reasons for asymmetrical flow during ISF being discussed. Chapter 6 concludes with an estimation of the number of spacers that should be used to ensure minimum flow channel widths during insertion.

6.1 Possible Misalignments during Insertion

Misalignments that might occur during ISF are illustrated in Figure 6-1:
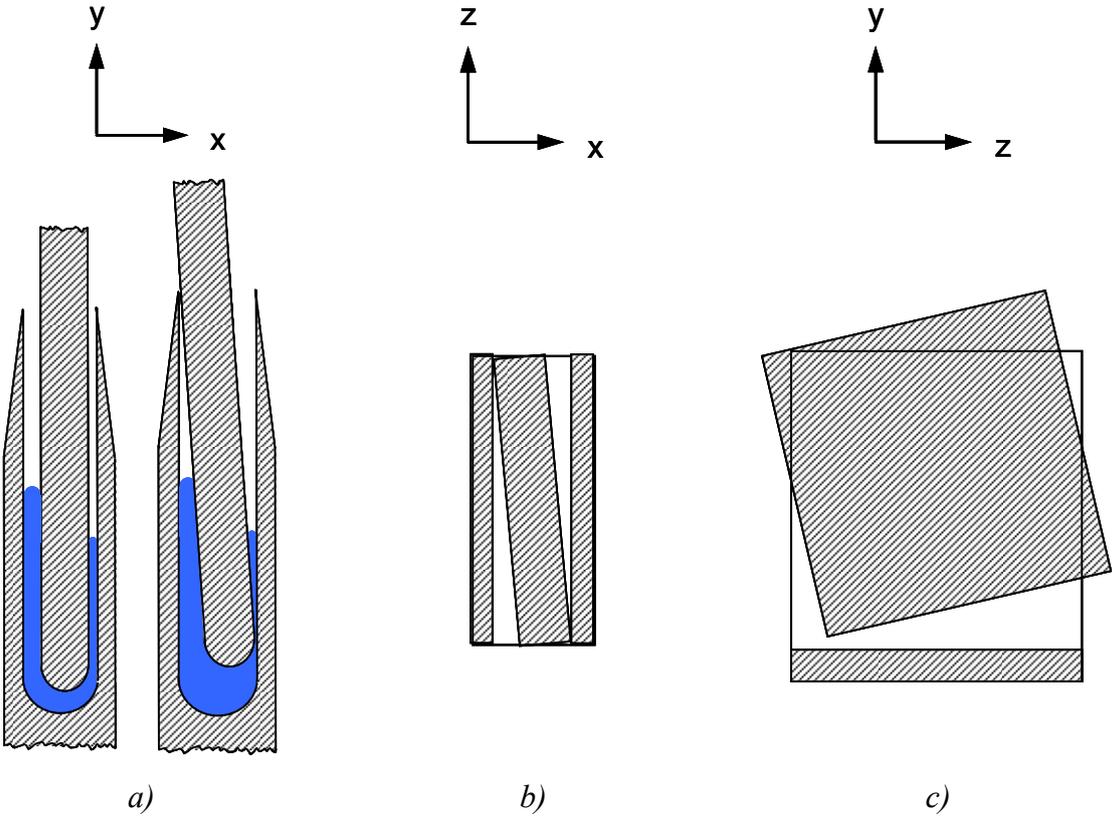
Figure 6-1: Possible misalignments that can occur during ISF: a) Lateral (x-axis) and angular misalignment around z-axis; b) Angular misalignment around y-axis; c) Angular misalignment around x-axis.

Misalignments can be either angular or lateral. The two flow channels are affected by lateral misalignment relative to the *x*-axis and by angular misalignment around the *y*-axis and *z*-axis (Figure 6-1 a) and b)). Angular misalignment around the *x*-axis (Figure 6-1 c)), however, would not necessarily affect the flow channel width, but might cause significant adhesive flow in the *z*-direction.

Lateral misalignment is expected to be the most common dimensional variation and hence is discussed in depth in the following Sections 6.2 and 6.3.

6.2 Causes of Lateral Misalignment

The nominal dimensions of a Pi-slot cross section typically used for ISF are presented in Figure 6-2:
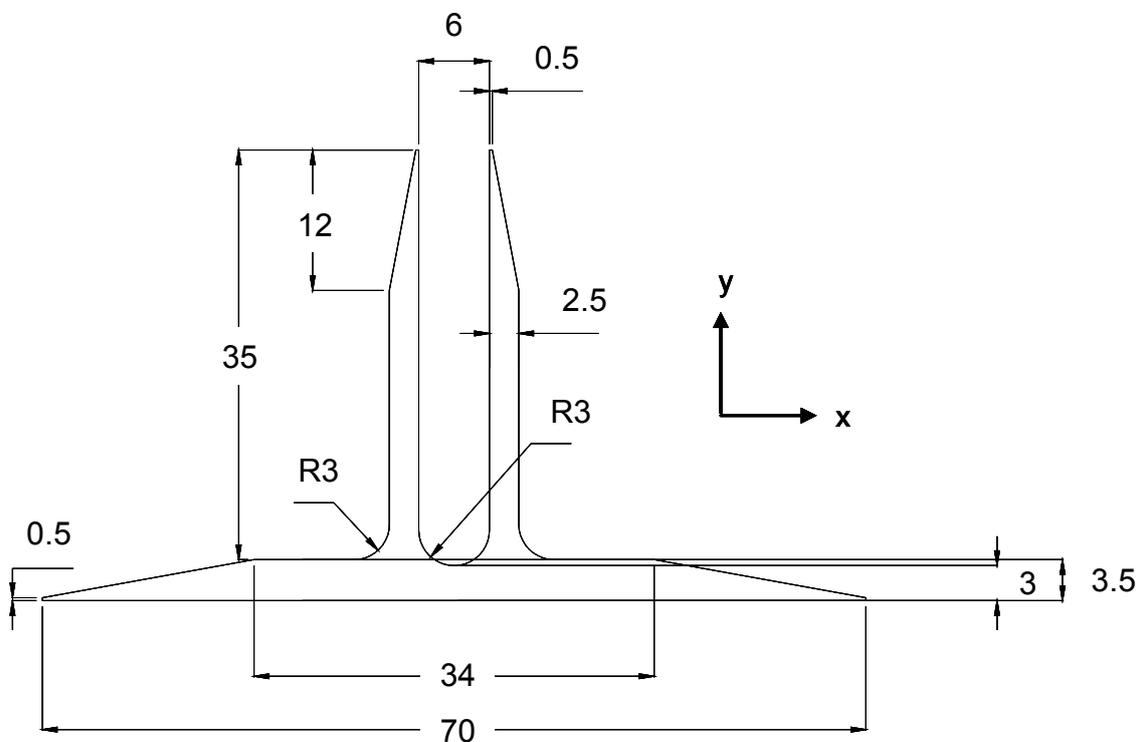
Figure 6-2: Key dimensions that define the Pi-slot structure and that are specified in the MoJo project (MoJo, 2007).

Of particular interest for the analysis of ISF bonding is the Pi-slot height (35.5 mm), which is referred to as H_1 throughout the studies, and the Pi-slot width (6.0 mm), also referred to as $2b$. The counter part to be bonded with the Pi-slot is the insertion plate. Its nominal width ($2a$) is 5.0 mm. When the insertion plate is aligned exactly symmetrically between the Pi-slot walls, the resulting flow channel widths (δ) on both sides of the insertion plate are equal and 0.5 mm.

However, in practice a number of issues have lead to dimensional variations in Pi-joints. These dimensional variations are caused by

- manufacturing tolerances of the composite components,
- process induced distortions during ISF and
- misalignments between the composite bonding partners during insertion of the insertion plate.

All of these lead to flow channel width variations and consequently affect the adhesive flow during ISF. As the quality of a Pi-joint is significantly influenced by the bondlines, an improper adhesive distribution would have a significant impact on the Pi-joint quality.

6.2.1 Manufacturing tolerances

In Mojo (2007), various dimensional tolerances of composite laminates have been defined. Table 26 lists those that are relevant for the current study:

Table 26: Manufacturing tolerances as specified in the Mojo project (MoJo, 2007) and the resulting flow channel widths.

Feature	Nominal length [mm]	Minimum tolerance [mm]	Maximum tolerance [mm]	Expected range [mm]
Insertion plate width	5.0	-0.2	0.2	4.8 – 5.2
Pi-slot width	6.0	0	0.2	6.0 – 6.2
Minimum total flow channel width	$\delta_{min} = 6.0 - 5.2 = 0.8$			
Maximum total flow channel width	$\delta_{max} = 6.2 - 4.8 = 1.4$			

From the manufacturing tolerances a total flow channel width range was derived. An additional tolerance of interest is the straightness or flatness deviation, illustrated in Figure 6-3:
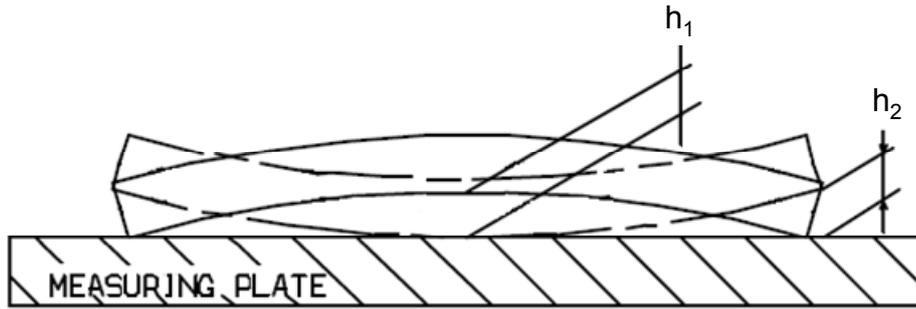
Figure 6-3: The permissible flatness deviation as defined in Mojo (2007).

No definition is provided of a length scale over which the permissible flatness deviations h_1 and h_2 are defined in (MoJo, 2007). Hence, for the purpose of the present work we assumed the length scale to be defined as the approximate length of the side panels of the A-level demonstrator (MoJo, 2009), 1320 mm.

6.2.2 Spring-in effect

The Pi-joint under consideration can be approximated by two back to back flanged laminates (Liu, 2009). A well known distortion of flange laminates – also referred to as the spring-in effect – might occur after de-moulding due to thermal contractions as well as resin cure shrinkage in both the in-plane and through-thickness directions. Less contraction is expected in the circumferential direction, so that consequently the flange angle tends to close (Liu, 2006). Figure 6-4 illustrates the Pi-joint representation by two back to back flanged laminates and the expected deflection of the laminates.
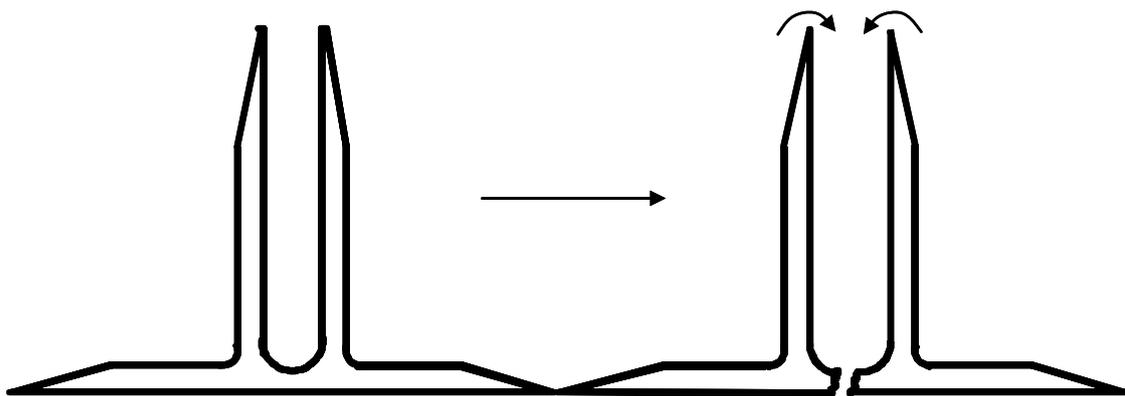
Figure 6-4: Two back-to-back flanged laminates approximating the Pi-slot for the description of the spring-in effect (Liu, 2009).

It is believed, however, that a flanged laminate's distortion would in the present case actually result in a slight opening-up. This is mainly due to the lay-up of the Pi-slot, which

is comprised of stitched NCF (Non-crimp fabric) layers (Figure 6-5). Competing distortion can be expected due to the NCF layers of L and U shapes, which are defined in the following figure. Hence, net distortion would be reduced significantly, instead leading to open-up of the Pi-slot due to one additional layer of NCF in the L shape.
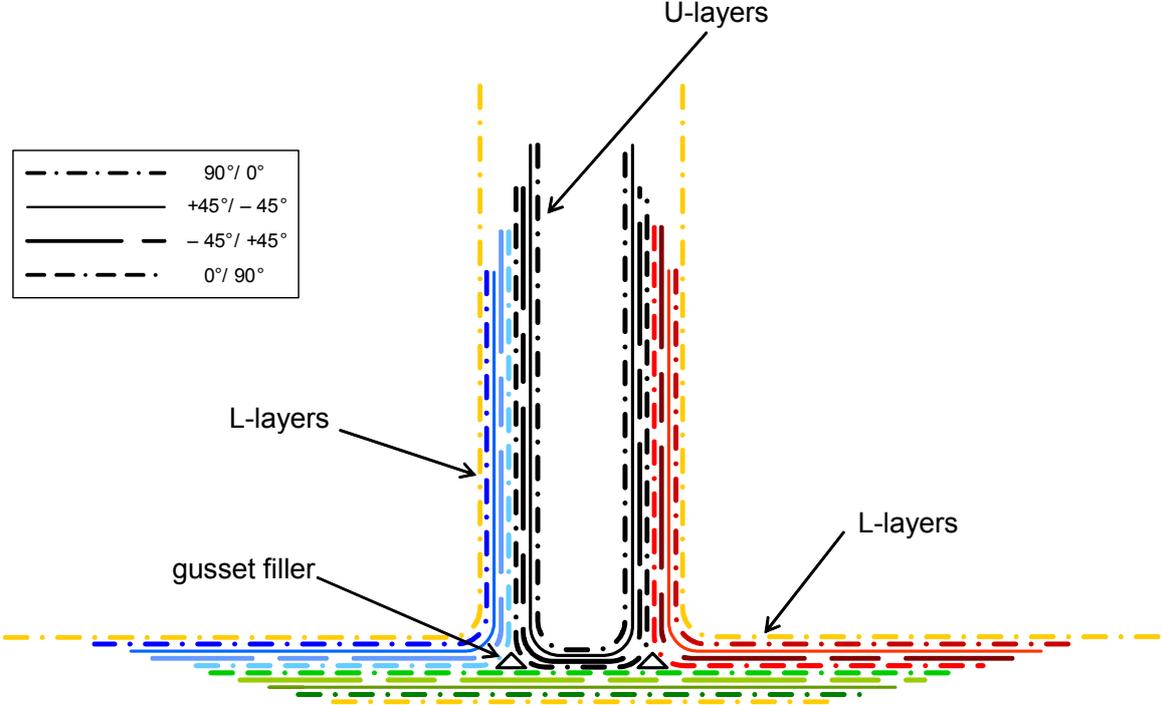
Figure 6-5: Lay-up of the Pi-slot; the fibre layers can be distinguished through the different colours, and fibre-orientation is specified in the legend through different line types.

For an approximation of the net distortion of the tip of the flange – which represents the tip of the Pi-slot – a spring-out angle of 0.5° was assumed. This would result in a 0.3 mm deflection of the tip.

6.2.3 Process induced Pi-slot distortion

Due to penetration of the insertion plate into the adhesive, a pressure builds within the adhesive. This pressure forces the adhesive to flow into the flow channels. It also distributes along the Pi-slot walls, as shown previously in Figure 3-12 on page 73, and may lead to a deflection of them. Assuming the Pi-slot wall deflection is uncoupled from the adhesive flow i.e. no fluid structure interaction, an estimation of the deflection can be made by applying slender beam theory. This assumption would tend to overestimate the deflection as no pressure would be released due to a spring-out of the Pi-slot walls. A

process induced deflection of the Pi-slot wall due to insertion pressure is illustrated in Figure 6-6.
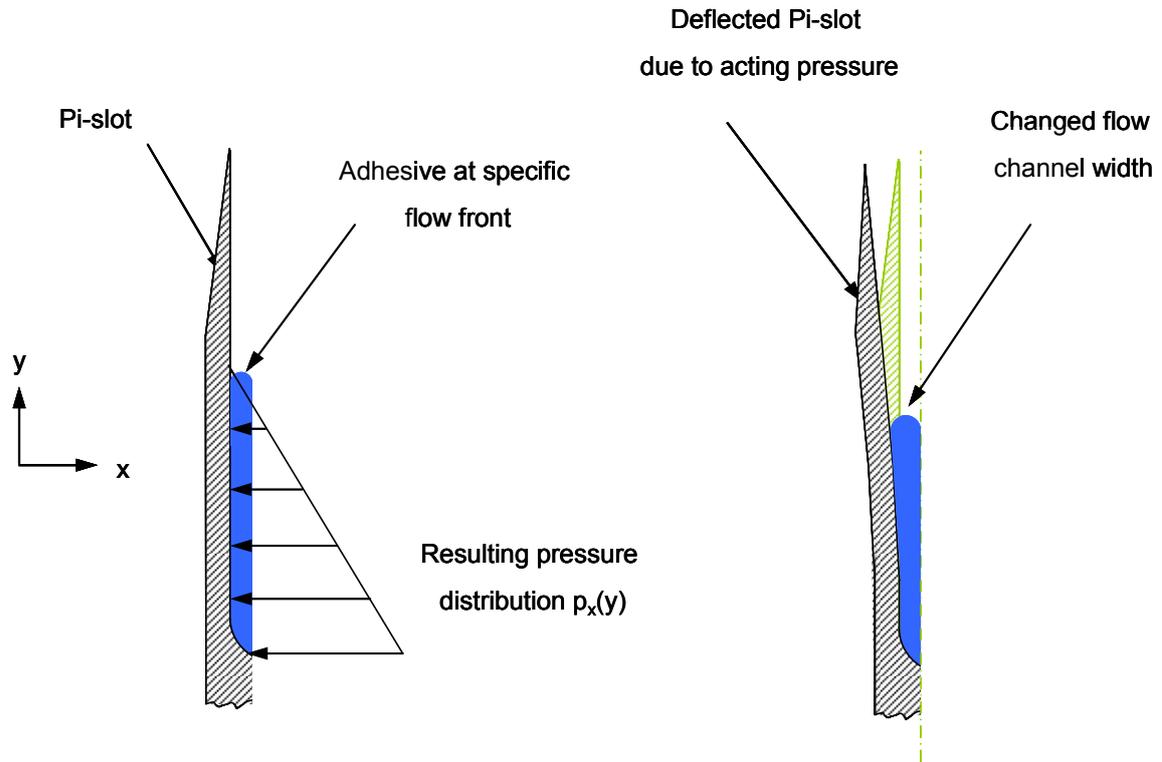
Figure 6-6: Illustration of the Pi-slot wall deflection due to insertion pressure leading to a broadening of the flow channel; the pressure is caused by the flow of the adhesive.

A cantilever beam model was derived to estimate the Pi-slot wall distortion, with the boundary condition at the bottom being fixed into the wall as a cantilever. An illustration of this model can be seen in Figure 6-7.
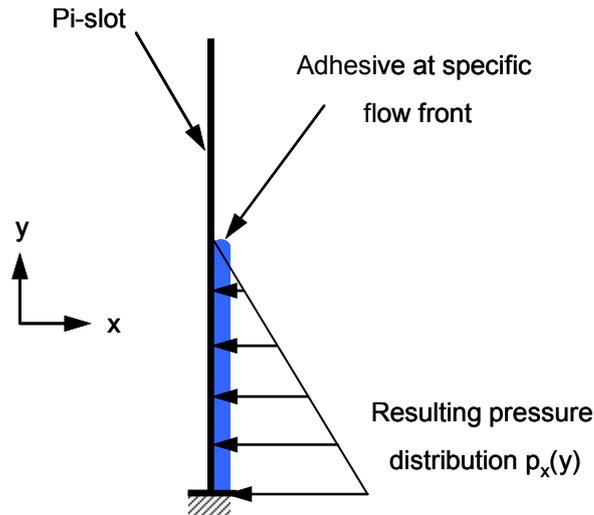
Figure 6-7: Beam model to approximate the Pi-slot wall deflection; boundary conditions at the bottom of the Pi-slot is fixed into the wall as a cantilever.

An investigation of the effect of Pi-slot wall deflection on adhesive flow was conducted and is reported on in Section 7.3. There, the problem is presented assuming a coupling between the adhesive flow and the Pi-slot deflection, hence taking into account a fluid structure interaction.

6.3 Lateral Misalignment Effect on the Adhesive Flow

In Section 6.2 the causes of lateral misalignment in the adhesive's flow during the ISF processes were discussed. Flow channel widths vary in laterally misaligned insertions so that an asymmetric adhesive distribution may be experienced.

This would result in a deterioration of the Pi-joint quality once the adhesive in the flow channels cures and the bondlines are built. Different flow channel widths and an expected adhesive distribution are demonstrated in Figure 6-8.
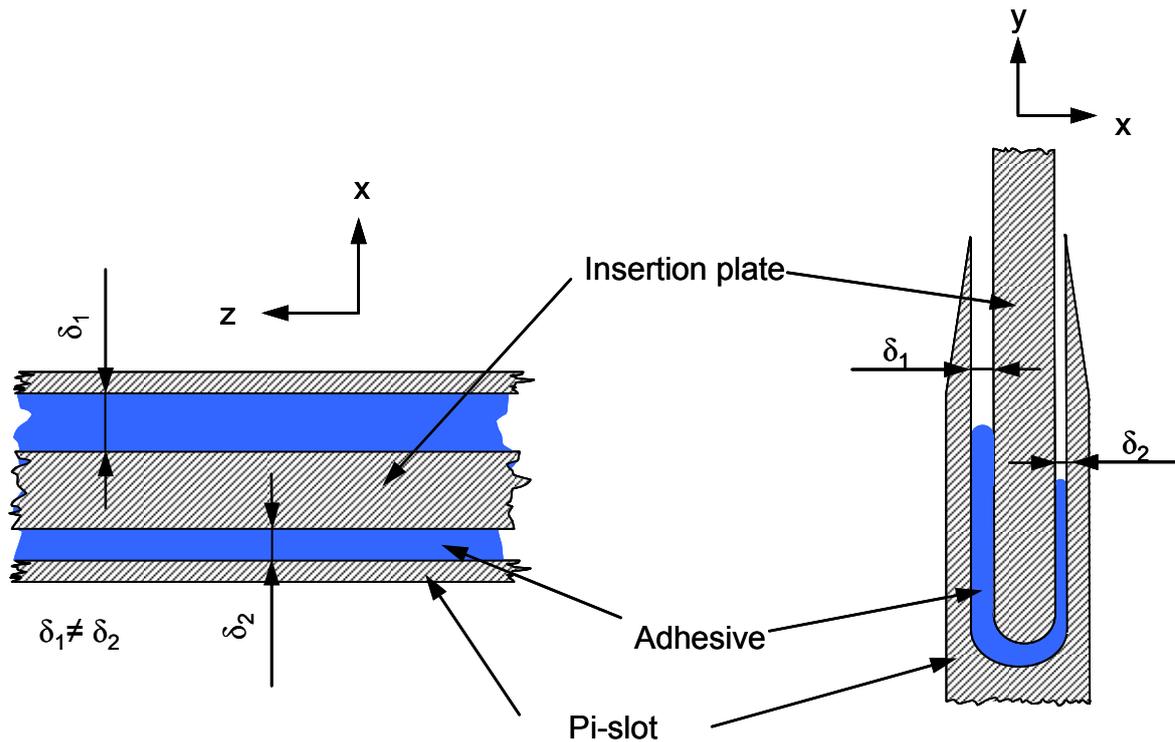
Figure 6-8: Schematic illustration of lateral misalignment resulting in different flow channel widths δ_1 and δ_2,, shown as a top- and a cross-sectional view.

The results of how lateral misalignment affects the adhesive flow within the flow channels are discussed first, and ISF-specific dimensionless parameters are derived. In sub-Section 6.3.1.2 the emphasis is on the sensitivity of lateral misalignment effects on the insertion speed and in sub-Section 6.3.1.3 on the adhesive viscosity. The initial adhesive amount effect on the adhesive distribution was analysed and results are presented in sub-Section 6.3.1.4. Furthermore, the effect of the total flow channel widths on adhesive flow is considered. The last two sections of this chapter deal with the analysis of causes for asymmetrical adhesive flow (sub-Section 6.3.2) and with the effect of insertion head shape on the adhesive flow.

6.3.1 Results and discussion

6.3.1.1 Effect of the flow channel width ratio

The results presented were obtained for insertion speeds of 60 mm/min and adhesive viscosities for the 70 – 30 weight percent EA 9395 to EA 9396 and using the five parameter rational model discussed in sub-Section 4.4.5. The initially applied adhesive volume was 125 volume-percent of the volume to be filled. The dimensions of the joint

were 5.0 mm and 6.0 mm for the insertion plate and the Pi-slot width, respectively, resulting in a total flow channel width of $\delta_{total} = 1.0$ mm. The asymmetry of the two flow channels is represented by the ratio between the narrow (N) and the wide (W) flow channel widths, it is referred to as $\xi=N/W$.

Firstly the adhesive distribution for a perfectly aligned case is shown, for this case the resulting flow channel widths are 0.5 mm:
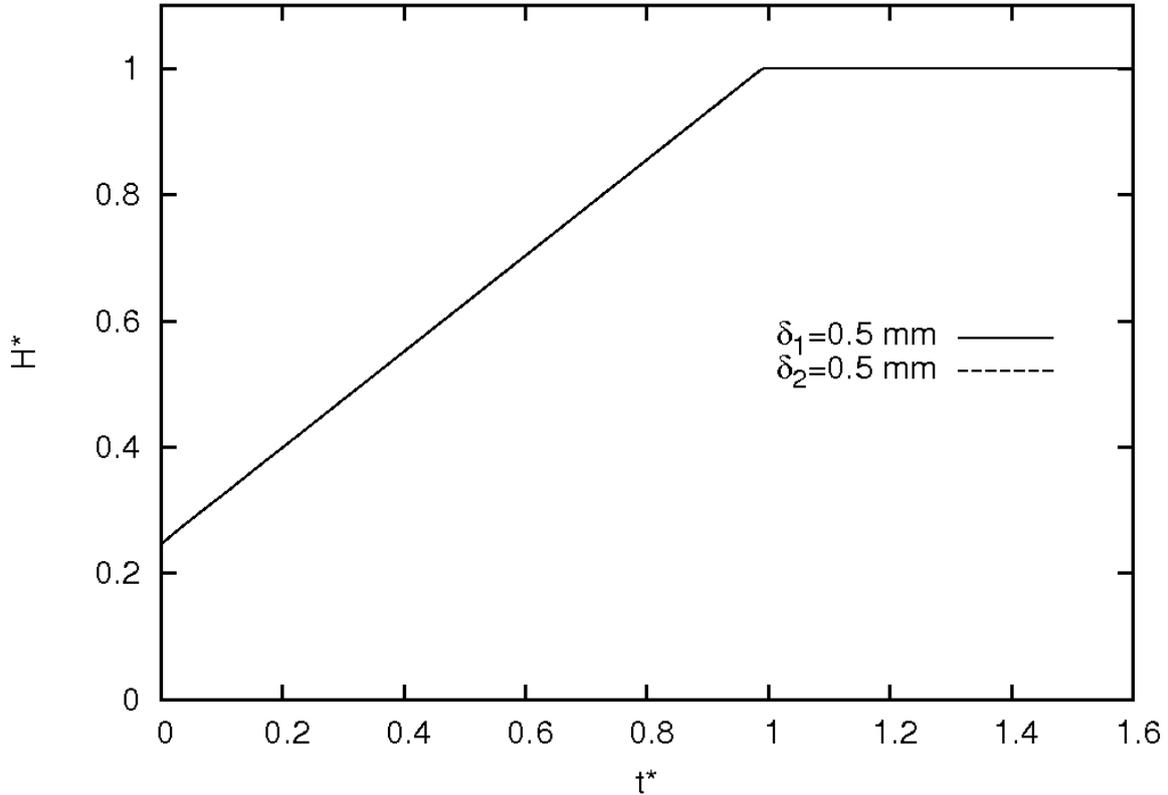
Figure 6-9: Numerically predicted fill heights with respect to dimensionless time for a perfectly aligned insertion represented by 826 points within an interval of 1.6 dimensionless time units t*.

In Figure 6-9 H^* is defined as the flow front c plus the initial adhesive height H_0 divided by the total Pi-slot height H_1 and is plotted against dimensionless time. We defined this parameter as the fill height:

$$H^* = \frac{c + H_0}{H_1} \qquad (6\text{-}1)$$

The definition of c, H_0 and H_1 can be found in Figure 3-8 on page 69. At a dimensionless time t*=1 the flow front reaches the top of the slot, hence H^* is 1. As expected, for an insertion without misalignment the flow fronts in both channels are

identical. The initial adhesive amount of 125 volume percent is represented for this particular geometry by an initial fill height of 0.25.

In Figure 6-10 the effect of laterally misaligned cases on the fill height is shown with respect to time. Results of three simulations are presented where the flow channel widths were as follows: 0.5 mm on both sides of the insertion plate equivalent to the case presented in Figure 6-9; 0.4 mm and 0.6 mm, thus a misaligned case of 0.1 mm; and finally 0.3 mm and 0.7 mm, thus a misalignment of 0.2 mm. A parameter that was introduced above and is now used is the ratio between the narrow and the wide flow channel, specified by ξ. For the results presented in Figure 6-10, $\xi = 0.5/0.5 = 1$ for the simulation without misalignment, $\xi = 0.4/0.6 = 0.667$ and $\xi = 0.3/0.7 = 0.430$ for the 0.1 mm and the 0.2 mm misaligned case, respectively.
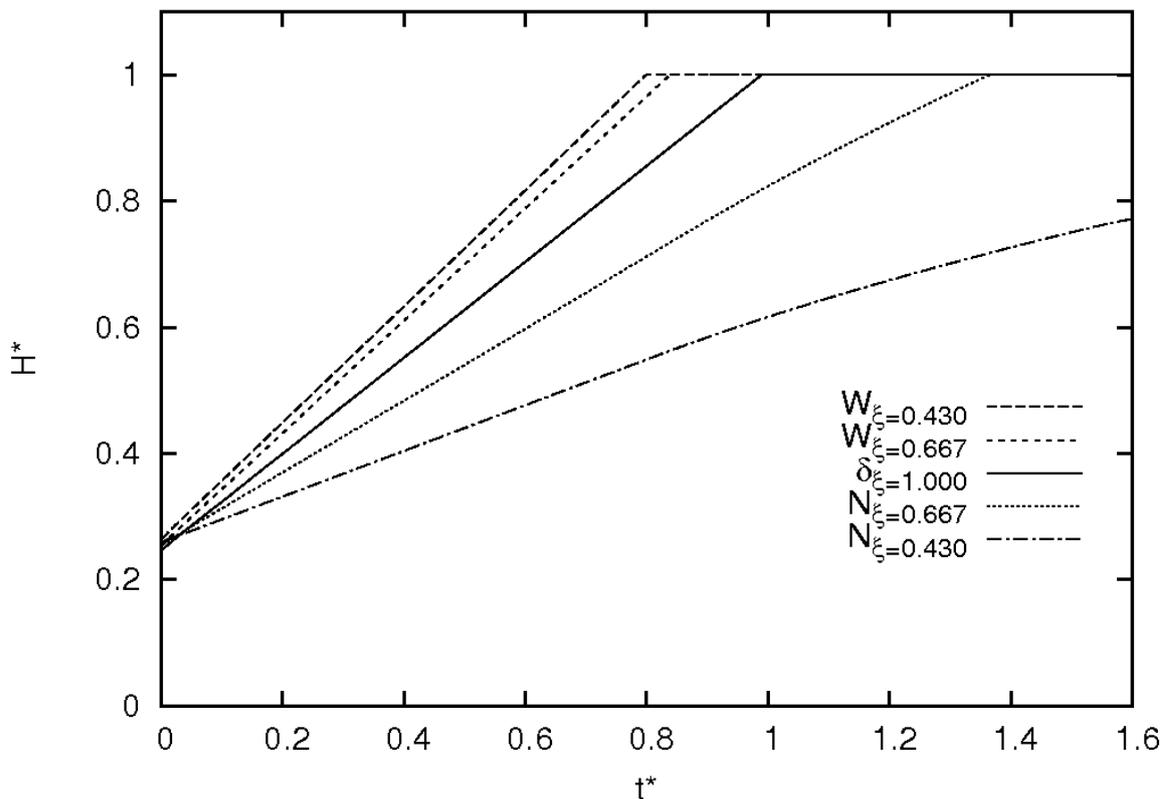
Figure 6-10: Numerically predicted fill heights in the narrow and the wide flow channel with respect to dimensionless time for $\xi = 1$, $\xi = 0.667$ and $\xi = 0.430$.

The results demonstrate that the wider channels fill quicker than the narrower channels. For $\xi = 0.667$ the wide as well as the narrow flow channel could be filled completely as can be seen through the short dashed line and the dotted line which both reach a fill height

of 1. However, the narrow flow channel for $\xi = 0.430$ (dot-dashed line) could not be filled completely. *H** is only about 0.8 when the insertion stops.

Further cases that were studied include a 0.3 mm misaligned case ($\xi = 0.2/0.8 = 0.250$) as well as a 0.4 mm misaligned case ($\xi = 0.1/0.9 = 0.111$). From the results shown in Figure 6-10 it can be concluded – and was obtained from the simulations – that the wider channels can be filled completely. These results are therefore not shown in Figure 6-11. Instead, only the flow of the adhesive in the narrow flow channels is presented:
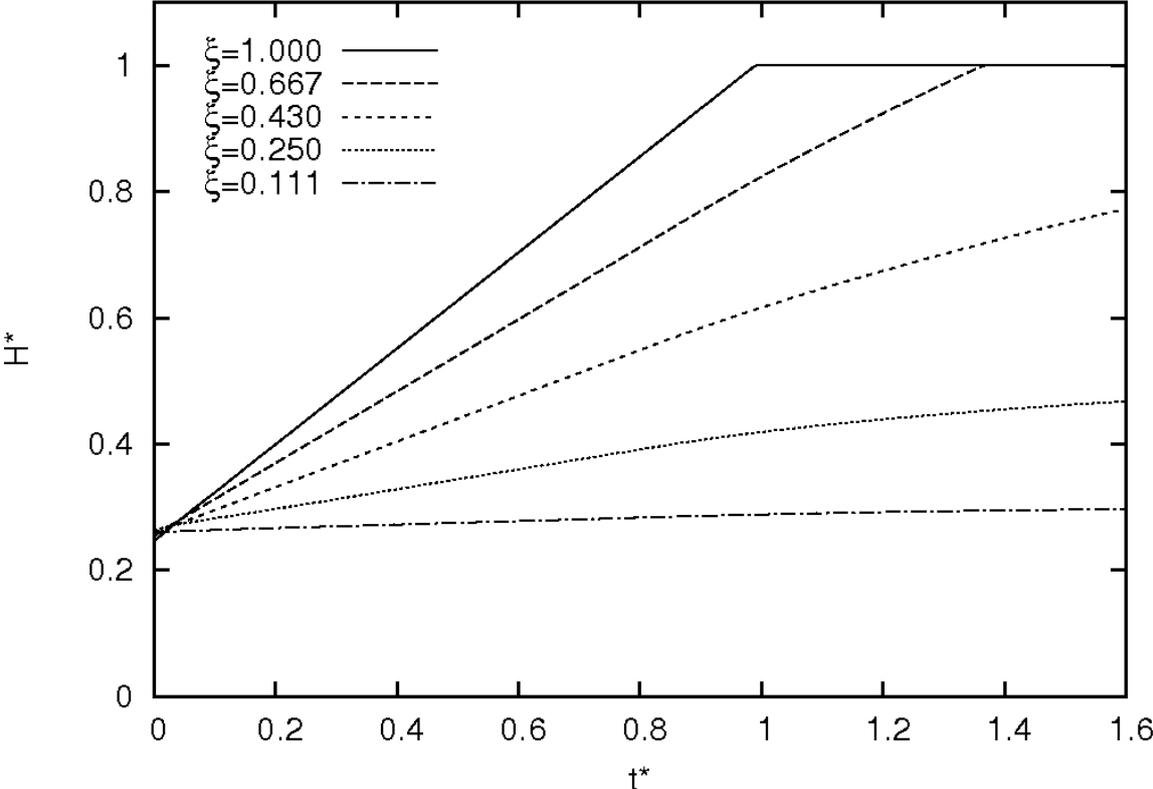
Figure 6-11: Numerically predicted fill heights with respect to dimensionless time in the narrow flow channel for different ξ ratios.

The initial adhesive amount remained constant at about 0.25 as indicated by the fill height at *t** = 0. The 0.1 mm wide flow channel exhibits hardly any flow of the adhesive during the flow process. Almost the entire adhesive amount is displaced into the wider channel. At the end of the flow process the fill height for the 0.1 mm wide channel is 0.33. A higher fill height is achieved for the 0.2 mm wide channel with about 0.52. The other results are as presented in Figure 6-10.

In Table 27 the fill heights for results plotted in Figure 6-11 are summarised for two specific dimensionless times.

Table 27: Fill levels in the narrow and the wide flow channel for different ξ for dimensionless times of 1 and 1.57.

ξ	H^*			
	$t^* = 1$		$t^* = 1.57$	
	δ_N	δ_W	δ_N	δ_W
1.000	1	1	1	1
0.667	0.82	1	1	1
0.430	0.62	1	0.76	1
0.250	0.44	1	0.51	1
0.111	0.31	1	0.32	1

The trend resulting from Table 27 shows that the fill level in the narrow channel varies directly with ξ. It also indicates that the flow front in the narrow flow channel continues to increase after the wide flow channel is filled. This can be observed in Table 28 as H^* in the narrow flow channel increases from 1 to 1.57 dimensionless time units.

A relationship was developed between the fill height and the degree of misalignment ξ and is presented in the following. A new variable, ψ, was defined as a measure of the difference in the extent of fill between the two channels:

$$\psi = \frac{c_{narrow}}{c_{wide}} \qquad\qquad (6\text{-}2)$$

The flow front ratio ψ is plotted against dimensionless time in Figure 6-12 for different ξ ratios:
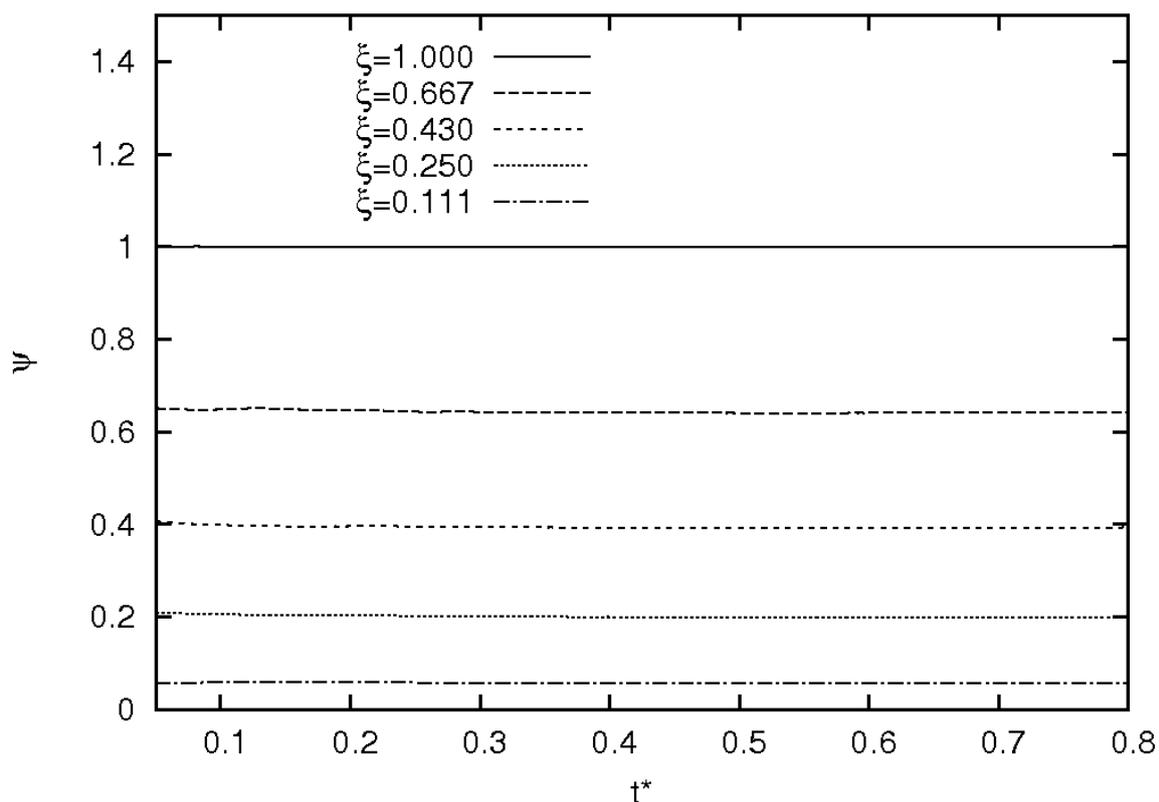
Figure 6-12: Numerically predicted flow front ratio ψ versus t* for different flow channel width ratios ξ.

We notice that for different flow channel width ratios ξ different constant flow front ratios ψ were obtained. Note the dimensionless time scale, which is terminated at 0.8 units. At this time the adhesive begins to flow out of the wider flow channel. The flow front ratio is independent of the flow front position only while both flow channels are not filled entirely, which is not true for $t^*>0.8$. In sub-section 6.3.2 the causes that lead to the asymmetrical adhesive distribution for laterally misaligned insertions will be discussed. There it will be shown that the position of a pressure maximum underneath the insertion plate causes the adhesive distribution. The pressure maximum position depends on the ξ-ratio. As long as both the adhesive flow front in the narrow and in the wide flow channel remain within the flow channels, i.e. do not flow out at the top of the flow channel, the pressure maximum position remains unchanged. Consequently, the flow front ratio ψ is independent of the dimensionless time within this range.

In Figure 6-13, the flow front ratio is plotted with respect to the flow channel width ratio.
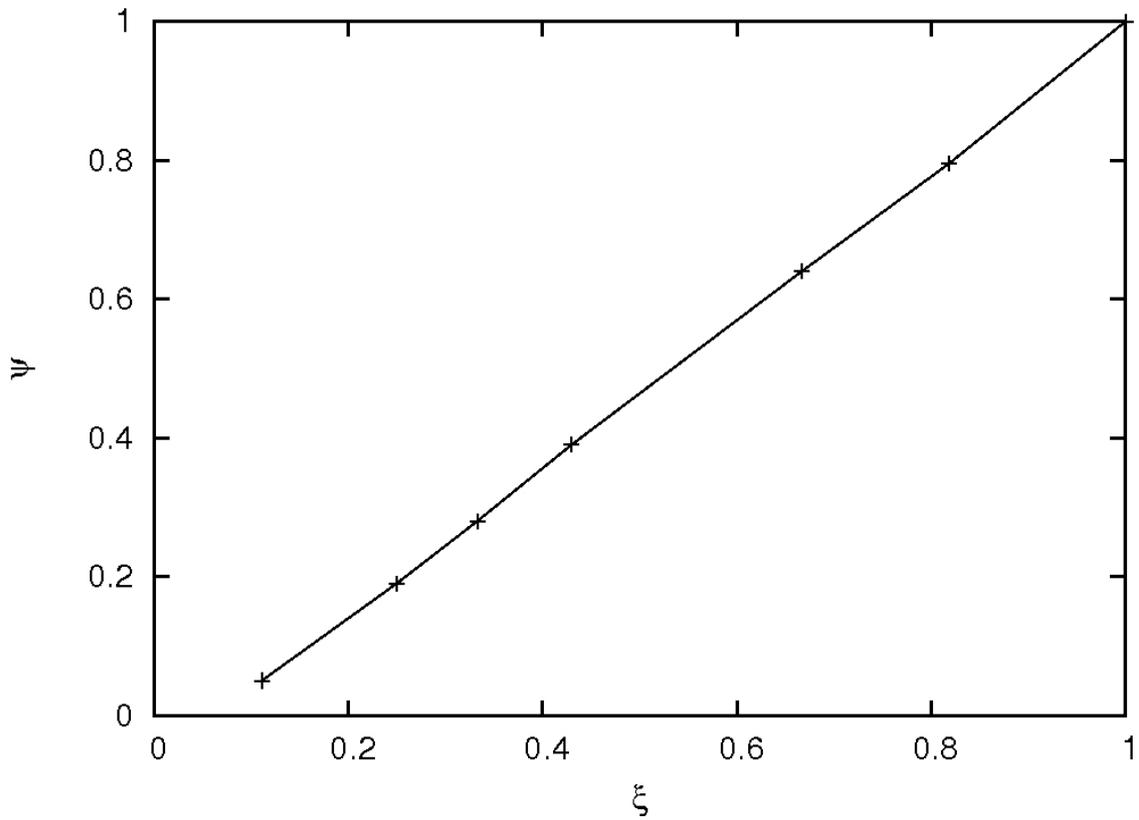
Figure 6-13: Relationship between the flow front ratio and the flow channel width ratio derived from the numerical predictions.

Clearly, from an inspection of Fig.6.13, the relationship between flow front ratio and the flow channel width is linear. If this is fitted by regression one obtains

$$\psi = 1.0683\xi - 0.0728 .$$ <div style="text-align: right">(6-3)</div>

However, this is clearly wrong at a flow channel width ratio of 0, i.e. when the narrow flow channel width is closed; here, the flow of the adhesive can only be into the wide channel and consequently the flow front ratio must also be 0. Given the form of the data and applying this constraint, it would seem that a physically better and more general fit would be $\xi = \psi$, i.e. the flow front ratio is always equal to the flow channel width ratio. The argument below presents a rational basis for such a relationship.

$$\psi = \xi$$ <div style="text-align: right">(6-3a)</div>

The cause of the adhesive distribution will be shown in sub-Section 6.3.3 to be the maximum pressure position underneath the insertion plate. This position depends on the flow channel width ratio, being shifted closer to the narrow flow channel with decreasing flow channel width ratio. Given that the flow distribution is equal for $\xi = 1$ and, as stated

above, if $\xi = 0$ ψ must be 0, and finally for all other investigated flow channel width ratios ξ the approximation $\xi = \psi$ is close, equation (6–3a) is valid for the considered range of parameters.

Hence, for a given flow channel width ratio ξ the flow front ratio ψ can be derived for the considered input parameters. The dependence of the relation on the input parameters was also tested and results will be reported on in the following sub-section.

Then, assuming the adhesive begins to flow out of the wider flow channel, the flow front in the narrow flow channel can also be derived, and the missing amount of adhesive in the narrow flow channel can be calculated. This amount can then be added to the initial adhesive amount so that complete flow channel filling is ensured if equation (6-3a) is independent of the initial adhesive amount. This is validated in sub-Section 6.3.1.4. We summarised the procedure to ensure entire filling of both flow channels for laterally misaligned insertions:

a) Measure dimensions of the Pi-slot and insertion plate,

b) derive minimum adhesive volume to theoretically fill flow channels and area underneath the insertion plate head entirely,

c) include a safety factor of e.g. 1.1,

d) calculate the minimum initial adhesive height in the Pi-slot, $\overline{H}_0$, resulting from the adhesive volume,

e) estimate lateral misalignment which results from the spacer diameter (spacer diameter should be chosen as perfectly aligned flow channel width minus 10 %, so 0.45 mm for a 0.5 mm flow channel width),

f) calculate the resulting worst case flow channel width ratio ξ,

g) estimate flow front in narrow flow channel when wide flow channel just fills according to $c_N = H_1 \psi = H_1 \xi$,

h) calculate H_2, which specifies the unfilled narrow flow channel length, $H_2 = H_1 - c_N$,

i) and update H_0 according to addition of H_2 and $\overline{H}_0$.

This approach is conservative because as shown in Table 27 the flow front in the narrow flow channel continues to increase after the adhesive flows out of the wide flow channel. Hence, a 2nd equation was derived, which would be valid after the adhesive flows out of the wide flow channel.

First, the flow front ratios with respect to dimensionless time for different flow channel width ratios were considered (Figure 6-14). The time period was defined from the point when the adhesive flows out of the wide flow channel until either the flow front in the narrow flow channel reaches the top (e.g. for $\xi = 0.667$ in Figure 6-14) or until the end of the flow process (all other ξ ratios in Figure 6-14) is reached.
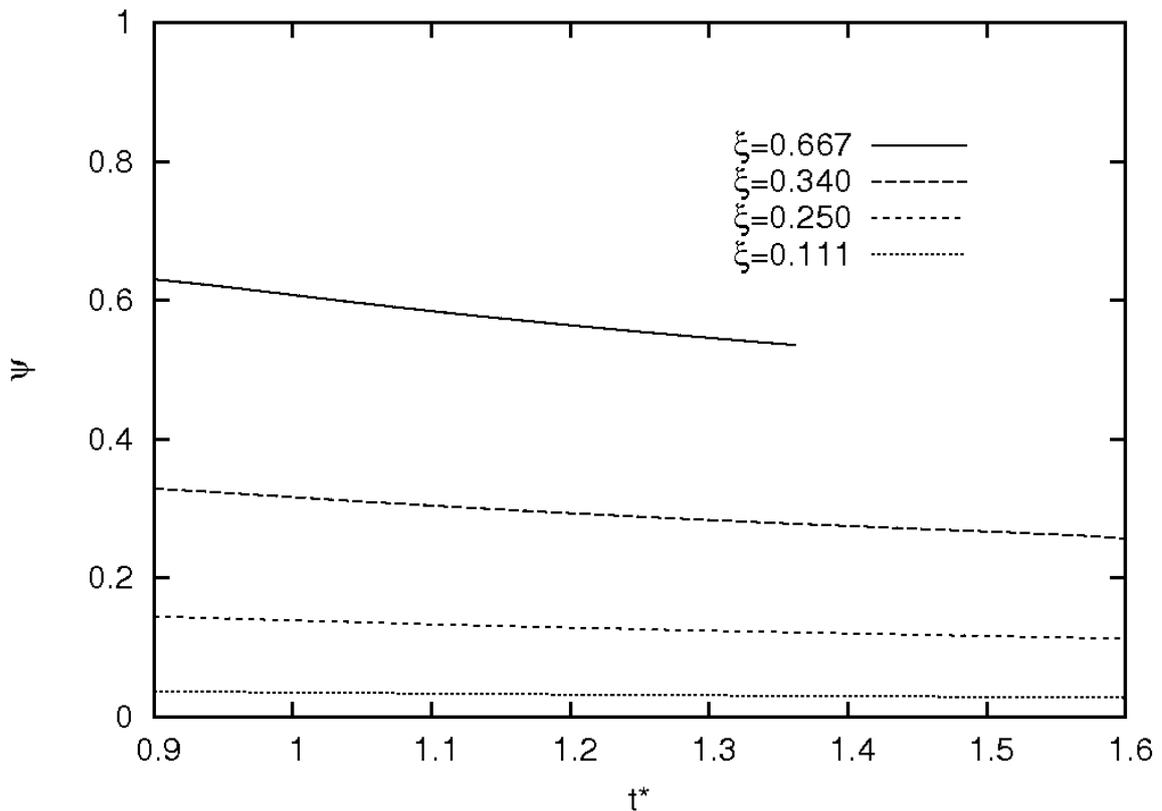
Figure 6-14: Flow front ratios for different flow channel width ratios after the adhesive has reached the outflow in the wide flow channel.

The flow front ratio decreases linearly with dimensionless time for all misalignments. The rate of decrease increases with increasing ξ. One dimensionless time to derive a relation between the flow front ratio ξ and the flow channel width ratio ψ was specified, which would provide a worst case scenario; this is when the ISF process terminates because the flow front ratio value ψ is minimum. In the cases considered in Figure 6-14 this time is 1.6. For the $\xi = 0.667$ case, the ψ value chosen was the one when the adhesive flows out of the narrow flow channel at $t^* = 1.37$. The relations are plotted in Figure 6-15:
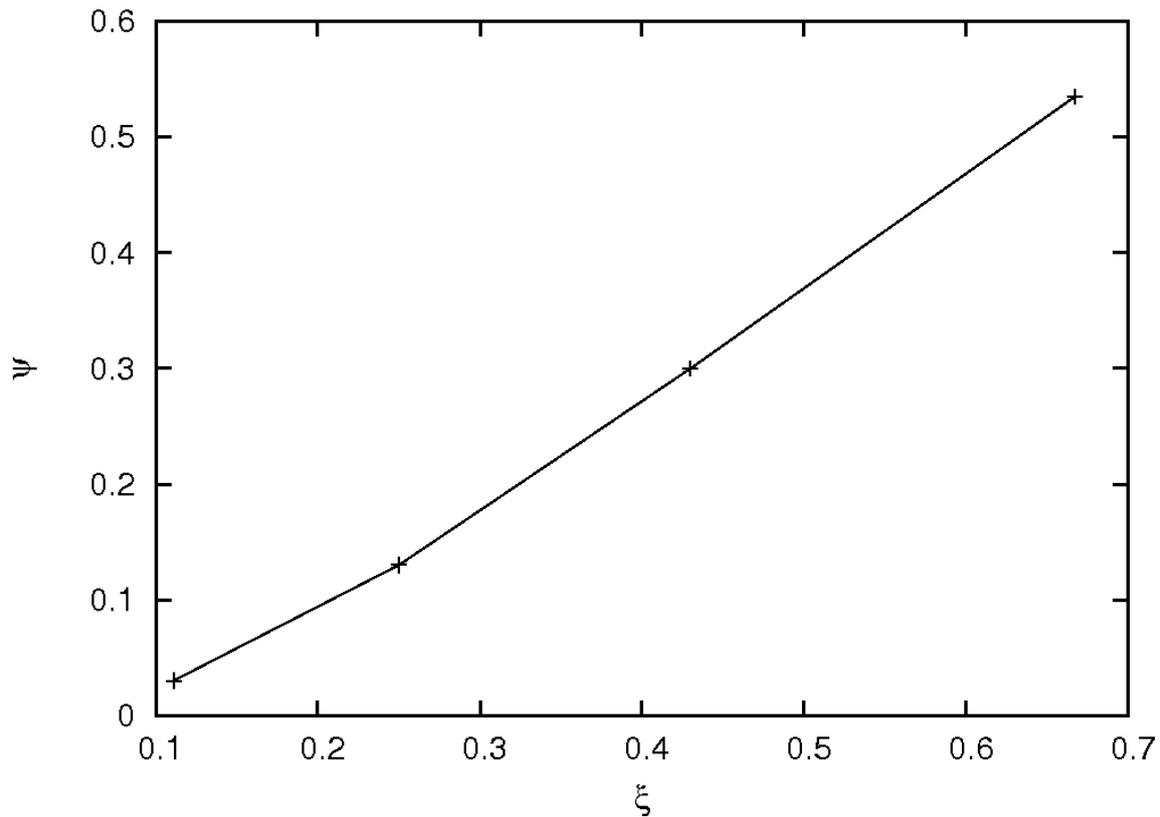
Figure 6-15: Relation between the flow front ratio and flow channel width ratio for a specifed dimensionless time of t*=1.35.

Again an approximately linear relation was obtained between the flow front ratio ψ and the flow channel width ratio ξ. The flow front ratio is now referred to as ψ_2:

$$\psi_2 = 0.9167\xi - 0.0852 \qquad (6\text{-}4)$$

A second procedure is proposed to estimate the necessary initial adhesive amount to ensure complete flow channel filling. This procedure will be presented in sub-Section 6.3.1.4 where the effect of initial adhesive amount on adhesive flow was evaluated. The effect of insertion speed, adhesive viscosity, insertion plate width and insertion plate head shape is also considered in the following sub-section.

6.3.1.2 Effect of the insertion speed

Absolute Pi-joint dimensions remained unchanged to those presented in the previous sub-section. The flow channel width ratio was specified as 0.430. For these parameters the insertion speed was derived for an adhesive viscosity of $70 - 30$ weight percent EA 9395 to EA 9396 and the fill height H^* determined with respect to dimensionless time (Figure 6-16).
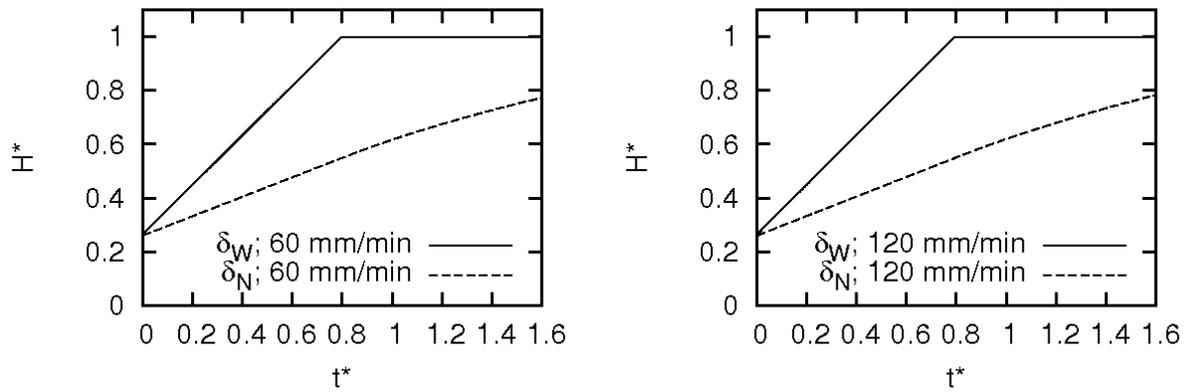
Figure 6-16: Predicted fill heights with respect to dimensionless time in the wide and narrow flow channel (ξ = 0.430) for two different insertion speeds and 70 – 30 weight percent EA 9395 to EA 9396.

At different insertion speeds (60 and 120 mm/min), small differences can be observed from the predicted fill heights for different process conditions. Hence, for the range of input variables considered here the effect of insertion speed on the fill height is negligible. It is highly likely that the insertion speed does not affect the $ξ$-$ψ$-relationship, however further study is necessary to validate this.

6.3.1.3 Effect of the adhesive viscosity

The input parameters remained the same as in the previous sub-section 6.3.1.2. At low insertion speeds of 60 mm/min, the adhesive viscosity was varied and the fill height H^* was predicted. The effect of the adhesive viscosity on the fill height H^* is illustrated in Figure 6-17.
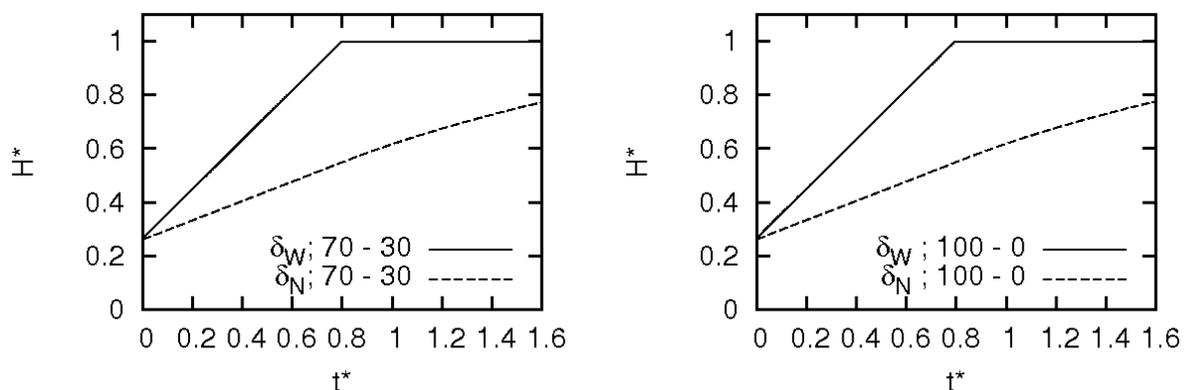
Figure 6-17: Predicted fill heights with respect to dimensionless time in the wide and narrow flow channel (ξ = 0.430) for two different adhesive viscosities at an insertion speed of 60 mm/min.

The adhesive viscosity scarcely affects the transient fill height. Hence, it was concluded that most probably the adhesive viscosity does not affect the relationship derived between the flow channel width ratio and the flow front ratio in the considered range. In general, it is assumed that this relationship is not affected by the adhesive viscosity. To ensure this independence, an extension of the adhesive viscosity range simulated is needed.

6.3.1.4 Effect of the initial adhesive amount

Using baseline input variables, the initial adhesive amount applied into the Pi-slot before starting the bonding process was varied. To evaluate this effect on the adhesive flow, a flow channel width ratio of 0.430 was considered. This parameter was selected as the previous simulations had found that the narrow flow channel could not be entirely filled for an initial adhesive amount of 125 volume-percent. Plots illustrating fill heights in the narrow channel for four simulations differing in the initial adhesive amount are presented in Figure 6-18.
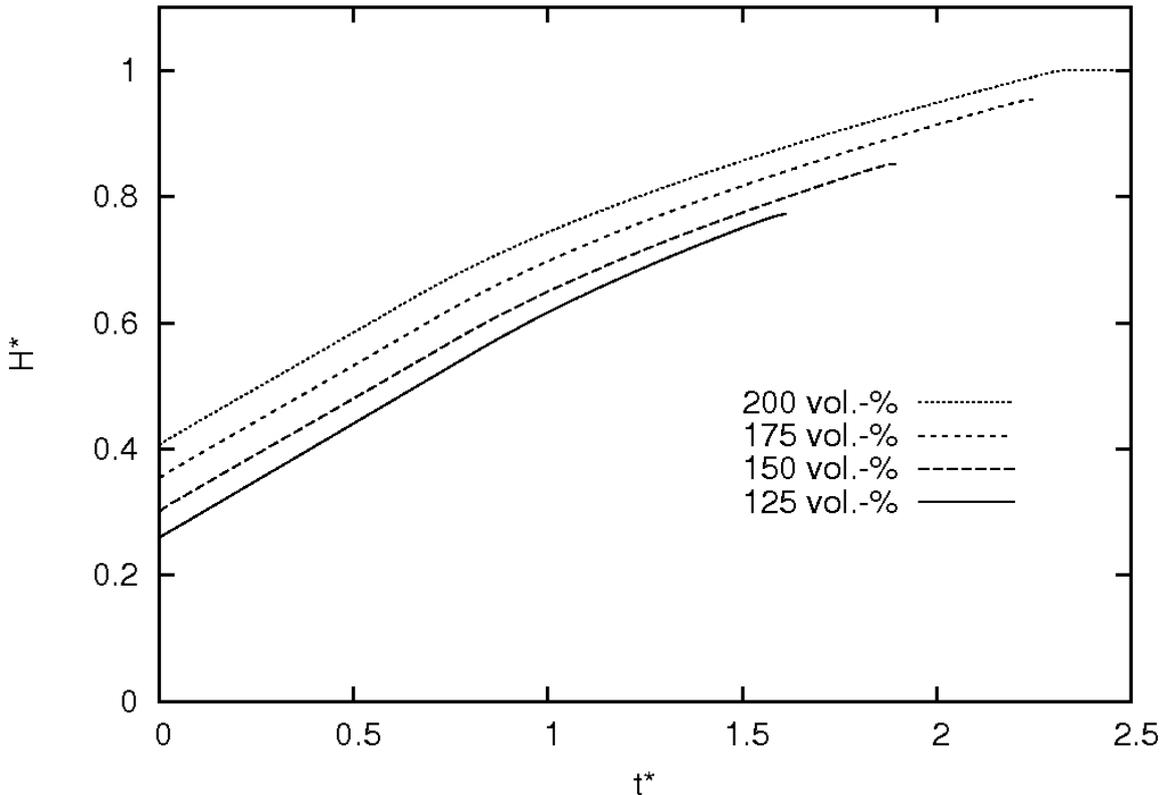
Figure 6-18: Fill height as a function of dimensionless time in the narrow channel for a ξ ratio of 0.430 for different initial adhesive amounts.

As expected, fill heights increase with dimensionless time for all considered simulations. The total flow time until the ISF process terminates varies with the initial adhesive amount. The initial adhesive fill height H^* at $t^* = 0$ is also affected by the initial adhesive amount. The initial fill height is 0.410 for an initial adhesive amount of 200 volume percent whereas for 125 volume-percent the fill height is 0.25. It can be seen that the narrow flow channel can be filled for the case where 200 volume percent was applied ($t^* = 2.30$). For none of the other cases presented here can the top of the flow channel be reached. An approximately linear increase can be seen initially in the slopes of the plots, followed by a slightly flatter second increase. This again indicates that the outflow of the adhesive has occurred in the wider channel, which clearly occurs earlier for the initially higher filled channels.

Deriving the flow front ratio ψ from the numerical results presented in Figure 6-17 with equation (6-3), it was found that for this value of ξ the flow front ratios varyied between 0.38 and 0.39 for initial adhesive amounts between 125 and 200 volume percent as long as both flow channels were not filled entirely.

As indicated in sub-Section 6.3.1.1, a second procedure was developed to ensure full filling of flow channels that can be applied for times after the wide flow channel is filled with adhesive entirely. This procedure was applied to the results for varying flow channel widths for a flow channel width ratio of 0.430. The following variables were defined:

- $H_{0, stop}$ was defined as the distance the insertion plate can travel from its initial position until touching the Pi-slot bottom;
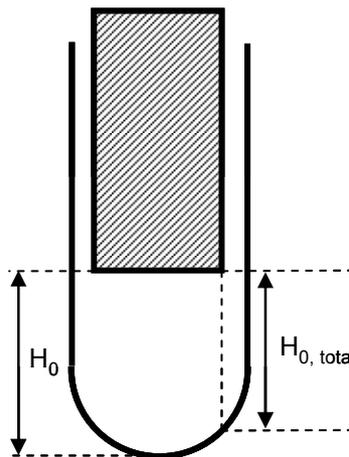
Figure 6-19: Definition of $H_{0, total}$ which is used for the second procedure to ensure entire filling of the narrow flow channel in a misaligned insertion process.

- c_{W0} and c_{N0} were defined as the flow front positions in the wide and the narrow flow channel, respectively, when the adhesive flows out of the wider channel, and c_{W2} and c_{N2} were the flow fronts after that time;

- $c_{N2,total}$ was defined as the sum c_{N0} and c_{N2}, and $c_{N2, missing}$ was defined as the flow channel height H_1 minus the initial adhesive height H_0 plus $c_{N2,total}$

- H_0^* was the entire distance travelled at that time, and h^* was the remaining possible travel distance before the insertion plate and Pi-slot touch.

Having defined these variables, the procedure was as follows:

1   Assume H_0 and calculate $H_{0, stop}$;

2   calculate c_{W0} and c_{N0} with

$$c_{w0} = H_1 - H_0 \qquad (6\text{-}5)$$

$$\psi = (1.068333\xi - 0.0728) = \frac{c_{N0}}{c_{W0}} ; \qquad (6\text{-}6)$$

3   calculate H_0^* and h^* with

$$2aH_0^* = c_{N0}\delta_N + c_{w0}\delta_w \qquad (6\text{-}7)$$

$$h^* = H_{0,total} - H_0^* ; \qquad (6\text{-}8)$$

4   calculate c_{N2} from

$$\psi_2 = (0.9167\xi - 0.0852) = \frac{c_{N2}}{c_{W2}} \qquad (6\text{-}9)$$

$$2ah^* = c_{N2}\delta_N + c_{w2}\delta_w \qquad (6\text{-}10)$$

$$\Rightarrow c_{N2} = 2ah^* \psi_2 \frac{1}{\delta_w + \delta_N\psi_2} ; \qquad (6\text{-}11)$$

5   calculate $c_{2,total}$ which results from c_{N0} and c_{N2}, and add to the initial adhesive height H_0, and subtract from H_1, to find out missing flow front in narrow channel, hence $c_{N2, missing} = H_1 - H_0 + c_{N0} + c_{N2}$;

6   finally, terminate if $c_{N2, missing}$ is less than 0, but add $c_{N2, missing}$ to H_0 and start from 1 if $c_{N2, missing}$ is greater 0.

This procedure was applied for $\xi=0.430$ when the initial adhesive amount was defined as 125 volume percent. It was calculated that applying an initial adhesive amount of

189 volume percent should result in a complete filling of the narrow flow channel. Comparing this with Figure 6-18 we notice that complete filling is achieved somewhere between 175 and 200 initial volume percent, hence the estimation is in line with the numerical results. Compared with the procedure proposed in sub-Section 6.3.1.1, this approach requires more calculation in determining the minimum required initial adhesive amount; however, this second procedure is more accurate, being consistent with the numerical predictions, and hence has the capacity to reduce adhesive wastage.

6.3.1.5 Effect of the total flow channel width

The effect of varying the insertion plate width on the distribution of the adhesive within the flow channels was also investigated. For this purpose the Pi-slot width was kept constant (6.0 mm) and the insertion plate width was varied between 4.8 and 5.2 mm. Other input variables that were kept constant were the insertion speed (60 mm/min), the adhesive viscosity (70 – 30 volume percent ratio mixture of EA 9395 to EA 9396) and the initial adhesive amount (125 volume percent).

Figure 6-20 presents the fill heights within the narrow channel with respect to dimensionless time for three different ξ ratios (1.5, 2.3 and 3), each for three different total flow channel widths (0.8, 1.0, 1.2 mm).
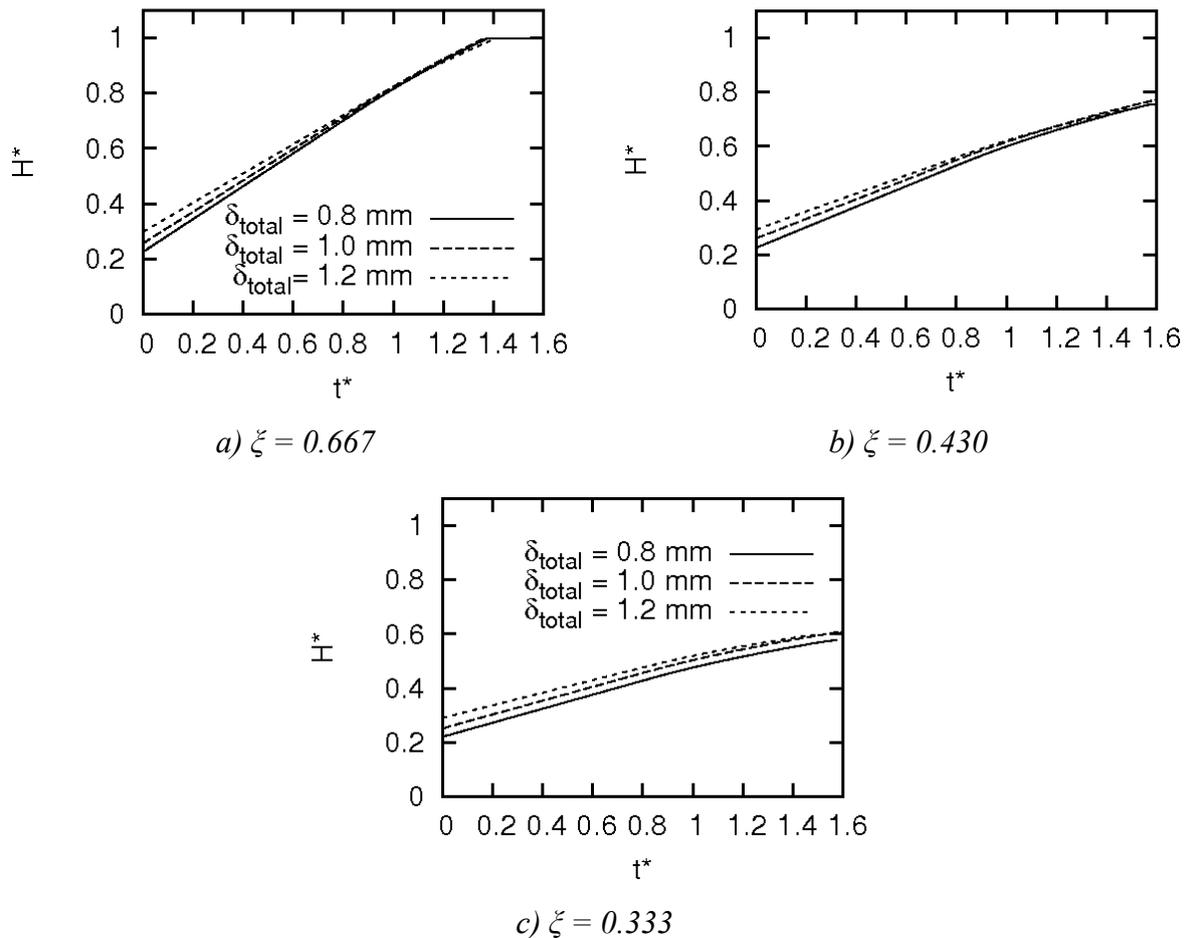
Figure 6-20: Effect of the total flow channel width on the fill height versus dimensionless time for a) $\xi = 0.667$, b) $\xi = 0.430$, and c) $\xi = 0.333$.

The graphs show that the dimensionless adhesive amount at time $t^*=0$ varies slightly for different δ_{total}. This is because the initial adhesive amount of 125 volume percent differs for different absolute dimensions, with the widest total flow channel width of 1.2 having the highest adhesive amount at $t^*=0$ in all three cases.

Considering a ξ ratio of 0.667 (Figure 6-20 a)), it appears that there is less resistance to the flow in those cases where δ_{total} is smaller. Consequently, the gradient H^*/t^* is highest for $\delta_{total} = 0.8$ mm, indicating the fastest filling out of the three investigated cases. The slowest filling rate occurs for the widest total channel. This trend can also be observed when the ξ ratio is decreased. For example, Figure 6-20 b) (ξ ratio 0.430) indicates fastest filling for the narrowest flow channels, although the flow channels cannot be filled completely. For the smallest ξ ratio investigated the difference in filling the flow channels for different total flow channel widths is not as strong as for the lower ξ ratios. From these results it is concluded that there is little dependence on the filling of the flow channels

from the total flow channel width. This can be seen from the different filling gradients. The effect seems to weaken for higher ξ ratios.

To emphasize the effect of total flow channel width on flow front ratios ψ these are plotted for the above-presented flow channel width ratios in Figure 6-21.
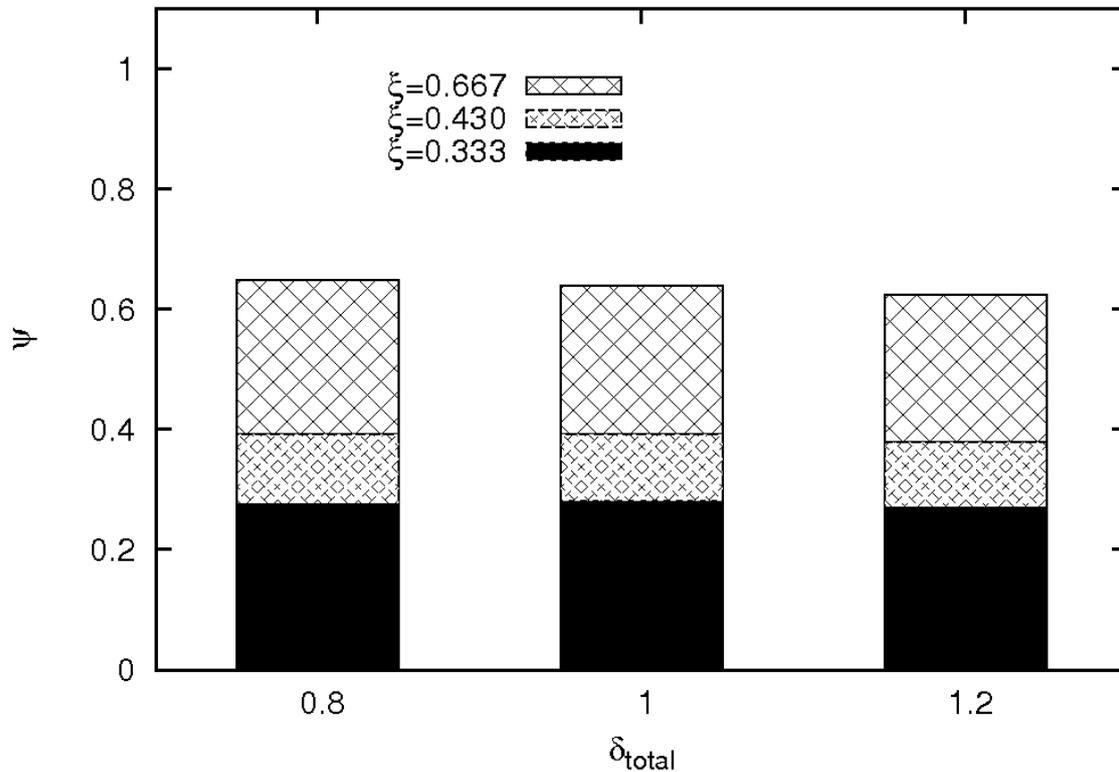
Figure 6-21: Flow channel width effect on the flow front ratio ψ, resulting from a variation of the insertion plate width, plotted for three different flow channel width ratios ξ.

Figure 6-21 shows that there is little difference in the flow front ratios for the differenct widths. With increasing flow channel width the flow front ratios appear to decrease slightly. For example for the highest flow channel width ratio considered (0.667), the flow front ratio decreases from 0.645 to 0.624 for an increase in total flow channel width from 0.8 to 1.2 mm. This trend weakens for smaller ξ ratios, for example for $\xi = 0.333$ ψ only decreases from 0.272 to 0.269.

In summary, it has been shown that there is a dependence between the ξ ratio and the adhesive distribution during an ISF process. The flow within the narrow channel was examined for a number of simulations where several input parameters were varied, i.e. the insertion speed and adhesive viscosity. Both have little effect on the adhesive flow fronts. Similarly, the initial adhesive fill height also only slightly affected the flow front ratio ψ,

Finally, it has been found that the flow front ratio ψ decreases slightly with increasing total flow channel width δ_{total}. This effect was stronger for higher flow channel width ratios ξ.

6.3.2 Explanation of asymmetrical adhesive flow

Within this sub-section the causes of an asymmetrical adhesive distribution within misaligned joints are examined. The sample used for the analysis was the ξ ratio case of 0.430 with an insertion plate width of 5.0 mm and Pi-slot width of 6.0 mm, i.e. a misalignment of 0.2 mm. The resulting flow channel widths were 0.7 mm and 0.3 mm. The input parameters were 60 mm/min for the insertion speed and 70-30 weight percent EA 9395 to EA 9396 adhesive viscosity.

The pressure distributions underneath the insertion plate for a symmetrically aligned case and ξ = 0.430 are shown in Figure 6-22 at t^* = 0.28.

a)   b)
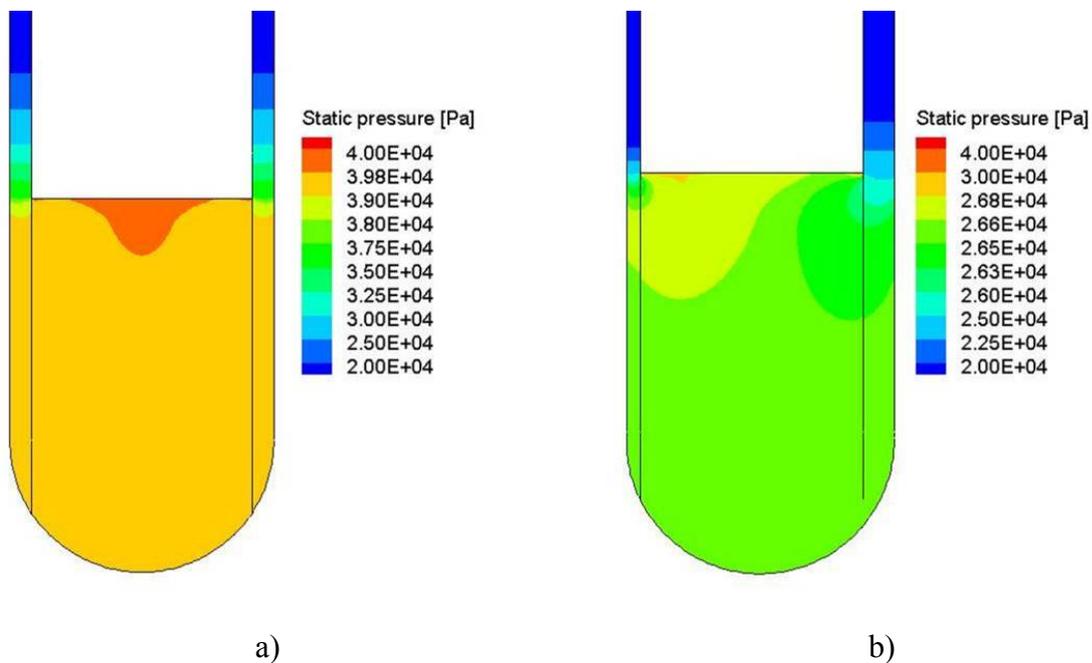
Figure 6-22: Static pressure distribution within the flow domain for t*=0.28 for a perfectly aligned insertion of a) ξ = 1 and a laterally misaligned insertion defined by b) ξ = 0.430.

A pressure maximum exists in the area centred underneath the insertion plate bottom for the aligned case (Figure 6-22 a)). In Figure 6-22 b), the pressure maximum is positioned closer to the narrow channel. As the particles' motion would be expected to be away from the maximum pressure, and in addition given there is only one pressure peak in the flow domain, the position of the maximum pressure is considered as the main cause for the distribution of the adhesive.

Streamlines within the flow domain of the $\xi = 0.430$ case for the same time to illustrate the flow of the adhesive where considered and are illustrated in Figure 6-23.
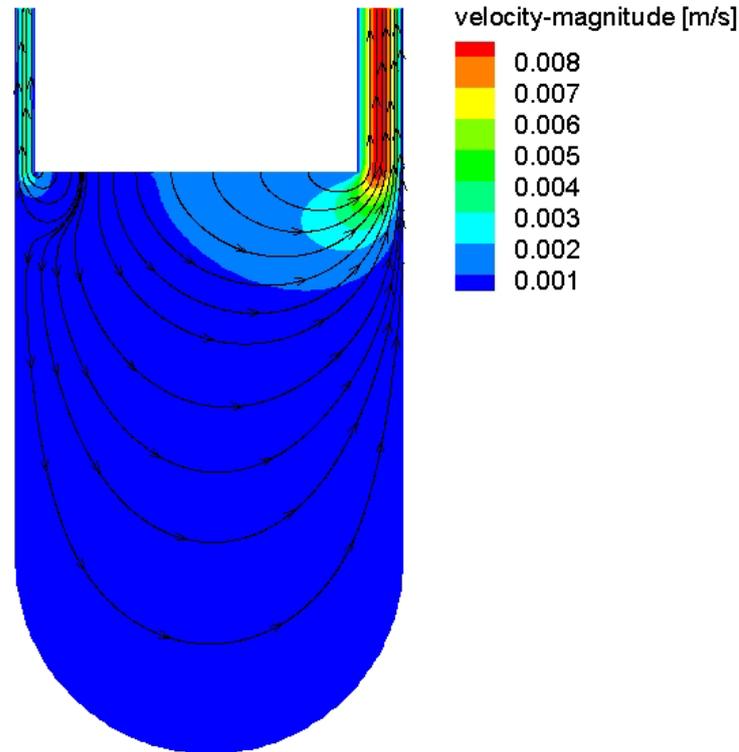
Figure 6-23: Streamlines implying the flow of the adhesive for a misaligned insertion defined by $\xi = 0.430$ at $t^* = 0.28$.

These streamlines indicate that the main flow direction from underneath the insertion plate is directed towards the wider flow channel. The streamlines are directed away from the maximum pressure location; as there is only one maximum pressure in the flow domain, its location is considered as the cause for the distribution of the adhesive.

For the cases studied in sub-Section 6.3.1.1 the pressure distributions underneath the insertion plate were determined at $t^* = 0.28$. The results are displayed in Figure 6-24. Within Figure 6-24 an *x*-position of -3 mm represents the left Pi-slot wall position and the right wall is at 3 mm. For the perfectly aligned case of equal 0.5 mm flow channel width on both sides the left insertion plate wall is located at -2.5 mm and the right insertion plate wall is located at +2.5 mm.
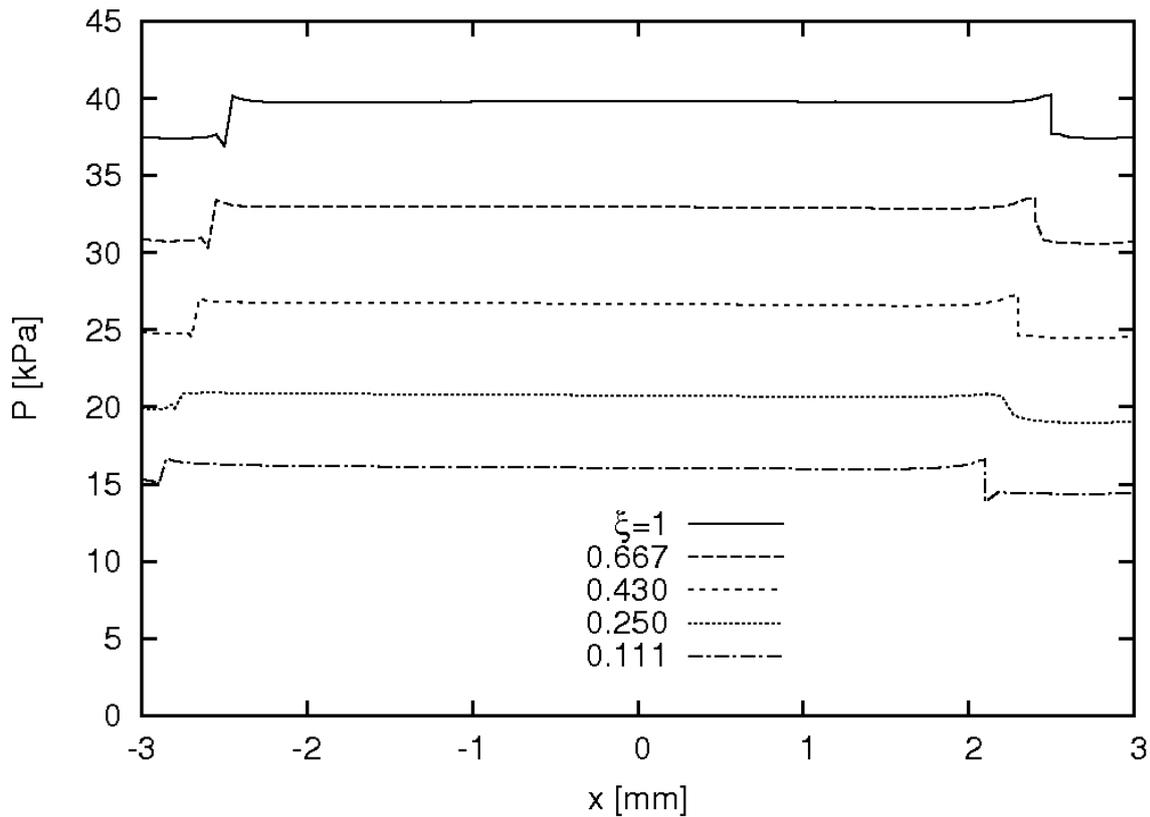
Figure 6-24: Pressure distribution along the insertion plate bottom for differently misaligned cases for t*=0.28.

For all cases in Figure 6-24 there is a similar shape to the pressure profile along the *x*-axis. The pressure is always higher underneath the insertion plate compared to the pressure that is in the flow channels, hence next to the insertion plate. As the degree of misalignment increases the left flow channel width decreases, which is indicated by the shift of the graph to the left hand side for higher misalignments. The insertion plate width remains constant for all cases at 5.0 mm.

Figure 6-24 shows that the pressure distribution under the insertion plate changes only slightly with misalignment. For each case a pressure maximum was detected, with its position depending on the misalignment. For example, in the non-misaligned case this maximum is located in the middle underneath the insertion plate bottom. It is displaced towards the narrower flow channel when the insertion plate is misaligned with greater displacements for greater misalignments (decreasing ξ).

To emphasize the maximum pressure location, the *dp/dx* gradient along the insertion bottom plate for the same cases is plotted in Figure 6-25.
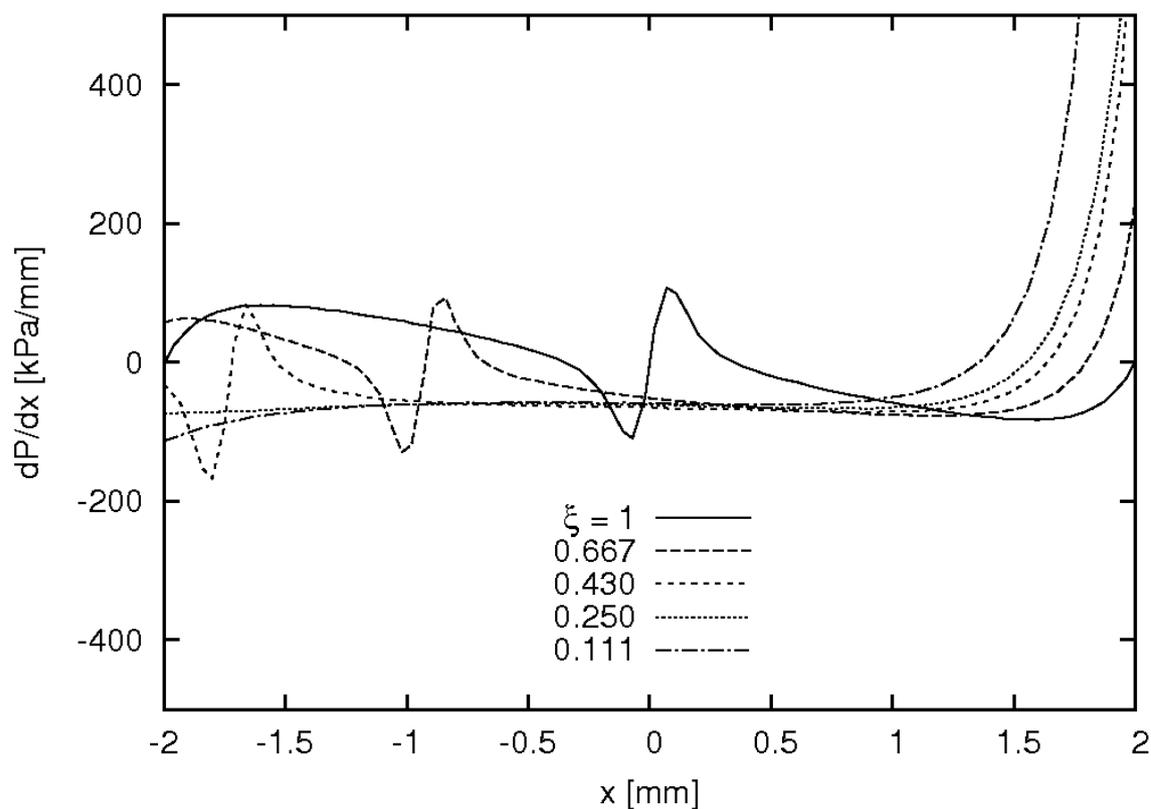
Figure 6-25: Pressure gradients along the insertion plate bottom for different misaligned cases for t*=0.28.

For the symmetrically aligned case and misalignments of 0.1 mm (ξ = 0.667) and 0.2 mm (ξ = 0.430) there are three zero *dp/dx*-position in the middle region underneath the insertion plate.This area is where the maximum pressures are found for these cases, and as described above, the particles' motion was away from these positions. For the other misaligned cases the position of the maximum pressure is located out of the plotting region and melds with another pressure peak which is located at the corner of the insertion plate at the narrow flow channel side. For these cases the adhesive flow is also away from the pressure maximum location, which results in more adhesive flowing towards the wider flow channel side.

6.3.3 Effect of different insertion head shapes

The effect of the insertion plate gemetry on the adhesive distribution was investigated to see whether there is a favourable design that would allow improved filling of the narrow flow channel if the plate is misaligned. The investigated insertion head shape designs were those illustrated in Figure 5-24 on page 151.

Keeping the insertion plate and Pi-slot widths constant, the insertion plate was misaligned with 0.1 mm. The resulting flow channel width ratio ξ is $0.4/0.6 = 0.667$. Material and process parameters were adhesive viscosity $=70 - 30$ mix, insertion speed $=60$ mm/min and the initial adhesive amount $=125$ volume percent; all remained constant for these tests. The fill height with respect to the time is plotted for the four different insertion head shapes in Figure 6-26.
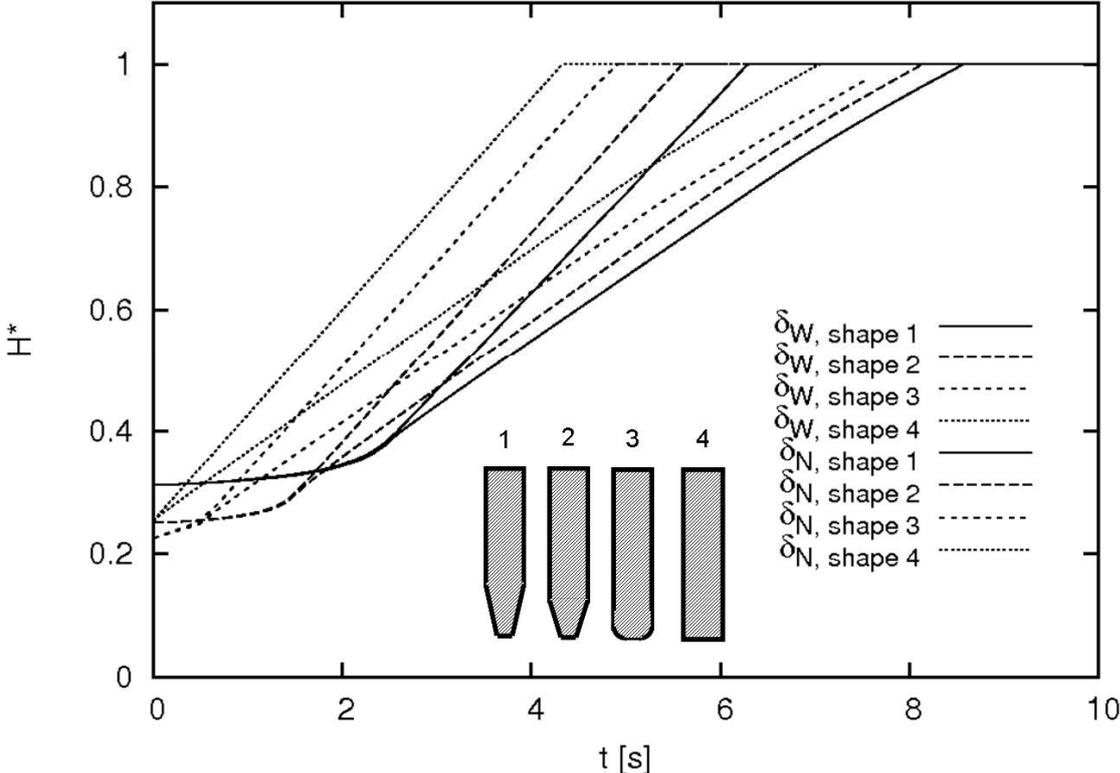
Figure 6-26: Transient fill height in the wide (W) and narrow (N) flow channels for different insertion head shapes.

As expected, the wider flow channels fill more quickly than the narrow ones but there is some difference in the rate at which the wider flow channel fills with head shape. Interestingly the rectangular design (shape 4) fills first, then the rounded head (shape 3) and finally the two tapered heads, with design 1 filling last. This general trend results from the initial adhesive flow; for the rectangular head the adhesive flows directly into the flow channels. However, for the rounded and more so for the tapered heads, the adhesive fills the tapered or rounded areas of the insertion plate head between the insertion head and the Pi-slot walls first, and only then begins to fill the flow channels. Hence the filling is slower simply due to the law of mass conservation and due to larger areas for the rounded and tapered heads to be filled compared to the rectangular head.

In all but one case (the rounded shape) all the narrow flow channels filled. For the rounded case the narrow channel did not fill due to the having an insufficient initial adhesive amount. As mentioned previously, when applying 125 volume percent the absolute amount of adhesive flowing out at the top of the flow channels for the rounded case is considerably smaller than the amount in, for example, the rectangular case. Applying more initial adhesive amount than 125 volume percent would be needed when the insertion plate head is rounded to ensure complete filling. In general, the quickest filling is achieved with the rectangular head due to the reason that the adhesive fills the flow channels directly, which is not the case for all other investigated head shapes, as described in the previous paragraph.

To evaluate the effect of insertion head shapes on the adhesive flow in both flow channels we derived flow front ratios for the investigated ξ ratio with respect to insertion head shape (Figure 6-27):
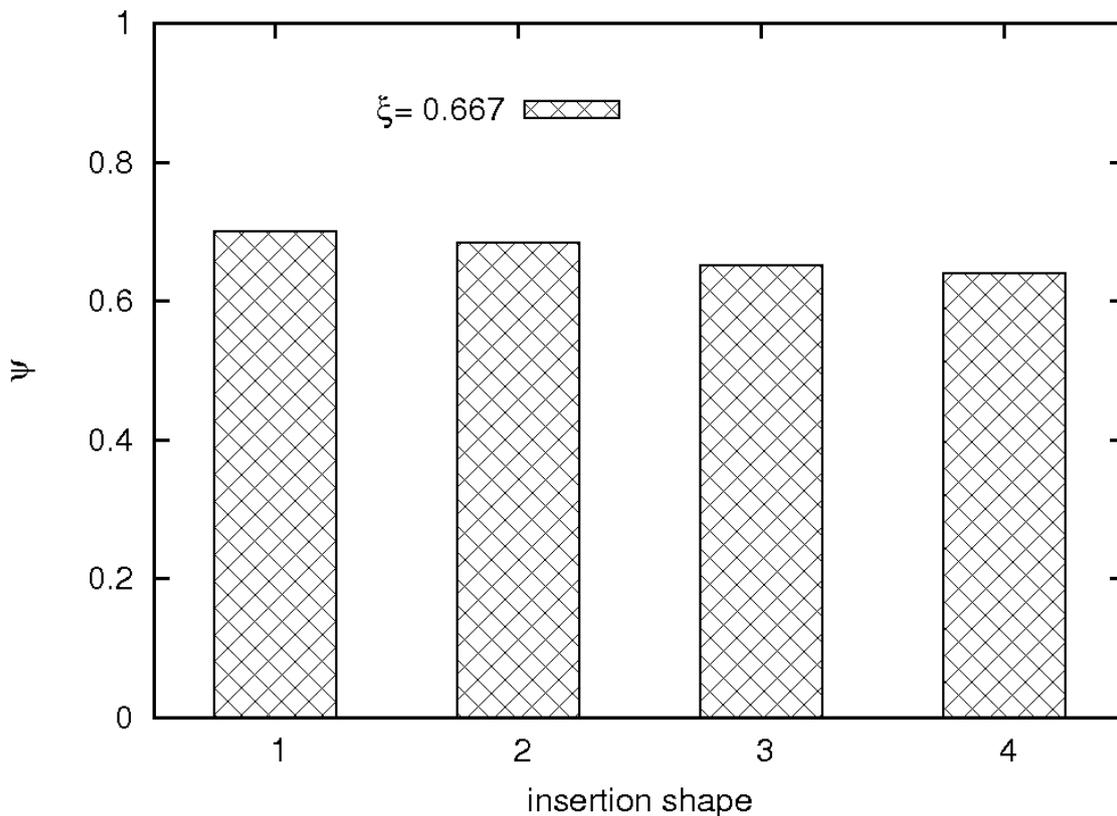
Figure 6-27: Flow front ratios for different head shapes for a misaligned insertion defined by ξ =0.667.

More equal adhesive distributions are predicted for both tapered insertion head shapes, which referred to as shape 1, which has a longer taper, and shape 2, which is tapered

shorter. The more equal filling with tapered insertion heads is due to the initial adhesive distribution before the adhesive flows into that flow channel's area which remains constant in width. The equal filling of the area between the tapered region of the insertion head and the Pi-slot walls can be explained as follows: the ratio of the flow channel widths in this area is close to 1 because the total flow channel width is large. In the initial stages of the process the local flow channel width ratio for the longer tapered shape (shape 1) would be $\zeta_{local} = 2.65/2.85 = 0.93$. The adhesive flow would behave as in an almost perfectly aligned case. Once the adhesive is displaced further and reaches the region where the flow channel widths are different, the distribution becomes asymmetrical, as can be observed from Figure 6-26 for the longer tapered shape (shape 1) after about 2.5 s.

To sum up, adhesive distribution was affected by the insertion head shape, with the most symmetric adhesive flow observed for tapered heads. The rectangular insertion plate head which was modelled in most of the presented simulations throughout this research showed the least equal adhesive distribution. Hence, simulating the rectangular shape can be considered as a worst case scenario.

6.4 Mitigating the Effects of Lateral Misalignment

In this section, the number of spacers needed to control alignment between the insertion plate and the Pi-slot, and hence flow channel width, is discussed. The results of a calculation of the bending forces on the insertion plate through applied spacers are also discussed.

6.4.1 Use of spacers

If the insertion plate and the Pi-slot were perfectly straight, did not vary in thickness, and remained so during the ISF only two spacers, one positioned at each end of the joint, would be needed to allow perfect alignment between the two components. However, in Section 6.1 it was shown that manufacturing tolerances and process-induced distortion are very common and will affect the flow channel widths. To ensure a pre-defined required flow channel width ratio, more spacers need to be applied over the Pi-joint length to force the insertion plate to bend back within the Pi-slot. The number of required spacers was estimated and results of the necessary number of spacers for a certain set-up are presented within this sub-section. In sub-Section 6.4.2, the force necessary to bend the insertion plate is calculated.

The minimum distance between two spacers required was derived by applying the following assumptions (Liu, 2009):

– The insertion plate is rectangular with dimensions as specified in Figure 6-28 being 300 mm, 5 mm and 1320 mm for the height *H*, width *W* and length *L*;
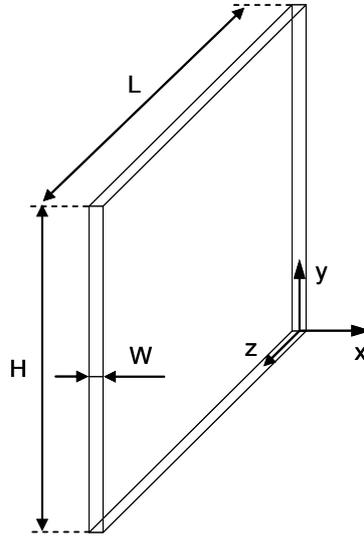
Figure 6-28: Variables defining the dimensions of the insertion plate.

– There is no penetration of spacer into the composites (i.e. the spacers restrain the insertion plate);

– the Pi-slot is perfectly straight and does not deform during ISF;

– bending of the insertion plate in the *z*-direction is assumed to form a circular arc (MoJo, 2007);

– as illustrated in Figure 6-29 after the spacers are applied the insertion plate region between the two spacers also bends as a circular arc;

– the deflection limit is set to 10% of the total flow channel width of a standard Pi-joint, hence 0.1 mm.
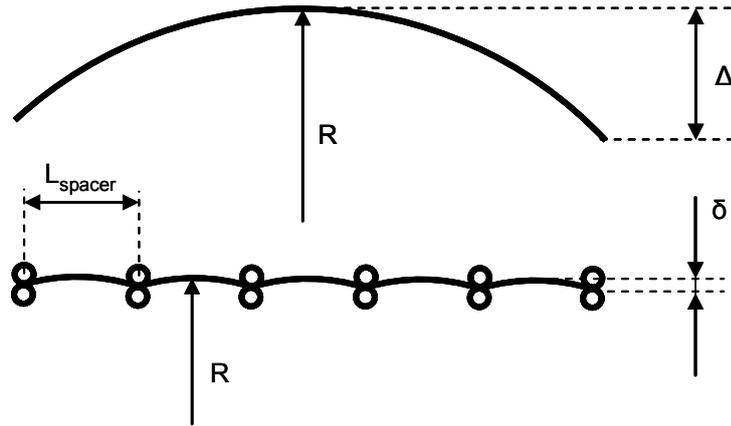
Figure 6-29: Circularly bended insertion plate before and after restrained by spacers.

To calculate the radius of bending, geometrical relations according to Figure 6-30 and provided in equation (6-12) were used:

$$R = \frac{\Delta^2 + (L/2)^2}{2\Delta} \qquad (6\text{-}12)$$
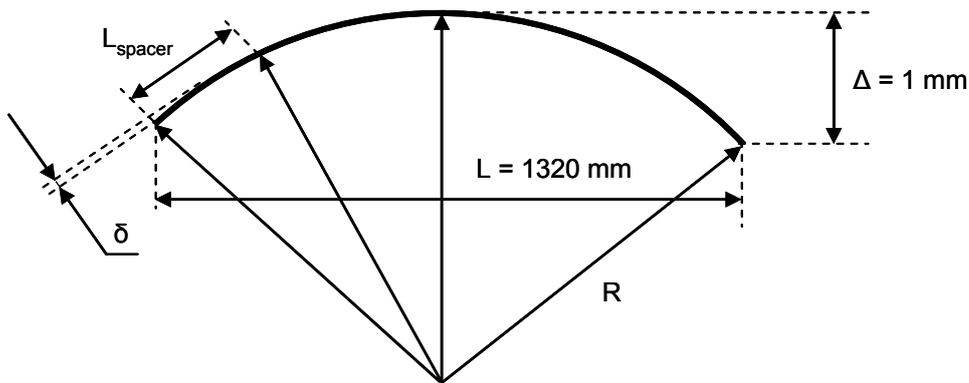
Figure 6-30: Geometrical relations for estimating the number of spacers (not to scale).

The radius R was calculated to 217.8 m if L and Δ were substituted into equation (6-12). Rearranging and solving for L_{spacer} according to the geometrical relations from Figure 6-30, the distance between two spacers can be calculated as:

$$L_{spacer} = 2\sqrt{2R\delta - \delta^2} \qquad (6\text{-}13)$$

For the specified values of L (1320 mm) and deflections limits for δ (0.1 mm) the calculated distance was 417.4 mm. Hence five spacers would be needed with an actual distance between each spacer of 330 mm.

6.4.2 Bending forces on insertion plate due to spacers

To calculate the bending forces acting on the insertion plate due to applied spacers, we assumed the insertion plate to behave as a simply supported beam, as shown in Figure 6-31 for the case considered in sub-Section 6.4.1:
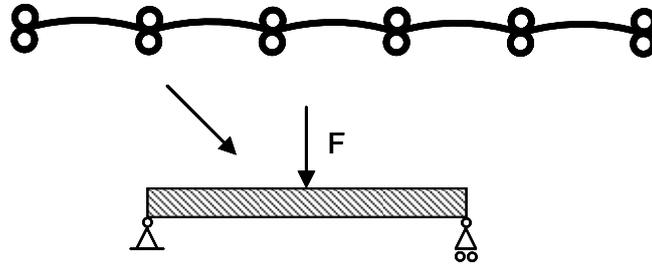
Figure 6-31: A simply supported beam model applied for the calculation of the bending force that acts at the insertion plate due to spacers.

The middle spacer was substituted with a force *F*. Before calculating *F*, the actual distance between spacers was derived to be 1320 mm/5 = 330 mm and from equation (6-13) the actual deflection to be $\delta = 0.06$ mm. Now, applying the classic beam theory (efunda, 2009), the force to cause a deflection of δ can be calculated as:

$$F = -\delta \frac{48\ EI}{\left(2L_{spacer}\right)^3} = -\delta \frac{6\ EI}{\left(L_{spacer}\right)^3} \qquad (6\text{-}14)$$

E specifies the Young's modulus (in-plane) of the insertion plate, which is taken as 50 GPa, and which was provided for the insertion plate as a good approximation although considered as isotropic, which indeed is not the case for a composite. *I* is the moment of inertia of the beam section and L_{spacer} was taken as 330 mm. *I* can be calculated as

$$I = \frac{HW^3}{12} = \frac{300 * 5^3}{12} = 3125\ mm^4. \qquad (6\text{-}15)$$

Substituting all variables into equation (6-14) results in a force of 1.57 N.

6.5 Summary

Misalignments that may occur during ISF are angular or lateral, with the latter found to be the most critical one for the adhesive distribution as it affects the flow channel widths. Lateral misalignment and a variation of flow channel widths can be caused by manufacturing tolerances, composite spring-in effects and can be induced through the insertion process.

It was found that the adhesive flow strongly depends on the flow channel width ratio, showing a linear relation between the flow front ratio and the flow channel width ratio of the narrow and wide flow channel. This relation is not affected by the insertion speed, the adhesive viscosity nor the initial adhesive amount for the ranges considered, and scarcely depends on the total flow channel width. Following the research done here, two procedures were proposed to ensure entire filling of the narrow flow channel.

The insertion plate head shape was found to affect the relation between the flow front ratio and the flow channel width ratio. The rectangular shape is found to be the one that results in the poorest filling of the channels in terms of equal adhesive distribution, while the most equal filling of the flow channels is found for the longer tapered insertion head design.

Finally, mitigation of lateral misalignment effects can be achieved through the use of spacers. The distance between the spacers depends on the required tolerancing, using the case studied here as an example, an approach was developed for determining spacer placement to meet tolerancing required. The consequential bending forces acting on the insertion plate due to the spacers were also calculated.

7 Extensions of the Numerical Model for Insertion Squeeze Flow

This chapter contains four sections. First, insertion squeeze flow (ISF) at constant insertion force is considered. Following this a variation of the ISF process is examined, which considers the pre-application of adhesive onto the Pi-slot walls. Third, the effect of the fluid structure interaction (FSI) on the adhesive flow during ISF at constant speed is analysed, i.e., to examine the effect of slot distortion during the process due to the high pressures on the walls. Finally, the two-dimensional (2D) numerical model presented in previous chapters is extended into a three-dimensional (3D) model to consider possible 3D flow variations and the effect of spanwise misalignment. The chapter is summarised with concluding remarks.

7.1 Insertion Squeeze Flow at Constant Insertion Force

7.1.1 Introduction

An ISF process can be conducted using controlled insertion, with either constant speed or constant force. In a constant force controlled insertion mode, as implied, the insertion plate movement is achieved through the application of a constant force upon the insertion plate. In practice, a constant force insertion can be achieved through the use of pneumatic pressure cylinders.

Considering basic physical relations describing the problem, drag forces acting on the insertion plate resist the motion of the insertion plate. As mentioned earlier, these drag forces can be subdivided into two components: the shear force on the sidewalls and the pressure force on the bottom wall of the insertion plate. In the constant speed insertion analysis, these force components represent the retarding force, that frequently has been referred to as the insertion force. For constant speed insertions, this force was observed to increase with displacement of the insertion plate. Hence, it would be expected that during a constant force insertion, the motion of the insertion plate would slow the further it descends into the adhesive because of the increasing resisting pressure and shear.

Within Section 7.1 a numerical model is developed which simulates an ISF process conducted at constant force insertion. The variables recorded include the insertion plate speed, acting forces and pressures, as well as the adhesive flow in the flow channels. For

validation purposes, we considered if the above described physical actions can actually be observed. A comparison is made between the constant force and the constant speed variants with reference to the insertion speed versus displacement behaviour.

7.1.2 Numerical Method

Within Fluent the velocity components can be set to apply a prescribed motion to a specified boundary. A force cannot directly be specified to act at a boundary. The time-dependent velocity of a moving boundary that results from an applied force has to be calculated as part of the time-stepping procedure.

The approach applied to derive the moving boundary velocity is based on a force balance on the moving object, which in this case is the insertion plate. Figure 7-1 illustrates the problem set-up again at the left. On the right, parameters are introduced which have to be taken into consideration for a force balance on a moving insertion plate.
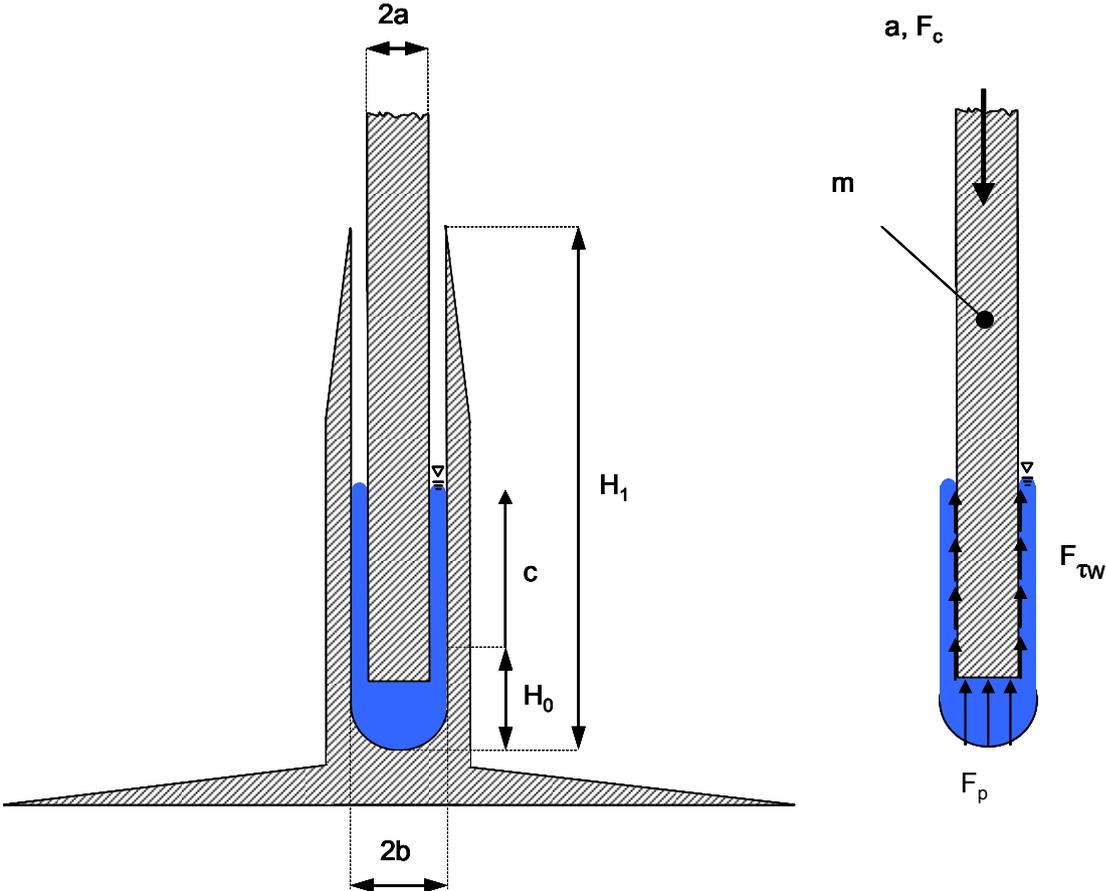
Figure 7-1: Schematic problem set-up and definition of parameters for the force balance.

On the right hand side of Figure 7-1, *a* represents the acceleration of the insertion plate, F_c is the constant force applied to the insertion plate, F_p is the pressure force and $F_{\tau W}$ is the

wall shear force. It is assumed that the insertion is strictly in the verical direction so that only the verical force balance is of interest. The mass of the insertion plate is represented by the symbol *m*.

Applying a force balance on the insertion plate in the vertical direction gives:

$$a \cdot m = F_p + F_{\tau W} - F_c \qquad (7\text{-}1)$$

Writing the acceleration *a* in terms of the rate of change of the velocity (*dv/dt*) and rearranging gives an expression for the change in insertion plate velocity over a timestep:

$$dv = \frac{dt}{m} \cdot \left[F_p + F_{\tau W} - F_c \right] \qquad (7\text{-}2)$$

Thus the velocity can be incremented each timestep to maintain the constant insertion force. In this expression, F_c and *m* are constant, while F_p, $F_{\tau W}$ (and possibly *dt*) are time-dependent variables, hence an iterative update is required. This can be accomplished by using a *user-defined function* (UDF) within the Fluent software to return the velocity given the force components.

The Fluent UDF manual states that "A user-defined function, or UDF, is a function […] that can be dynamically loaded with the Fluent solver to enhance the standard features of the code", ll. 16-17, p. 1-1,(Fluent, 2005a). It is written by the user in the C programming language and makes use of predefined macros that are provided by Fluent and defined in header files (Fluent, 2005a). The Fluent UDF user guide (Fluent, 2005c) gives details on the construction of UDFs.

In the case considered here, a constant-force moving-boundary UDF was programmed and applied to simulate a constant force ISF process. The programmed UDF file is provided in Appendix A.

The following block diagram is provided to show the interaction of the UDF and the flow solver of Fluent:

UDF:

balancing acting forces,
determining dv,
adjusting v += dv

FLUENT:

moving insertion plate with v,
predicting resisting forces

Providing insertion
velocity to FLUENT

Providing resisting
forces to UDF
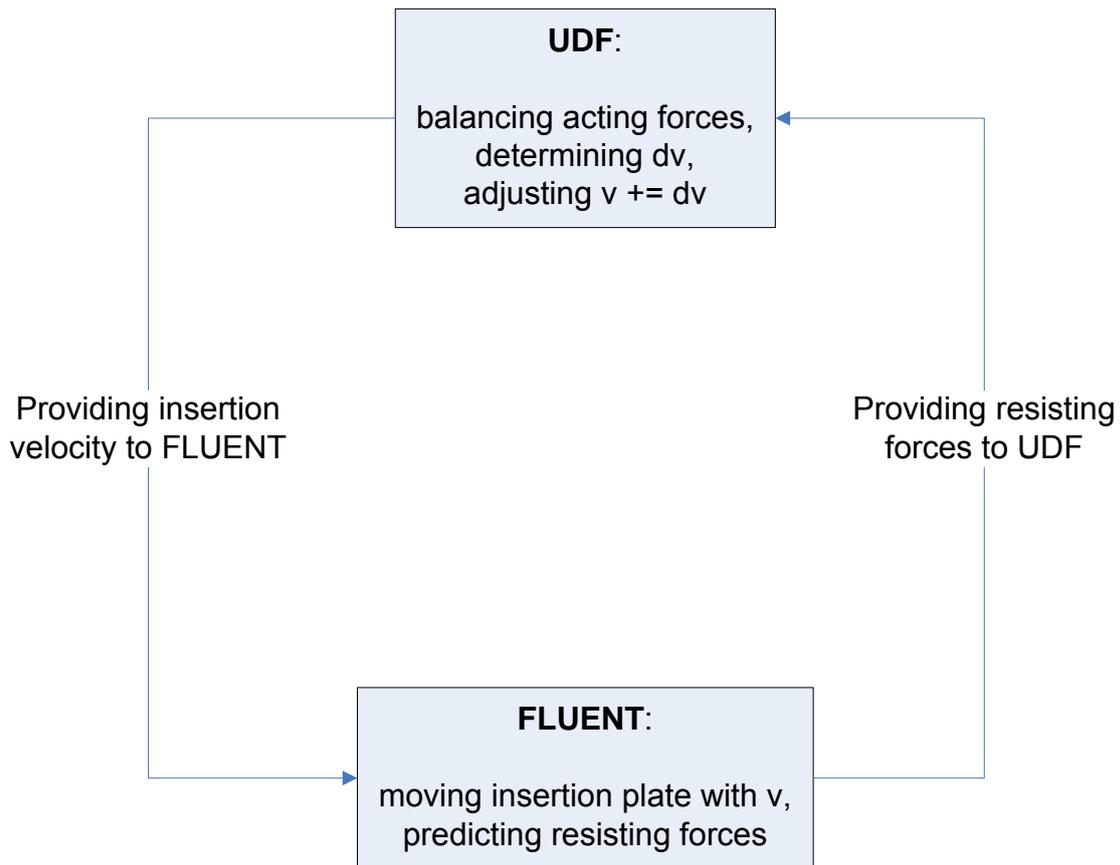
Figure 7-2: Block diagram showing the interaction between the constant force UDF and the Fluent software.

Based on the forces acting, within the UDF the force balance calculation is conducted according to equation (7-2). The computed velocity change is added to the velocity at the previous time step (n-1), which is passed to the flow solver to define the plate boundary velocity. Fluent then applies the newly determined velocity for timestep n to the moving boundary and advances to the next timestep (n+1) when iteration terminates if convergence criteria of the continuity and momentum equations are reached. The boundary moves according to this velocity. Pressure and shear forces along the insertion plate walls are calculated and provided to the UDF. Using these newly obtained forces, the rate of velocity change for the next time step (n+1) is calculated within the UDF, then the velocity is updated and provided to Fluent again. This procedure is conducted every time step.

7.1.3 Results and discussion

The results presented in this section were obtained from the numerical model for constant force insertion for the set of the baseline parameters unless otherwise stated. The baseline parameters were a constant insertion force of 3000 N/m, an adhesive viscosity for

a 70-30 weight percent ratio EA 9395 to EA 9396 implemented according to the five parameter rational model, and standard dimensions, which were 5.00 mm insertion plate width, 6.00 mm Pi-slot width and 35.5 mm Pi-slot height. The Pi-slot bottom inner radius was 3 mm. The selected value for the standard constant insertion force was set from an estimation of the imposed pneumatic cylinder pressure on the insertion plate during the practical insertion process (Scholler, 2007). The widths of the gaps between the insertion plate and the Pi-slot wall (flow channel widths) were 0.5 mm for the aligned case. The volume of adhesive was specified as 125% of the volume required to fill the flow channels completely when the insertion plate reaches its final position. The shape of the insertion plate head was rectangular.

Figure 7-3 shows a plot of the insertion plate speed as a function of the displacement of the insertion plate during the ISF process.
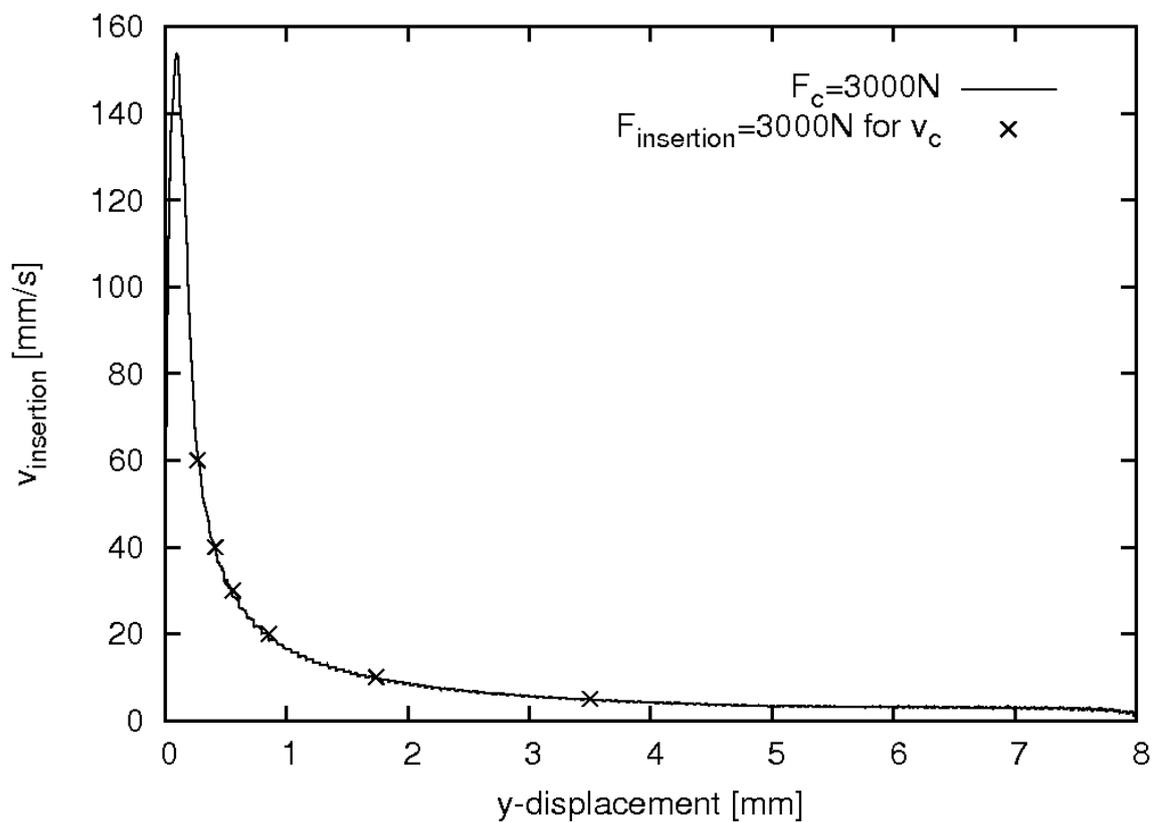
Figure 7-3: Insertion plate velocity as a function of the insertion plate position for a constant force of 3000 N/m. The crosses show results from constant speed tests when the insertion force is equal to 3000 N/m.

The *y*-axis shows the speed of the insertion plate in the vertical direction that results from the constant force induced motion. This speed is plotted against the insertion plate position.

The solid line shows the results for the insertion plate speed directly obtained from a simulation at constant applied force. The crosses indicate results from constant speed insertion studies at 60, 40, 30, 20, 10 and 5 mm/s. These points correspond to when the insertion force is 3000 N/m. They were determined from insertion force versus insertion plate displacement graphs for the constant speed cases. An example is provided in Figure 7-4 below showing the behaviour for an insertion speed of 30 mm/s.
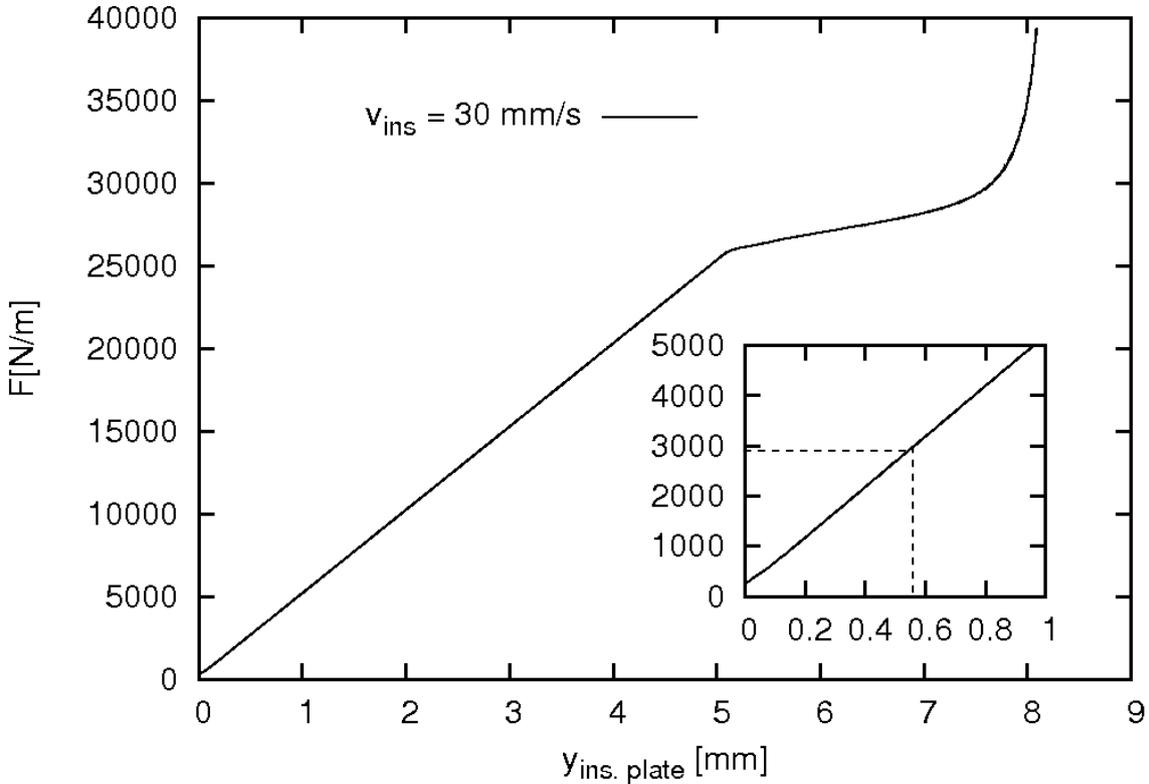
Figure 7-4: Insertion force versus insertion plate position for an insertion speed of 30 mm/s.

In the magnified inset within Figure 7-4 an insertion force of 3000 N/m can be seen to correspond to a displacement of 0.57 mm. This displacement matches well with the value for constant force insertion (also 0.57 mm). When comparing results from the constant force insertion and constant speed insertion tests it is clear that that the values agree very well. Further constant force-constant speed comparisons not presented here also show the same tight match. Hence it was concluded that it is possible to determine the insertion plate

speed versus position behaviour indirectly from several constant speed insertion simulations.

In Figure 7-5 a plot is illustrated of insertion plate speed versus dimensionless time $t*$ for an insertion force at 3000 N/m:
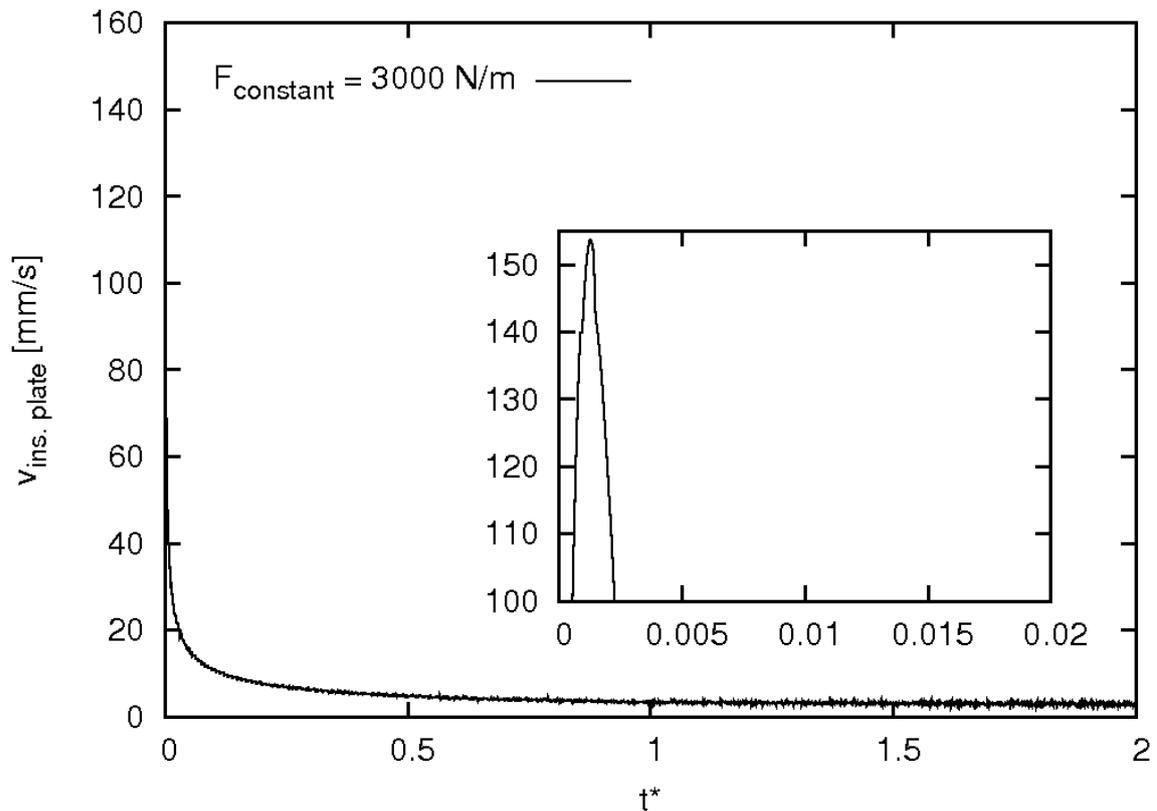
Figure 7-5: Insertion plate speed plotted against dimensionless time for a constant force insertion at 3000 N/m.

The time was non-dimensionalised by dividing the process time by the time period for the adhesive to reach the top of the flow channels. The insertion speed increases significantly in the initial stages of the process (until $t* = 0.00125$) before decelerating afterwards. The insertion speed appears to reach an asymptotic value from a dimensionless time of about 1 onwards.

The behaviour of the insertion speed versus time reflects what would be expected during insertion under a constant force: to begin with, the plate speed would increase as the plate accerlerates until drag increases to a value that is higher than the imposed constant force. Thus subsequently the plate will decelerate, leading to a slowing of the motion.

The initial insertion plate speed increase can be explained by considering equation (7-2) and Figure 7-6. In Figure 7-6 the drag force on the insertion plate, i.e. the pressure force at

the insertion plate bottom and the shear forces along the insertion plate side walls, is plotted against dimensionless time.
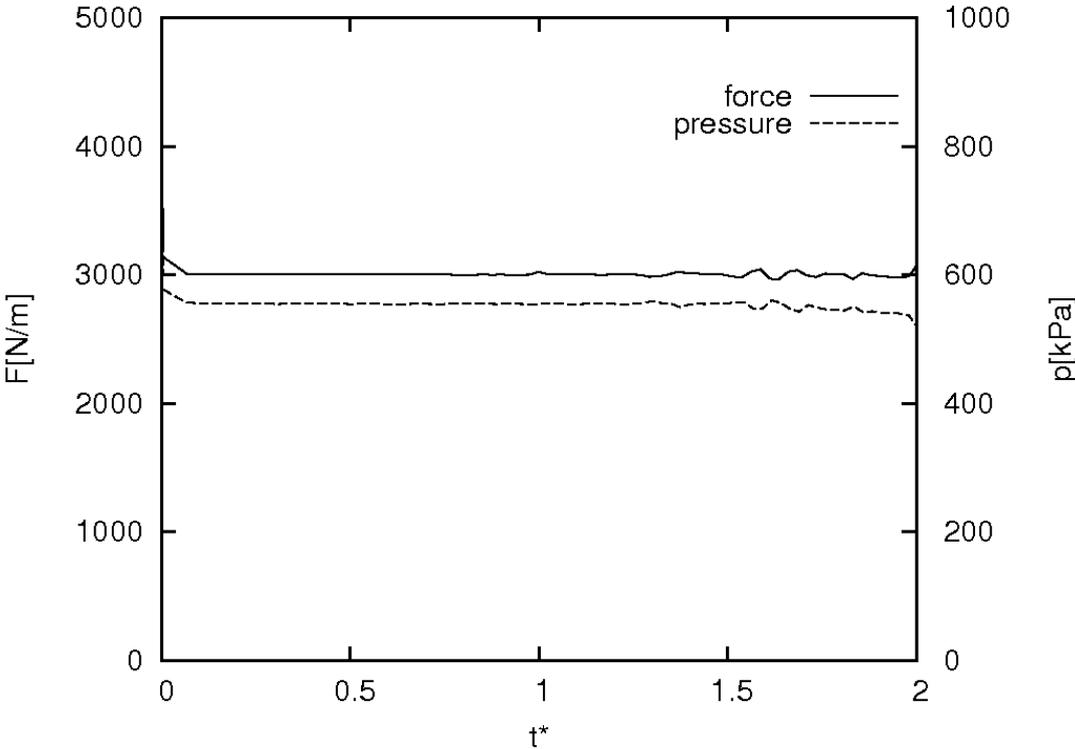
Figure 7-6: Drag force on the insertion plate with respect to dimensionless time shown by the solid line. The maximum pressure acting at the Pi-slot walls (dotted line) with respect to dimensionless time is also shown.

The drag force increases initially (hardly seen in the figure), reaches its peak before decreasing to a magnitude of slightly in excess of 3000 N/m after about $t^* = 0.05$. The smaller the drag force over the beginning stage of the process, the larger the resultant downward force and hence the larger the (negative) acceleration. Hence, as long as the constant applied force is higher than the drag force the insertion plate speed will increase ($t^*<0.00125$).

The speed reaches its peak at the moment when the drag force values become greater than the applied force. After this time the acceleration becomes positive, leading to a positive *dv* value and thus to a decrease in the insertion speed ($t^*>0.00125$). For this case, these events are summarised.

$$dv = \frac{dt}{m} \cdot \left[F_p + F_{\tau W} - F_c \right] \qquad (7-2)$$

$$0 \leq t* < 0.00125 : F_{drag} = F_p + F_{\tau W} < F_c$$

$$\Rightarrow dv < 0$$

$$v_n = v_{n-1} + dv \Rightarrow |v_n| > |v_{n+1}| \qquad (7-3)$$

$$t* > 0.00125 : F_{drag} > F_c$$

$$\Rightarrow dv > 0 \Rightarrow |v_n| < |v_{n-1}|$$

After reaching a peak, the drag force plotted in Figure 7-6 decreases slowly until it reaches a similar, but slightly larger, value to the applied constant force. This is reflected in the continuing deceleration of the insertion plate. The slowing continues reasonably smoothly until a non-dimensional time of approximately one. At that time the adhesive reaches the top of the Pi-slot and starts to be extruded out the ends. Hence after this time, it could be expected that the configuration contributing to the drag, i.e., the adhesive in the filled gaps applying a shear force to the plate and the pressure at the plate end, does not change at the same rate. Thus it could be expected that the insertion velocity would maintain an almost constant value beyond this time. The observed insertion speed variation with displacement, or time, supports this explanation. Note that there is some variation of the drag from the constant applied force especially at larger times. It is unclear whether this is a resolution/convergence issue or a result of nonlinear flow effects associated with the adhesive flowing out into the open domain or secondary flows at the bottom of the slot.

The pressure acting along the Pi-slot walls is now considered in view of the fact that it can potentially cause distortion of the slot. Recall that for the constant speed simulations, a relationship could be established between the insertion force and the pressure on the Pi-slot walls. For the constant force insertion results here, it is again noticed that there might be a relationship between these two parameters. Therefore in Figure 7-6 the maximum pressure acting at the side walls of the Pi-slots is plotted with respect to dimensionless time, shown by the dotted line. Also, from the constant insertion speed simulation results, it was shown that the local pressure maximum was always found at the root of the Pi-slot wall (Figure 5—17, page 138).

Considering the pressure graph presented in Figure 7-6, it is noticed that the pressure increases significantly at the very beginning, then decreases slightly before becoming constant. A similar trend was detected for the transient drag forces acting on the insertion plate; hence, it was supposed that a connection between the (plate) force and the (Pi-slot) pressure exists.

After the initial, sharp increase, followed by a less severe decrease, the pressure levels out at a magnitude of about 555 kPa. Dividing the drag force of approximately 3000 N/m by the pressure acting as was previously done for the constant speed simulations in Table 24, page 141, the value of F [N/m] / p [kPa] = 5.405 [10^3m] is obtained. This is within 0.2 % to the force-pressure ratio derived for the constant insertion speed simulations (see sub-Section 5.3.3).

An important parameter for ISF processes conducted at constant force is the process time. Several simulations were set up with varying constant force values and their effect on the process time was studied. The simulations used the baseline parameters specified earlier and the constant applied force levels set to 400 N/m and 2000 N/m in addition to the already presented case of 3000 N/m. A 'stop'-position was defined at which the process time is compared for different values of the applied force. The chosen 'stop'-position corresponds to after the insertion plate has travelled 8 mm from its starting posititition; the closest distance between the insertion plate head and the Pi-slot bottom is then 1 mm. The y-displacement of the insertion plate with respect to flow time is presented in Figure 7-7:
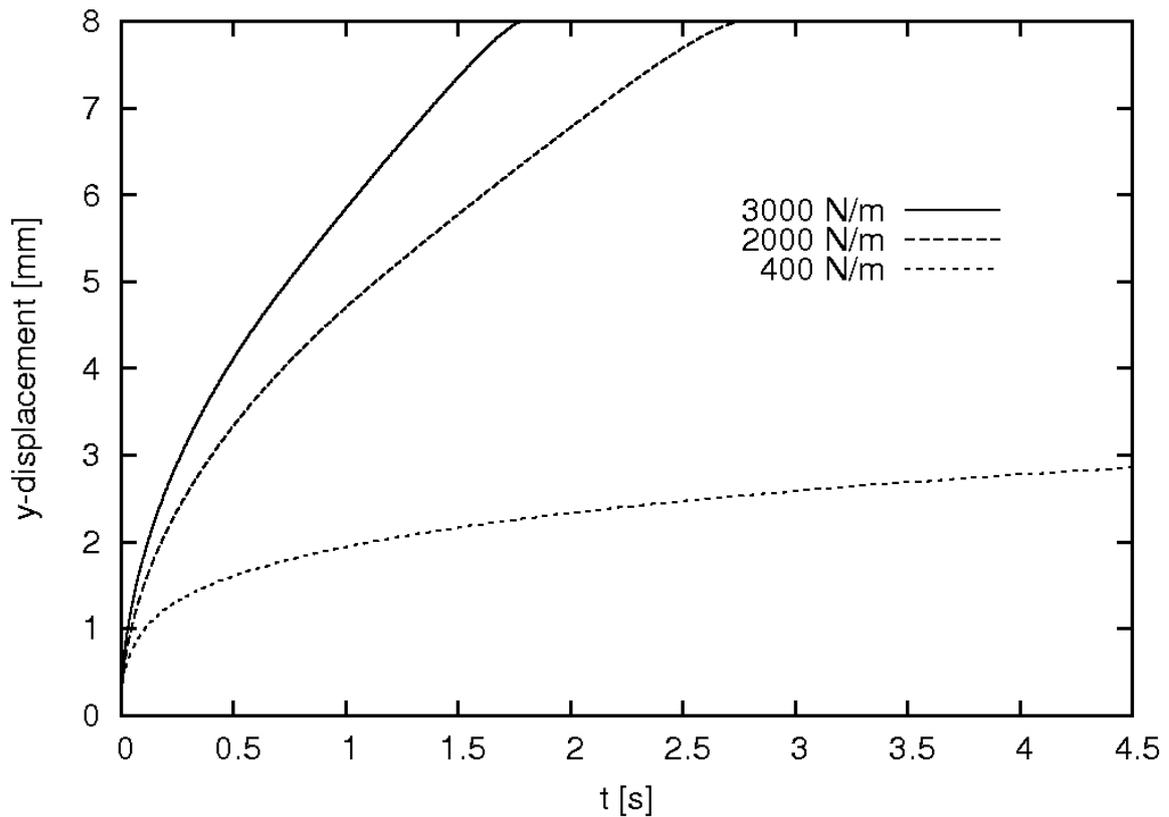
Figure 7-7: Displacement of the insertion plate from its original position plotted against process time for different applied forces.

In line with previously presented results, the displacement increases rapidly at first and then slows down with increasing flow time because the adhesive's resistance against flowing increases as the flow channels fill. For the 2000 N/m and the 3000 N/m simulations, the simulation could be conducted until reaching the 'stop' position. The process time decreases from 1.31 s for 2000 N/m to 0.77 s when the applied force is 3000 N/m.

When the applied force was decreased to 400 N/m, the 'stop'-position could not be reached. The simulation was terminated after running for 336 h (2 weeks) and after that time the displacement was only 2.9 mm for a flow time of 4.5 s. The large simulation time resulted from the requirement that the adaptive timestep for the constant force simulations had to be very small, resulting in a timestep size of the order of (O^{-6}). The small timestep was required to avoid oscillation of the solution, which would cause divergence otherwise. The oscillation would appear if the change in velocity over a timestep became very small. The effect was more pronounced for smaller applied forces hence the timestep size had to

be decreased compared with the timestep size specified for the higher force simulations (2000 N/m, 3000 N/m).

Finally, the effect of a misalignment during plate insertion on the adhesive distribution is considered. The dimensions of the insertion plate and the Pi-slot remained the same but the insertion plate was displaced laterally by a value of 0.1 mm. Resulting flow channel widths for this misaligned case were therefore 0.6 and 0.4 mm for the wide and the narrow channel. This corresponds to a dimensionless flow channel width ratio $\xi = 0.667$.

Figure 7-8 illustrates the behaviour of the fill height H^* versus non-dimensionalised time.
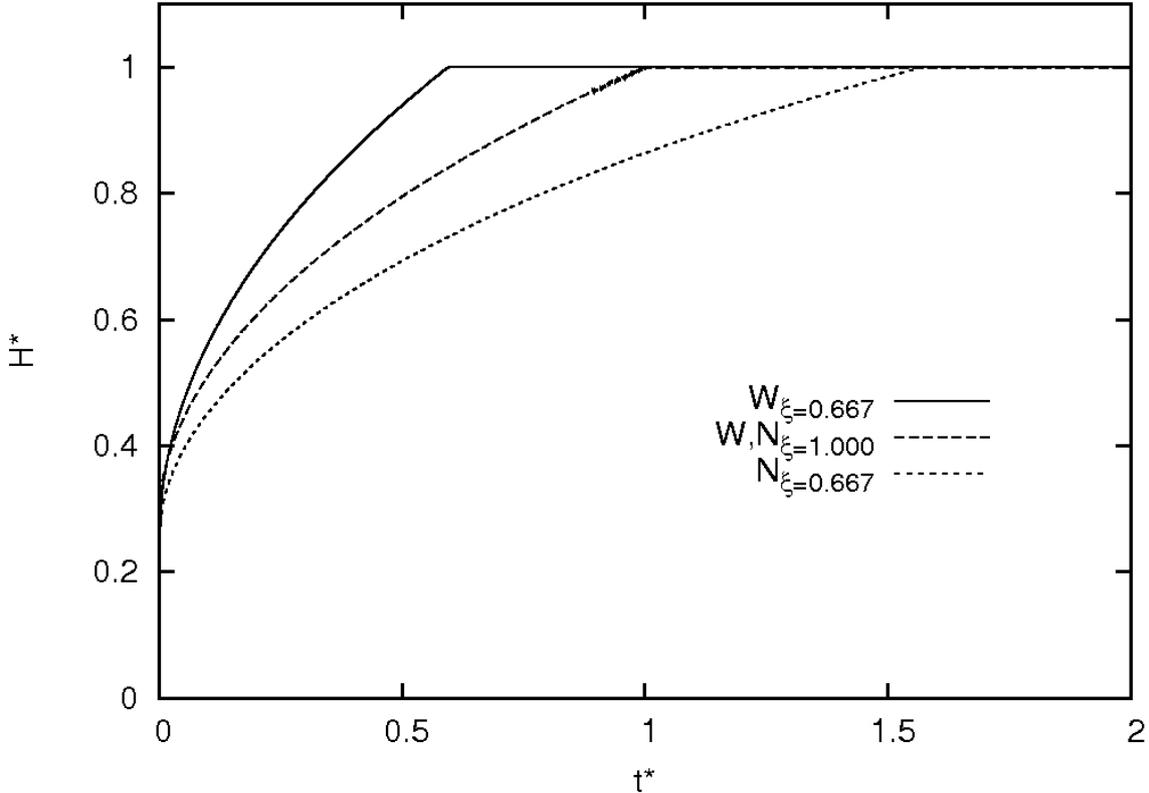
Figure 7-8: Adhesive flow comparison between a misaligned and a perfectly aligned constant force ISF process.

The time scale used to non-dimensionalise was the time for the complete filling of both flow channels for the aligned case. As indicated in Figure 7-8 filling of both flow channels for a misaligned insertion with a flow channel width ratio of 0.667 is possible. The wider flow channel fills more quickly; the narrower flow channel is filled after a dimensionless time of about 1.55.

These observations tally with those for constant insertion speed insertions. Agreement between the simulations with $\xi = 0.667$ is obtained, in the sense that both flow channels fill and, of course, that the wider flow channel fills first.

Next, the positions of the flow fronts in the channels were considered by examining the height ratio of the narrow and wide channel, referred to as ψ. This ratio is plotted against time in Figure 7-9.
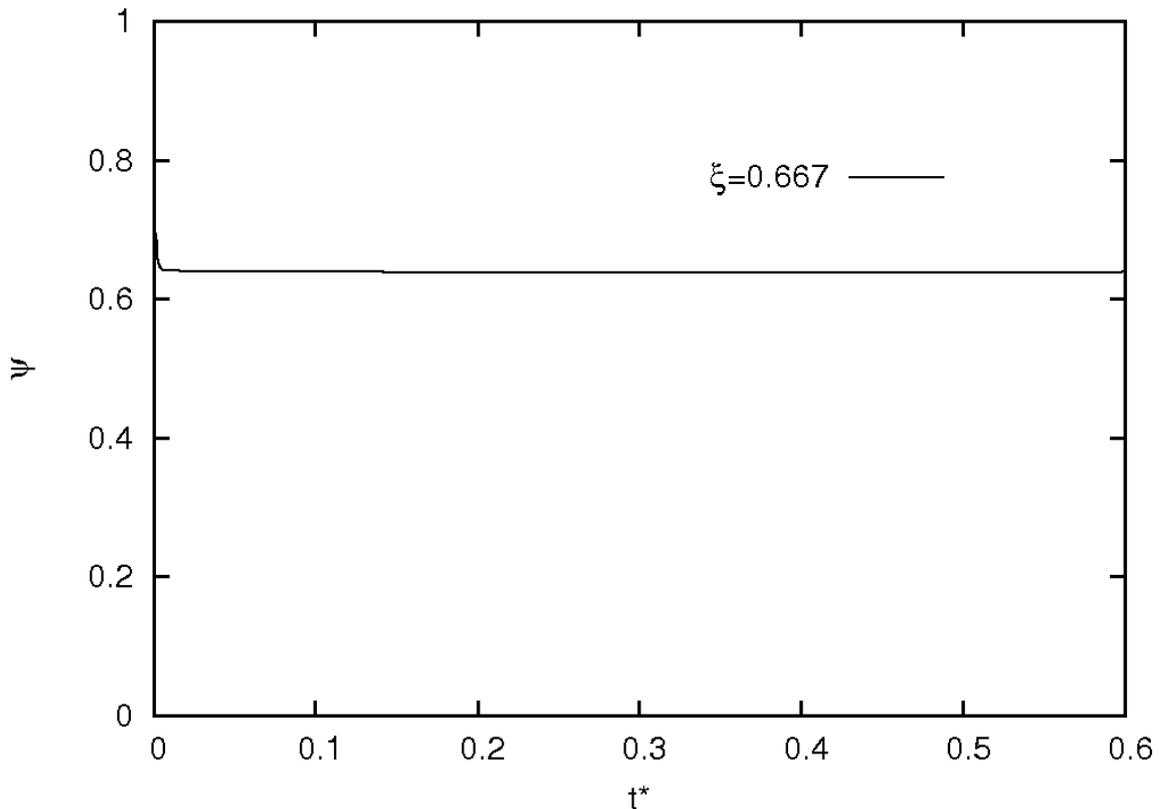
Figure 7-9: Flow front ratio as a function of dimensionless time (ξ=0.667).

Except at the very beginning, the graph shows that the flow front ratio is independent of time for the considered case of $\xi = 0.667$, at least up to a dimensionless time of $t^*=0.6$. This time corresponds to the period before the adhesive starts to flow out of the wider channel. The ratio remains constant with a value of 0.638.

Recalling the results for the constant speed insertion again, especially considering Figure 6-12 on page 174, it can be seen that for $\xi = 0.667$ the values obtained from the constant speed insertion and the values from the constant force insertion are very close to each other. This result indicates that Figure 6-12 can be applied for constant force insertions as well. To support this suggestion, an explanation is provided why the constant

insertion speed and the constant insertion force insertions provide similar relationships between the output parameters.

The Reynolds numbers for both constant speed and constant force insertion were considered. For a constant speed insertion, the Reynolds number is in the order of 10^{-4}, calculated with the following values:

- Density $\rho = 10^3$ kg/m^3,
- Flow velocity $v = 10^{-2}$ m/s, derived from insertion speed of 60 mm/min,
- Length scale $L = 10^{-3}$ m, derived from the flow channel width,
- Adhesive viscosity $\eta = 10$ kg/(ms), derived from viscosity versus shear rate graphs at high shear rates which correspond to the flow velocity;
- All applied values are conservative values within a reasonable range in a sense to derive a *Re* number as high as possible.

For a constant force insertion, the Reynolds number is in the order of 10^{-2}, calculated with the following values:

- Density $\rho = 10^3$ kg/m^3,
- Flow velocity $v = 10^1$ m/s, derived from a maximum insertion speed at a constant force insertion with 3000 N/m,
- Length scale $L = 10^{-3}$ m, derived from the flow channel width,
- Adhesive viscosity $\eta = 10$ kg/(ms), derived from viscosity versus shear rate graphs at high shear rates which correspond to the flow velocity;
- All applied values are conservative values within a reasonable range in a sense to derive a *Re* number as high as possible.

Hence, the Reynolds numbers for both insertion types are clearly considerably less than unity, constituting a low Reynolds number flow. This flow typically is governed by a balance between pressure and viscous forces with inertia effects being negligibly small (Munson, 2006). For immersed body flows such as the one considered here, the drag force D consists of two parts; the friction drag due to wall shear stresses and the pressure or form drag due to pressure forces (Munson, 2006). Furthermore, the drag coefficient c_D, defined as $D/(1/2\ \rho v^2 A)$, becomes inversely proportional to the Reynolds number. The relation between the Reynolds number and the acting drag for the provided information is considered:

$$c_D = \frac{D}{\rho \frac{v^2}{2} A} \qquad\qquad (3\!-\!35)$$

$$D = F_{drag} = F_p + F_{\tau W}$$

$$c_D = \frac{2C}{Re} \; ; \text{if } Re < 1; \text{ C being a body shape dependent constant}$$

$$c_D = \frac{D}{\rho \frac{v^2}{2} A} = \frac{2C}{Re} \qquad\qquad (7\text{-}4)$$

$$D = F_p + F_{\tau W} = \frac{2C\rho \frac{v^2}{2} A}{Re} = \frac{2C\rho \frac{v^2}{2} A}{\dfrac{\rho v L}{\eta}} = \frac{C v A \eta}{L} \qquad\qquad (7\text{-}5)$$

It is clear from equation (7-5) that the drag is a function of the flow velocity. In addition, the pressure varies linearly along the flow channel. This is true for both the constant speed and the constant force cases, hence there is a correlation between them and results obtained for one are valid for the other insertion technique.

In conclusion, it was shown that for cases such that $Re < 1$, the different methods of insertion (constant speed or constant force) provide equivalent results. This means that for the considered range of input parameters presented within this research, relationships established from the constant speed insertion can be applied to constant force insertions.

7.2 Insertion Squeeze Flow with Adhesive Pre-Application

One variation of the ISF process might include pre-applying a thin layer of adhesive on the insertion plate side walls before conducting the ISF process. A favourable adhesive flow could be expected in practice as the adhesive would flow over a smoother surface. To generate this layer adhesive would be applied on the insertion plate walls and excessive material would be wiped off using a spatula or some similar device. Remaining adhesive would fill valleys in the composite surface that result from the manufacturing process due to the use of peel-plies.

When numerically setting up this modified ISF process, the layer of cells adjacent to the insertion plate was patched with adhesive. Two cases were studied: one where the same

adhesive was applied for the layer and into the Pi-slot bottom and a second where the adhesives differed from each other. The two adhesives were of different viscosity according to adhesive mixtures that represent the highest and lowest possible viscosities. An analysis was undertaken to determine in which way the pre-applied adhesive affected the adhesive flow within the flow channels.

The mesh used for this analysis differed slightly from the standard mesh used for the previously presented results in the way that more vertical cell layers within the flow channels were used. Furthermore, the cell layers became finer the closer they were to the insertion plate wall.

The characteristic flow dimensions were held constant according to the previously presented results for aligned studies. In terms of input parameters, the insertion speed was specified as 60 mm/min. The shear viscosity was selected according to adhesive mixtures between EA 9395 and EA 9396 of $100 - 0$ and $70 - 30$ weight percent. For the case where the same adhesive was pre-applied along the insertion plate walls and within the Pi-slot bottom, the lower viscous mixture was modelled. For the case that involved a three-phase analysis – when the adhesive on the insertion plate walls differed from the adhesive placed in the bottom of the Pi-slot – a mixture of $100 - 0$ was applied into the Pi-slot and the lower viscous adhesive was patched onto adjacent layers next to the insertion plate walls. In Fluent, it was not possible to patch two different UDF material models to regions within the flow domain. Consequently, the five-parameter rational model could not be implemented for the three phase flow analysis. The adhesive shear viscosity was defined according to the Power law. To ensure comparability, the adhesive was also implemented as a Power law fluid for the two-phase flow simulation.

To illustrate the adhesive pre-application the initial adhesive distribution is shown in Figure 7-10.
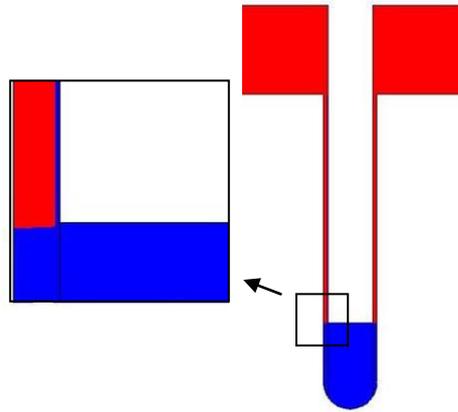
Figure 7-10: Initial adhesive distribution including pre-applied adhesive on the insertion plate side walls. Blue shows the initial location of the adhesive.

The red colour represents air and the blue colour represents adhesive. The adhesive that is pre-applied on the side walls can be, as mentioned earlier, either the same or a different material.

The output obtained from this analysis provides information about the filling characteristics of the flow channels. The filling resulting from a standard ISF process was compared to that from an adhesive pre-applied ISF process. The results are presented in Figure 7-11 as the fill height versus dimensionless time. The fill height H^* was defined previously in equation (6-1) as the the flow front c plus the initial adhesive height H_0 divided by the total flow channel height H_1.,

$$H^* = \frac{c + H_0}{H_1} \; .$$

<div align="right">(6-1)</div>
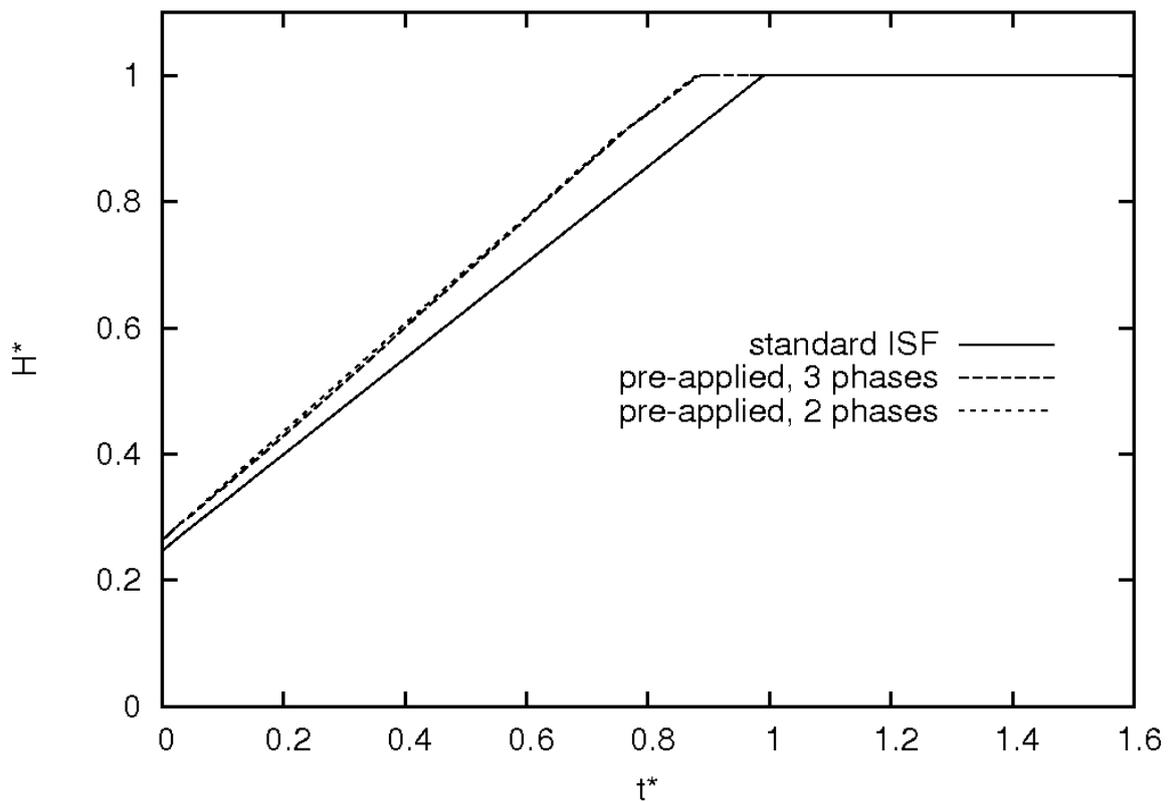
Figure 7-11: Comparison of fill heights for a pre-applied and a standard ISF bonding process as a function of dimensionless time. The pre-applied variant was conducted with two and with three phases, which are presented by the dotted lines.

There is clearly little difference between the two- and three-phase flow pre-applied cases. The pre-application cases generally fills more quickly due to the adhesive already within the flow channels. However, using this procedure would add another labour-intensive step to the ISF process and in turn increase the total process time. A further consideration would appear to be from oxidization of a micro-layer of the pre-applied adhesive. There is evidence that joint quality would be affected due to the reduction of bonding strength from oxidization (Petrie, 2004).

7.3 Insertion Squeeze Flow including Fluid-Structure Interaction

7.3.1 Introduction

For the numerical results presented so far, the Pi-slot wall boundaries are assumed to be rigid. However, in practice the Pi-slot walls may deflect if the pressure acting on them is large enough, increasing the width of the flow channels. Consequently, the flow of the

adhesive would be affected, and the pressure resulting from the adhesive flow would change as well. This fluid-structure interaction will be investigated further in this section.

In sub-Section 7.3.2, the methodology and problem set-up for the fluid-structure interaction (FSI) is introduced. Sub-Section 7.3.3 deals with results obtained from numerical simulations which take the FSI into consideration, investigating the effect of input variables such as Pi-slot wall stiffness and adhesive viscosity on output variables such as the deflection of the Pi-slot walls and the adhesive flow within the flow channels.

7.3.2 Numerical method

From the results for constant speed insertions, a pressure distribution along the Pi-slot walls could be determined, for example, as presented in Figure 5-16 on page 138. The pressure maximum was found at the root of the Pi-slot and decreased linearly within the flow channel dropping to zero gauge pressure at the adhesive flow front. To derive a wall deflection equation, the pressure is assumed to decrease linearly from the root to the flow front position. In fact, in the area underneath the insertion plate head, the pressure is uniform along the Pi-slot wall. This was observed within Figure 5-16 where the pressure remained constant between a Pi-slot position of 0 mm and 5 mm. It was assumed that the linear pressure distribution has a minor effect on the results due to two reasons: first, the distance between the insertion head plate and Pi-slot bottom decreases with respect to time, indeed, approaching an entirely triangular distribution. Second, in the very beginning, when the greatest differences exist between the assumed and actual pressure distribution, the pressure is comparably small. The pressure increases with time, as can be observed in Figure 5-17, page 139, and hence is expected to cause a larger distortion towards the end of the insertion process. By that time, the area of uniformly distributed pressure becomes even smaller and the pressure distribution is nearly linearly distributed along the Pi-slot, with a maximum at the root and a minimum at the flow front. Figure 7-12 illustrates the actual and assumed pressure distribution:
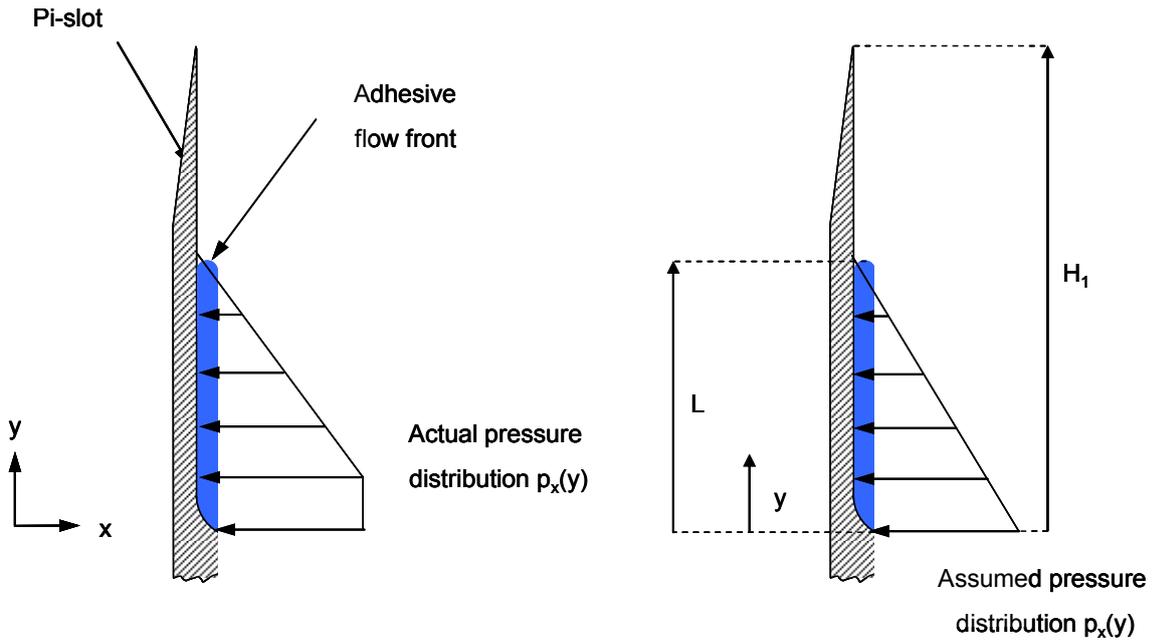
Figure 7-12: Schematic of the actual and assumed pressure distribution along the Pi-slot wall. This pressure results from the adhesive flow which is also shown in the figure for one examplary time.

For the assumed and the actual pressure distribution, the error was calculated for analytical solutions when the adhesive reaches the top of the flow channel. This error is in the order of

$$e = \left(1 - \frac{H_1^4}{H_1^4 - lH_1^3}\right)100\% = \left(1 - \frac{H_1}{H_1 - l}\right)100\% . \qquad (7\text{-}6)$$

Given the values for the Pi-slot height $H_1 = 35.5$ mm and the remaining distance between the insertion plate head and the Pi-slot bottom $l = 0.65$ mm, the error $e = 1.87\%$. Given that the error is only very small and conservative, meaning that the distortion resulting from the actual pressure distribution would be smaller, it was decided that the assumed pressure distribution is justified to be used for the simulations.

To derive a beam deflection equation for the Pi-slot wall distortion, the Euler Bernoulli beam equation was applied, modelling the Pi-slot wall as a cantilever beam.

$$EI\frac{d^4w_1}{dy^4} = q_0\left(\frac{y}{L} - 1\right) \qquad \text{for } 0 \le y \le L \qquad (7\text{-}7)$$

$$EI\frac{d^4w_2}{dy^4} = 0 \qquad\qquad \text{for } L \le y \le H_1 \qquad (7\text{-}8)$$

Within equations (7-7) and (7-8), E is the stiffness of the composite, I is the second moment of area, w is the deflection in the y-direction, q_0 is the loading per unit length and L is the position of the adhesive flow front.

Based on these equations, a function is derived for the deflection of the cantilever beam (Pi-slot wall):

$$w_1(y) = \frac{p_{max}}{10ELt^3}\left(y^5 - 5y^4L + 10y^3L^2 - 10y^2L^3\right) \quad \text{for } 0 \leq y \leq L \qquad (7\text{-}9)$$

$$w_2(y) = \frac{p_{max}}{10Et}\left(L^4 - 5yL^3\right) \qquad \qquad \text{for } L \leq y \leq H_1 \qquad (7\text{-}10)$$

Within equations (7-9) and (7-10), the load per length q_0 was substituted by the maximum pressure p_{max} multiplied with the length l of the Pi-slot in the z-direction. The second moment of area I was substituted by $1/12*l*t^3$, with t being the thickness of the Pi-slot wall. The deflection is illustrated schematically in Figure 7-13:
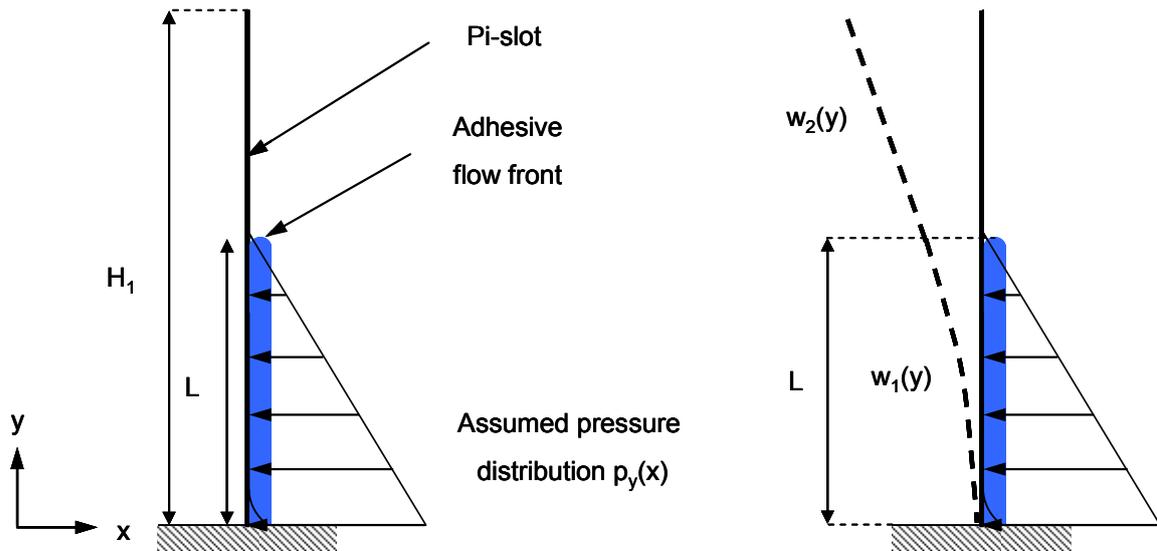
Figure 7-13: Illustrated simplification of Pi-slot wall as a cantilever beam; representation of the deflection of the beam due to the acting pressure.

To implement the Pi-slot deflection into Fluent, several UDF c-files had to be developed. The first type of UDF had the purpose of determining the flow front of the adhesive within the flow channel. The flow front was expressed through the variable L. A "DEFINE_EXECUTE_AT_END"-macro was used for this purpose (Fluent, 2005b). This

UDF was called once every time-step, meaning that the exchange of information takes place once per time-step.

The second type of UDF was called every iteration to update the maximum pressure value, calculate the deflection of the Pi-slot wall boundaries and send the accordingly updated Pi-slot wall node position back to Fluent. This second UDF used two pre-defined macros: a "DEFINE_ADJUST"- and a "DEFINE_GEOMETRY"-macro ((Fluent, 2005b). One c-file for each UDF type is attached in Appendix B. Figure 7-14 shows a flow chart that illustrates the interaction between the UDF-files and Fluent:
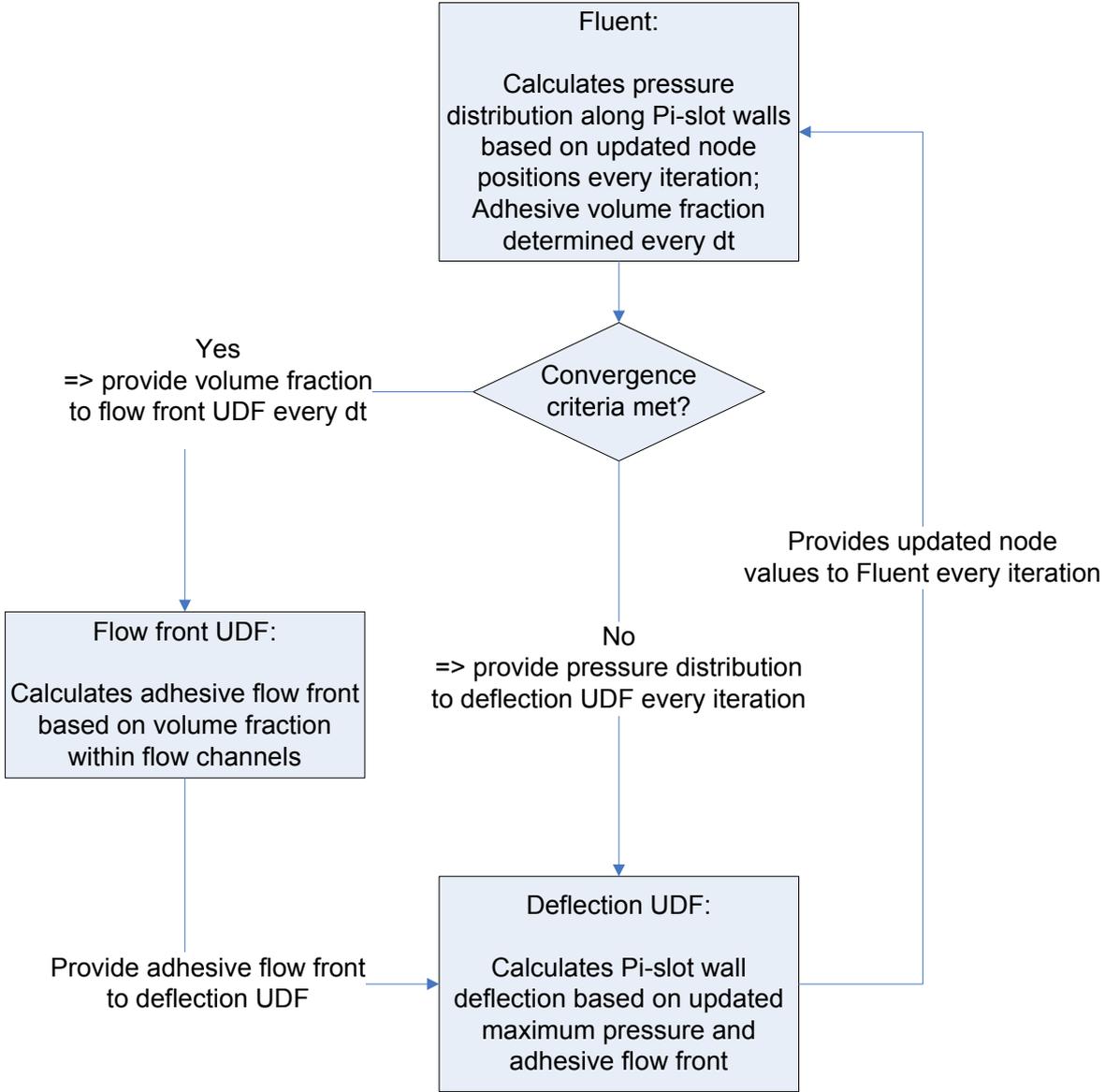
Figure 7-14: Flow chart for updating the Pi-slot wall boundary nodes based on the adhesive flow front position and pressure distribution along the Pi-slot walls.

The meshes developed and used for the simulation are shown in Figure 7-15:
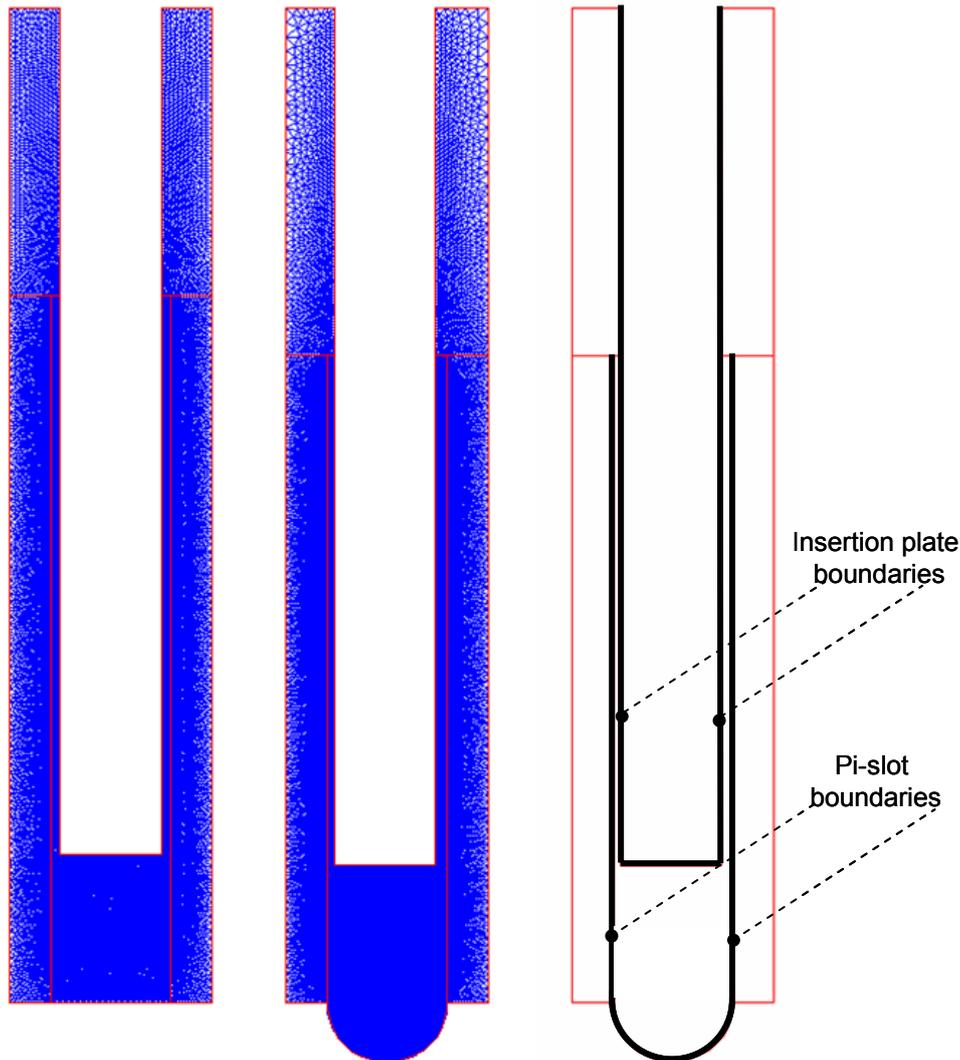
Figure 7-15: Mesh set-up for the FSI simulations; the rightmost image emphasizes the Pi-slot- and insertion plate-boundaries.

In Figure 7-15, the leftmost mesh was used to simulate the FSI within the ISF process with a simplified, rectangular bottom shape of the Pi-slot; the second mesh employed the original Pi-slot shape used in all results presented so far (inner radius of 3.0 mm for the Pi-slot bottom); the third image in the Figure emphasizes the Pi-slot and insertion plate boundaries. The purpose of the mesh domain that is outside of the Pi-slot walls is to allow motion of the nodes that represent the Pi-slot wall boundary.

7.3.3 Results and discussion

The FSI simulations were conducted for baseline input parameters: insertion speed was 60 mm/min, adhesive viscosity was adjusted according to $70 - 30$ weight percent ratio of EA 9395 to EA 9396 using the five parameter rational model, Pi-slot stiffness was 50 GPa,

the resulting flow channel width was 0.5 mm as insertion plate thickness and Pi-slot width were 5.0 mm and 6.0 mm, respectively. Pi-slot height remained at 35.5 mm and the adhesive amount applied was 125 volume-percent. The insertion plate head shape was rectangular.

For all the aligned simulations, the Pi-slot bottom was not modelled with an inner radius, but was rectangular, as shown in the left mesh of Figure 7-15. The reason for this change was to simplify the geometry.

For the results analysing adhesive flow in misaligned cases, the original Pi-slot geometry, as presented in the middle illustration of Figure 7-15, was used. First, we considered the Pi-slot deflection at the top of the Pi-slot walls for a baseline case and results are presented in Figure 7-16:
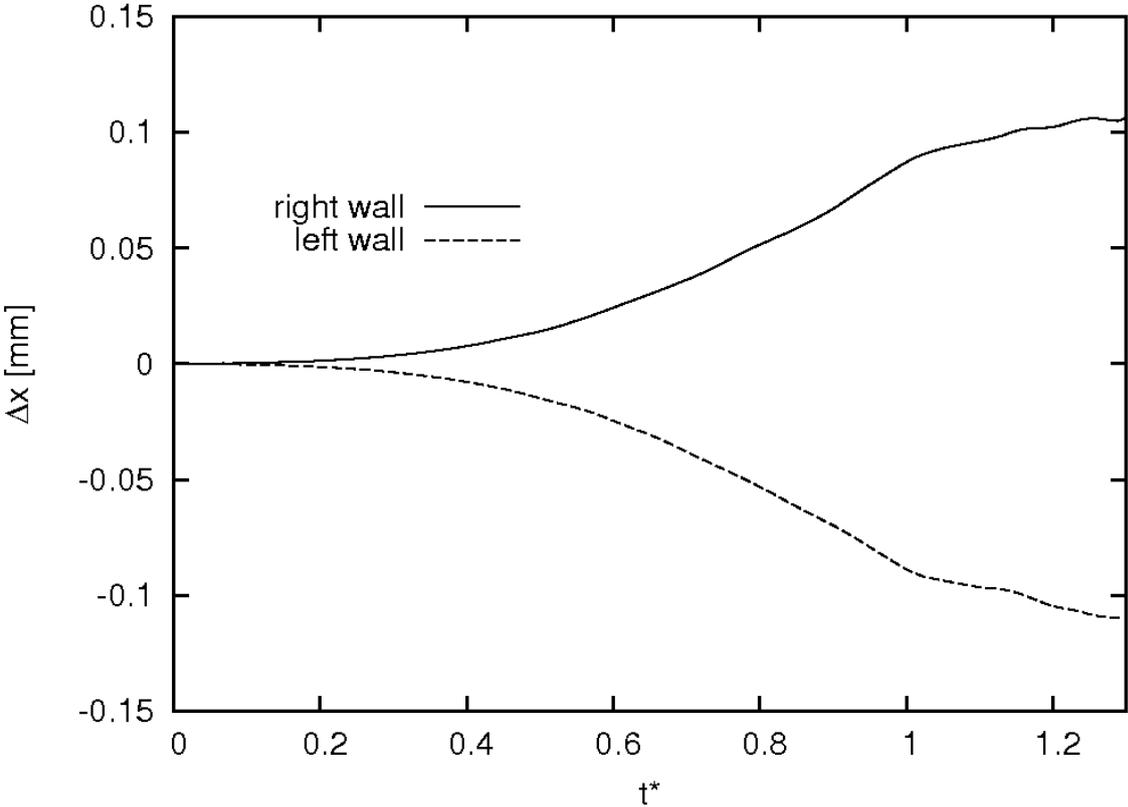
Figure 7-16: Pi-slot wall top distortion due to the adhesive flow for baseline parameters.

Δx shows the displacement of the left and right Pi-slot wall tops with respect to non-dimensionalised time. The usual procedure was applied of non-dimensionalising the flow time, dividing by a time T specified as the time period needed to fill both flow channels of the baseline geometry completely. Both Pi-slot walls are deflected outwards, hence Δx is negative for the left Pi-slot wall and positive for the right. The magnitude of the maximum

deflection is about 0.11 mm, which corresponds to an overall widening of the flow channel of 22 %. A visible deflection is not noticed before a dimensionless time of about 0.175. The Pi-slot walls begin to widen from this time onwards at increasing rate. When the adhesive begins to flow out of the flow channels, the Pi-slot width at the top has increased to about 6.2 mm. The rate of widening of the Pi-slot decreases afterwards.

The observed widening continues at an increasing rate until $t^*=1$. This behaviour is now considered in more depth. First, the deflection equation $w_2(y)$ at the top of the Pi-slot ($y=H_1$) is restated:

$$w_2(y = H_1) = \frac{p_{max}}{10Et^3}\left(L^4 - 5yH_1^3\right) \qquad \text{for } L \le y \le H_1 \qquad (7\text{-}11)$$

The deflection at the Pi-slot top $w_2(y)$ is a 1st order function of the maximum pressure and a 4th order function of the adhesive depth. The flow front position is directly proportional to flow time, and hence dimensionless time. Given the deflection is a 4th order function of the flow front, the deflection would be expected to increase at an increasing rate. Further, the transient maximum pressure acting at the Pi-slot walls for constant insertion speeds was determined to increase linearly up to $t^*=1$ (sub-Section 5.3.2). However, this was for rigid boundaries. For flexible boundaries, the pressure increases at decreasing rates. This can be derived from the drag coefficient history along the insertion plate which is shown below in Figure 7-19 on page 224 and which indicates the transient pressure. Overall the deflection increases at an increasing rate because of the sensitivity to flow front position.

Next, a comparison of the deflection of each Pi-slot wall to the other (Figure 7-17) is made to determine the accuracy of the numerical solution:
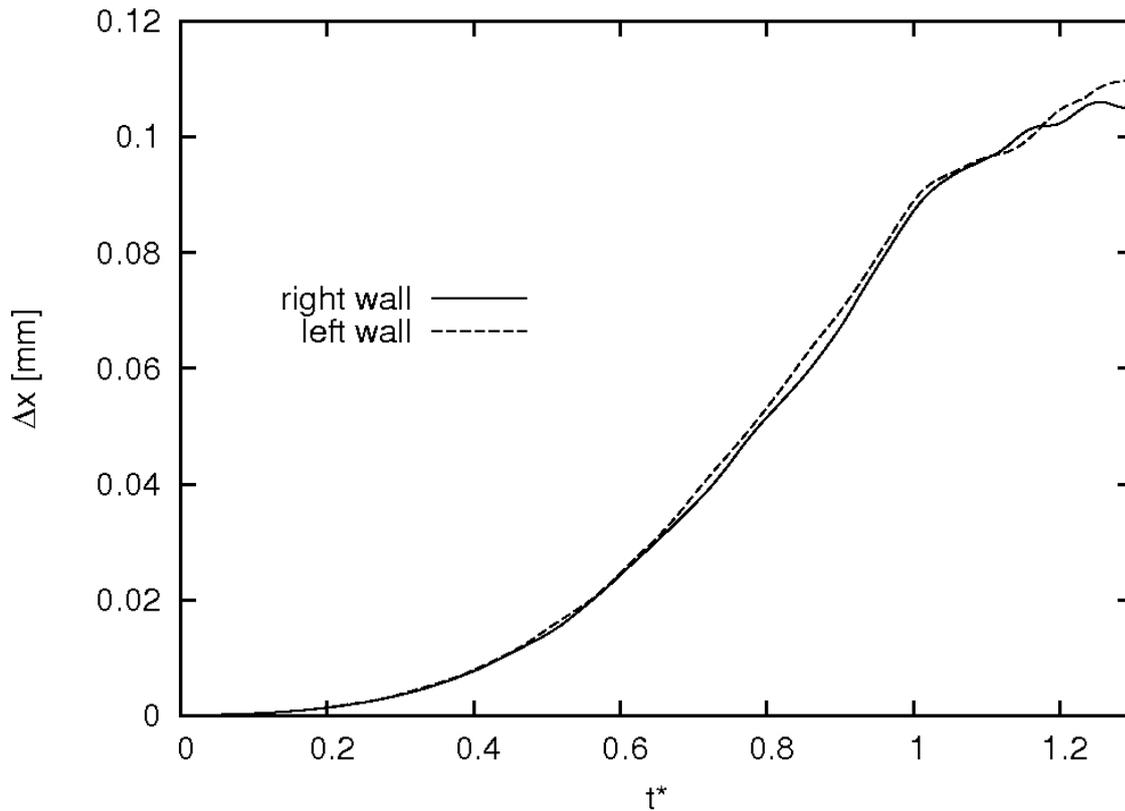
Figure 7-17: A comparison between the distortion of the left and the right Pi-slot wall for baseline parameters.

Until a dimensionless time of about 1.1, only relatively minor differences can be observed between both deflections. These most probably are due to spatial discretisation differences, which might lead to slightly different solution errors and thus slightly different pressure distributions in the two flow channels. The differences become more apparent from a dimensionless time of about 1.1 onwards. This might be caused by the coarser mesh in the flow domain above the flow channels, in which the adhesive begins to flow out at that time. The accuracy of the solution appears to be acceptable as the flow channel width variation, which has an impact on the adhesive flow, only varies on $O(10^{-2})$ mm.

The effect of different Pi-slot wall stiffness as well as adhesive viscosities on the deflection is illustrated in Figure 7-18.
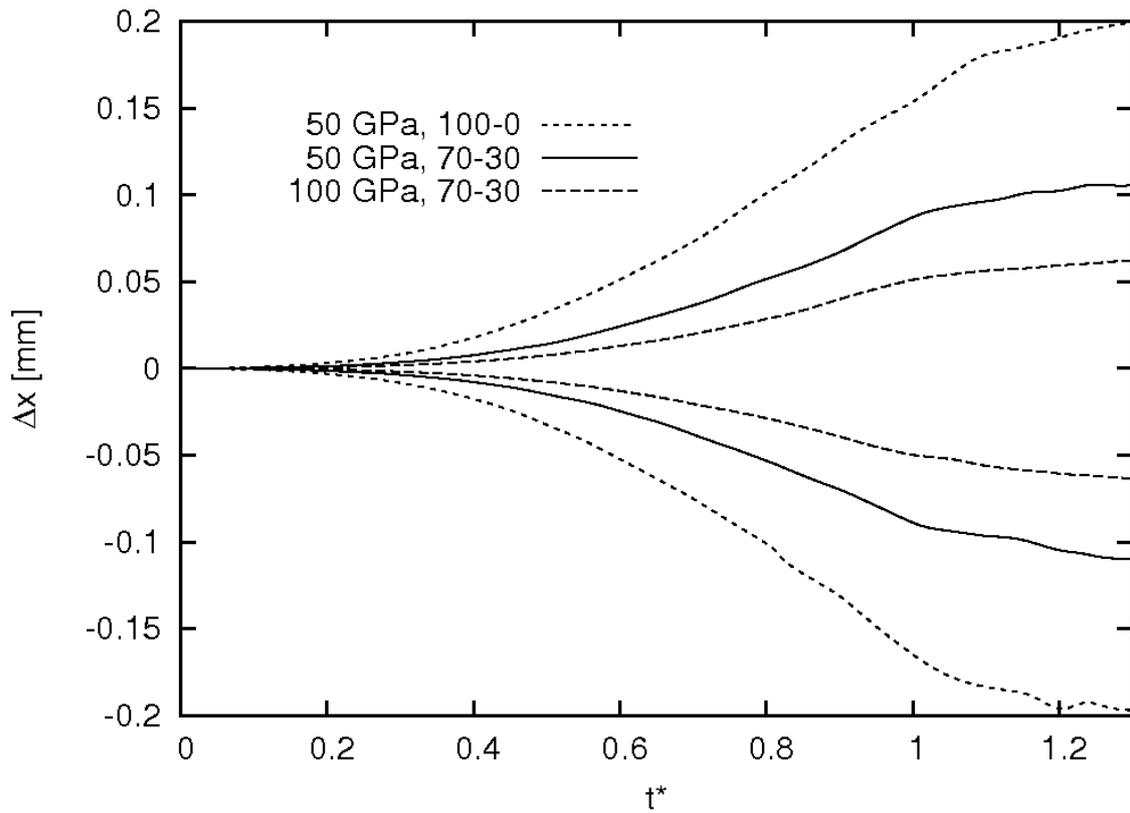
Figure 7-18: Pi-slot distortion as a function of dimensionless time for different composite stiffnesses and adhesive viscosities.

In line with expectations, a higher Pi-slot wall stiffness increases rigidity and hence leads to smaller deflections. The impact of an increased adhesive viscosity also becomes obvious: the drag coefficient along the insertion plate increases for higher adhesive viscosities, hence the pressure acting along the Pi-slot walls increases. Consequently, the Pi-slot walls deflect to a higher degree.

The insertion force is plotted with respect to dimensionless time in Figure 7-19.
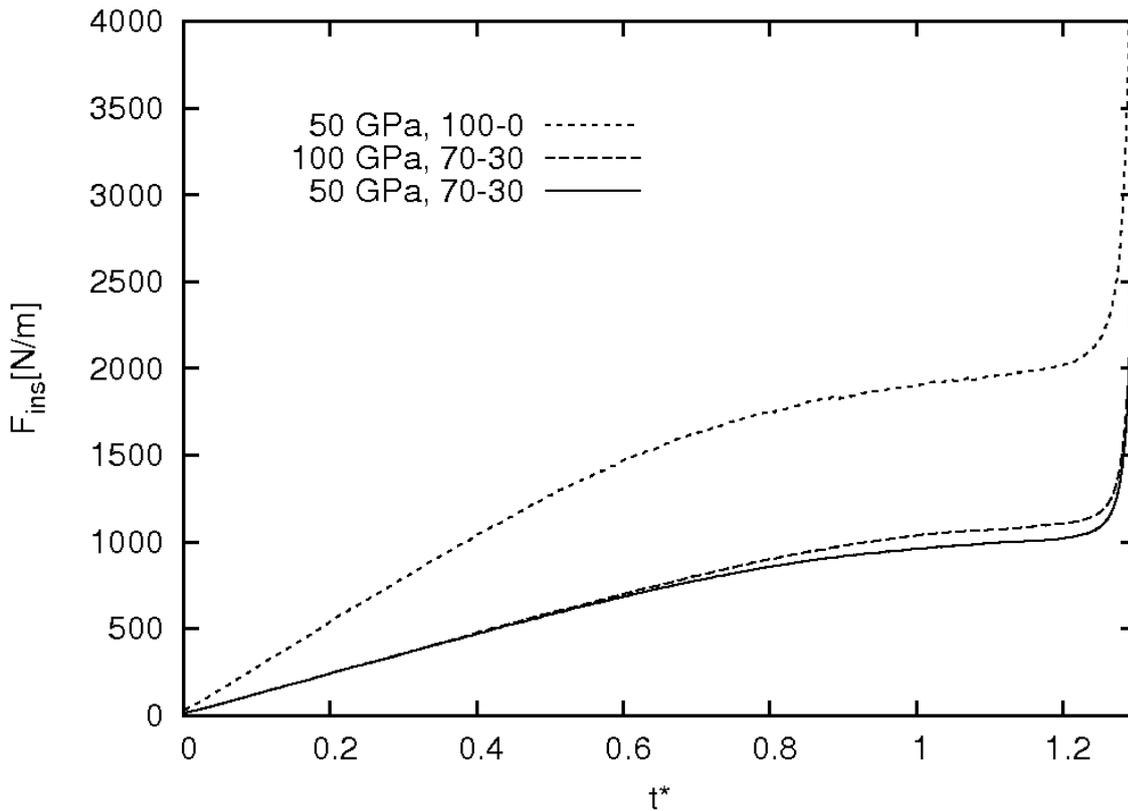
Figure 7-19: Insertion force as a function of dimensionless time for different Pi-slot wall stiffnesses and adhesive viscosities.

Up to a dimensionless time of about 0.5, the increase of the insertion force is approximately linear. The increase happens at a lower rate between a dimensionless time of 0.5 and 1.2. The widening of the Pi-slot and hence an increased width of the flow channels is assumed to be responsible for the below-linear increase. Additionally, after a dimensionless time of 1 unit the adhesive flowing out of the flow channels enhances this effect.

Considering the effect of different wall stiffness on the insertion force, it is observed that the force is higher for stiffer walls. The flexibility allows the Pi-slot walls to be deflected comparably to a greater degree, consequently leading to wider flow channels. It has been shown previously (Figure 5-31 on page 160) that lower insertion forces are detected for greater flow channel widths. The adhesive viscosity effect remains the same as determined in previous chapters, so that higher insertion forces result from increased viscosities.

The consideration of FSI was continued with a study of its effect on the adhesive flow within a misaligned joint. As mentioned above, we considered a Pi-slot geometry with a

rounded bottom. The misalignment ratio considered was $\xi = 0.667$, so that the flow channel widths were 0.6 mm and 0.4 mm for the wide and narrow flow channel, respectively. The adhesive flow resulting from this simulation was compared to an aligned insertion simulation with the same rounded Pi-slot bottom. In Figure 7-20, the flow front plus the initial adhesive height divided by the total flow channel height is plotted against dimensionless time.
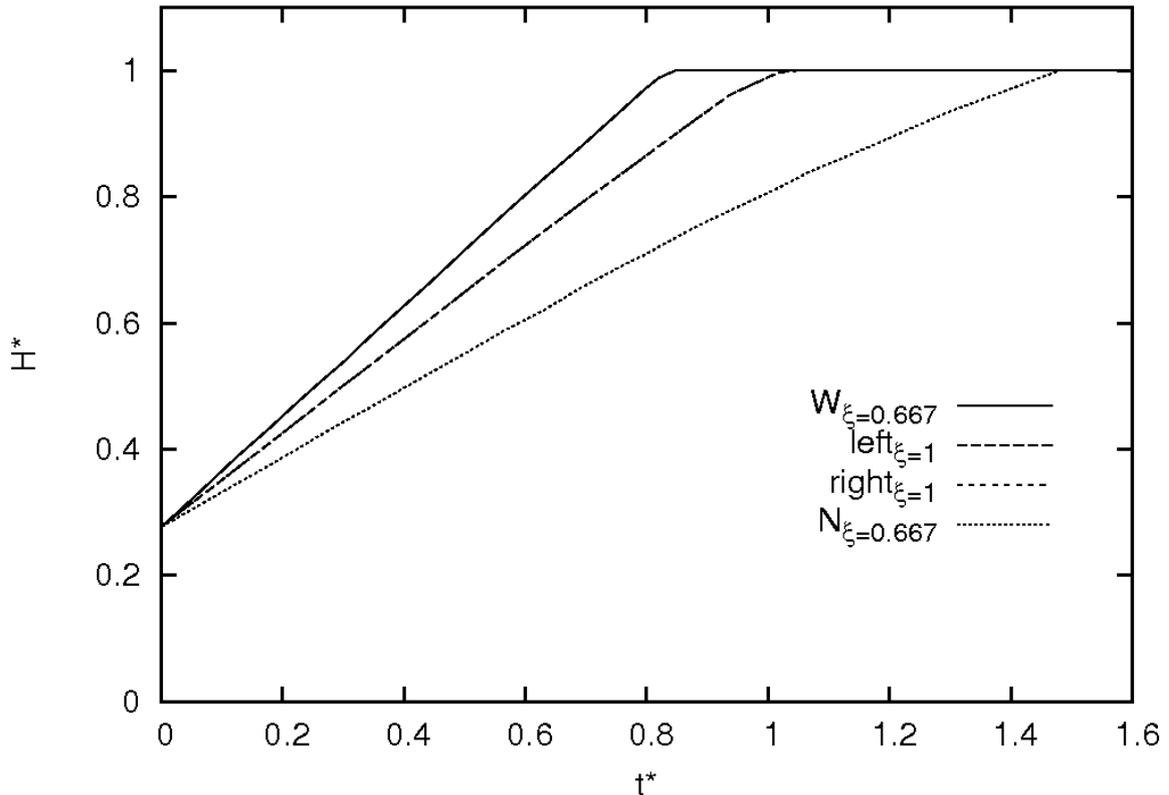
Figure 7-20: Transient fill height for an aligned and a misaligned FSI simulation.

For the aligned case it is noticed that the adhesive flow fronts in both flow channels agree very well. This shows the small effect of discrepancies in the Pi-slot wall deflection discussed earlier and illustrated in Figure 7-17. Considering the misaligned case, the adhesive still fills both flow channels. The duration of filling is longer for both flow channels when compared with the simulations where the flow channel width remained constant (Figure 6-10 on page 171). This would be expected as the flow channel area to be filled is comparably larger in the simulations where FSI is taken into consideration. To emphasize this comparison, Figure 7-21 is plotted to compare the flow fronts.
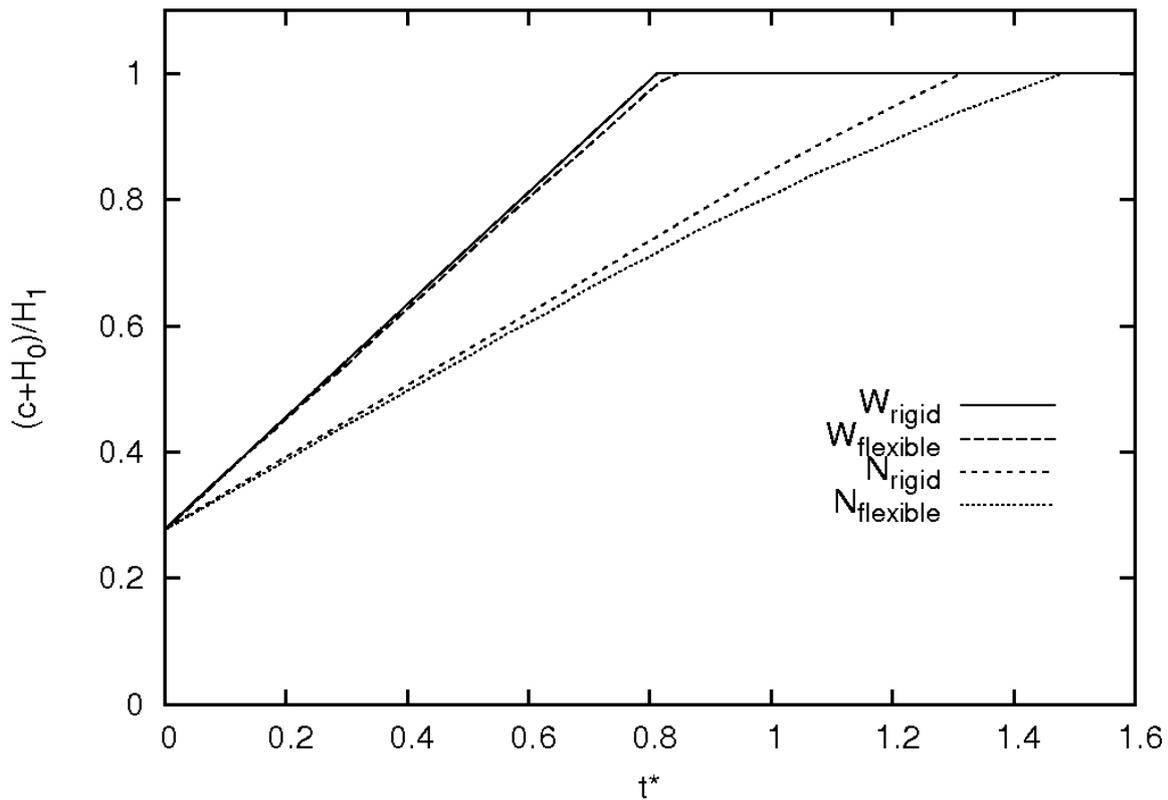
Figure 7-21: The effect of flexible vs. rigid boundary conditions on fill heights (ξ=0.667).

Clearly, the time period to fill the flow channels is larger when taking into consideration the flexibility of the Pi-slot walls. This effect becomes enhanced for longer process times as the walls deflect further due to increasing pressure. The process time to fill the narrow flow channel in the case of flexible Pi-slot walls is 10.6 % longer than the one for rigid walls. In generating a robust ISF process, it may be preferable to minimize the opening of the Pi-slot walls in order to accelerate the filling of the flow channels. One possibility would be to support the Pi-slot walls during insertion to minimise deflection. A second possibility would be to stop the insertion process and wait for the adhesive pressure to ease, which would allow a springing back of the composite Pi-slot walls to their original shape. This second option would further lead to a filling of the flow channels with adhesive. Therefore it is proposed to stop the insertion process after the time corresponding to the filling of an undeflected case, so that the Pi-slot walls would retract and fill the remaining space of the fill channel.

To conclude, the results obtained from FSI simulations of the ISF process are considered as physically meaningful. Effects of stiffness of the Pi-slot walls and adhesive viscosity are in line with expectations. This shows that the ISF process can be modelled

numerically while taking into account the interaction between the adhesive and the Pi-slot walls. Indeed, the adhesive flow causes a widening of the flow channels, hence affecting the adhesive flow. Two options were suggested to minimize Pi-slot walls deflection during insertion.

7.4 3D Numerical Model for Insertion Squeeze Flow

7.4.1 Problem setup

In sub-Section 3.5.1 on page 68 the two-dimensional (2D) problem setup was introduced. In this section, the general parameters remain as they were defined for the 2D simulation. An insertion plate and Pi-slot comprise the joint and the flow domain to consider adhesive flow in the flow channels. Key dimensions defining the geometry to be simulated can be found on page 68. In addition, the Pi-slot bottom was changed from round to rectangular. Length of the joint, specified as w, equals $3H_1$. Two flow domains were developed and are shown in Figure 7-22.
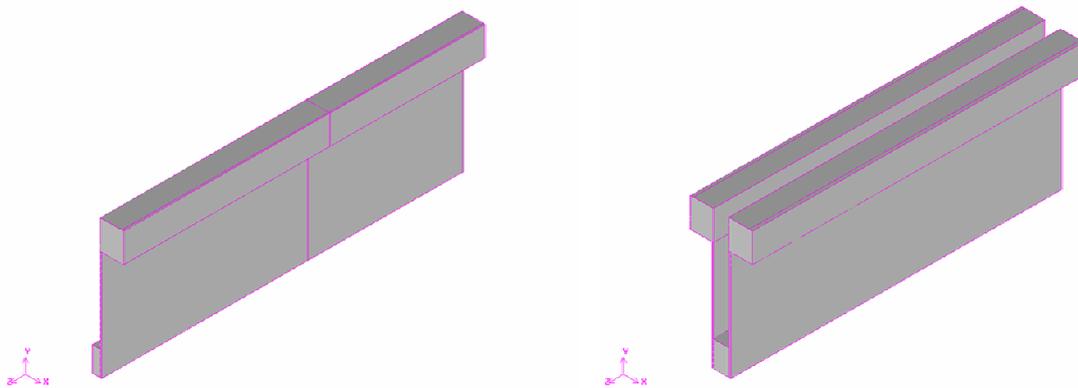
Figure 7-22: Flow domains for 3D ISF simulations.

On the left the setup is symmetrical along the z-axis. The flow channel width remained constant as b-$a = 0.5$ mm. On the right hand side of Figure 7-22, a different setup is illustrated, lacking symmetry along the z-axis, which is shown schematically in Figure 7-23. This setup was used to include a misalignment around the y-axis of the insertion plate relative to the Pi-slot. Hence the flow channel width ratio varies along the z-axis, being perfectly laterally aligned on one end (0.5 – 0.5 mm) and altering to a laterally misaligned joint (0.4 – 0.6 mm) at the other. It is referred to the wide and narrow flow channel sides. The wide flow channel side is defined as that flow channel which varies from 0.5 mm to

0.6 mm along the z-axis. In the narrow flow channel side the flow channel varies from 0.5 mm to 0.4 mm. An illustration clarifies this situation (Figure 7-23).
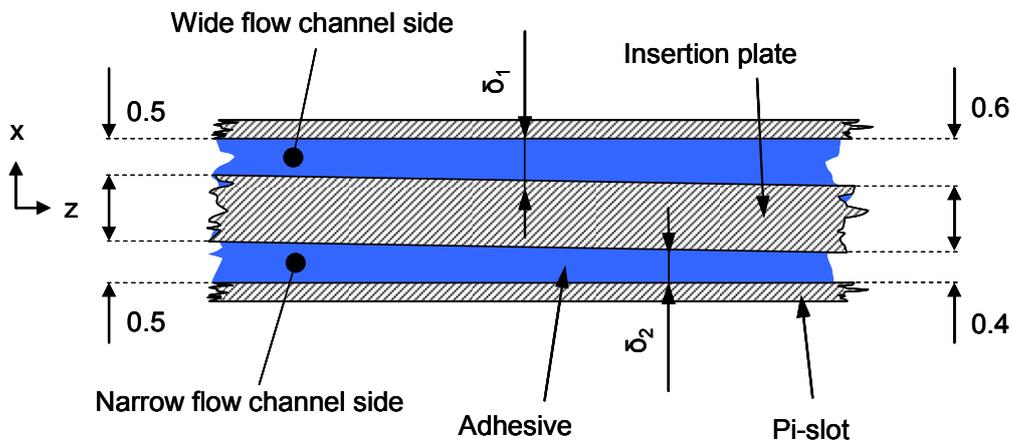
Figure 7-23: Illustration of misalignment around the y-axis as analysed in the 3D ISF simulations.

No changes other than the mentioned symmetry were applied to define boundary conditions in the model compared to those already used for the 2D simulations; hence, all walls were specified as rigid and impermeable with no slip boundary conditions, the flow domain being confined between these walls. The side boundary conditions in the z-direction were specified as symmetry. Moving walls with a prescribed translational motion define the insertion plate walls. Only a constant speed ISF process is considered in this section. Interface surfaces ensure sliding of mesh elements between the domain contained underneath the insertion plate and the domain representing the flow channels in that domain region.

A purely rectangular mesh was used except for the outflow volumes above the flow channels. In the z-direction, the mesh was coarse, due to the aspect ratio $w/(b\text{-}a)$ being >>1, with the major flow variation expected in the y-direction. Ten elements along the flow channel width were specified as for the spatially resolved 2D case. For spatial mesh resolution purposes in the z-direction, two simulations were setup, using a coarser and a finer mesh in the z-direction. Both meshes produced essentially identical results in terms of adhesive distribution. Furthermore, a consideration of the adhesive distribution for the first setup was conducted; it was tested whether the adhesive distributes equally in the z-direction, as would be expected for a constant flow channel width, and this was observed, and is presented in the following sub-section. Consequently, the simulations show evidence of being spatially resolved.

7.4.2 Results and discussion

Input variables applied for the symmetrical case are specified as 60 mm/min for constant insertion speed, 70 – 30 adhesive viscosity according to weight percentage mixing ratio of EA 9395 to EA 9396, applying the five-parameter rational model for viscosity calculations and 125 volume percent initial adhesive amount. Figure 7-24 shows the adhesive distribution (red colour) within the flow domain, at the moment when the insertion plate has almost reached the Pi-slot bottom.
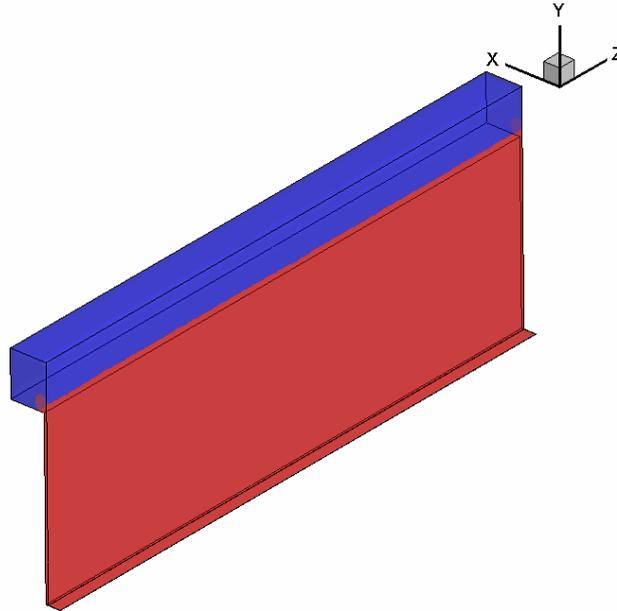
Figure 7-24: Adhesive distribution (shown as red) for an aligned symmetrical 3D ISF simulation; the rest of the flow domain is filled with air (in blue).

Within the flow domain, air (shown as blue) is only contained in the outflow region at the top of the flow channels. The adhesive is distributed evenly within the flow channels and excessive adhesive partially fills the outflow region.

Next, the effect of a longitudinal misalignment (misalignment around the y-axis) on the adhesive flow applying a numerical 3D analysis is investigated. The second flow domain described in sub-Section 7.4.1 was used for this purpose. Input parameters remain as specified previously for the symmetrical case. The fill height H* (defined through the flow front height c and initial adhesive height H_0 divided by the Pi-slot height H_1) is plotted against non-dimensionalised time t* in Figure 7-25.
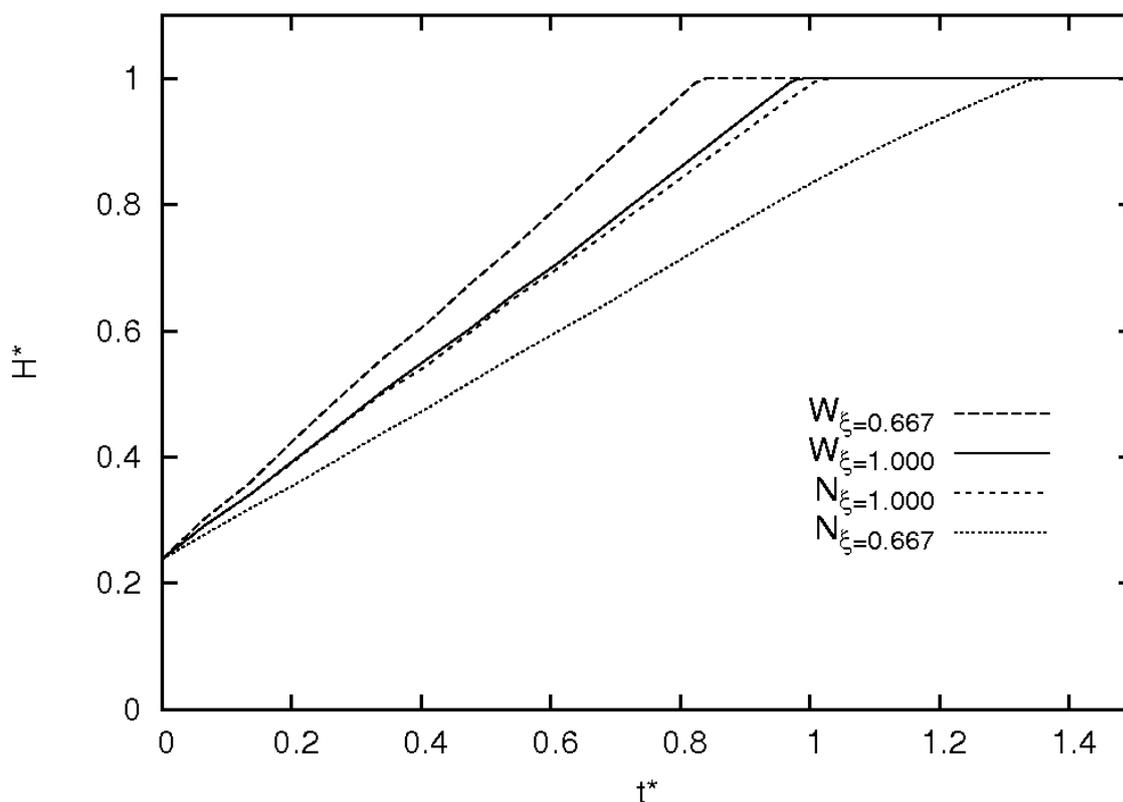
Figure 7-25: Adhesive fill height versus dimensionless time for a longitudinally misaligned insertion plate.

As usual, the flow time is non-dimensionalised by the time taken to entirely fill the flow channels. An adhesive flow distribution is observed similar to the one determined during the 2D simulations; in the laterally misaligned region of the joint the wider flow channel fills first after approximately 0.83 dimensionless time units. The adhesive in the narrower channel does not start to flow out before approximately 1.38 dimensionless time units.

To obtain an understanding of the effect of the longitudinal misalignment, that region of the joint is considered where no lateral misalignment (graphs marked as $W_{\xi=1.000}$ and $N_{\xi=1.000}$ in Figure 7-25) occurs. For no longitudinal misalignment it is known from 2D simulations that at $t^* = 1$ the adhesive reaches the flow channel top.

Considering this non-misaligned region of the joint, the flow channels fill after different time periods. The flow channel that is on the wider flow channel side – marked as $W_{\xi=1.000}$ in Figure 7-25 – fills after about 0.98 dimensionless time units, whereas the other flow channel fills after about 1.02 dimensionless time units. Hence it is concluded that there is only a very small effect of longitudinal misalignment on the distribution of the adhesive

during ISF which, in the presented case (so a longitudinal misalignment of 0.1 mm for a length over $3*H_1$), shows a filling time over the length of $t* = 1\pm0.02$ units.

This affects the ISF process in a way that the insertion plate has to be moved down further compared to a perfectly aligned joint to ensure filling of both flow channels. For the adhesive to reach the top of the flow channel in the narrower flow channel side in the aligned region, the insertion plate has to move the following further distance:

$$h = t \cdot v_{ins} = t * \cdot T \cdot v_{ins} = 0.02 \cdot 5.4125s \cdot 1mm / s = 0.10825mm \qquad (7\text{-}12)$$

After moving down an additional 0.10825 mm, the adhesive reaches the top of the flow channel on the narrow flow channel side in the perfectly aligned region. This distance could be added to the initial adhesive amount H_0 to suppress the effect of longitudinal displacement for the current setup.

The wider flow channel side most probably fills more quickly as the lateral misalignment leads to an unequal adhesive distribution in the x-direction. More adhesive in general flows into the wider channel. However, the effect experienced due to misalignment around the y-axis for the considered dimensional range hardly seriously impacts the adhesive distribution. This variation was evaluated to be negligibly small in terms of affecting the Pi-joint quality.

To sum up, two different 3D simulations were set up and used to obtain information on adhesive flow during constant speed ISF. A particular focus was on the effect of longitudinal misalignment, which cannot be considered in 2D simulations. Indeed, there appears to be an effect of longitudinal misalignment on the adhesive flow, but it has been evaluated to be very small. An increase in the initial amount of adhesive was presented as a solution to minimise this effect.

7.5 Summary

In this chapter, simulations of the ISF process for constant applied insertion forces were presented. It was found that dependences determined from ISF simulations at constant insertion speed remain valid for ISF under constant force. These dependences include those between the insertion force and the pressure acting on the Pi-slot walls, and the adhesive distribution for one laterally misaligned insertion study. This observed behaviour can be traced to the low Reynolds numbers involved given the material properties of the adhesive, and the slot geometry and typical insertion times. The Reynolds numbers are typically considerably less than one so the nonlinear term in the governing Navier-Stokes

equations can be ignored. This means that the insertion flows are (non-Newtonian) Stokes flows – effectively reversible and not sensitive to the history to define the flow state.

Also considered was a numerical model for the simulation of an ISF process for which the Pi-slot walls have a thin layer of pre-applied adhesive. Indeed, the flow channels fill more quickly for this modified process; however, in practice this would mean an additional process step.

Furthermore, fluid-structure interaction was incorporated into the numerical model for ISF at constant insertion speed. The deflection of the Pi-slot walls with respect to time for simulations including varying adhesive viscosities and composite stiffnesses were determined. The effect of flexible Pi-slot walls on the adhesive flow was compared to adhesive flow when the Pi-slot walls were specified as rigid. It was found that it becomes more difficult to fill the narrow flow channel; support of the Pi-slot walls or stopping the insertion process to release adhesive pressure were proposed to overcome eventual difficulties in practice.

Finally, in the 3D numerical model for ISF at constant insertion speed, the misalignment in a longitudinal direction resulting from a rotation around the *y*-axis was presented and its effect on the adhesive flow evaluated. It was shown that this type of misalignment has only a minor effect on the adhesive flow for the considered realistic misalignment range.

8 Conclusions and Future Work

8.1 Conclusions

The broad aim of this research work was to obtain an understanding of the adhesive flow during insertion squeeze flow (ISF) in order to support the development of an adhesive bonding process for a skin-to-spar structure that is used in various aircraft components. The adhesive flow during an ISF process was numerically modelled with computational fluid dynamics (CFD) software, and the model predictions led to a detailed understanding so that the development of an ISF bonding process can be supported.

Concerning suitable adhesives for the ISF process, two adhesives were selected and tested: the high viscous Hysol EA 9395 and the low viscous Hysol EA 9396. The two adhesives were mixed to taper required viscosities. According to ISF process requirements for the adhesive viscosity, suitable mixing ratios were determined as $85 - 15$ and $70 - 30$ weight percent of EA 9395 and EA 9396 for the lowest viscosity ratio. The highest adhesive viscosity was specified as EA 9395 only.

The adhesives investigated were found to be shear-thinning, non-Newtonian fluids. The adhesives showed little time-dependence and negligible elasticity. In simulating the insertion squeeze flow, a power law and a five parameter rational model were selected to represent the adhesive viscosities with respect to shear rate. The power law model proved less accurate in predicting the adhesives' shear viscosities and was unacceptably inaccurate at higher shear rates. The five parameter rational model provided a more accurate prediction over the entire shear rate region under consideration.

A numerical model to simulate adhesive flow during ISF at constant insertion speed was developed. From a simplified two-dimensional (2D) numerical model for ISF using a Newtonian fluid (constant shear viscosity), the insertion force was found to depend linearly on the insertion speed and on the shear viscosity. This agreed well with findings of Smith et al. (Smith et al., 1948), and also with predictions that have been determined from a derived analytical model for Newtonian ISF.

The numerical model for ISF was further developed through the implementation of the constitutive adhesive material models derived and used to predict insertion forces and pressures during ISF at constant insertion speed for perfectly aligned insertions.

The main findings from this numerical model include:

- The insertion force increases linearly with time until the adhesive reaches the top of the flow channels. The insertion force increases at a lower rate afterwards. When the insertion plate head and the Pi-slot bottom are close, a significant insertion force increase can be observed with decreasing distance. This can be explained through the principles of mass conservation.

- For a 70 – 30 weight percent mixture of EA 9395 to EA 9396, the insertion force was found to be linearly related to the insertion speed for a dimensionless time of 1. When fitted by regression analysis the data gave a fit of

$$F_{spec} = 15.324 v_{ins} + 49.2 \text{ with } 5 < v_{ins} < 120 \text{ mm/min.} \qquad (8\text{-}1)$$

  Clearly, this fit is unphysical at zero insertion speed and also may not apply at very low and very high speeds. Hence, it should only be applied for the tested insertion speed range.

- Considerably lower insertion forces were predicted if the lower viscous adhesive EA 9396 is added to EA 9395.

- The gauge pressure acting on the Pi-slot walls was determined as zero at the flow front, increasing linearly towards the root of the Pi-slot wall. The pressure was caused by the adhesive flow into the flow channels between the insertion plate and the Pi-slot walls. It was found that the maximum pressure was dependent on the insertion force. The maximum pressure [kPa] acting on the Pi-slot wall could be estimated by multiplying the insertion force [N/m] with a factor of 5.4 m^{-3} for a rectangular insertion plate head shape. This relationship was also derived for two tapered and one rounded insertion head shape design, but with slightly different factors.

- Considering the insertion speed effect on the maximum pressure for one specific time ($t^* = 1$), the following relationship was found, similarly to the dependence of the insertion force on the insertion speed, and is also valid for the investigated insertion speed range:

$$p_{max} = 2.827 v_{ins} + 9.076 \text{ with } 5 < v_{ins} < 120 \text{ mm/min} \qquad (8\text{-}2)$$

− This was determined for an adhesive mixture between EA 9395 and EA 9396 of 70 − 30 weight percent. Equivalent to the predictions of the insertion forces, the maximum pressure along the Pi-slot walls could also be decreased considerably if EA 9396 was prevalent in the adhesive.

One main requirement to guarantee Pi-joint quality was the even adhesive distribution within the flow channels. Possible misalignments were enumareted and determined as angular or lateral, with the latter affecting the adhesive distribution significantly. Consequently, analysis focussed on adhesive distribution in laterally misaligned joints.

In the numerical model the effect of lateral misalignment on the adhesive flow was evaluated and the main findings are as follows:

− The adhesive distribution in laterally misaligned joints was mainly governed by the flow channel width ratio ξ, which was defined as the narrow flow channel width divided by the wide one. In general, the wide flow channel filled more quickly compared to the narrow flow channel.

− If 125 volume percent adhesive was used initially, both flow channels could be filled for $\xi = 0.4/0.6 = 0.667$; this corresponded to a lateral misalignment of 0.1 mm in case of a total flow channel width of 1.0 mm.

− A linear relation was derived between ξ and the flow front ratio ψ as long as the flow channels were not entirely filled ($\xi = \psi$). A second linear relation with a smaller gradient was derived after the adhesive flowed out of the wide channel.

− Two procedures were proposed to ensure entire filling of both flow channels, applying the derived relationships.

− Insertion speed, adhesive viscosity, insertion plate width and initial adhesive amount showed minor effects on the ξ-ψ-relation for the considered ranges. The insertion plate head shape, however, influenced this relation, and it was found that the rectangular insertion plate head shape was the one with the most unequal adhesive distribution, hence could be considered as the most conservative approach.

From the extensions of the proposed 2D numerical model to simulate ISF, the following main outcomes were derived:

- 2D numerical simulations of ISF at constant force insertion were conducted and the computer time has been found to increase with decreasing applied constant insertion forces.

- The relationships derived for filling of laterally misaligned joints for constant speed ISF have been found to be also valid for constant force ISF (ξ =0.667). The relations are likely to be also valid for other ξ –ratios, but this has not yet been tested. Further work, at different flow channel width ratios at constant force insertions, would be needed to test this.

- The same relation between insertion force and maximum pressure along the Pi-slot walls that was found for constant insertion speed ISF has also been derived for constant force ISF.

- Incorporating fluid structure interaction (FSI) into the numerical model for constant insertion speed ISF showed an effect on the adhesive distribution. In comparison with an ISF process conducted with rigid Pi-slot walls, the filling of the narrow flow channel takes 10.6 % longer if Pi-slot walls are flexible. This was determined for a misaligned case of ξ = 0.667 and an initial adhesive volume of 125 %.

- Two possibilities have been proposed and are considered as highly likely to eliminate widening of the Pi-slot due to adhesive pressure: first, interrupting the insertion process would allow the pressure to release and, hence, the Pi-slot walls to bounce back; second, an external Pi-slot wall support would restrict the Pi-slot deflection.

- Three-dimensional (3D) simulations indicated little effect on adhesive distribution for a misalignment in the longitudinal direction (z-direction, rotation around the y-axis) for a misalignment defined as a 0.1 mm along a length of $3\,H_1$. It is considered possible that stronger longitudinal misalignments would have a stronger effect on the adhesive distribution, which would have to be validated in future studies.

8.2 Future Work

Due to the detailed understanding of the ISF bonding process developed during this study, there arises the urgent need to conduct the ISF bonding process in practice, with the aim of applying this technique in production scale.

With this broad aim in mind, there are a number of specific aspects that should be considered in order to develop a simple and robust practical ISF process:

To avoid the use of spacers for ensurance of minimal bondline thickness, it is suggested to integrate spacers during the manufacturing process of the composites. For example, appropriate tool design could leave space for the creation of resin pools on the surface of the insertion plate. These pools would remain on the insertion plate, should be positioned in the region of lowest shear stresses (i.e. in the middle of the Pi-slot height), and ensure a minimal achievable bondline thickness.

A device for the dispension of adhesive is required. ISF experiments have shown that the distribution of the adhesive into the Pi-slot before the insertion was started was a challenging task when conducted manually. Further, an equal distribution of the adhesive within the Pi-slot could not be ensured. Consequently, there exists the necessity for the development of a suitable device to distribute the adhesive automatically into the Pi-slot.

For tapered Pi-slot ends (in the z-direction), the development of features to stop adhesive side-flow were briefly investigated in the current research work (results not presented), with an end dam solution promising significant reduction of adhesive side flow. Integration of this or a slightly altered solution into the ISF bonding process is required.

Finally, the design of a bonding device to conduct the ISF bonding process should be realised, in a way that the process can be conducted in a relatively simple way.

There also exists the possibility to extend the numerical studies based on the predictions from the numerical model for ISF:

Simulatios for problem setups considering different lateral misalignments for ISF at constant force might be tested. Results can be compared with the ξ-ψ-relationship obtained from constant speed simulations. If the trends observed are confirmed, the determined ξ-ψ-relationship is ensured to also be valid for constant force ISF over a larger lateral misalignment range.

Further 3D-simulations with different longitudinal misalignments could be beneficial to analyse its effect on adhesive distribution. A relation between the degree of longitudinal misalignment and the affected adhesive distribution may be derived and guidelines for required tolerances established.

Finally, the variation of the insertion plate width could be tested on its effect on the relationship between the insertion force and the maximum pressure on the Pi-slot wall. The

relation could be adjusted if required in a way that another variable (the insertion plate width) would be embedded within the relationship.

References

ADAMS, M. J., AYDIN, I., BRISCOE, B. J. & SINHA, S. K. (1997) A finite element analysis of the squeeze flow of an elasto-viscoplastic paste material. *Journal of Non-Newtonian Fluid Mechanics,* 71, 41-57.

ADAMS, R. D. (1987) Theoretical Stress Analysis of Adhesively Bonded Joints. IN MATTHEWS, F. L. (Ed.) *Joining fibre-reinforced plastics.* London and New York, Elsevier Applied Science, 185-226.

ADAMS, R. D., ATKINS, R.W., HARRIS, J.A., KINLOCH, A.J. (1986) Stress Analysis and Failure Properties of Carbon-Fibre-Reinforced-Plastic/Steel Double-Lap Joints. *Journal of Adhesion,* 20, 29 - 53.

ARGON, A. S. (1973) A theory for the low-temperature plastic deformation of glassy polymers. *Philosophical Magazine,* 28, 839-865.

ASTM International (2001), D 4440 - 01. Standard Test Method for Plastics: Dynamic Mechanical Properties Melt Rheology. ASTM International, West Conshohocken, PA, United States.

ASTM International (2005), D 2196 - 05. Standard Test Methods for Rheological Properties of Non-Newtonian Materials by Rotational (Brookfield type) Viscometer. ASTM International, West Conshohocken, PA, United States.

BARTH, T. J. & JESPERSEN, D. (1989) The design and application of upwind schemes on unstructured meshes. Technical Report AIAA-89-0366. *AIAA 27th Aerospace Sciences Meeting.* Reno, Nevada.

BOEK, E. S., PADDING, J.T., ANDERSON, V.J., TARDY, P.M.J., CRAWSHAW, J.P., PEARSON, J.R.A. (2005) Constitutive equations for extensional flow of wormlike micelles: stability analysis of the Bautista-Manero model. *Journal of Non-Newtonian Fluid Mechanics,* 126, 39-46.

BOYCE, M. C., PARKS, D.M., ARGON, A.S. (1988) Large inelastic deformation of glassy polymers. Part I: Rate dependent constitutive model. *Mechanics of Materials,* 7, 15-33.

CARREAU, P. J., DE KLEE, D.C.R., CHHABRA, R.P. (1997) *Rheology of Polymeric Systems*, Carl Hanser Verlag, Muenchen.

COLLINGS, T. A. (1987) Experimentally Determined Strength of Mechanically Fastened Joints. IN MATTHEWS, F. L. (Ed.) *Joining fibre-reinforced plastics.* London, New York, Elsevier Applied Science Publishers LTD, 9 - 63.

COOK, W. (1982) Rheological studies of the setting of water-based cements. *Australian Dental Journal,* 29, 44 - 49.

COX, R. G. (1986) The dynamics of the spreading of liquids on a solid surface. *Journal of Fluid Mechanics,* 168, 169-194.

DUPAIX, R. B., BOYCE, M.C. (2007) Constitutive modeling of the finite strain behaviour of amorphous polymers in and above the glass transition. *Mechanics of Materials,* 39, 39-52.

DUSSAN, E. B., RAME, V., GAROFF, S. (1991) On identifying the appropriate boundary conditions at a moving contact line: An experimental investigation. *Journal of Fluid Mechanics,* 230, 97-101.

EFUNDA (2009) Euler Bernoulli Beam Equation. www.efunda.com

FERRY, J. D. (1961) *Viscoelastic Properties of Polymers*, John Wiley & Sons, New York, London.

FLETCHER, C. A. J. (1991) *Computational Techniques for Fluid Dynamics*, Springer Verlag.

FLUENT (2005a) UDF User guide: Chapter 1, Starting and executing Fluent.

FLUENT (2005b) UDF User guide: Chapter 4, Reading and writing files.

FLUENT (2005c) UDF User guide: Chapters 1 - 12.

FLUENT (2005d) User Guide.

HART-SMITH, L. J. (1987) Design of Adhesively Bonded Joints. IN MATTHEWS, F. L. (Ed.) *Joining fibre-reinforced plastics.* London, New York, Elsevier Applied Science Publisher LTD., 271-311.

HART-SMITH, L. J. (2002) Adhesive bonding of composite structures - progress to date and some remaining challenges. *Journal of Composites Technology and Research,* 24, 133-153.

HAWARD, R. N., THACKRAY, G. (1968) The use of a mathematical model to describe isothermal stress-strain curves in glassy thermoplastics. *Proceedings of the Royal Society of London, Series A: Mathematical and Physical Sciences,* 302, 453-472.

HERSCHEL, W. H., BULKLEY, R. (1926) Measurement of consistency as applied to rubber-benzene solutions. *Proceedings of the American Society for Testing Materials,* 26, 621-633.

HIRT, C. W. & NICHOLS, B. D. (1981) Volume of fluid (vof) method for the dynamics of free boundaries. *Journal of Computational Physics,* 39, 201-225.

HOCKING, L. M., RIVERS, A.D. (1982) The spreading of a drop by capillary action. *Journal of Fluid Mechanics,* 121, 425.

HOLMAN, J. P., (1994) *Experimental Methods for Engineers,* McGraw-Hill.

HUGHES, W. F. & BRIGHTON, J. A. (1991) *Fluid Dynamics*, Schaum's Outline Series.

JACKSON, A., LIU, X., PATON, R. (2006) Squeeze Flow Characteristic of Thermoplastic Polymer. *Composite Structures,* 75, 179-184.

KELLER, T., VALLÉE, T. (2005) Adhesively bonded lap joints from pultruded GFRP profiles. *Composites: Part B,* 36, 331 - 340.

KILWIN, J. J., NEWCOMER, R.J. (2006a) Minimum Bond Thickness Assembly Feature Assurance. *Patent Application Publication,* BOEING. US2006/0113451 A1, United States

KILWIN, J. J., PISZAR, J.S., MATHIESEN, C.B. (2006b) Adhesive Injection Process For Pi-Joint Assemblies. *Patent Application Publication,* BOEING. US 2006/0243382 A1, United States

LAUN, H. M., RADY, M., HASSEGER, O. (1999) Analytical solution for squeeze flow with partial wall slip. *Journal of Non-Newtonian Fluid Mechanics,* 81, 1-15.

LEIDER, P. J. (1974) Squeezing flow between parallel disks II. *Industrial and Engineering Chemical Fundamentals,* 13, 342-346.

LIU, X. (2006) Prediction of distortion in flanged laminates using viscoelastic model. CRC-ACS TM07006.

LIU, X., BURKA, P, SHEARIDAN, J, THOMPSON, M, PATON, R (2009) Deliverable D7.2.2: "On Tolerance Control of Pi-joints during ISF Bonding Process".

LOCTITE (2007) Hysol EA 9395 Epoxy Paste Adhesive - Material Data Sheet. Bay Point, CA, Loctite Corporation.

MALKIN, A. (1994) *Rheology Fundamentals,* Toronto, Canada, ChemTech Publishing.

MANNAN, S. H., WHALLEY, D.C., OGUNJIMI, Y.O., WILLIAMS, D.J. (1995) Modelling of the initial stages off the anisotropic adhesive joint assembly process. *IEEE Electronic Manufacturing Technology Symposium.* Omiya, Japan.

MATTHEWS, F. L. (1987a) *Joining Fibre-Reinforced Plastics*, Elsevier Science & Technology.

MATTHEWS, F. L. (1987b) Joining Fibre-Reinforced Plastics: Introduction. IN MATTHEWS, F. L. (Ed.) *Joining Fibre-Reinforced Plastics.* London, New York, Elsevier Applied Science Publishers LTD, 4-8.

MATTHEWS, F. L., LEONG, W.K. (1980) *Proc. 3rd Int. Conference on Composite Materials*.

MATTHEWS, F. L., NIXON, A. AND WANT, G.R. (1976) *Bolting and riveting in fibre-reinforced plastics. Proc. Reinforced Plastics Congress.* Brighton, The British Plastics Federation, London.

MEETEN, G. H. (2002) Constant-force squeeze flow of soft solids. *Rheological Acta,* 41, 557-566.

MEETEN, G. H. (2004) Effects of plate roughness in squeeze flow rheometry. *Journal of Non-Newtonian Fluid Mechanics,* 124, 51-60.

MENGES, G., HABERSTROH, E., MICHAELI, W., SCHMACHTENBERG, E. (2002) Verhalten in der Schmelze. *Werkstoffkunde Kunststoffe.* Carl Hanser Verlag München Wien, 87-111.

MOJO (2006) Modular Joints for Composite Aircraft Components. Appendix I. Description of Work.

MOJO (2007) Deliverable D2.1.1: Report of load cases and overall geometry for verification structure, including material and process requirements.

MOJO (2009) Deliverable D2.3.2.2, "Final drawing set of A-level components: composite parts".

MUNSON, B., YOUNG, DF, OKIISHI, TH (2006) *Fundamentals of Fluid Mechanics,* New Jersey, John Wiley & Sons, Inc.

NAVY (2005) Aircraft Primary Structure Adhesive Binding Development. *Status Report September 2005.*

OKA, S. (1960) The Principles of Rheometry. IN EIRICH, F. (Ed.) *Rheology - theory and practice.* New York, Academic Press, 17-82.

OPLINGER, D. W. (1994) Effects of adherend deflections in single lap joints. *International Journal of Solids and Structures,* 31, 2565-2587.

PANTANKAR, S. V. & SPALDING, D. B. (1972) A calculation procedure for hear, mass and momentum transfer in three-dimensional flows. *International Journal of Heat and Mass Transfer,* 15, 1787 - 1806.

PARKS, D. M., ARGON, A.S., BAGEPALLI, B. (1984) Large elastic-plastic deformation of glassy polymers. *MIT program in Polymer Science and Technology Report.*

PETRIE, E. (2004) Handbook of Adhesives and Sealants. McGraw-Hill.

POTTER, K. D., DAVIES, R., BARRETT, M., GODBEHERE, A., BATEUP, L., WISNOM, M., MILLS, A. (2001a) Heavily loaded bonded composite structure: design, manufacture and test of 'I' beam specimens. *Composite Structures,* 51, 389-399.

POTTER, K. D., GUILD,F.J., HARVEY, H.J., WISNOM, M.R. , ADAMS, R.D. (2001b) Understanding and control of adhesive crack propagation in bonded joints between carbon fibre composite adherends I. Experimental. *International Journal of Adhesion & Adhesives,* 21, 435-443.

REICHL, P. (2002) Flow Past A Cylinder Close To A Free Surface. *Department of Mechanical Engineering.* Melbourne, Monash University.

RENTON, V. J., VINSON, J.R. (1977) Analysis of adhesively bonded joints between panels of composite materials. *Journal of Applied Mechanics,* 44, 101-107.

RHEOMETRICS (1991) *Rheometrics Fluids Spectrometer II (RFS II) Owner's Manual,* New Jersey, USA.

RITTER, G. (2005) Adhesive bonding studied for joints in aricraft structures. *Advanced Materials and Processes,* July 1, 2005, 21.

RUSSEL, J. D. (2006) Composites Affordability Initiative: Transitioning Advanced Aerospace Technologies through Cost and Risk Reduction. *The AMMTIAC Quarterly,* 1.

RUSSEL, J. D. (2007) Market Trends: The Composite Affordability Initiative, Part I. http://www.compositesworld.com/columns/market-trends-the-composites-affordability-initiative-part-i.aspx

SABAR, H., BERVEILLER, M., FAVIER, V., BERBENNI, S. (2002) A new class of micro-macro models for elastic-viscoplastic heterogeneous materials. *International Journal of Solids and Structures,* 39, 3257-3276.

SCHOLLER, J. (2007) Pneumatic cylinder pressure. Augsburg.

SCHROEDER, W. (2000) *Fluidmechanik,* Aachen, Wissenschaftsverlag Mainz in Aachen.

SCOTT, J. R. (1931) Theory and application of parallel-plate plastometer. *Trans. Int. Rubber Ind.,* 7, 169-175.

SEEVARATNAM, G., WALKER, L.M., RAME, E., GAROFF, S. (2005) Wetting by simple room-temperature polymer melts: Deviations from Newtonian behavior. *Journal of Colloid Interface Science,* 284, 265-270.

SEEVARATNAM, G. K., SUO, Y., RAME, E., WALKER, L.M., GAROFF, S. (2007) Dynamic wetting of shear thinning fluids. *Physics of Fluids,* 19, 012103-1 - 012103-9.

SHENEY, A. V. (1999) *Rheology of filled polymer systems*, Kluwer Academic Publisher, The Netherlands.

SHERWOOD, J. D. (2008) Transient flow of viscoelastic, thixotropic fluid in a vane rheometer or infinite slot. *Journal of Non-Newtonian Fluid Mechanics,* 154, 109-119.

SHIN, K. C., LEE, J. J. & LEE, D. G. (2000) A study on the lap shear strength of a co-cured single lap joint. *J. Adhesion Sci. Technol.,* 14, 123-139.

SHIN, K. C., LEE, J.J. (2003) Effects of bond parameters on fatigue characteristics of a cocured double lap joint subjected to cyclic tensile load. *The Journal of Adhesion,* 79, 581-596.

SMITH, T., FERRY, J. & SCHREMP, F. (1948) Measurements of the Mechanical Properties of Polymer Solutions by Electromagnetic Transducers. *Journal of Applied Physics,* 20, 144-153.

SPEEDMIXER^{TM,} F. I. (2009) Specializing in centrifugal mixing technology; DAC 150 Series. http://www.speedmixer.com/dac150series.php

SPENCER, A. J. M. (2001) A theory of viscoplasticity for fabric-reinforced composites. *Journal of Mechanics and Physics of Solids,* 49, 2667-2687.

TSAI, M. Y., MORTON, J. (1994) An evaluation of analytical and numerical solutions to the single-lap joint. *International Journal of Solids and Structures,* 31, 2537-2563.

TSAI, M. Y., OPLINGER, D.W., MORTON, J. (1998) Improved theoretical solutions for adhesive lap joints. *International Journal of Solids and Structures,* 35, 1163-1185.

UHLHERR, P. (2009) Discussion about thixotropic measurements results. Monash University, Clayton Campus, Melbourne, Victoria.

VERSTEEG, H. K. & MALALASEKERA, W. (1995) *An introduction to Computational Fluid Dynamics, The Finite Volume Method*, Logman Scientific and Technical.

VOLKERSEN, O. (1938) Die Nietkraftverteilung in zugbeanspruchten konstanten Laschenquerschnitten. *Luftfahrtforschung,* 15, 41-47.

VOLKERSEN, O. (1965) Recherches sur la théorie des assemblages collés. *Journal metallique,* 4.

WANG, Y., DU, X. (2005) Nonlinear Constitutive Model of Uncured Epoxy Resin. *Journal of Macromolecular Science, Part B: Physics,* 44, 177-184.

WONG, R. (1992) Sandwich Constructions in the Starship. *SAMPE Symposium and Exhibition: Materials working for you in the 21st Century,* 37, 186-197.

YOUNGS, D. L. (Ed.) (1982) *Time-Dependent Multi-Material Flow with Large Fluid Distortion*, Academic Press.

Appendix A

The constant force UDF developed to impose a velocity to the moving boundary within a constant force controlled insertion process is provided below. A define centre of gravity motion (DEFINE_CG_MOTION) macro function provided by Fluent is used to impose the motion of the boundary to the required thread (insertion plate walls). Required parameters are provided by Fluent for each time step, i.e. the pressure force and wall shear forces, and their values are used to conduct a force balance with the purpose to derive the actual velocity of the insertion plate caused by the implied constant force.

```
#include "udf.h"

static real v_prev = 0.0;

DEFINE_CG_MOTION(constant_force, dt, vel, omega, time, dtime)
{
    Domain *d;

    Thread *t;
    Thread *insertionbottom;
    Thread *insertionleft;
    Thread *insertionright;

    face_t f;
    real NV_VEC(A);
    real force, wall_shear_force_left, wall_shear_force_right, total_force, dv;

    int zoneID1 = 8;
    int zoneID2 = 9;
    int zoneID3 = 7;

    float constant_force = 3000.0;
    float weight_force = 0;
```

```
float mass_plate = 10;




/* set scalar velocities - indicated by capital S in NV_S - to 0.0 */
NV_S(vel, = , 0.0);
NV_S(omega, = , 0.0);

if (!Data_Valid_P())
        return;

d = Get_Domain(1);
/* get the thread pointer from the fluent solver for which this
   motion will be defined */
t = DT_THREAD(dt);




/* compute the pressure force by getting the pressure
   for each face from fluent in looping over all faces;
   multiply the pressure for each cell with its vector
   magnitude */
insertionbottom = Lookup_Thread(d,zoneID1);
force = 0.0;
begin_f_loop(f,insertionbottom)
        {
        F_AREA(A,f,insertionbottom);
        force += F_P(f,insertionbottom) * NV_MAG(A);
        }
end_f_loop(f,insertionbottom);
Message ("pressure_force = %f \n", force);




/* calculate wall shear forces left wall */
insertionleft = Lookup_Thread(d,zoneID2);
```

```
wall_shear_force_left = 0.0;
begin_f_loop(f,insertionleft)
{
F_AREA(A,f,insertionleft);
wall_shear_force_left    +=    NV_MAG(F_STORAGE_R_N3V(f,insertionleft,
SV_WALL_SHEAR)); // sum up wall shear forces along left insertion wall
}
end_f_loop(f,insertionleft)
Message ("wall_shear_force_left = %f \n", wall_shear_force_left);



/* calculate wall shear forces right wall */
insertionright = Lookup_Thread(d,zoneID3);
wall_shear_force_right = 0.0;
begin_f_loop(f,insertionright)
{
F_AREA(A,f,insertionright);
wall_shear_force_right    +=    NV_MAG(F_STORAGE_R_N3V(f,insertionright,
SV_WALL_SHEAR));
}
end_f_loop(f,insertionright)
Message ("wall_shear_force_right = %f \n", wall_shear_force_right);



/* calculate the change in velocity according to force balance on body */
total_force = force + wall_shear_force_left + wall_shear_force_right;
dv = dtime / mass_plate * (total_force - constant_force - weight_force);
v_prev += dv;
Message ("time = %f, y_vel = %f, force = %f\n", time, v_prev, total_force);


/* set y-component of velocity */
vel[1] = v_prev;
}
```

Appendix B

The fluid structure interaction UDF developed to consider flexibility of Pi-slot walls is provided below. A define geometry (DEFINE_CG_MOTION) macro function provided by Fluent is used to generate an every time step updating thread along which the tip of the Pi-slot walls is able to move. A DEFINE_ADJUST macro function is developed to calculate – based on the adhesive pressure and the flow front position, which is called from another UDF – the deflection of the Pi-slot walls and supply Fluent with this information. The flow front UDF is developed on the basis of a DEFINE_EXECUTE_AT_END UDF. More details can be found in (Fluent, 2005b)

```
#include "udf.h"

DEFINE_GEOM(fsi_plane_left, domain, dt, position)
{
    position[1] = 0.0345;
}

DEFINE_ADJUST(slot_left_FSI,d)
{
 Thread *tf;
 Thread *slot_left_bottom;

 face_t f;
 Node *node_p;
 real x,y;
 real E = 50000000000;
 real w = 0.0025;
 real h = 1.35;
 real u;
 real L;
 real V = 0.0;
```

```
int i = 0;
int n;
int zoneID1 = 5;
int zoneID2 = 14;
float p_max;



/* Get the maximum pressure that is used in the beam deflection    */
/* calculation to predict the deflection of the slot walls         */

  slot_left_bottom = Lookup_Thread(d,zoneID1);
  p_max = 0.0;
  begin_f_loop(f,slot_left_bottom)
  {
      F_P(f,slot_left_bottom);
      p_max = F_P(f,slot_left_bottom);
      //Message ("pmax = %f \n", p_max);
  }
  end_f_loop(f,slot_left_bottom);
  Message ("p_max = %f \n", p_max);



/* Get the flow front values so that it is known at which position */
/* of the adhesive is in order to use the correct beam defl. eqn.  */

  tf = Lookup_Thread(d,zoneID2);

  begin_f_loop(f,tf)
  {
      i = i + 1;
      //Message ("F_UDSI() = %f\n", F_UDSI(f,tf,0));
      V += F_UDSI(f,tf,0);
      //Message (" V = %f \n", V);
  }
```

```
    end_f_loop(f,tf);
    Message (" V = %f \n", V);
    F_UDMI(f,tf,0) = V / i;


    if(V == 0)
        L = 0.0064;
    else
        L = 0.0355 * (1 - F_UDMI(f,tf,0));


    Message ("F_UDMI = %f \n", F_UDMI(f,tf,0));
    Message ("L = %f \n", L);



    /* Set/activate the deforming flag on adjacent cell zone, which      */
    /* means that the cells adjacent to the deforming wall will also be  */
    /* deformed, in order to avoid skewness.                             */



    SET_DEFORMING_THREAD_FLAG (THREAD_T0 (tf));



    /* Loop over the deforming boundary zone's faces;                    */
    /* inner loop loops over all nodes of a given face;                  */
    /* Thus, since one node can belong to several faces, one must guard  */
    /* against operating on a given node more than once:                 */

    begin_f_loop (f, tf)
      {
        f_node_loop (f, tf, n)
        {
          node_p = F_NODE (f, tf, n);


          /* Update the current node only if it has not been            */
```

```
                    /* previously visited:                      */
    //       if (NODE_POS_NEED_UPDATE (node_p))
    //         {
              /* Set flag to indicate that the current node's       */
                        /* position has been updated, so that it will not be   */
              /* updated during a future pass through the loop:       */
              NODE_POS_UPDATED (node_p);


                  y     = NODE_Y (node_p);



                  if(y <= L)
                  {
                          x = NODE_X (node_p);
                          x  =  -0.003  +  p_max  *(pow(y,5)  -  5*pow(y,4)*L  +
10*pow(y,3)*pow(L,2)

                                  - 10*pow(y,2)*pow(L,3)) / (10*E*L*pow(w,3));
                          NODE_X (node_p) = x;
                  }


                  else if (y > L)
                  {
                          x = NODE_X (node_p);
                    x  =  -0.003  +  p_max  *(pow(L,4)  -  5*pow(L,3)*y)  /
(10*E*pow(w,3));

                          NODE_X (node_p) = x;
                  }
          }
    //    }
      }
    end_f_loop (f, tf);
    Message ("x-coord-left = %f, y-coord-left = %f, PMAX-left = %f \n", x, y, p_max);
    }
/*************************END OF UDF*************************/
```

```c
# include "udf.h"
# define domain_ID 2

DEFINE_EXECUTE_AT_END(volume_fraction_left)
{

  Domain *domain;
  Thread *tf;
  face_t f;
  int zoneID1 = 14;
  float i = 0.0;
  float V = 0.0;

  domain = Get_Domain(domain_ID);
  tf = Lookup_Thread(domain,zoneID1);

  Message("i = %f \n", i);

  /* Fill UDS with the variable. */

    begin_f_loop (f,tf)
     {
       i = i + 1;
              F_UDSI(f,tf,0) = F_VOF(f,tf);
              //V += F_UDSI(f,tf,0);
              /*V = V / i;
              F_UDMI(f,tf,0) = V;
              Message("F_UDSI = %f    V = %f \n", F_UDSI(f,tf,0), V);*/
     }
    end_f_loop (f,tf)

  Message("i = %f \n", i);
  V = V / i;
```

```
    F_UDMI(f,tf,0) = V;


    Message("V / i = %f \n", V);
    Message("F_UDMI(0) = %f \n", F_UDMI(f,tf,0));
    Message("F_UDSI(0) = %f \n", F_UDSI(f,tf,0));


}
/***************************END OF UDF***************************/
```